# Rolling Isolation Systems:

# Modeling, Analysis, and Assessment

by

Philip Scott Harvey, Jr.

Department of Civil and Environmental Engineering
Duke University

Date: _____

Approved:

_____
Henri P. Gavin, Supervisor

_____
Wilkins Aquino

_____
Earl H. Dowell

_____
Omar M. Knio

_____
Lawrence N. Virgin

Dissertation submitted in partial fulfillment of the requirements for the degree of
Doctor of Philosophy in the Department of Civil and Environmental Engineering
in the Graduate School of Duke University

2013

# Abstract

(Civil and Environmental Engineering)

# Rolling Isolation Systems: Modeling, Analysis, and Assessment

by

Philip Scott Harvey, Jr.

Department of Civil and Environmental Engineering
Duke University

Date: _____

Approved:

_____
Henri P. Gavin, Supervisor

_____
Wilkins Aquino

_____
Earl H. Dowell

_____
Omar M. Knio

_____
Lawrence N. Virgin

An abstract of a dissertation submitted in partial fulfillment of the requirements for the degree of Doctor of Philosophy in the Department of Civil and Environmental Engineering in the Graduate School of Duke University

2013

# Abstract

The rolling isolation system (RIS) studied in this dissertation functions on the principle of a rolling pendulum; an isolated object rests on a steel frame that is supported at its corners by ball-bearings that roll between shallow steel bowls, dynamically decoupling the floor motion from the response of the object. The primary focus of this dissertation is to develop predictive models that can capture experimentally-observed phenomena and to advance the state-of-the-art by proposing new isolation technologies to surmount current performance limitations. To wit, a double RIS increases the system's displacement capacity, and semi-active and passive damped RISs suppress the system's displacement response.

This dissertation illustrates the performance of various high-performance isolation strategies using experimentally-validated predictive models. Effective modeling of RISs is complicated by the nonholonomic and chaotic nature of these systems which to date has not received much attention. Motivated by this observation, the first part of this dissertation addresses the high-fidelity modeling of a single, undamped RIS, and later this theory is augmented to account for the double (or stacked) configuration and the supplemental damping via rubber-coated bowl surfaces. The system's potential energy function (i.e. conical bowl shape) and energy dissipation model are calibrated to free-response experiments. Forced-response experiments successfully validate the models by comparing measured and predicted peak displacement and acceleration responses over a range of operating conditions.

Following the experimental analyses, numerical simulations demonstrate the potential

benefits of the proposed technologies. This dissertation presents a method to optimize damping force trajectories subject to constraints imposed by the physical implementation of a particular controllable damper. Potential improvements in terms of acceleration response are shown to be achievable with the semi-active RIS. Finally, extensive time-history analyses establish how the undamped and damped RISs perform when located inside biaxial, hysteretic, multi-story structures under recorded earthquake ground motions. General design recommendations, supported by critical-disturbance spectra and peak-response distributions, are prescribed so as to ensure the uninterrupted operation of vital equipment.

To my loving parents Philip and Susan Harvey

# Contents

**Abstract** **iv**

**List of Tables** **xv**

**List of Figures** **xvi**

**List of Symbols and Abbreviations** **xxi**

**Acknowledgements** **xxvi**

**1 Introduction** **1**

1.1 Seismic Isolation for Vibration-Sensitive Secondary Structures . . . . . 2

1.2 High-Performance Rolling Isolation . . . . . 6

1.2.1 Increase displacement capacity . . . . . 8

1.2.2 Decrease displacement demand . . . . . 8

1.2.3 Intelligent adaptive isolation . . . . . 11

1.3 Dissertation Overview . . . . . 12

1.3.1 Research contributions . . . . . 12

1.3.2 Organization . . . . . 14

**2 The Calculus of Variations and Nonholonomic Dynamics** **16**

2.1 Background . . . . . 16

2.2 Hamilton's Principle . . . . . 17

2.3 System Dynamics . . . . . 19

2.3.1 Holonomic system . . . . . 19

2.3.2 Nonholonomic system . . . . . 20
2.3.3 Dissipative forces . . . . . 24
**3 The Nonholonomic and Chaotic Nature of a Rolling Isolation System 25**
3.1 Background . . . . . 25
3.2 Equations of State . . . . . 28
3.2.1 Kinetic energy . . . . . 30
3.2.2 Potential energy . . . . . 31
3.2.3 Kinematics of rolling ball-bearings . . . . . 33
3.2.4 Fundamental nonholonomic form of Lagrange's equation . . . . . 35
3.2.5 System dynamics . . . . . 39
3.3 Energy Conservation . . . . . 40
3.4 Bowl Fitting . . . . . 42
3.5 Energy Dissipation . . . . . 44
3.6 Numerical Results . . . . . 48
3.6.1 Confirmation of energy conservation . . . . . 49
3.6.2 Chaotic response . . . . . 49
3.6.3 Effect of the bowl profile on system responses . . . . . 52
3.7 Summary . . . . . 53
**4 A Simplified and Experimentally-Validated Predictive Model of a Rolling Isolation System 55**
4.1 Background . . . . . 55
4.2 Simplified Model of a Rolling Isolation System . . . . . 57
4.2.1 Geometry and notation . . . . . 57
4.2.2 Kinematics of rolling ball-bearings . . . . . 58
4.2.3 Equations of motion . . . . . 59
4.3 Experimental Set-up . . . . . 59

4.4 Bowl-shape Function . . . 61
4.4.1 Experimental characterization . . . 62
4.5 Experimental Validation of the Predictive Model . . . 65
4.5.1 Idealized floor motion model . . . 65
4.5.2 Experiment design . . . 67
4.5.3 Peak response quantities . . . 69
4.5.4 Peak response spectra . . . 70
4.6 Frontiers of Impact . . . 74
4.7 Summary . . . 76
4.7.1 Possible extensions . . . 77
**5 Vibration Suppression Using Double Rolling Isolation Systems: Theory 79**
5.1 Background . . . 79
5.2 Equations of Motion . . . 81
5.2.1 Kinetic energy . . . 82
5.2.2 Potential energy . . . 85
5.2.3 Kinematics of rolling ball-bearings . . . 87
5.2.4 Fundamental nonholonomic form of Lagrange's equation . . . 88
5.2.5 System dynamics . . . 93
5.3 Numerical Simulations . . . 93
5.3.1 Unforced response . . . 94
5.3.2 Forced response . . . 97
5.4 Summary . . . 101
**6 Vibration Suppression Using Double Rolling Isolation Systems: Experimental Validation 102**
6.1 Background . . . 102
6.2 Simplified Model of a Double Rolling Isolation System . . . 103

6.2.1 Geometry and notation . . . 103
6.2.2 Kinematics of rolling ball-bearings . . . 105
6.2.3 Equations of motion . . . 106
6.3 Experimental Set-up . . . 107
6.4 Experiment Design . . . 109
6.5 Experimental Validation of the Predictive Model . . . 110
6.5.1 Peak response spectra . . . 113
6.6 Summary . . . 115
**7 Optimal Performance of Constrained Control Systems 117**
7.1 Background . . . 117
7.2 Necessary Conditions for Optimality . . . 121
7.2.1 Linear-quadratic constrained control . . . 125
7.3 Optimal Constrained Control Law . . . 126
7.4 Semi-Active Control . . . 128
7.4.1 Semi-active force constraint . . . 128
7.4.2 Implementation of saturation function for semi-active systems . . . 129
7.5 Numerical Example . . . 131
7.5.1 Tuned-mass-damper system . . . 131
7.5.2 Pulse-like disturbance model . . . 133
7.5.3 Performance index and numerical values . . . 135
7.5.4 MATLAB procedure . . . 136
7.5.5 Optimized semi-active control trajectories . . . 137
7.6 Summary . . . 139
7.6.1 Possible extensions . . . 140

**8 Assessment of a Semi-Active Rolling Isolation System 142**

8.1 Background . . . 142

8.2 Linear Model of an Isolation System . . . 143

8.2.1 Semi-active force constraints . . . 145

8.2.2 Semi-active control to reduce accelerations . . . 146

8.2.3 Disturbance Model . . . 147

8.3 Simulation Results . . . 148

8.3.1 Isolation Control Schemes . . . 149

8.3.2 Single-degree-of-freedom system . . . 150

8.3.3 Three-degree-of-freedom system . . . 152

8.4 Summary . . . 155

**9 Vibration Suppression Using Damped Rolling Isolation Systems: Theory and Experimental Validation 159**

9.1 Background . . . 159

9.2 Simplified Model of a Damped Rolling Isolation System . . . 162

9.2.1 Geometry and notation . . . 162

9.2.2 Kinematics of rolling ball-bearings . . . 163

9.2.3 Equations of motion . . . 164

9.2.4 Bowl-shape function . . . 164

9.3 Experimental Characterization of Rolling Resistance . . . 166

9.3.1 Experimental set-up . . . 166

9.3.2 Hierarchical modeling . . . 167

9.4 Experimental Validation of the Predictive Model . . . 171

9.4.1 Experimental set-up . . . 171

9.4.2 Prediction of free responses . . . 172

9.4.3 Disturbance model for forced-response tests . . . 174

9.4.4 Experiment design . . . . . 174
9.4.5 Prediction of forced-response time histories . . . . . 175
9.4.6 Prediction of peak response spectra . . . . . 178
9.5 Frontiers of Impact Revisited . . . . . 180
9.6 Summary . . . . . 183

**10 Assessment of the Seismic Performance of Undamped and Damped Rolling Isolation Systems 184**

10.1 Background . . . . . 184
10.2 Structural Systems Considered . . . . . 185
10.3 Model Reduction for Hysteretic Systems . . . . . 187
10.3.1 Dynamic Guyan condensation . . . . . 188
10.3.2 Extended Rayleigh damping . . . . . 189
10.3.3 Three-dimensional, symmetrical model . . . . . 190
10.3.4 Treatment of biaxial hysteresis . . . . . 191
10.3.5 Model verification via pushover analyses . . . . . 194
10.4 Selected Earthquake Ground Motions . . . . . 195
10.5 Assessment of the Seismic Performance of Rolling Isolation Systems . . 198
10.5.1 Response analysis . . . . . 198
10.5.2 General design guidelines . . . . . 207
10.6 Summary . . . . . 210

**11 Summary, Conclusions, and Future Work 213**

11.1 Summary and Conclusions . . . . . 213
11.2 Future Work . . . . . 216

**A On the Chaotic Response of a Nonlinear Rolling Isolation System 218**

A.1 Background . . . . . 219
A.2 Mathematical Modeling . . . . . 221

A.2.1 Bowl profile function . . . 222
A.2.2 Force-displacement relationship . . . 222
A.2.3 Mass-dependent damping model . . . 223
A.3 Numerical Simulation . . . 224
A.3.1 Unforced response . . . 224
A.3.2 Harmonically-forced response . . . 226
A.4 Summary . . . 231
**B Assessing the Accuracy of Vision-Based Accelerometry 233**
B.1 Background . . . 234
B.2 Photogrammetric Procedure . . . 235
B.2.1 The set-up . . . 235
B.2.2 Video image processing and calibration . . . 235
B.2.3 Computing acceleration from position . . . 235
B.3 Experimental Accuracy Assessment . . . 236
B.3.1 Sine-sweep signal tracking . . . 236
B.3.2 Video signal synchronization . . . 237
B.4 Results and Discussion . . . 237
B.4.1 Time-series analyses . . . 237
B.4.2 Sensitivity of acceleration accuracy . . . 241
B.5 Summary . . . 241
**C Optimal Control MATLAB Functions 243**
**D Truly Isotropic Biaxial Hysteresis with Arbitrary Knee Sharpness 245**
D.1 Introduction . . . 245
D.2 Background . . . 246
D.2.1 Bouc-Wen uniaxial hysteretic model . . . 246

D.2.2 Park-Wen biaxial hysteretic model . . . . . 247
D.2.3 Wang-Wen biaxial hysteretic model . . . . . 248
D.3 A Truly Isotropic Biaxial Hysteretic Model . . . . . 249
D.4 Numerical Examples . . . . . 250
D.4.1 Unidirectional motion . . . . . 250
D.4.2 Bidirectional motion . . . . . 252
D.5 Summary . . . . . 252
**Bibliography** **254**
**Biography** **271**

# List of Tables


3.1 Estimated mean and coefficient of variation for fit parameters $\beta_i$ . . . . . 43

3.2 Experimentally fitted parameter $C_\mathrm{d}$ with mean and coefficient of variation 47

3.3 Numerically generated fitted damping coefficient $C_\mathrm{b}$ for varying mass. . . 48

4.1 Fitted bowl gradient function parameters . . . . . 64

4.2 Peak shake table velocities for single, undamped RIS experiments . . . . 68

4.3 Critical disturbance amplitude for an undamped RIS . . . . . 74

4.4 Parameter values for the ASCE 7-10 spectrum design . . . . . 76

6.1 Peak shake table velocities for double, undamped RIS experiments . . . . 108

7.1 Parameter values used in simulation. . . . . 133

8.1 Semi-active control simulation parameters . . . . . 148

8.2 Simulated pulse strengths and periods . . . . . 153

8.3 Three-degree-of-freedom performance objectives under four control regimes 158

9.1 Peak shake table velocities for sing, damped RIS experiments . . . . . 175

9.2 Critical disturbance amplitude for a damped RIS . . . . . 180

10.1 Natural frequencies for the full model and the reduced model . . . . . 187

10.2 Scaled peak ground velocities of the selected ground motions . . . . . 197

10.3 Floor height coefficients . . . . . 199

10.4 Far-Fault ground motions . . . . . 211

10.5 Near-Fault without a pulse ground motions . . . . . 212

10.6 Near-Fault with a pulse ground motions . . . . . 212

# List of Figures


1.1 Iso-Base seismic isolation platform and Iso-Base bearing . . . . . 1

1.2 Common vibration isolation technologies . . . . . 3

1.3 Damped rolling isolations systems . . . . . 9

2.1 Actual and varied paths in extended configuration space . . . . . 19

2.2 A depiction of the variation constraints in extended velocity space . . . . 23

3.1 Exploded view of a single rolling isolation system . . . . . 26

3.2 Rolling equipment isolation system geometry and notation. . . . . 29

3.3 Geometry of a sphere rolling between two non-parallel surfaces. . . . . 33

3.4 3D bowl-shape measurement analysis. . . . . 42

3.5 Photogrammetry measured bowl shapes for a clamped bowl and dished surface data with nonlinear fitted bowl parameterization. . . . . 43

3.6 Experimental setup using three string potentiometers. . . . . 44

3.7 Energy dissipation histories for varying mass using three methods. . . . . 45

3.8 Experimentally fitted damping parameter $C_{\mathrm{d}}$ and approximate damping ratio $\zeta$ for varying mass $m$. . . . . 46

3.9 Free response of single RIS with and without viscous damping. . . . . 48

3.10 Comparison between the free-response trajectories $\bar{x}(t)$, $\bar{y}(t)$, and $\bar{\theta}(t)$ for three initial conditions: measured and predicted. . . . . 50

4.1 Experimental shaking table with rolling equipment isolation system . . . 60

4.2 An example video frame used for the displacement measurements with five LEDs switched on. . . . . 61

4.3 Installed bowl with clamped/free boundary conditions and plastic puck support . . . . . 62

4.4 Experimental free-response displacement and acceleration trajectories . . 63

4.5 Acceleration-displacement relationship of four free-response measurements with the fitted bowl-gradient function and the bowl height . . . . . 64

4.6 Displacement and acceleration input applied to shaking table table: moderate disturbance at $T_p$ = 1 s . . . . . 68

4.7 Measured and predicted displacement and rotation responses of the heavy system: moderate disturbance at $T_p$ = 1.25 s . . . . . 70

4.8 Measured and predicted displacement and rotation responses of the heavy system: strong disturbance at $T_p$ = 0.85 s . . . . . 70

4.9 Measured and predicted acceleration responses of the heavy system: moderate disturbance at $T_p$ = 1.25 s . . . . . 71

4.10 Measured and predicted acceleration responses of the heavy system: strong disturbance at $T_p$ = 0.85 s . . . . . 71

4.11 Peak displacement and acceleration pulse response spectra for the single, undamped rolling isolation system . . . . . 72

4.12 Seismic design spectrum for a single, undamped rolling isolation system. 75

5.1 Exploded view of a double rolling isolation system . . . . . 81

5.2 Double rolling isolation system geometry . . . . . 82

5.3 Geometry of a sphere rolling between two non-parallel surfaces . . . . . 87

5.4 Bowl-shape height and gradient used in double RIS numerical simulations. 94

5.5 Free response of a double RIS without damping. . . . . 95

5.6 Free response of a double RIS with viscous damping. . . . . 97

5.7 Pulse-like disturbances used in the double RIS forced response. . . . . 98

5.8 Forced response of a double RIS: moderate disturbance. . . . . 99

5.9 Forced response of a double RIS: strong disturbance. . . . . 100

6.1 Experimental shaking table with a double rolling isolation system. . . . . 107

6.2 Displacement and acceleration input applied to shaking table table for the strong disturbance with $T_p = 0.85$ s . . . . . 109

6.3 Measured and predicted displacement and rotation responses of the heavy system for the strong disturbance at $T_p = 0.85$ s . . . . . 110

6.4 Measured and predicted displacement and rotation responses of the heavy system for the moderate disturbance at $T_p = 1.60$ s . . . . . 111

6.5 Measured and predicted acceleration responses of the heavy system for the strong disturbance at $T_p = 0.85$ s . . . . . 111

6.6 Measured and predicted acceleration responses of the heavy system for the moderate disturbance at $T_p = 1.60$ s . . . . . 112

6.7 Peak displacement and acceleration pulse response spectra for the double, undamped rolling isolation system . . . . . 114

7.1 Saturation function visualization in extended state space . . . . . 128

7.2 Sector-bound constraint for semi-active damping device . . . . . 129

7.3 Structural model of a single-degree-of-freedom structure with TMD . . . 131

7.4 Acceleration, velocity, and displacement time histories of a pulse-like ground motion and a recorded ground motion . . . . . 135

7.5 Responses to a pulse-like disturbance: optimal, passive, clipped LQR, and uncontrolled . . . . . 138

7.6 Normalized constraint and normalized Lagrange multiplier time histories 138

7.7 Converged control force histories from three initial guesses . . . . . 139

7.8 Responses to a recorded ground motion: optimal, passive, clipped LQR, and uncontrolled . . . . . 139

8.1 Semi-active actuator configuration and platform geometry . . . . . 144

8.2 Pulse-like disturbance acceleration . . . . . 147

8.3 Single-degree-of-freedom optimal control trajectories . . . . . 152

8.4 Single-degree-of-freedom pulse-response spectra . . . . . 153

8.5 Three-degree-of-freedom optimal control trajectories . . . . . 157

9.1 Exploded view of a damped rolling isolation system. . . . . 161

9.2 Damped rolling isolation system geometry. . . . . 162

9.3 Nominal, total, and divot bowl-height $\eta$ and bowl-slope $\eta'$ functions versus bowl radius $r$ . . . . . 166

9.4 Schematic and photograph of the rolling resistance experimental set-up . 167

9.5 Measured shaking table velocity; measured and fitted rolling resistance $R_r$ time histories: $P = 901$ N . . . . . 168

9.6 Fitted and measured rolling resistance $R_r$ versus displacement and velocity for a load of $P_k = 901$ N. . . . . 169

9.7 Fitted and measured force amplitude $\mu$ versus the applied load $P$ . . . . . 170

9.8 Experimental shaking table with damped RIS, steel ball-bearing resting on ("virgin") rubber sheet, and divot formed at the center of the rubber sheet 171

9.9 Measured and predicted free-response histories with initial displacement $\bar{x}_0$ 173

9.10 Measured and predicted free-response histories with initial displacement $\bar{y}_0$ 173

9.11 Measured displacement, velocity and acceleration input applied to shaking table table . . . . . 176

9.12 Measured and predicted displacement and acceleration responses of the light system: strong disturbance at $T_p = 0.50$ s . . . . . 177

9.13 Measured and predicted displacement and acceleration responses of the light system: moderate disturbance at $T_p = 1.00$ s . . . . . 177

9.14 Measured and predicted peak displacement and acceleration pulse response spectra for light system and heavy system . . . . . 179

9.15 Seismic equipment isolation design spectrum for damped and undamped single rolling isolation systems . . . . . 181

10.1 Planar frames used as representative designs . . . . . 186

10.2 Extended Rayleigh damping . . . . . 190

10.3 Representative hysteresis loops . . . . . 193

10.4 Base shear force versus drift ratio . . . . . 196

10.5 Base shear force versus 1st-story drift ratio for varying knee-sharpness parameter . . . . . 197

10.6 Peak displacement empirical CDFs for 4-story, flexible structure . . . . . 201

10.7 Peak displacement empirical CDFs for 4-story, rigid structure . . . . . 202

10.8 Peak displacement empirical CDFs for 8-story, flexible structure . . . . . 203

10.9 Peak displacement empirical CDFs for 8-story, rigid structure . . . . . 204

10.10 Peak displacement empirical CDFs for 12-story, flexible structure . . . . 205

10.11 Peak displacement empirical CDFs for 12-story, rigid structure . . . . . 206

10.12 Peak acceleration empirical CDFs for flexible structures . . . . . 208

10.13 Peak acceleration empirical CDFs for rigid structures . . . . . 209

A.1 Schematic of a rolling isolation system, and experimental ISO-Base ball-bearing and bowl . . . . . 220

A.2 Force-displacement relationship and bowl curvature . . . . . 222

A.3 Undamped natural period $T_n$. . . . . 225

A.4 Unforced response simulation: time-history trajectories and phase projection 226

A.5 Comparison of DFT for periodic and chaotic responses . . . . . 227

A.6 Chaotic boundaries and an example of a chaotic attractor . . . . . 228

A.7 Largest Lyapunov exponent $\lambda_{max}$ and bifurcation diagram with periodic windows ($\omega = 1.5625\pi$ rad/s), and phase projections for four amplitudes . 229

A.8 Largest Lyapunov exponent $\lambda_{max}$ and bifurcation diagram with periodic windows ($A = 8$ m/s$^2$), and phase projections for four frequencies . . . . 230

B.1 LVDT and MEMS accelerometer measurements after signal processing . 238

B.2 Video signal synchronization . . . . . 238

B.3 Absolute displacement error and relative displacement error . . . . . 239

B.4 Absolute acceleration error and relative acceleration error . . . . . 240

B.5 Contours of equal absolute acceleration error in $\bar{d}$-$\bar{f}$ and $\bar{a}$-$\bar{f}$ space. . . . . 242

D.1 Unidirectional hysteretic behavior of Wang-Wen model and proposed model 251

D.2 Bidirectional hysteretic behavior of Wang-Wen model and proposed model 252

# List of Symbols and Abbreviations

## Symbols

Vectors and matrices are denoted by bold lowercase and uppercase letters, respectively. The transpose of a matrix is denoted by the superscript $(\cdot)^\mathsf{T}$, normalized (unit) vectors are denoted by the over-hat $\hat{(\cdot)} = (\cdot)/\|\cdot\|$, and a temporal derivative is denoted by an over-dot, $\dot{(\,)} = \mathrm{d}(\,)/\mathrm{d}t$. Below is a non-exhaustive list of symbols used in this dissertation.

*Calculus of Variations*

| | |
|---|---|
| $\mathbf{c}$ | Inequality constraint vector. |
| $\mathbf{g}$ | Equality constraint vector. |
| $J$ | Cost functional. |
| $J_\mathrm{A}$ | Augmented cost functional. |
| $L$ | Lagrangian function. |
| $\mathbf{z}$ | Generalized coordinate vector. |
| $\boldsymbol{\lambda}$ | Equality constraint multiplier or costate vector. |
| $\Lambda$ | Augmented Lagrangian function. |
| $\boldsymbol{\mu}$ | Inequality constraint multiplier. |

*Rolling Isolation System Model*

| | |
|---|---|
| $\boldsymbol{a}_\mathrm{T}$ | Total acceleration vector of top-frame's centroid. |
| $a_\mathrm{T}^\mathrm{max}$ | Peak total acceleration. |
| $a$, $b$ | Top-platform dimensions. |

| | |
|---|---|
| $C_{\mathrm{b}}$ | Viscous ball damping coefficient. |
| $C_{\mathrm{d}}$ | Fitted equivalent damping rate. |
| $\boldsymbol{d}_{\mathrm{R}}$ | Relative translational displacement vector of top-frame's centroid. |
| $d_{\mathrm{R}}^{\max}$ | Peak relative translational displacement. |
| $E$ | Total energy of system. |
| $e_x$, $e_y$ | Equipment mass eccentricity. |
| $\mathbf{f}_{\mathcal{L}i}$, $\mathbf{f}_{\mathcal{U}i}$ | Gravitational restoring forces attributed to the lower- and upper-bowls. |
| $g$ | Gravitational acceleration. |
| $h_i$ | Height of top-platform at the center of the $i$th bowl. |
| $\eta$ | Proposed radial profile function. |
| $I$ | Equipment mass moment of inertia about centroid. |
| $m$ | Mass of isolated equipment. |
| $\mathbf{p}_i$ | Relative displacement vector of bowl $i$ w.r.t. bottom-frame. |
| $\mathbf{q}_i$ | Relative displacement vector of ball $i$ w.r.t. top-frame. |
| $Q_z^{\mathrm{C}}$ | Constraint force for generalized coordinate $z$. |
| $Q_z^{\mathrm{D}}$ | Non-potential, dissipative forces for generalized coordinate $z$. |
| $\mathbf{r}_i$ | Relative displacement vector of ball $i$ w.r.t. bottom-frame. |
| $\mathbf{R}_\theta$ | Rotation matrix through angle $\theta$. |
| $T$ | Unconstrained kinetic energy function. |
| $V$ | Potential energy function. |
| $\mathbf{v}_i$ | Top-frame velocity vector at $i$th ball location. |
| $v_x$, $v_y$, $v_\theta$ | Global velocities of the center of mass. |
| $w_x$, $w_y$, $w_\theta$ | Translational and rotational base disturbances. |
| $\bar{x}$, $\bar{y}$ | Relative displacements of top-frame. |
| $\alpha_i$ | Polynomial bowl fit parameters. |
| $\beta_i$ | Conical bowl fit parameters. |

| | |
|---|---|
| $\lambda_{\max}$ | Largest Lyanpunov exponent. |
| $\phi_{\mathcal{L}i}$, $\phi_{\mathcal{U}i}$ | Angles of $i$th lower- and upper-bowl parallel to $\mathbf{v}_i$. |
| $\varphi_i$ | Ball velocity ratio. |
| $\bar{\theta}$ | Relative rotation of top-frame. |
| $\zeta$ | Damping ratio. |

*Constrained Optimal Control*

| | |
|---|---|
| $\mathbf{A}$ | State dynamics matrix. |
| $\mathbf{B}$ | Control input matrix. |
| $c_{k,\max}$ | Peak damping rate for device $k$. |
| $\mathbf{f}$ | State dynamics function. |
| $F_{sk}$ | Time-lagged semi-active force for device $k$. |
| $\mathbf{G}$ | Exogenous disturbance input matrix. |
| $H$ | Hamiltonian function. |
| $\mathbf{Q}$ | Quadratic state weighting matrix. |
| $\mathbf{R}$ | Quadratic control weighting matrix. |
| $\mathbf{S}$ | Bilinear state-control weighting matrix. |
| $t_{\mathrm{f}}$ | Finite-horizon terminal time. |
| $T_u$ | Actuator time lag. |
| $\mathbf{u}$ | Control input vector. |
| $u_{k,\max}$ | Peak force for device $k$. |
| $u_{\text{active}}$ | Active or unconstrained control force. |
| $v_k$ | Velocity across actuator $k$. |
| $\mathbf{w}$ | Exogenous disturbance input vector. |
| $\mathbf{x}$ | State vector. |
| $\alpha$ | Parabolic bowl curvature. |
| $\Pi_i$ | Control performance metrics. |

*Damped Rolling Isolation System*

| | |
|---|---|
| $\mathbf{f}_{\mathrm{D}i}$ | Damping force vector. |
| $P$ | Vertical, compressive load on ball-bearing. |
| $R_{\mathrm{r}}$ | Rolling resistance. |
| $\mu$ | Load-dependent force level. |

*Hazard Analysis and Model Reduction*

| | |
|---|---|
| $\tilde{\boldsymbol{C}}$ | Reduced-model damping matrix. |
| $\boldsymbol{d}$ | Full-model displacement vector. |
| $\boldsymbol{M}$ | Full-model mass matrix. |
| $\tilde{\boldsymbol{M}}$ | Reduced-model mass matrix. |
| $\boldsymbol{K}$ | Full-model stiffness matrix. |
| $\tilde{\boldsymbol{K}}$ | Reduced-model stiffness matrix. |
| $u_{\mathrm{g}}$ | Earthquake ground motion. |
| $\boldsymbol{u}_x$, $\boldsymbol{u}_y$ | Inter-story displacement vectors relative. |
| $\boldsymbol{x}$, $\boldsymbol{y}$ | Displacement vectors relative to the structure's base. |
| $\boldsymbol{z}_x$, $\boldsymbol{z}_y$ | Hysteretic displacement vectors. |
| $\beta_i$ | Hysteresis parameter. |
| $\gamma_i$ | Hysteresis parameter. |
| $\boldsymbol{\iota}$ | Biaxial interaction function. |
| $\kappa$ | Post- to pre-yield stiffness ratio. |
| $\eta$ | Hysteretic knee-sharpness parameter. |

## Abbreviations

Below is a non-exhaustive list of abbreviations used in this dissertation.

| | |
|---|---|
| ARE | Algebraic Riccati equation. |

| | |
|---|---|
| CDF | Cumulative distribution function. |
| CV | Coefficient of variation. |
| FF | Far-Fault. |
| LE | Lyapunov exponent. |
| LM | Levenberg-Marquardt. |
| LQ | Linear-quadratic. |
| LQR | Linear-quadratic regulator. |
| LTI | Linear time-invariant. |
| NFNP | Near-Fault with no pulse. |
| NFP | Near-Fault with pulse. |
| PGA | Peak ground acceleration. |
| PGV | Peak ground velocity. |
| PSA | Pseudo spectral acceleration. |
| RIS | Rolling isolation system. |
| SDOF | Single-degree-of-freedom. |
| TPBVP | Two-point boundary-value problem. |

# Acknowledgements

First and foremost, I should like to acknowledge Prof. Henri Gavin who served as my advisor and my friend throughtout the past four years. During my doctoral research at Duke University, Prof. Gavin allowed me to pursue the problems I found most interesting, leading to fascinating results in tangent fields (nonholonomic—who knew?!). The guidance and support that Prof. Gavin has given me made possible the completion of this research, and I look forward to future collaborations for many years to come.

Special thanks are given to Profs. Wilkins Aquino, Earl Dowell, Omar Knio and Lawrence Virgin for serving on my committee, for reviewing my Ph.D. dissertation, and for their invaluable advice during my doctoral research. I would also like to thank Prof. Jeffrey Scruggs who made many valuable suggestions with the optimal control portion of this dissertation. Additionally, Profs. Kabala, Nadeau and Schaad have guided me, in and out of the classroom, throughout my undergraduate and graduate time at Duke. Their support is gratefully acknowledged. I am grateful to John Tyson of Trilion Optical Test Systems for the digital photogrammetry and to Don Hubbard of WorkSafe Technologies for providing ISO-Base isolation platforms which were used in the experimental portion of this work.

I would also like to take this opportunity to thank my fellow graduate students who made my graduate school experience more than just bearable, but downright fun. In particular, I would like to acknowledge Richard Wiebe for serving as a great colleague and friend through thick and thin (read: Quals, Prelim and Defense and graduation). Richard

was always there to answer my questions about nonlinear dynamics and chaos, which lead to a co-authored publication. I would like to show my sincere thanks to my research group—Ian Cassidy, Gérard Zéhil and Jenni Rinker—for sharing their collective expertise. Ian deserves special recognition for mentoring me and teaching me the way of graduate school and publications. Additionally, I would like to thank my girlfriend Tierney Foster-Wittig, my Dain's Place trivia team—Richard, Ian, Tierney, Tiffany Wilson, Amy Heilman, Kate Abshire and Sarah Brody—, and many more for their friendship and support during our many shared graduate school experiences.

Finally, I thank my loving family—Philip, Susan and Ginger Harvey—for their support through the whole process. Y'all are the best family I could ever hope for, and this work would not have been possible without your continuing encouragement.

This material is based upon work supported by the the Civilian Research and Development Foundation for the Independent States of the Former Soviet Union (CRDF) under Award No. MG1-2319-CH-02 and by the National Science Foundation under Grant No. NSF-CMMI-0704959 (NEES Research), and Grant No. NSF-CMS-0402490 (NEES Operations) and Grant No. NSF-CMMI-0900324. Any opinions, findings, and conclusions or recommendations expressed in this material are those of the authors and do not necessarily reflect the views of the National Science Foundation or the CRDF.

# 1

# Introduction

Systems that mitigate earthquake hazards by enabling the uninterrupted operation of computing facilities, telecommunication networks, and lifeline systems reduce the potential of property, economic, and human losses. Equipment isolation is a promising solution for protecting *mission-critical* systems and *valuable* property from earthquake hazards [2–4]. For example, rolling isolations systems (RISs) are a promising isolation technology with numerous installations and have been the subject of considerable research over the last decade. In particular, the ISO-Base Seismic Isolation Platform, manufactured by Work-

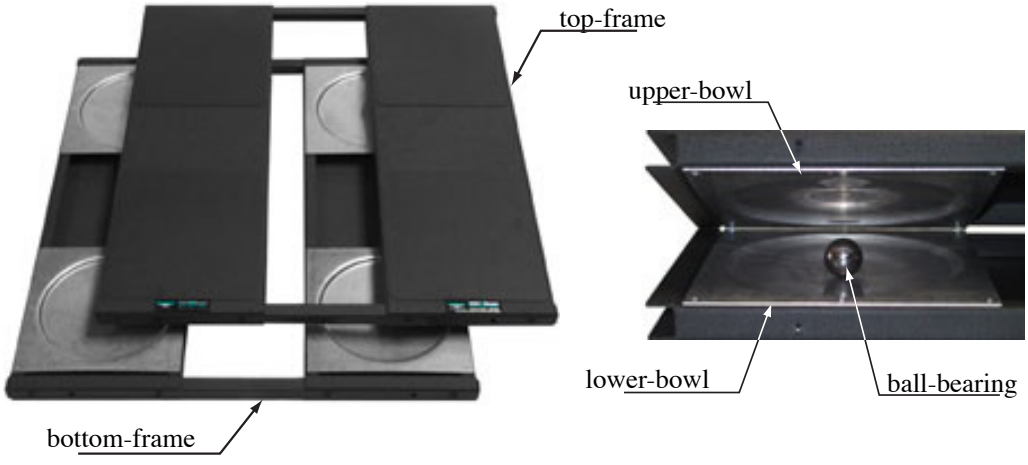


FIGURE 1.1: Iso-Base seismic isolation platform and Iso-Base bearing [1].

Safe Technologies [1] and shown in Figure 1.1, is a common type of RIS and will serve as the prototype in this dissertation. The focus of this dissertation is to develop and experimentally validate models to be used for analyzing the isolation capabilities of RISs, and to propose and test novel approaches to improve the performance of these systems. The work is intended to be an initial, seminal step towards *high-performance* equipment isolation via an improved understanding of the dynamical mechanisms of the system.

## 1.1 Seismic Isolation for Vibration-Sensitive Secondary Structures

The societal and economic impacts of earthquakes have risen sharply over recent decades and will continue to escalate due to the fragility of, and our dependence upon, critical infrastructure facilities. Buildings such as hospitals and emergency command centers need to remain functional during and after major earthquakes for the public welfare and safety. Furthermore, regional and national economic stability now depends upon data centers, telecommunication networks, industrial facilities, and technology centers. Disruption of service in these facilities may result in major direct and indirect economic losses [5]. It is of utmost importance to design and build earthquake resistant primary structures to avoid damage or even collapse. Of equal importance is the protection of secondary structures housed within the primary structure [6]. These secondary structures may be broadly categorized as follow: architectural components (e.g. stairways, cladding), building contents (e.g. artwork, valuable property), and mechanical and electrical equipment (e.g. mainframes, LAN racks, electronics enclosures, telecommunications switches). Note that secondary structures are often alternatively called "nonstructural components," "nonstructural elements," "secondary systems," and "equipment" in various references.

The floor motion in an earthquake-excited structure may cause toppling of free-standing equipment and/or excessively-large relative displacements [7–9]. Restraining or tying down the equipment may prevent toppling and decrease relative displacements, but in-

creases the loads sustained by the equipment [10]. To date, a number of different isolation techniques have been developed and utilized on structures and equipment; e.g. isolation bearings [11–14], sliding isolators [15–27], and rolling isolation systems [28–38]. Figure 1.2 depicts a few common isolation technologies. All are fundamentally similar—the isolated structure (or object) is mechanically decoupled from the ground (or floor) via a compliant, sliding, or rolling interface. In effect, the period of the isolated system is lengthened and shifted away from the predominant periods of the disturbance, reducing resonant effects. Isolation systems are designed to accommodate large relative displacements, allowing for the incorporation of passive damping systems [21, 36] or semi-active control systems [13, 39–42]. RISs are the focus of this dissertation, but valuable insight may be gleaned from the isolation bearing and the sliding isolator literature.

The basic configuration of RISs allows for a broad range of rolling-surface profiles. The dynamic response of RISs depends explicitly on the geometry of the the rolling surface. If the rolling surface is flat, the isolator is incapable of re-centering, in which case a supplemental device may be used to produce restoring forces [33]. Jangid [30] investi-

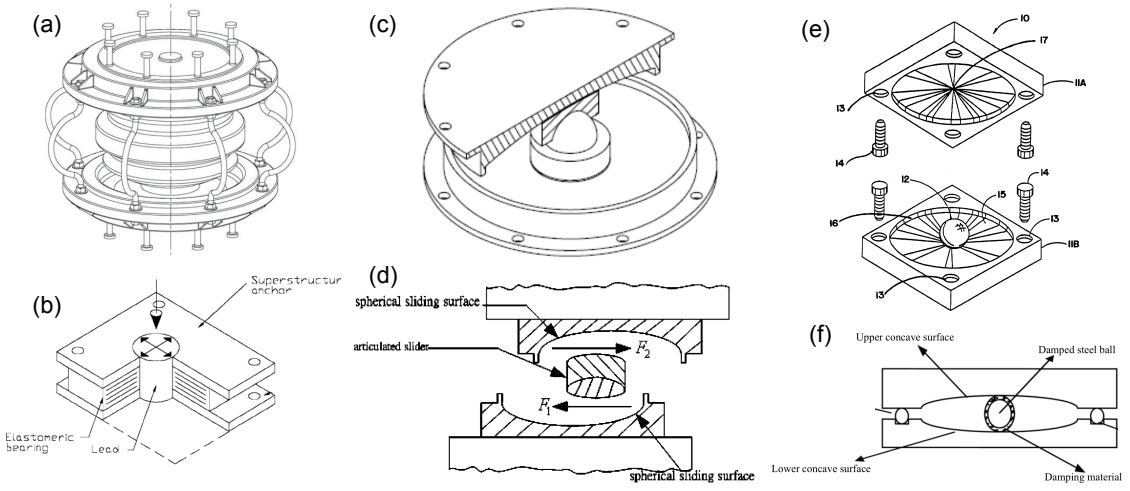


FIGURE 1.2: Common vibration isolation technologies: (a) roll-in-cage isolation system from Ref. [11], (b) lead-rubber isolator from Ref. [14], (c) double friction-pendulum bearing from [20], (d) multiple friction pendulum system isolator from Ref. [18], (e) ball-in-cone rolling isolation system from Ref. [37], and (f) static dynamics interchangeable-ball pendulum system from Ref. [36].

gated the seismic response of a flexible multi-story shear type buildings isolated by rolling rods with a re-centering device, and showed that the rolling rods are quite effective in reducing the stochastic response of the structure against earthquake excitation. Later, Jangid and Londhe [29] modeled and investigated a nonlinear isolation system which possessed elliptical rolling rods. Chung *et al.* [28] modeled a similar rolling rod isolator which incorporated an eccentric pin location; the eccentric nonlinear rolling isolator was shown to outperform the linear isolator under a suite of earthquake ground motions.

In order to eliminate the need of a supplemental re-centering device, the rolling rods or ball-bearings can be interposed between recessed grooves or bowls. Zhou *et al.* [31] proposed a ball system with spherical grooves and studied a base-isolate building with the proposed isolator. In the case of parabolic and spherical rolling surfaces [36], the frequency is nearly constant, which has been shown to be detrimental to the isolation performance near resonance [15, 31]. The ISO-Base platform [37], which is the focus of this dissertation, has (nominally) conical recessed bowls. Conical rolling surfaces produce constant gravitational restoring forces independent of the displacement, limiting the total acceleration experienced by the isolated object [34]. Cui [43] designed, built, and modeled a concrete ball-in-cone isolator based on a similar geometry to the ISO-Base system. In none of these studies were the ball-bearing (or in the planar case roller) dynamics modeled or even mentioned.

Only recently have researchers recognized that the ball-bearings roll without slipping, which implies a constraint on their motion. Antonyuk and Plakhtienko [32, 44] modeled the motion of an RIS with restorative properties, but limited their analysis to rectilinear motion, for which the condition of rolling without slipping is simply a holonomic (geometric) constraint. Whereas, actual RISs are *nonholonomic* and need to be modeled as such. Following the procedure laid out by Legeza [45] which used Appell's energetic approach, Matta *et al.* [46] modeled the nonholonomic dynamics of a rolling pendulum tuned-mass-damper (TMD) vibration absorber. The 'no-slipping and no-detaching' con-

dition was expressed as a kinematic relation (nonholonomic constraint), but Matta *et al.* neglected rotations and assumed that, "because the two identical surfaces are always diametrically opposite to the ball centre by virtue of the symmetry of the configuration, the position of the upper surface relative to the ball centre equals the position of the ball centre relative to the lower surface." However, this is not the case experimentally. Rotations develop from translational motion and the ball-bearings become un-centered. In this dissertation (and Ref. [38]), we eliminate this assumption and are able to model the *true* response of RISs.

The *prediction* of the response of RISs and thus the *evaluation* of their ability protect building contents requires models that can capture the observed non-linear behavior of actual isolation systems subjected to multiaxis shaking. The behavior of RISs are highly complex, and yet the models previously developed in the literature are rudimentary. To date, researchers have primarily focused on the the uniaxial behavior of equipment isolation systems, neglecting the coupling between transverse responses. Therefore, the first objective of this dissertation is to fill the current gap in the modeling of RISs.

Reports of experimental tests on RISs are sparse, especially for multiaxis disturbances. Lin *et al.* [35] performed single-axis shaking table tests on a free-rolling-rod isolation system, similar to the system in Ref. [30], and validated a simple, theoretical model. Guerreiro *et al.* [33], Muhr and Bergamo [47], and Foti *et al.* [48] all studied the same rolling-ball rubber-layer isolation systems which incorporated rubber re-centering springs. All three papers described uniaxial shaking table tests, and all three showed effective reduction of the acceleration levels induced in the structures isolated with such devices. Kasalanti *et al.* [34] performed a preliminary investigation of the behavior of ball-in-cone RISs in bridge isolation applications; the study makes general observations, such as reduction in pier shear force and deck accelerations, but does not attempt to address multiaxial responses. Recently, Tsai *et al.* [36] reported on tridirectional shaking table tests of a 'static dynamics interchangeable-ball pendulum system' (SDI-BPS), in which the steel

ball-bearings are encased in rubber for supplemental damping. Considerable reductions (~50-80 %) in peak acceleration were seen as compared to fixed-base equipment. To date, the most comprehensive series of experiments (free and forced responses) on RISs was performed by Cui [43], in which concrete ball-in-cone isolators with solid rubber and polyurethane balls were used to isolated an entire raised floor in a building. The isolation system was experimentally subjected to sinusoidal and earthquake excitations, both uniaxially and biaxially. Because the concrete RIS is heavily damped, the unidirectional and bidirectional tests showed similar results in terms of peak acceleration responses and small angles of rotation were observed. However, lightly-damped RISs, such as the ISO-Base platform, exhibit strong coupling in orthogonal directions and large rotations. The second objective of this dissertation is to conduct experiments to validate the predictive models derived herein; in these experiments we will analyze the bidirectional response of RISs.

## 1.2 High-Performance Rolling Isolation

Isolation systems have limited displacement capacities. The object resting atop the upper surface is isolated from the disturbance applied through the lower surface via relative motion across the interface. In RISs, a 'lip' at the edge of the rolling and sliding surfaces (shown in Figure 1.2) acts as hard displacement limits on the balls' and articulated sliders' displacements. The isolation systems' displacement capacities are determined by the contact of the balls and sliders with the bowl lip. When the isolator's displacement capacity is insufficient to meet the demands of a disturbance, the performance of the isolator is diminished due to impacts, giving rise to high acceleration responses in the isolated object. To the author's knowledge, this effect has not been addressed in the sliding isolation literature; this is in part due to the higher levels of energy dissipation in these systems and thus smaller displacement responses, in general. The ISO-Base technical documentation [49] states "if the displacement capacity is exceeded, ... either the ball will be forced back into

the dish or the ball will jump out of the dish," in which case the RIS will cease to isolate as intended but "will not fail in a manner that creates a risk to life-safety or to the [isolated object]." Nevertheless, impacts should be avoided at all costs.

Lightly-damped RISs represent a popular method for the seismic protection of fragile objects [37, 50], and these systems can perform extremely well when their displacement demands are small (< 10–15 cm) [41, 51]. However, the suitability of RISs for floor motions corresponding to a structure's design-basis earthquake depends substantially on the peak displacement responses to these floor motions. An experimental and numerical assessment of an undamped RIS shows the challenges of implementing lightly-damped RISs for high intensity motions [52]. An RIS designed for strong (infrequent) floor motions would have either a larger displacement capacity [53] or supplemental damping to reduce displacement demands.

We have theoretically and experimentally demonstrated that RISs may have a deficient displacement capacity when subjected to moderate to strong disturbances at or near their natural period (approximately 1–3 s). Thus, the potential exists for improved performance by means of innovative design concepts. Namely, the following three approaches will be investigated in this dissertation and will serve as major contributions to the field of equipment protection:

1. Increase the displacement capacity by stacking two RISs one on top of the other;
2. Decrease the displacement demand by introducing supplemental passive damping;
3. Intelligently control energy extraction via adaptive (or smart) isolation.

In this dissertation we will numerically assess the potential performance gains achievable using these proposed high-performance isolation techniques through extensive case study.

### *1.2.1 Increase displacement capacity*

Two methods for increasing the displacement capacity of RISs are: (i) increase the bowl diameter and (ii) stack multiple (in this case two) isolators one on top of each other. The former method, while seemingly more practical, has two major shortcomings. First, by increasing the bowl diameter with the platform footprint is held fixed, the four supporting points of the platform (i.e. the apex of the bowls where the ball-bearings rest) are more centrally located. If the platform displacement or mass eccentricity are large enough, the top-frame may overturn. Second, for a conical bowl profile, if the bowl diameter is doubled, then the ball-bearing diameter must also be doubled to ensure adequate clearance between the upper- and lower-bowl under zero displacement. The cost of a steel ball-bearing increases exponentially with diameter, so this approach is cost prohibitive.

The latter method overcomes the shortcomings and of the former method, and is therefore the focus of this dissertation. The proposed double (or stacked) RIS comprises two RISs stacked one on top of the other. The displacement capacity of the stacked configuration is effectively double that of the individual subsystems. Application of this approach to RISs has yet to be investigated, with exception of this dissertation and Refs. [53, 54]. On a related note, the recent studies by Fenz and Constantinou [20, 21] investigated a double and a triple friction pendulum isolation bearing, which has sliding surfaces of different displacement capacities and different coefficients of friction. In that study, the entire focus was on the adaptive stiffness and adaptive damping over displacement amplitudes—*not* on expanding the displacement capacity.

### *1.2.2 Decrease displacement demand*

Harvey and Gavin [38] demonstrated that the energy dissipation in RISs associated with steel ball-bearings rolling between steel dishes is nearly negligible. As such, the second approach toward high-performance equipment isolation is to increasing the inherent en-

ergy dissipation, which will act to decrease the displacement demand. Two methods for supplementing damping in RISs are: (i) encase the steel ball-bearings with a damping material [36] use rubber (or polyurethane) balls [43], and (ii) bonding viscoelastic layers to the counter-facing rolling surfaces [33,47,48]. Both approaches act to increase the rolling resistance and thus increase energy dissipation, decrease isolator displacements, and improve performance over undamped RISs. Example damped RISs are shown in Figure 1.3.

Tsai *et al.* [36] proposed encasing the steel ball-bearing in a "special damping material" (e.g. rubber) to increase the damping and prevent scratches and damage to the steel bowls. The damped RIS of that study is shown in Figure 1.3(a). In the study, it was noted that "the special material covering the steel ball that supports the weight of the vibration sensitive equipment for a long period of time in its service life span causes permanent deformation due to plastic deformation in the damping material." The same, if not worse, can be expected for solid rubber or polyurethane balls, such as those used by Cui [43]. In

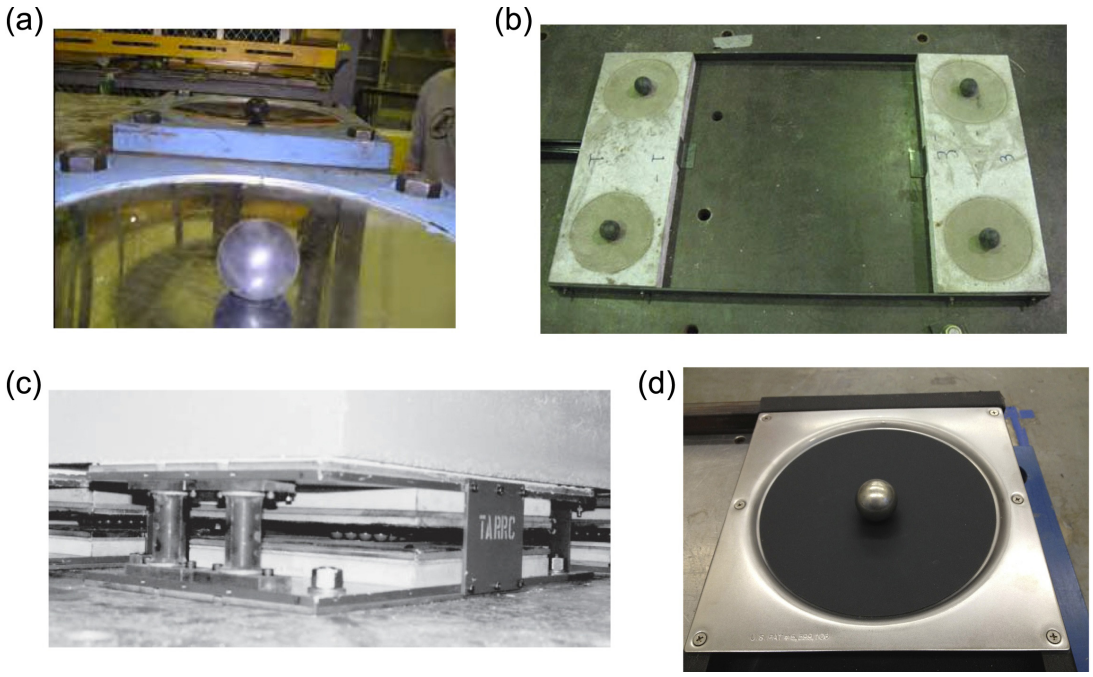


FIGURE 1.3: Supplementally damped rolling isolation systems: (a) SDI-BPS with rubber-coated steel balls from Ref. [36], (b) concrete ball-in-cone isolator with solid rubber/polyurethane balls from Ref. [43], (c) rolling-ball rubber-layer isolation system with rubber re-centering springs from [33], and (d) rubber-bonded recessed bowl used in this dissertation.

both cases, damage to the damping material or rubber ball after sustaining a certain period of service loadings, in the form of de-lamination or squashing, may affect the isolation efficiency [36]. Alternatively, steel ball-bearings can be used in conjunction with rubber-bonded rolling surfaces, localizing the plastic deformations to the bowls' apices. Figure 1.3(c) shows a rolling-ball rubber-layer isolation system [33]. In all prior investigations into bonding viscoelastic sheets to RISs [33, 47, 48], the rolling surfaces were flat and required elastic re-centering springs. To overcome this limitation, rolling isolation systems provide re-centering via gravitational potential energy. The rubber-bonded recessed bowl, which will be analyzed in this dissertation, is shown in Figure 1.3(d).

In the study by Cui [43], an experimental RIS, in effect, combined the previous two approaches in an isolation system with solid rubber and polyurethane balls and concrete bowls instead of steel. Free vibration tests attempted to quantify an equivalent viscous damping ratio but were unsuccessful. However, it was concluded that the system was heavily damped—only two and four full cycles of free-response motion were observed for the rubber balls and polyurethane balls, respectively. That study also noted that the vibration period is displacement and direction dependent.

It is worthwhile to note that extensively more research has been performed on sliding-type isolators, which function on the same pendulum principle of most RISs. As such, many of the results and conclusions are transferrable to the study of RISs. For example, the sliding surface geometry has been optimized to attenuate responses over a wide range of disturbance frequencies via variable-curvature surfaces [22, 23], multiple sliding surfaces [19, 26], and varying friction coefficients [15, 20]. Sliding isolators also benefit from friction which acts as an energy dissipation mechanism; when the coefficient of friction is increased, deformations across the isolator are decreased at the expense of increasing the total accelerations [55]. Insight from these studies have helped guide the research in this dissertation.

### *1.2.3 Intelligent adaptive isolation*

Passive damping (e.g. rubber rolling surfaces) is effective in reducing isolator drifts, but may increase equipment accelerations at high frequencies [56]. To combat this effect, two other prominent solutions applied to isolated structures are active and semi-active control. Active control refers to systems that require large power sources to generate desirable control forces, but are effective for a wide frequency range. Semi-active control systems combine the capabilities of passive and active systems; using the motion of the structure, adaptable forces are generated by adjusting the dynamic properties (e.g. stiffness and damping) without requiring large power sources [41]. Semi-active control systems are attractive due to their guaranteed stability, low cost, and low power consumption [57, 58].

It is common practice to evaluate the performance of semi-actively controlled systems for a particular disturbance and feedback law and to compare the result to a passively controlled system. This method of performance evaluation is insufficient to assess the *potential* of semi-active control systems, as the performance of a semi-active device may vary greatly depending on the choice of the feedback law. To fully evaluate the potential benefit of a semi-active controls system it is best to examine its optimal performance. Methods of trajectory optimization may be used to determine the best possible performance achievable within the constraints of a particular semi-active device, the structural system into which it is applied, and the external forcing. Previous methods have involved constraint relaxation [59], receding horizon approximations [60], or neglecting the disturbance in feedback law synthesis [61, 62], and are sub-optimal. The solution to the optimal semi-active control problem requires an algorithm to calculate *optimal* open-loop control trajectories for general inequality constraints. One of the focuses of this dissertation centers around developing an algorithm which would allow a performance evaluation of semi-active control in conjunction with RISs, and assess whether such an application has promise.

## 1.3 Dissertation Overview

### *1.3.1 Research contributions*

The purpose of this dissertation is to develop and experimentally validate models to be used for analyzing the isolation capabilities of RISs, and to propose and test new approaches to improve the performance of these systems. Specifically, this work addresses the challenge of modeling the complex behavior of RISs, as well as account for the *non-holonomic* constraints of rolling-without-slipping and the associated *multiaxial*, nonlinear dynamics. In existing models, these challenges have not been addressed correctly or completely. By surmounting these challenges and deriving *valid* models, we will improve our understanding of RISs and be better able to develop high-performance design innovations, which is the second major focus of this dissertation, i.e. double, semi-active, and damped RISs. The proposed innovations are theoretically and experimentally assessed for viability and efficacy. Traditionally, secondary-system seismic performance research focuses on planar analyses of primary and secondary structures and treats the secondary system model as an afterthought—in most cases, taken to be linear. This type of analysis neglects the fact that RISs are complex systems and accordingly these analyses are unrealistic. The seismic performance of RISs needs to be assessed under realistic operating conditions (i.e. the floor responses of biaxial, hysteretic structures subject to actual ground motion records), using experimentally-validated predictive models. The research methods and models presented herein are intentionally developed to be as general as possible, and can and should be applied to future isolation advancements.

Motivated by the above observations, this dissertation presents four main research contributions to the field of equipment isolation:

1. The derivation of a high-fidelity mathematical model for RISs subject to bidirectional excitations. Unlike a majority of research that exists in the literature, which focuses on uniaxial responses and neglects the nonholonomic constraints, we present a model that is able to capture the complex dynamics of an actual RIS (i.e. coupling between transverse and rotational displacements and chaotic nature). In addition, we experimentally validate the predictive model for free and forced responses over a wide range of operating conditions.

2. Two RIS innovations—a double RIS and a damped RIS—to improve the existing system's performance are investigated. Specifically, we derive and experimentally validate analytical models for the double and the damped RISs. One can view these proposed models as a design tool to predict the isolator's response to various loading conditions that may not be replicable in the laboratory. Motivated by this result, the models are used to compute the spectrum of peak floor motions for which displacement demands equal capacity. These spectra can then be compared to representative floor motion spectra provided by design codes (e.g. ASCE 7-10).

3. A method to compute optimal open-loop trajectories for systems subject to state and control inequality constraints. We employ Pontryagin's minimum principle to determine optimal Lagrange multipliers enforcing the inequality constraints, and in so doing, this problem is formulated as a nonlinear two-point, boundary-value problem whose solution meets the necessary condition for optimality. The optimal performance of inequality constrained control systems is calculable, allowing for comparison to previous, sub-optimal solutions. The method is applied to the control of damping forces in an RIS subjected to constraints imposed by the physical implementation of a particular controllable damper.

4. An evaluation of the seismic performance of undamped and damped RISs located

inside six code-designed structures, which are representative of existing buildings in California. Unlike the analyses performed in previous studies, we consider the biaxial horizontal response of the structure instead of the uniaxial response. A new approach to model reduction for hysteretic systems is presented, in which the structure's orthogonal responses are coupled by a novel, biaxial hysteretic model. We conduct extensive time-history analyses and construct empirical CDFs of peak responses, from which general design recommendations are suggested.

### *1.3.2 Organization*

The material in this dissertation draws heavily from the author's journal articles that have been published or are currently under review. As such, each chapter corresponds to one or two papers and thus functions as a self-contained unit. This dissertation is organized as follows where the corresponding publication is noted by the reference. Chapter 2 introduces the calculus of variations with application to the modeling of dynamical systems and optimal control, and derives the Euler-Lagrange equations which serve as the backbone to this dissertation. Chapter 3 focuses on the modeling of an RIS, satisfying the nonholonomic constraints and showing that the system is chaotic [38]; Appendix A further expands the analysis of the chaotic response presented in Chapter 3 [63]. Chapter 4 simplifies the mathematical model in Chapter 3 and validates the simplified model under free and forced responses [52]. Chapter 5 expands the model in Chapter 3 to a double RIS [53]. In Chapter 6, the double RIS model is simplified and validated for a range of operating conditions [54]. Chapter 7 extends the Euler-Lagrange equations to the optimal control of inequality constrained systems. A method to solve the necessary conditions for optimality [39] is described and numerically demonstrated [64], and Appendix C gives sample code to implement the method. Chapter 8 uses the constrained control theory of Chapter 7 to asses the performance and viability of a semi-active RIS [39]. Chapter 9 further expands the theory in Chapter 3 to account for supplemental damping in RISs.

A series of experimental tests are used to calibrate the rolling resistance model, and the damped RIS model is validated and used to asses the improved performance over the undamped RIS [65]. Finally, Chapter 10 evaluates and compares the seismic performance of undamped and damped RISs inside multi-story hysteretic structures, in which a biaxial hysteretic model [66] (Appendix D) couples the structure's response in orthogonal directions. Through extensive time-history analyses we suggest design recommendations.

# 2

# The Calculus of Variations and Nonholonomic Dynamics

## 2.1 Background

The calculus of variation is the branch of mathematics that deals with extremizing functionals, as opposed to extremizing functions in ordinary calculus. This chapter lays out the foundation for modeling and control of equipment isolation systems by deriving the necessary conditions for optimality for a broad class of optimization problems. Applying Hamilton's principle to a constrained system we find the Euler-Lagrange equations of the calculus of variations. From this result, Lagrange's equations of motion for holonomic systems are deduced, but are shown to be invalid for nonholonomic systems; instead the more general d'Alembert-Lagrange principle must be used to find the equations of state. In Chapter 7 the Euler-Lagrange equations are then used to find the necessary conditions of optimality for the continuous optimal controller. These results are essential to the modeling and control of EISs supplying the backbone to this dissertation.

## 2.2 Hamilton's Principle

Hamilton's principle states a system described by $N$ generalized coordinates

$$\mathbf{z}(t) = [z_1(t)\ z_2(t)\ \cdots\ z_N(t)]^\mathsf{T}$$

between two specified states $\mathbf{z}_0 \equiv \mathbf{z}(t_0)$ and $\mathbf{z}_\mathrm{f} \equiv \mathbf{z}(t_\mathrm{f})$ at two specified times $t_0$ and $t_\mathrm{f}$, respectively, undergoes the trajectory $\mathbf{z}(t)$ whose action has a stationary value [67]. Consider the continuous-time cost functional

$$J = \int_{t_0}^{t_\mathrm{f}} L(\mathbf{z}, \dot{\mathbf{z}}, t)\ \mathrm{d}t \tag{2.1}$$

which is to be minimized subject to a set of equality constraints

$$\mathbf{g}(\mathbf{z}, \dot{\mathbf{z}}, t) = \mathbf{0} \tag{2.2}$$

and a set of algebraic path constraints

$$\mathbf{c}(\mathbf{z}, t) \leq \mathbf{0}\ . \tag{2.3}$$

We introduce Lagrange multipliers $\boldsymbol{\lambda}(t)$ and $\boldsymbol{\mu}(t)$ to enforce the constraints (2.2) and (2.3), respectively. Note $\mu_i(t) \geq 0,\ \forall i, t$. Thus, the augmented cost is given by

$$J_\mathrm{A} = \int_{t_0}^{t_\mathrm{f}} \Lambda(\mathbf{z}, \dot{\mathbf{z}}, \boldsymbol{\lambda}, \boldsymbol{\mu}; t)\ \mathrm{d}t \tag{2.4}$$

where $\Lambda(\mathbf{z}, \dot{\mathbf{z}}, \boldsymbol{\lambda}, \boldsymbol{\mu}; t) \equiv L(\mathbf{z}, \dot{\mathbf{z}}, t) + \boldsymbol{\lambda}^\mathsf{T}\mathbf{g}(\mathbf{z}, \dot{\mathbf{z}}, t) + \boldsymbol{\mu}^\mathsf{T}\mathbf{c}(\mathbf{z}, t)$ is the augmented Lagrangian function. According to Hamilton's principle, the extremal (equilibrium) trajectories extremize Equation (2.4); its variation in these conditions is zero:

$$\delta J_\mathrm{A} = \delta \int_{t_0}^{t_\mathrm{f}} \Lambda(\mathbf{z}, \dot{\mathbf{z}}, \boldsymbol{\lambda}, \boldsymbol{\mu}; t)\ \mathrm{d}t = \int_{t_0}^{t_\mathrm{f}} \delta\Lambda(\mathbf{z}, \dot{\mathbf{z}}, \boldsymbol{\lambda}, \boldsymbol{\mu}; t)\ \mathrm{d}t = 0\ . \tag{2.5}$$

The free variations $\delta\mathbf{z}$ and $\delta\boldsymbol{\lambda}$ and constrained variations

$$\delta\mu_i \begin{cases} \geq 0: & \mu_i = 0 \\ \text{unconstrained}: & \mu_i > 0 \end{cases},\ \forall\ i$$

of the augmented cost (2.5) is given by

$$\delta J_{\mathrm{A}} = \int_{t_0}^{t_{\mathrm{f}}} \left( \frac{\partial \Lambda}{\partial \mathbf{z}} \delta \mathbf{z} + \frac{\partial \Lambda}{\partial \dot{\mathbf{z}}} \delta \dot{\mathbf{z}} + \frac{\partial \Lambda}{\partial \boldsymbol{\lambda}} \delta \boldsymbol{\lambda} + \frac{\partial \Lambda}{\partial \boldsymbol{\mu}} \delta \boldsymbol{\mu} \right) \mathrm{d}t \tag{2.6a}$$

$$= \int_{t_0}^{t_{\mathrm{f}}} \left( \frac{\partial \Lambda}{\partial \mathbf{z}} \delta \mathbf{z} + \frac{\partial \Lambda}{\partial \dot{\mathbf{z}}} \frac{\mathrm{d}}{\mathrm{d}t} (\delta \mathbf{z}) + \frac{\partial \Lambda}{\partial \boldsymbol{\lambda}} \delta \boldsymbol{\lambda} + \frac{\partial \Lambda}{\partial \boldsymbol{\mu}} \delta \boldsymbol{\mu} \right) \mathrm{d}t \tag{2.6b}$$

$$= \frac{\partial \Lambda}{\partial \dot{\mathbf{z}}} \delta \mathbf{z} \Big|_{t_0}^{t_{\mathrm{f}}} + \int_{t_0}^{t_{\mathrm{f}}} \left[ \left( \frac{\partial \Lambda}{\partial \mathbf{z}} - \frac{\mathrm{d}}{\mathrm{d}t} \left( \frac{\partial \Lambda}{\partial \dot{\mathbf{z}}} \right) \right) \delta \mathbf{z} + \frac{\partial \Lambda}{\partial \boldsymbol{\lambda}} \delta \boldsymbol{\lambda} + \frac{\partial \Lambda}{\partial \boldsymbol{\mu}} \delta \boldsymbol{\mu} \right] \mathrm{d}t \, . \tag{2.6c}$$

To get from Equation (2.6a) to (2.6b) we have assumed the 'traditional' commutation rule: $\delta \dot{\mathbf{z}} = \mathrm{d}(\delta \mathbf{z})/\mathrm{d}t$; then integration by parts is used to find Equation (2.6c). Figure 2.1 shows extremal and varied paths in extended configuration space. In Hamilton's principle, the end-points are fixed in configuration space and time; thus, the perturbations vanish at both fixed end points, $(\partial \Lambda / \partial \dot{\mathbf{z}}) \delta \mathbf{z} \big|_{t_0}^{t_{\mathrm{f}}} = 0$. Furthermore, the variations $\delta \mathbf{z}$, $\delta \boldsymbol{\lambda}$, and $\delta \boldsymbol{\mu}$ are arbitrary and contemporaneous variations, i.e. with time held fixed. The stationarity of Equation (2.6c) for arbitrary time limits $t_0$ and $t_{\mathrm{f}}$ implies each term must equal zero, resulting in the Euler-Lagrange equations:

$$\frac{\partial \Lambda}{\partial \mathbf{z}} - \frac{\mathrm{d}}{\mathrm{d}t} \left( \frac{\partial \Lambda}{\partial \dot{\mathbf{z}}} \right) = \mathbf{0} \tag{2.7a}$$

$$\frac{\partial \Lambda}{\partial \boldsymbol{\lambda}} = \mathbf{g}(\mathbf{z}, \dot{\mathbf{z}}, t) = \mathbf{0} \tag{2.7b}$$

$$\frac{\partial \Lambda}{\partial \boldsymbol{\mu}} = \mathbf{c}(\mathbf{z}, t) \leq \mathbf{0} \, . \tag{2.7c}$$

Note that Equations (2.7b) and (2.7c) merely restate the constraint equations.

The Euler-Lagrange equations are a powerful tool in both the modeling of dynamical systems and the optimal control of such systems. In the subsequent sections, Equations (2.7a)–(2.7c) will be manipulated to derive Lagrange's principle for a holonomic system, but shown to be fallacious in the case of a nonholonomic system—the necessary corrections are made. Then, the necessary conditions for optimality of a constrained control system are derived in Chapter 7.

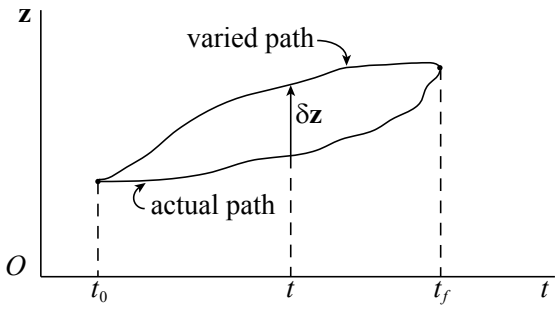


FIGURE 2.1: Actual and varied paths in extended configuration space.

## 2.3 System Dynamics

In this section, we apply the results of the previous section to modeling a dynamical system. First, the Euler-Lagrange equations are applied to a holonomic system; the result – Lagrange's equations – is well established yet powerful. Next, a nonholonomic system is investigated. It is shown that Equations (2.7a)–(2.7c) lead to incorrect dynamical equations for the general case of nonholonomic constraints. The correct nonholonomic equations of state under general velocity constraints must be found using an appropriate approach, e.g. d'Alembert-Lagrange principle [67], Gauss's principle of least constraint [68], etc.

### *2.3.1 Holonomic system*

Assume a holonomic system in which the constraint (2.2) is independent of the generalized coordinate rate of change, i.e. $\mathbf{g} = \mathbf{g}(\mathbf{z}, t)$, for example, a path constraint or a displacement bound. Define the Lagrangian function to be $L(\mathbf{z}, \dot{\mathbf{z}}, t) \equiv T(\mathbf{z}, \dot{\mathbf{z}}, t) - V(\mathbf{z}, t)$ in which

$$T(\mathbf{z}, \dot{\mathbf{z}}, t) \equiv \text{unconstrained kinetic energy function, and}$$

$$V(\mathbf{z}, t) \equiv \text{potential energy function.}$$

Without the inequality constraint (2.3), Euler-Lagrange's equation (2.7a) reduces to

$$\frac{\mathrm{d}}{\mathrm{d}t}\left(\frac{\partial T}{\partial \dot{\mathbf{z}}}\right) - \frac{\partial T}{\partial \mathbf{z}} + \frac{\partial V}{\partial \mathbf{z}} = \boldsymbol{\lambda}^{\mathsf{T}} \frac{\partial \mathbf{g}}{\partial \mathbf{z}} \,. \tag{2.8}$$

The constraint $\mathbf{g}(\mathbf{z}, t) = \mathbf{0}$ is also recovered as a consequence of Equation (2.7b). Equation (2.8) is Lagrange's principle or Lagrange's equations of motion for a holonomic system—a

powerful tool in deriving equations of motion for holonomic dynamical systems.

By introducing Lagrange multipliers $\boldsymbol{\lambda}$ to enforce the holonomic constraint, the number of unknowns in the system increases. In order to find consistent trajectories of $\mathbf{z}$ and $\boldsymbol{\lambda}$, the state dynamics (2.8) must be solved in conjunction with the constraint (2.2). Then having solved for $\boldsymbol{\lambda}$, the holonomic constraint force $\mathbf{Q}^{\mathrm{C}} = \boldsymbol{\lambda}^{\mathsf{T}}(\partial\mathbf{g}/\partial\mathbf{z})$ which constrains the system in accordance with $\mathbf{g}(\mathbf{z}, t)$ may be solved for immediately.

### *2.3.2 Nonholonomic system*

Now consider a dynamical system with general nonholonomic constraints of the form (2.2)—non-integrable kinematic relationships that directly restrict the velocities/accelerations of the state [69]. Nonholonomic constraints are non-integrable and hence cannot be used to reduce the order of the system such as in the case of holonomic constraints. If Equation (2.2) were integrable, we could determine at least some of the coordinates $z_i(t)$ in closed form thereby eliminating them as dynamic variables. As will be seen in Chapter 3, nonholonomic constraints arise in the modeling of the rolling of the ball bearing for the rolling isolation system.

Applying Hamilton's principle to the nonholonomically constrained system, the Euler-Lagrange's equation (2.7a) reduces to

$$\frac{\mathrm{d}}{\mathrm{d}t}\left(\frac{\partial T}{\partial \dot{\mathbf{z}}}\right) - \frac{\partial T}{\partial \mathbf{z}} + \frac{\partial V}{\partial \mathbf{z}} = \boldsymbol{\lambda}^{\mathsf{T}}\left[\frac{\partial \mathbf{g}}{\partial \mathbf{z}} - \frac{\mathrm{d}}{\mathrm{d}t}\left(\frac{\partial \mathbf{g}}{\partial \dot{\mathbf{z}}}\right)\right] - \dot{\boldsymbol{\lambda}}^{\mathsf{T}}\frac{\partial \mathbf{g}}{\partial \dot{\mathbf{z}}} \,. \tag{2.9}$$

Equations (2.9) were first proposed by Ref. [70] but retracted, and since have been rediscovered [71] as the variational nonholonomic equations. However, these dynamical equations for the general case of nonholonomic constraints are incorrect [67] and lack theoretical foundation [69]. In general, the solution path of a nonholonomic system will not result in a stationary value of the action integral (2.1).

The recent work of Flannery [69] dispels the enigma of nonholonomic constraints by deriving transpositional relations for non-integrable velocity constraints. The basis

for the 'traditional' transpositional relation is that the variations are contemporaneous, i.e. the d and the $\delta$ operations commute; strictly speaking, contemporaneous only means $\mathrm{d}(\delta t) = \delta(\mathrm{d}t) = 0$, and not that $\mathrm{d}(\delta\mathbf{z}) = \delta(\mathrm{d}\mathbf{z})$. Therefore, the 'traditional' transpositional relation does not hold true in constrained velocity spaces:

$$\delta\dot{\mathbf{z}} \neq \mathrm{d}(\delta\mathbf{z})/\mathrm{d}t \ .$$

Flannery [69] derives new transpositional relations without any assumptions, which guarantees the perturbed states are compatible with the constraints—the commutation rule $\delta\dot{\mathbf{z}} = \mathrm{d}(\delta\mathbf{z})/\mathrm{d}t$ does not. It has been shown [69] that the new transpositional rule does not permit the valid construction of a constrained Hamilton principle for nonholonomic systems—even though the perturbed states are dynamically admissible. Instead, the equations of state must be found from the more general d'Alembert-Lagrange principle [72] respecting the the restrictions on $\delta\mathbf{z}$, viz.

$$\left[\frac{\mathrm{d}}{\mathrm{d}t}\left(\frac{\partial L}{\partial\dot{\mathbf{z}}}\right) - \frac{\partial L}{\partial\mathbf{z}}\right]\delta\mathbf{z} = \mathbf{Q}^{\mathrm{C}}\delta\mathbf{z} = 0 \qquad \text{(d'Alembert-Lagrange principle).} \tag{2.10}$$

where $\mathbf{Q}^{\mathrm{C}}$ are the generalized constraint forces. Note the virtual work of the generalized constraint forces must equal zero:

$$\delta W = \mathbf{Q}^{\mathrm{C}}\delta\mathbf{z} = 0 \ . \tag{2.11}$$

The variation in the constraint $\delta\mathbf{g}$ at the perturbed state due to a variation of the physical state by a virtual displacement $\delta\mathbf{z}$ under frozen constraints is

$$\delta\mathbf{g} = \mathbf{g}(\mathbf{z} + \delta\mathbf{z}, \dot{\mathbf{z}} + \delta\dot{\mathbf{z}}, t) - \mathbf{g}(\mathbf{z}, \dot{\mathbf{z}}, t) \tag{2.12}$$

which, when expanded through a Taylor series and truncated at first order (i.e. under infinitesimal displacements), gives

$$\delta\mathbf{g} = \left(\frac{\partial\mathbf{g}}{\partial\mathbf{z}}\right)\delta\mathbf{z} + \left(\frac{\partial\mathbf{g}}{\partial\dot{\mathbf{z}}}\right)\delta\dot{\mathbf{z}} = \mathbf{0} \ . \tag{2.13}$$

Under frozen constraints the variation $\delta\mathbf{g}$ must be zero. Because the Jacobian is normal to $\mathbf{g}$, the displacements $\delta\mathbf{z}$ and $\delta\dot{\mathbf{z}}$ must be tangential to the $\mathbf{g}$ surface; therefore, the displaced states lie on the manifold of the constraint $\mathbf{g}$. Hence, the necessary conditions on displacements $\delta\mathbf{z}$ must be developed.

Differentiation of the constraint $\mathbf{g}$ gives the linear-acceleration form,

$$\dot{\mathbf{g}} = \left(\frac{\partial \mathbf{g}}{\partial \dot{\mathbf{z}}}\right)\ddot{\mathbf{z}} + \left(\frac{\partial \mathbf{g}}{\partial \mathbf{z}}\right)\dot{\mathbf{z}} + \frac{\partial \mathbf{g}}{\partial t} = \mathbf{0}\,. \tag{2.14}$$

For the $c$-dimensional nonholonomic constraint $\mathbf{g}$, let us partition the generalized coordinate vector as $\mathbf{z} \equiv [\mathbf{z}_\mathrm{i}\ \mathbf{z}_\mathrm{d}]$ where $\mathbf{z}_\mathrm{i} \in \mathbb{R}^{N-c}$ are the independent coordinates and $\mathbf{z}_\mathrm{d} \in \mathbb{R}^c$ are the dependent coordinates. There exists a functional relationship $\mathbf{z}_\mathrm{d} = \mathbf{z}_\mathrm{d}(\mathbf{z}_\mathrm{i}, t)$ relating the dependent coordinate to the independent coordinates. This relationship cannot be found analytically though because the constraint is non-integrable. Thus, Equation (2.14) decomposes as

$$\dot{\mathbf{g}} = \left(\frac{\partial \mathbf{g}}{\partial \dot{\mathbf{z}}_\mathrm{d}}\right)\ddot{\mathbf{z}}_\mathrm{d} + \left(\frac{\partial \mathbf{g}}{\partial \dot{\mathbf{z}}_\mathrm{i}}\right)\ddot{\mathbf{z}}_\mathrm{i} + \left(\frac{\partial \mathbf{g}}{\partial \mathbf{z}}\right)\dot{\mathbf{z}} + \frac{\partial \mathbf{g}}{\partial t} = \mathbf{0}\,. \tag{2.15}$$

The solution of Equation (2.15) for the dependent accelerations are given as follows:

$$\ddot{\mathbf{z}}_\mathrm{d} = -\left(\frac{\partial \mathbf{g}}{\partial \dot{\mathbf{z}}_\mathrm{d}}\right)^{-1}\left[\left(\frac{\partial \mathbf{g}}{\partial \dot{\mathbf{z}}_\mathrm{i}}\right)\ddot{\mathbf{z}}_\mathrm{i} + \left(\frac{\partial \mathbf{g}}{\partial \mathbf{z}}\right)\dot{\mathbf{z}} + \frac{\partial \mathbf{g}}{\partial t}\right]. \tag{2.16}$$

Though the relation $\mathbf{z}_\mathrm{d} = \mathbf{z}_\mathrm{d}(\mathbf{z}_\mathrm{i}, t)$ is unknown for non-integrable constraints, the dependent variations are known,

$$\delta\mathbf{z}_\mathrm{d} = \left(\frac{\partial \mathbf{z}_\mathrm{d}}{\partial \mathbf{z}_\mathrm{i}}\right)\delta\mathbf{z}_\mathrm{i} = \left(\frac{\partial \dot{\mathbf{z}}_\mathrm{d}}{\partial \dot{\mathbf{z}}_\mathrm{i}}\right)\delta\mathbf{z}_\mathrm{i} = \left(\frac{\partial \ddot{\mathbf{z}}_\mathrm{d}}{\partial \ddot{\mathbf{z}}_\mathrm{i}}\right)\delta\mathbf{z}_\mathrm{i}\,. \tag{2.17}$$

By Equation (2.16), the dependent variations in terms of the independent variations are given by

$$\delta\mathbf{z}_\mathrm{d} = \frac{\partial}{\partial \ddot{\mathbf{z}}_\mathrm{i}}\left\{-\left(\frac{\partial \mathbf{g}}{\partial \dot{\mathbf{z}}_\mathrm{d}}\right)^{-1}\left[\left(\frac{\partial \mathbf{g}}{\partial \dot{\mathbf{z}}_\mathrm{i}}\right)\ddot{\mathbf{z}}_\mathrm{i} + \left(\frac{\partial \mathbf{g}}{\partial \mathbf{z}}\right)\dot{\mathbf{z}} + \frac{\partial \mathbf{g}}{\partial t}\right]\right\}\delta\mathbf{z}_\mathrm{i} = -\left(\frac{\partial \mathbf{g}}{\partial \dot{\mathbf{z}}_\mathrm{d}}\right)^{-1}\left(\frac{\partial \mathbf{g}}{\partial \dot{\mathbf{z}}_\mathrm{i}}\right)\delta\mathbf{z}_\mathrm{i} \tag{2.18}$$

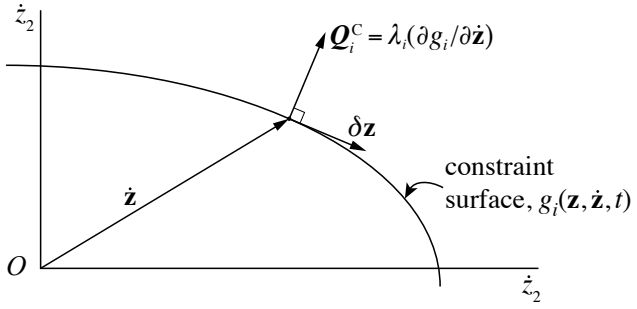


FIGURE 2.2: A depiction of the variation constraints in extended velocity space.

or

$$\left(\frac{\partial \mathbf{g}}{\partial \dot{\mathbf{z}}_\mathrm{d}}\right)\delta\mathbf{z}_\mathrm{d} + \left(\frac{\partial \mathbf{g}}{\partial \dot{\mathbf{z}}_\mathrm{i}}\right)\delta\mathbf{z}_\mathrm{i} = \mathbf{0}\ . \tag{2.19}$$

We recognize this to be the Chetaev equation, viz.

$$\left(\frac{\partial \mathbf{g}}{\partial \dot{\mathbf{z}}}\right)\delta\mathbf{z} \equiv \left(\frac{\partial \mathbf{g}}{\partial \dot{\mathbf{z}}_\mathrm{d}}\right)\delta\mathbf{z}_\mathrm{d} + \left(\frac{\partial \mathbf{g}}{\partial \dot{\mathbf{z}}_\mathrm{i}}\right)\delta\mathbf{z}_\mathrm{i} = \mathbf{0}\ . \tag{2.20}$$

Equation (2.20) is a tangency condition on $\delta\mathbf{z}$; the variation $\delta\mathbf{z}$ must be orthogonal to the gradient $\partial\mathbf{g}/\partial\dot{\mathbf{z}}$, which itself is normal to the constraint surface $\mathbf{g} = \mathbf{0}$. Thus, displaced coordinates must lie on the manifold of nonholonomic constraints $\mathbf{g} = \mathbf{0}$. Figure 2.2 depicts the restrictions on variation $\delta\mathbf{z}$ in an extended velocity space.

Taking the inner product of Equation (2.20) with Lagrange multiplier $\boldsymbol{\lambda}$, we obtain

$$\boldsymbol{\lambda}^\mathsf{T}\left(\frac{\partial \mathbf{g}}{\partial \dot{\mathbf{z}}}\right)\delta\mathbf{z} = 0 \tag{2.21}$$

Subtract Equation (2.20) from Equation (2.11) with the result

$$\left[\mathbf{Q}^\mathrm{C} - \boldsymbol{\lambda}^\mathsf{T}\left(\frac{\partial \mathbf{g}}{\partial \dot{\mathbf{z}}}\right)\right]\delta\mathbf{z} = 0\ . \tag{2.22}$$

Still the variation $\delta\mathbf{z}$ must satisfy the Chetaev equation, but with proper choice of $\boldsymbol{\lambda}$, the coefficient of $\delta\mathbf{z}$ vanishes, i.e.

$$\mathbf{Q}^\mathrm{C} = \boldsymbol{\lambda}^\mathsf{T}\left(\frac{\partial \mathbf{g}}{\partial \dot{\mathbf{z}}}\right) \tag{2.23}$$

and $\delta\mathbf{z}$ can be considered arbitrary. Substituting Equation (2.23) into the d'Alembert-Lagrange principle and invoking the arbitrariness of $\delta\mathbf{z}$, the fundamental form of Lagrange's equation is as follows:

$$\frac{\mathrm{d}}{\mathrm{d}t}\left(\frac{\partial T}{\partial \dot{\mathbf{z}}}\right) - \frac{\partial T}{\partial \mathbf{z}} + \frac{\partial V}{\partial \mathbf{z}} = \boldsymbol{\lambda}^{\mathsf{T}} \frac{\partial \mathbf{g}}{\partial \dot{\mathbf{z}}} \qquad \text{(nonholonomic equations of state).} \tag{2.24}$$

These are the correct equations of state for nonholonomic systems under the general velocity constraints in Equation (2.2) and are used in Chapter 3 to derive the equations of state of a rolling isolation system. Simultaneous solution of Equation (2.24) with the constraints (2.2) provides both the states $\{\mathbf{z}, \dot{\mathbf{z}}\}$ of the system and the Lagrange multipliers $\boldsymbol{\lambda}$, which determine the constraint force $\mathbf{Q}^{\mathrm{C}} = \boldsymbol{\lambda}^{\mathsf{T}}(\partial \mathbf{g}/\partial \dot{\mathbf{z}})$.

### *2.3.3 Dissipative forces*

Dissipative forces are not derivable from a potential energy function $V(\mathbf{z}, t)$. Hence, dissipative forces are not present in equations of motion derived using Lagrange's Equations (2.8) or nonholonomic equations of state (2.24). Dissipative terms are often introduced through known applied non-potential forces $\mathbf{Q}^{\mathrm{D}}$ where

$$Q^{\mathrm{D}}_{z_i} = -\boldsymbol{c}_i^{\mathsf{T}}(\mathbf{z}, t)\, \dot{\mathbf{z}}\,, \quad i = 1, ..., N. \tag{2.25}$$

Here, the $\boldsymbol{c}_i$'s are damping coefficients in generalized coordinates $\mathbf{z}$. Equations of motion (2.8) and (2.24) are augmented with these generalized forces to yield the following complete equations of state:

$$\frac{\mathrm{d}}{\mathrm{d}t}\left(\frac{\partial T}{\partial \dot{\mathbf{z}}}\right) - \frac{\partial T}{\partial \mathbf{z}} + \frac{\partial V}{\partial \mathbf{z}} = \mathbf{Q}^{\mathrm{D}} + \mathbf{Q}^{\mathrm{C}} \tag{2.26}$$

where $\mathbf{Q}^{\mathrm{C}}$ are the unknown forces which constrain the system. As previously noted, for a holonomic system $\mathbf{Q}^{\mathrm{C}} = \boldsymbol{\lambda}^{\mathsf{T}}(\partial \mathbf{g}/\partial \mathbf{z})$, and for a nonholonomic system $\mathbf{Q}^{\mathrm{C}} = \boldsymbol{\lambda}^{\mathsf{T}}(\partial \mathbf{g}/\partial \dot{\mathbf{z}})$.

# 3

# The Nonholonomic and Chaotic Nature of a Rolling Isolation System

## 3.1 Background

In this chapter we present the modeling of a rolling isolation system (RIS) used to protect objects from the hazards of horizontal shaking. The platform is built from four pairs of dished steel plates: four concave-up, attached to a shaking floor via a steel frame, and four concave-down, attached to the isolated object via a steel frame. Four steel ball-bearings, located between these dishes, allow the top and bottom platforms to roll with respect to one another. The shape of the dished bowl establishes the system's potential energy function. Large rotations between the platforms result in a nonlinear coupling between the angular acceleration and velocity and the platform rotation. In order for the four ball-bearings to remain in contact with the dishes during times of large angular rotation, the top-frame is assumed to conform to a saddle shape. The kinematics of the rolling contact impose a set of eight nonholonomic constraints to the translational and rotational dynamics of the platform center. The nonholonomic equations of state are found from the fundamental form of Lagrange's equation, which incorporates velocity constraints via Lagrange multipliers.

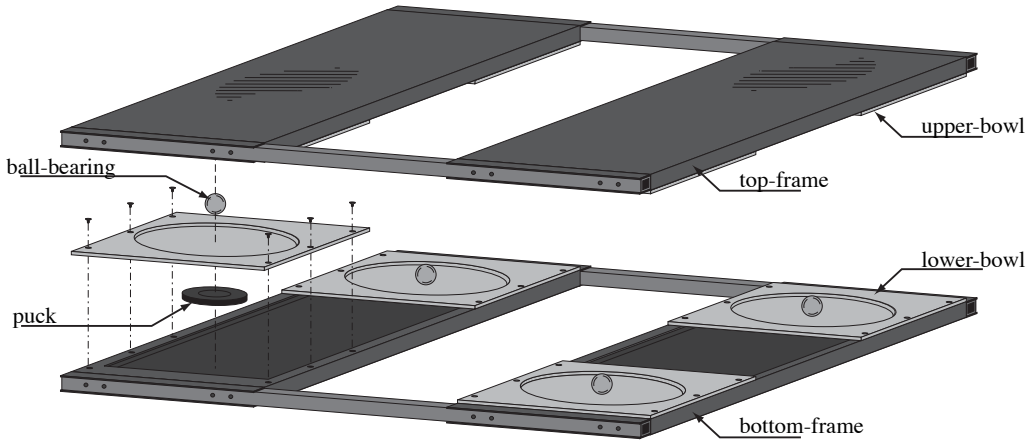


FIGURE 3.1: Exploded view of a rolling equipment isolation system.

Even in the absence of any mass or stiffness eccentricity, translational and rotational motions are nonlinearly coupled through the constraint of slip-free rolling. Uni-axial models can not be used to predict responses of these systems. Precise photogrammetric measurements of a sample of these steel bowls provide the data required to calibrate the potential energy function for this system. A viscous damping model calibrated to experimental free responses depends upon the mass of the isolated object. It is shown that, for the non-quadratic potential energy function of this particular system, free-response trajectories are strongly sensitive to slight perturbations in initial conditions, and that the system is, in fact, chaotic.

The RIS, shown in Figures 1.1 and 3.1, comprises a pair of frames. The bottom-frame contains four shallow bowls that are concave-up; the top-frame has four concave-down bowls. Four rigid steel ball-bearings, one between each pair of bowls, allow for the top frame to roll with respect to the bottom-frame. This configuration allows for a broad range of bowl profiles. If the bowls have parabolic profiles, the restoring force on the platform is proportional to the displacement, and in the uni-axial case, the system may be modeled as linear, simplifying the analysis. Thus, a parabolic system has a constant isolation frequency, which has been shown to be detrimental to the isolation performance near resonance [15]. If the bowls have cone-shaped profiles, the restoring force is nearly

constant as long as the platform rotations are small, and the accelerations sustained by the isolated equipment are limited by the slope of the dish, which may be designed to ensure the load on the equipment does not exceed tolerable limits [37]. The bowl profiles of the platforms studied are approximately quadratic near the bowl centers and are approximately cone-shaped at larger distances from the centers. It will be shown that large-amplitude free responses of RISs having this particular bowl shape are highly sensitive to initial conditions.

Passive vibration isolation systems are designed to be lightly-damped in order to provide good isolation at frequencies above the natural frequency of the system [73]. Friction pendulum systems exhibit higher damping than rolling pendulum isolators, and have been analytically modeled [24] and experimentally characterized [27] under multi-directional excitation. Uni-axial models are incapable of capturing the lateral-torsional coupling exhibited by rolling systems, even in the absence of mass and stiffness eccentricity. Earthquake ground motions, and associated structural responses are multi-axial phenomena and the simulation of response of these systems in the horizontal plane involves more than the superposition of uni-axial responses. However, existing models for RISs are either uni-axial, or do not involve the nonlinear coupling of translational and rotational responses that are associated with the large rotations typical of these systems (e.g. Ref. [46]).

The large-displacements associated with isolation systems, the kinematics of rolling between non-parallel surfaces, and the non-parabolic profiles commonly selected for RISs present challenges in deriving models capable of capturing the complex behavior of these systems. The free response of the RIS modeled in this paper is dominated by nonlinear coupling between translational and rotational motions. This coupling arises from the large-rotations these systems can undergo and the shape of their potential energy function. Modeling this behavior involves large-displacement analyses, careful treatment of the rolling contact, and precise modeling of the shape of the rolling surfaces.

In this chapter, equations of state are derived from kinetic and potential energies, and

the dynamics of the rolling ball-bearings are incorporated as kinematic constraints. The potential energy is essentially the height of the center of mass. Since the four corners of the top-frame are not co-planar when rotations are large, the height of the center of mass is determined from a saddle-shape interpolation between the heights at the four corners of the top-frame. The shape of the dishes is determined from high-resolution digital photogrammetry and an axisymmetric bowl profile is fit. By measuring a sample of sixteen bowls, the mean and variability of the bowl shapes are estimated. While simple damping treatments [74, 75] hold promise for reducing displacement demands, this study addresses lightly-damped isolation platforms, in which damping forces arise only at the interfaces between ball-bearings and steel bowls. For this study, a linear viscous damping model is calibrated from free-response measurements. To further simplify the analysis, the kinetic energy associated with vertical velocity is neglected. The resulting mathematical model demonstrates the highly coupled translational and rotational responses observed in experiments. Finally, the sensitivity to small variations to initial conditions is examined experimentally and numerically, via Lyapunov exponents.

## 3.2 Equations of State

The displaced configuration of an RIS is illustrated in Figure 3.2. The bottom-frame (dashed lines) has the $X_b$-$Y_b$ coordinate system, the top-frame (solid lines) has the $X_t$-$Y_t$ coordinate system, and the location of one of the four balls is shown to the right. The bottom-frame is excited by a disturbance $\boldsymbol{w}(t)$ that has $x$ and $y$ translational components $w_x(t)$ and $w_y(t)$. Hereinafter, vectors and matrices are denoted by bold lower-case and upper-case letters, respectively. In the applications for which RISs are used, significant base rotations are not observed. Therefore, rotational base-excitation is neglected here. With respect to the bottom-frame, the centroid of the top-frame is translated through displacements $\bar{x}(t)$ and $\bar{y}(t)$, and rotated by an angle $\bar{\theta}(t)$. The instantaneous centroidal velocities are $\dot{\bar{x}}(t)$, $\dot{\bar{y}}(t)$

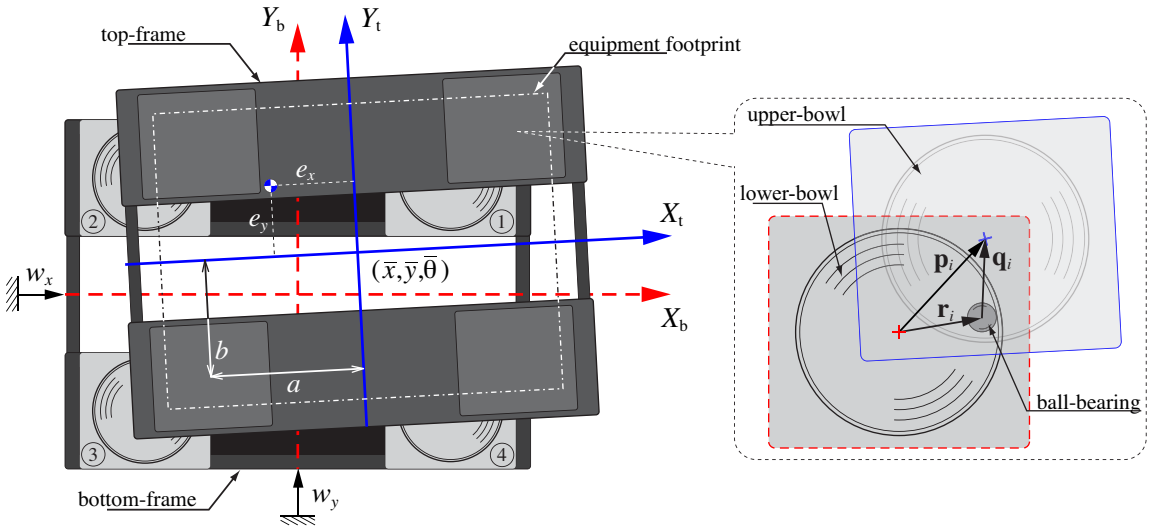


FIGURE 3.2: Rolling equipment isolation system geometry and notation.

and $\dot{\bar{\theta}}(t)$.

Knowing the location and velocity of the center of mass of the top-frame, expressions for the kinetic energy $T$ and potential energy $V$ of the top-frame may be derived. Then applying the fundamental form of Lagrange's principle, the equations of state for the seismic isolation platform [1] are determined, respecting the constraints imposed by the rolling ball-bearings.

In developing the model, various engineering approximations were used to simplify the derivation. Assumptions include the following: (a) the ball-bearing mass is negligible with respect to the top-frame mass; (b) the ball-bearing dimensions are negligibly small compared to the overall platform geometry; (c) the bowls are axisymmetric; (d) kinetic energy is modeled using the planar motion of the top platform—vertical velocity is not included in $T$; (e) the ball-bearings remain in contact throughout the platform's motion; (f) the point of rolling contact coincides with the ball-bearing centers; (g) for the purpose of computing gravitational potential energy, the effect of tilting of the bowls at the ball-bearing locations is negligible; and (h) a simplified mechanism for minor energy dissipation, viscous damping forces applied at the ball-bearing centers [76], is the sole source of energy dissipation in the system. Any further assumptions will be noted in the following

discussion.

### *3.2.1 Kinetic energy*

The mass $m$ of the system is attributed to the top-frame and equipment resting on the top-frame. In the top-frame's coordinates $X_t$-$Y_t$, the center of gravity of the isolated mass and equipment is located at $(e_x, e_y)$ with mass moment of inertia $I_{cm}$, while the centroid of the top-frame is located at $(0, 0)$. The kinetic energy $T$ of the system comes from the horizontal translational velocity and angular velocity of the center of mass with respect to an inertial reference. The kinetic energy is given as follows:

$$T(v_x, v_y, \omega) = \tfrac{1}{2}m(v_x^2 + v_y^2) + \tfrac{1}{2}I_{cm}\omega^2 \tag{3.1}$$

where $v_x$ and $v_y$ are the absolute translational velocities of the center of mass, and $\omega$ is the rotational velocity of the top-frame. The equipment is assumed to be rigidly-connected to the top-frame.

For a fixed point $(x_t, y_t)$ in the top-frame coordinates, its location in the bottom-frame coordinates $(x_b, y_b)$, given platform configuration $(\bar{x}, \bar{y}, \bar{\theta})$, is

$$\begin{bmatrix} x_b \\ y_b \end{bmatrix} = \begin{bmatrix} \bar{x} \\ \bar{y} \end{bmatrix} + \mathbf{R}_{\bar{\theta}} \begin{bmatrix} x_t \\ y_t \end{bmatrix} \tag{3.2}$$

where, in general, $\mathbf{R}_\theta$ is the rotation matrix through angle $\theta$ given by

$$\mathbf{R}_\theta = \mathbf{R}_\theta(\theta) = \begin{bmatrix} \cos\theta & -\sin\theta \\ \sin\theta & \cos\theta \end{bmatrix}.$$

The corresponding velocity in the bottom-frame reference system is as follows:

$$\begin{bmatrix} \dot{x}_b \\ \dot{y}_b \end{bmatrix} = \begin{bmatrix} \dot{\bar{x}} \\ \dot{\bar{y}} \end{bmatrix} + \dot{\bar{\theta}}\mathbf{R}'_{\bar{\theta}} \begin{bmatrix} x_t \\ y_t \end{bmatrix} \tag{3.3}$$

where the prime notation means differentiation with respect to the rotation angle, i.e. $\mathbf{R}'_\theta = \partial\mathbf{R}_\theta/\partial\theta$. Therefore, the absolute translational velocities of the center of mass are

$$\begin{bmatrix} v_x \\ v_y \end{bmatrix} = \begin{bmatrix} \dot{w}_x \\ \dot{w}_y \end{bmatrix} + \begin{bmatrix} \dot{\bar{x}} \\ \dot{\bar{y}} \end{bmatrix} + \dot{\bar{\theta}}\mathbf{R}'_{\bar{\theta}} \begin{bmatrix} e_x \\ e_y \end{bmatrix} \tag{3.4}$$

where $\dot{w}_x$ and $\dot{w}_y$ are the base velocities. The rotational velocity about the center of mass is the same as that about the centroid, i.e. $\omega = \dot{\bar{\theta}}$, with mass moment of inertia about the centroid given by $I = I_{\text{cm}} + m(e_x^2 + e_y^2)$. Thus, the kinetic energy of the system in terms of centroidal displacements and rotations is

$$T(\dot{\bar{x}}, \dot{\bar{y}}, \dot{\bar{\theta}}, \bar{\theta}) = \tfrac{1}{2}m\Big[(\dot{w}_x + \dot{\bar{x}})^2 + (\dot{w}_y + \dot{\bar{y}})^2\Big] + m\Big[(\dot{w}_y + \dot{\bar{y}})e_{\text{b}x} - (\dot{w}_x + \dot{\bar{x}})e_{\text{b}y}\Big]\dot{\bar{\theta}} + \tfrac{1}{2}I\dot{\bar{\theta}}^2 \quad (3.5)$$

where the mass eccentricity in the bottom-frame coordinates is given by

$$[e_{\text{b}x} \;\; e_{\text{b}y}]^\intercal = \mathbf{R}_{\bar{\theta}}[e_x \;\; e_y]^\intercal \; . \quad (3.6)$$

As is common in rotating reference frames, as we have here, the kinetic energy is a function of the velocities $(\dot{\bar{x}}, \dot{\bar{y}}, \dot{\bar{\theta}})$ and the top-frame rotation $\bar{\theta}$.

### *3.2.2 Potential energy*

Next, the potential energy of the system is determined. We have assumed the top-frame is flexible enough to accommodate out-of-plane deformation so that all four ball-bearings are in contact for any platform displacement or rotation. It has also been assumed that the out-of-plane deformation permits a small angle approximation, i.e. the bending of the top-frame corresponds only to vertical displacements at the bowl centers. Under these conditions, the deformation of the top-frame is approximately saddle-shaped with the following form:

$$\tilde{h}(x, y) = \gamma_0 + \gamma_1 x + \gamma_2 y + \gamma_3 xy \; . \quad (3.7)$$

The $X_{\text{t}}$-$Y_{\text{t}}$ coordinates of the bowl centers are given by $(a_i, b_i)$. For a rectangular platform, as illustrated in Figure 3.2,

$$\boldsymbol{a} = [a \;\; -a \;\; -a \;\; a]^\intercal \quad \text{and} \quad \boldsymbol{b} = [b \;\; b \;\; -b \;\; -b]^\intercal \; . \quad (3.8)$$

Knowing the heights at the center of the bowls on the top-frame $\boldsymbol{h} = [h_1 \; h_2 \; h_3 \; h_4]^\intercal$, the saddle-shape coefficients $\boldsymbol{\gamma} = [\gamma_0 \; \gamma_1 \; \gamma_2 \; \gamma_3]^\intercal$ are found by solving

$$\boldsymbol{h} = [\mathbf{1}_4 \;\; \boldsymbol{a} \;\; \boldsymbol{b} \;\; \boldsymbol{a} \circ \boldsymbol{b}]\,\boldsymbol{\gamma} \;\Rightarrow\; \boldsymbol{\gamma} = [\mathbf{1}_4 \;\; \boldsymbol{a} \;\; \boldsymbol{b} \;\; \boldsymbol{a} \circ \boldsymbol{b}]^{-1}\boldsymbol{h}$$

where $\boldsymbol{a}\circ\boldsymbol{b}$ is the element-wise multiplication of vectors $\boldsymbol{a}$ and $\boldsymbol{b}$, and $\mathbf{1}_4$ is the unit 4-vector.

The total potential energy of the system comes from the change in height of the center of mass, so

$$\tilde{h}(e_x, e_y) = [1 \;\; e_x \;\; e_y \;\; e_x e_y][\mathbf{1}_4 \;\; \boldsymbol{a} \;\; \boldsymbol{b} \;\; \boldsymbol{a}\circ\boldsymbol{b}]^{-1}\boldsymbol{h} = \boldsymbol{u}\boldsymbol{h}$$

where $\boldsymbol{u} = [1 \; e_x \; e_y \; e_x e_y \;][\mathbf{1}_4 \;\; \boldsymbol{a} \;\; \boldsymbol{b} \;\; \boldsymbol{a}\circ\boldsymbol{b}]^{-1}$ is conveniently independent of the motion of the platform and only depends on the geometry. Therefore, the potential energy of the system is

$$V(\bar{x}, \bar{y}, \bar{\theta}, \mathbf{r}_1, ..., \mathbf{r}_4) = mg\tilde{h}(e_x, e_y) = mg\boldsymbol{u}\boldsymbol{h}(\bar{x}, \bar{y}, \bar{\theta}, \mathbf{r}_1, ..., \mathbf{r}_4) \; . \tag{3.9}$$

The vector $\boldsymbol{u}$ allocates mass to the four upper-bowls such that the center of mass of the platform's payload is located at the proper location. With the assumption that the bowls remain horizontal, the height $h_i$ of the platform at the center of each upper-bowl is the sum of the heights of the respective lower- and upper-bowl at the point of the ball-bearing.

Notice that $V$ is dependent on the platform position $(\bar{x}, \bar{y}, \bar{\theta})$ and the ball-bearing locations $\mathbf{r}_i$ in so far as the heights of the top-frame corners depend on the ball-bearing locations. As seen in Figure 3.2, the locations of the ball-bearings with respect to the centers of the lower- and upper-bowls are determined by the two vectors $\mathbf{r}_i = [r_{ix} \; r_{iy}]^\intercal$ and $\mathbf{q}_i = [q_{ix} \; q_{iy}]^\intercal$. The vector $\mathbf{p}_i = [q_{ix} \; q_{iy}]^\intercal$ is the displacement of the center of the $i$th upper-bowl with respect to the center of the $i$th lower-bowl calculated as

$$\mathbf{p}_i(\bar{x}, \bar{y}, \bar{\theta}) = \begin{bmatrix} \bar{x} \\ \bar{y} \end{bmatrix} + (\mathbf{R}_{\bar{\theta}} - \mathbf{I}) \begin{bmatrix} a_i \\ b_i \end{bmatrix} \; . \tag{3.10}$$

Using the relationship $\mathbf{p}_i = \mathbf{r}_i + \mathbf{q}_i$, we can now find $\mathbf{q}_i$ as

$$\mathbf{q}_i(\bar{x}, \bar{y}, \bar{\theta}, \mathbf{r}_i) = \begin{bmatrix} \bar{x} \\ \bar{y} \end{bmatrix} + (\mathbf{R}_{\bar{\theta}} - \mathbf{I}) \begin{bmatrix} a_i \\ b_i \end{bmatrix} - \mathbf{r}_i \; . \tag{3.11}$$

It is now straight-forward to find the height of the $i$th bowl,

$$h_i \equiv h_i(\bar{x}, \bar{y}, \bar{\theta}, \mathbf{r}_i) = \eta(\|\mathbf{r}_i\|) + \eta(\|\mathbf{q}_i\|) \tag{3.12}$$

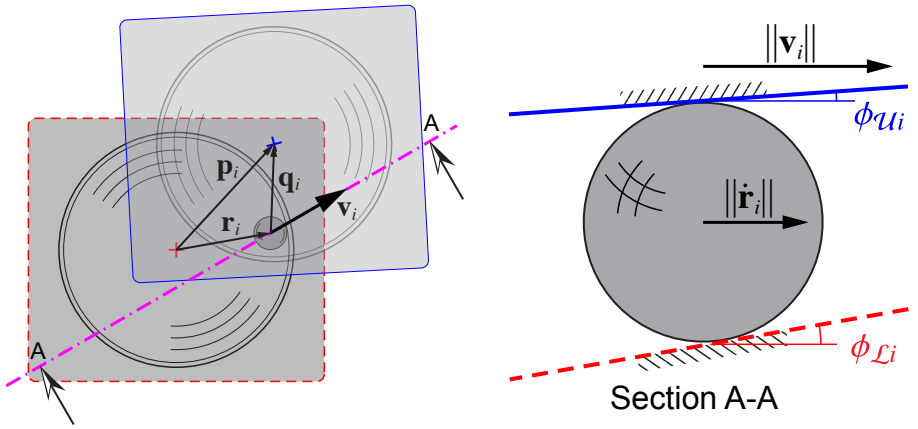


FIGURE 3.3: Geometry of a sphere rolling between two non-parallel surfaces.

where $\eta(r)$ is the bowl-shape function. All bowls are assumed axisymmetric; i.e., the height $\eta(r)$ is a function of only the radial distance of the ball with respect to the center of the $i$th lower- and upper-bowls.

### *3.2.3 Kinematics of rolling ball-bearings*

The potential energy and the ensuing equations of state depend upon the locations of the ball-bearings $\mathbf{r}_i$. Here we analyze the kinematics of spheres rolling between non-parallel planes to show that the ball-bearing positions cannot be determined uniquely from the platform position, but evolve according the relative velocities across the platform.

The mass ratio of the top-frame to the ball-bearing is of the order of 1,000:1; in this study we are neglecting the inertia of the ball-bearings. Inertialess ball-bearings are not affected by gravity and do not resist motion of the top-frame through their own inertia. If the top-frame were ever to lose contact with the ball-bearing, the model would need to include ball-bearing inertia in the ball dynamics. Including ball-bearing inertia would require explicit modeling of forces between the ball-bearings and contact surfaces.

From Equations (3.2) and (3.3), the velocity of the top-frame at the location of ball-bearing $i$ is found to be

$$\mathbf{v}_i = \begin{bmatrix} v_{xi} \\ v_{yi} \end{bmatrix} = \begin{bmatrix} \dot{\bar{x}} \\ \dot{\bar{y}} \end{bmatrix} + \dot{\bar{\theta}} \begin{bmatrix} 0 & -1 \\ 1 & 0 \end{bmatrix} \begin{bmatrix} x_{\text{ball},i} \\ y_{\text{ball},i} \end{bmatrix} \tag{3.13}$$

for which we have defined

$$\begin{bmatrix} x_{\text{ball},i} \\ y_{\text{ball},i} \end{bmatrix} = \begin{bmatrix} a_i \\ b_i \end{bmatrix} + \begin{bmatrix} r_{xi} \\ r_{yi} \end{bmatrix} - \begin{bmatrix} \bar{x} \\ \bar{y} \end{bmatrix} . \tag{3.14}$$

Assuming slip-free rolling at the ball-bowl contact points, the ball-bearings roll in the direction of the velocity of the top-frame (at the ball-bearing locations) with respect to the bottom-frame. The height of the $i$th bowl is given by Equation (3.12), and the gradients of the lower- and upper-bowls at the location of ball-bearing $i$ in the radial direction are as follows:

$$\nabla h_{\mathcal{L}i} = \eta'(\|\mathbf{r}_i\|)\,\hat{\mathbf{r}}_i \quad \text{and} \quad \nabla h_{\mathcal{U}i} = \eta'(\|\mathbf{q}_i\|)\,\hat{\mathbf{q}}_i \tag{3.15}$$

where $\eta'(r) = \mathrm{d}\eta(r)/\mathrm{d}r$ and the normalized vectors $\hat{\mathbf{r}}_i = \mathbf{r}_i/\|\mathbf{r}_i\|$ and $\hat{\mathbf{q}}_i = \mathbf{q}_i/\|\mathbf{q}_i\|$. Knowing $\mathbf{v}_i$, the velocity of the top-frame at ball-bearing $i$, the components of the bowl gradients in the plane of $\hat{\mathbf{v}}_i \equiv \mathbf{v}_i/\|\mathbf{v}_i\|$ are given by the inner product:

$$h'_{\mathcal{L}i} = \hat{\mathbf{v}}_i^{\mathsf{T}} \nabla h_{\mathcal{L}i} \;\text{ and }\; h'_{\mathcal{U}i} = \hat{\mathbf{v}}_i^{\mathsf{T}} \nabla h_{\mathcal{U}i}.$$

Now, we follow the work on the kinematics of a rolling ball-bearing on inclined surfaces where the upper-surface has a horizontal velocity $\mathbf{v}_i$. Referring to Figure 3.3, the angles of the bottom- and top-surfaces in the rolling direction are

$$\phi_{\mathcal{L}i} = \tan^{-1}(h'_{\mathcal{L}i}) \quad \text{and} \quad \phi_{\mathcal{U}i} = \tan^{-1}(h'_{\mathcal{U}i}) ,$$

and the magnitude of the ball-bearing's velocity parallel to $\mathbf{v}_i$ is

$$\|\dot{\mathbf{r}}_i\| = \frac{\cos\phi_{\mathcal{L}i}}{\cos\phi_{\mathcal{L}i} + \cos\phi_{\mathcal{U}i}} \|\mathbf{v}_i\| . \tag{3.16}$$

Thus, the condition for rolling without slipping of a ball-bearing is

$$\dot{\mathbf{r}}_i = \|\dot{\mathbf{r}}_i\|\,\hat{\mathbf{v}}_i \equiv \varphi_i \mathbf{v}_i , \;\; (i = 1, ..., 4) \tag{3.17}$$

where we have defined

$$\varphi_i \equiv \varphi_i(\bar{x}, \bar{y}, \bar{\theta}, \dot{\bar{x}}, \dot{\bar{y}}, \dot{\bar{\theta}}, \mathbf{r}_i) = \frac{\cos\phi_{\mathcal{L}i}}{\cos\phi_{\mathcal{L}i} + \cos\phi_{\mathcal{U}i}} . \tag{3.18}$$

The motion of each ball-bearing is completely prescribed by the motion of the top-frame; the ball-bearing dynamics are thus expressed as a kinematic condition (3.17).

Equation (3.17) represents eight nonlinear equations prescribing the evolution of the $(x_b, y_b)$ locations of the four ball-bearings. The evolution of ball-bearing positions $\mathbf{r}_i$ is nonlinear in the velocity and position of the top-frame, and is nonlinear in the position of the ball-bearing locations. This kind of kinematic condition is representative of generalized nonholonomic constraints [77]. These constraints can be expressed as

$$\mathbf{0} = \mathbf{g}_i = \dot{\mathbf{r}}_i - \varphi_i \mathbf{v}_i \ , \ (i = 1, ..., 4) \ . \tag{3.19}$$

It is useful to briefly consider the following two limiting cases: (a) For motion between horizontal planes, $\phi_{\mathcal{L}i} = \phi_{\mathcal{U}i} = 0$, the magnitude of the ball-bearing's velocity parallel to $\mathbf{v}_i$, given by Equation (3.16), reduces to $\|\dot{\mathbf{r}}_i\| = \|\mathbf{v}_i\|/2$. The ball-bearing's center velocity is half that of the relative velocity between the plates; at the point of contact with the lower-bowl, the velocity is zero; and at the point of contact with the upper-bowl, the velocity is equal to the relative velocity. (b) For motion between parallel inclined planes, $\phi_{\mathcal{L}i} = \phi_{\mathcal{U}i}$, Equation (3.17) reduces to $\dot{\mathbf{r}}_i = \mathbf{v}_i/2$. Regardless of the inclination, for parallel surfaces the horizontal velocity of the ball-bearing is half the relative velocity across the ball-bearing. Such a case arises when the ball-bearing falls on the centerline between the top and bottom bowl centers (for identical axisymmetric top and bottom bowls), i.e. $\mathbf{p}_i = \mathbf{r}_i + \mathbf{q}_i = 2\mathbf{r}_i$, and relative velocity $\mathbf{v}_i$ is co-linear with $\mathbf{p}_i$, i.e. $\mathbf{v}_i \propto \mathbf{p}_i$.

### *3.2.4 Fundamental nonholonomic form of Lagrange's equation*

In this study, the generalized coordinates $z \in \mathcal{Z} = \{\bar{x}, \bar{y}, \bar{\theta}, r_{1x}, r_{1y}, ..., r_{4x}, r_{4y}\}$ give the position and orientation of the center of the top-frame and the ball-bearing locations. Defining the Lagrangian in terms of these generalized coordinates to be

$$L \equiv L(\bar{x}, \bar{y}, \bar{\theta}, \dot{\bar{x}}, \dot{\bar{y}}, \dot{\bar{\theta}}, \mathbf{r}_1, ..., \mathbf{r}_4) = T(\dot{\bar{x}}, \dot{\bar{y}}, \dot{\bar{\theta}}, \bar{\theta}) - V(\bar{x}, \bar{y}, \bar{\theta}, \mathbf{r}_1, ..., \mathbf{r}_4) \ . \tag{3.20}$$

The fundamental nonholonomic form of Lagrange's equation [67] states that for any generalized coordinate $z$, the equation of state is given by:

$$\frac{\mathrm{d}}{\mathrm{d}t}\left(\frac{\partial L}{\partial \dot{z}}\right) - \frac{\partial L}{\partial z} = Q_z^{\mathrm{C}} + Q_z^{\mathrm{D}}. \tag{3.21}$$

Forces $Q_z^{\mathrm{C}}$ and $Q_z^{\mathrm{D}}$ are not derivable from potential energy functions. The forces $Q_z^{\mathrm{D}}$ are dissipative forces, corresponding to loss of energy, and are associated with micro-slip mechanisms over the finite contact surfaces between the steel ball-bearings and the steel bowls. These damping forces are relatively small and are determined from experimental data, as described in Section 3.5.

The forces $Q_z^{\mathrm{C}}$ of nonholonomic constraints (3.17) are non-dissipative and are given by

$$Q_z^{\mathrm{C}} = \sum_{i=1}^{4} \left(\frac{\partial \mathbf{g}_i}{\partial \dot{z}}\right)^{\mathsf{T}} \boldsymbol{\lambda}_i \tag{3.22}$$

where the $\boldsymbol{\lambda}_i$ are Lagrange multipliers [78]. These rolling contact forces enforce the constrained velocity trajectory of each ball-bearing and are transverse to the path of the ball-bearing. For the centroidal coordinates $z \in \{\bar{x}, \bar{y}, \bar{\theta}\}$, the constraints $\mathbf{g}_i$ depend on $\dot{z}$ non-linearly, though only through the ball-bearing velocity vector $\mathbf{v}_i$, viz.

$$\frac{\partial \mathbf{g}_i}{\partial \dot{z}} = -\left(\frac{\partial \varphi_i}{\partial \mathbf{v}_i}\frac{\partial \mathbf{v}_i}{\partial \dot{z}}\right)\mathbf{v}_i - \varphi_i \frac{\partial \mathbf{v}_i}{\partial \dot{z}}. \tag{3.23}$$

The details of the gradient $\partial\varphi_i/\partial\mathbf{v}_i$ are as follows:

$$\frac{\partial \varphi_k}{\partial \mathbf{v}_k} = \left(\frac{\cos\phi_{\mathcal{L}i}\sin\phi_{\mathcal{U}i}}{(\cos\phi_{\mathcal{L}i}+\cos\phi_{\mathcal{U}i})^2}\frac{\eta'(\|\mathbf{q}_i\|)\hat{\mathbf{q}}_i^{\mathsf{T}}}{1+{h'_{\mathcal{U}i}}^2} - \frac{\cos\phi_{\mathcal{U}i}\sin\phi_{\mathcal{L}i}}{(\cos\phi_{\mathcal{L}i}+\cos\phi_{\mathcal{U}i})^2}\frac{\eta'(\|\mathbf{r}_i\|)\hat{\mathbf{r}}_i^{\mathsf{T}}}{1+{h'_{\mathcal{L}i}}^2}\right)\frac{(\mathbf{I}-\hat{\mathbf{v}}_i\hat{\mathbf{v}}_i^{\mathsf{T}})}{\|\mathbf{v}_i\|}. \tag{3.24}$$

Whereas, for the ball-bearing coordinates $z \in \{r_{1x}, r_{1y}, ..., r_{4x}, r_{4y}\}$, the constraints $\mathbf{g}_i$ depend on $\dot{\mathbf{r}}_k$ linearly, and the Jacobian matrix $\partial\mathbf{g}_i/\partial\dot{\mathbf{r}}_k$ decouples as follows:

$$\frac{\partial \mathbf{g}_i}{\partial \dot{\mathbf{r}}_k} = \frac{\partial \dot{\mathbf{r}}_i}{\partial \dot{\mathbf{r}}_k} = \begin{cases} \mathbf{I}_{2\times 2}, & i = k \\ \mathbf{0}_{2\times 2}, & i \neq k \end{cases}. \tag{3.25}$$

With the assumption that the ball-bearing dimensions are small compared to the overall platform geometry, the point of rolling contact coincides with the ball-bearing centers. Dissipative forces acting on the platform centroid ($Q^{\mathrm{D}}_{\bar{x}}$, $Q^{\mathrm{D}}_{\bar{y}}$, and $Q^{\mathrm{D}}_{\bar{\theta}}$) are assumed to be zero. The dissipative forces acting at the ball-bearing centers are modeled as linear-viscous damping: $Q^{\mathrm{D}}_{r_{kx}} = -C_{\mathrm{b}}\dot{r}_{kx}$ and $Q^{\mathrm{D}}_{r_{ky}} = -C_{\mathrm{b}}\dot{r}_{ky}$. The consequence of this assumption follows in Section 3.2.5.

*The case of the generalized coordinate $\bar{x}$:*

Referring to Equation (3.21), and starting with the first term,

$$\frac{\mathrm{d}}{\mathrm{d}t}\left(\frac{\partial L}{\partial \dot{\bar{x}}}\right) = \frac{\mathrm{d}}{\mathrm{d}t}\left(\frac{\partial T}{\partial \dot{\bar{x}}}\right) = m(\ddot{w}_x + \ddot{\bar{x}}) - m\dot{e}_{\mathrm{b}y}\dot{\bar{\theta}} - me_{\mathrm{b}y}\ddot{\bar{\theta}} \tag{3.26}$$

in which $[\dot{e}_{\mathrm{b}x}\ \dot{e}_{\mathrm{b}y}]^{\mathsf{T}} = \dot{\bar{\theta}}\mathbf{R}'_{\bar{\theta}}[e_x\ e_y]^{\mathsf{T}}$. Referring to the second term in Equation (3.21), recall $V = mg\boldsymbol{u}\boldsymbol{h}$ and $h_i(\bar{x}, \bar{y}, \bar{\theta}, \mathbf{r}_i)$ is given by Equation (3.12). Then,

$$-\frac{\partial L}{\partial \bar{x}} = \frac{\partial V}{\partial \bar{x}} = mg\boldsymbol{u}\frac{\partial \boldsymbol{h}}{\partial \bar{x}} = mg\sum_{i=1}^{4} u_i \frac{\partial h_i}{\partial \bar{x}} \tag{3.27}$$

for which

$$\frac{\partial h_i}{\partial \bar{x}} = \frac{\partial}{\partial \bar{x}}\Big[\eta(\|\mathbf{r}_i\|) + \eta(\|\mathbf{q}_i(\bar{x}, \bar{y}, \bar{\theta}, \mathbf{r}_i)\|)\Big] = \eta'(\|\mathbf{q}_i\|)\left(\frac{\partial \mathbf{q}_i}{\partial \bar{x}}\right)^{\mathsf{T}}\hat{\mathbf{q}}_i = \eta'(\|\mathbf{q}_i\|)\begin{bmatrix}1\\0\end{bmatrix}^{\mathsf{T}}\hat{\mathbf{q}}_i. \tag{3.28}$$

As previously stated, $Q^{\mathrm{D}}_{\bar{x}}$ is taken to be zero. The constraint force $Q^{\mathrm{C}}_{\bar{x}}$ is given by

$$Q^{\mathrm{C}}_{\bar{x}} = -\sum_{i=1}^{4}\left(\left(\frac{\partial \varphi_i}{\partial \mathbf{v}_i}\begin{bmatrix}1\\0\end{bmatrix}\right)\mathbf{v}_i + \varphi_i\begin{bmatrix}1\\0\end{bmatrix}\right)^{\mathsf{T}}\boldsymbol{\lambda}_i \tag{3.29}$$

where $\partial\varphi_k/\partial\mathbf{v}_k$ is given by Equation (3.24) and $\boldsymbol{\lambda}_i$ have yet to be determined.

*The case of the generalized coordinate $\bar{y}$:*

Referring to Equation (3.21), and starting with the first term,

$$\frac{\mathrm{d}}{\mathrm{d}t}\left(\frac{\partial L}{\partial \dot{\bar{y}}}\right) = \frac{\mathrm{d}}{\mathrm{d}t}\left(\frac{\partial T}{\partial \dot{\bar{y}}}\right) = m(\ddot{w}_y + \ddot{\bar{y}}) + m\dot{e}_{\mathrm{b}x}\dot{\bar{\theta}} + me_{\mathrm{b}x}\ddot{\bar{\theta}} \tag{3.30}$$

where $\dot{e}_{bx}$ is given above. Referring to the second term in Equation (3.21), the process is similar to the procedure for $\bar{x}$, and

$$-\frac{\partial L}{\partial \bar{y}} = \frac{\partial V}{\partial \bar{y}} = mg\boldsymbol{u}\frac{\partial \boldsymbol{h}}{\partial \bar{y}} = mg\sum_{i=1}^{4} u_i \eta'(\|\mathbf{q}_i\|)\begin{bmatrix}0\\1\end{bmatrix}^{\mathsf{T}}\hat{\mathbf{q}}_i\,. \tag{3.31}$$

The non-potential force $Q_{\bar{y}}^{\mathrm{D}}$ is taken to be zero. Finally,

$$Q_{\bar{y}}^{\mathrm{C}} = -\sum_{i=1}^{4}\left(\left(\frac{\partial \varphi_i}{\partial \mathbf{v}_i}\begin{bmatrix}0\\1\end{bmatrix}\right)\mathbf{v}_i + \varphi_i\begin{bmatrix}0\\1\end{bmatrix}\right)^{\mathsf{T}}\boldsymbol{\lambda}_i \tag{3.32}$$

where $\partial\varphi_k/\partial\mathbf{v}_k$ is given by Equation (3.24) and $\boldsymbol{\lambda}_i$ have yet to be determined.

*The case of the generalized coordinate $\bar{\theta}$:*

Referring to Equation (3.21), and starting with the first term,

$$\frac{\mathrm{d}}{\mathrm{d}t}\left(\frac{\partial L}{\partial \dot{\bar{\theta}}}\right) = \frac{\mathrm{d}}{\mathrm{d}t}\left(\frac{\partial T}{\partial \dot{\bar{\theta}}}\right) = m\Big[(\ddot{w}_y + \ddot{\bar{y}})e_{bx} - (\ddot{w}_x + \ddot{\bar{x}})e_{by} + (\dot{w}_y + \dot{\bar{y}})\dot{e}_{bx} - (\dot{w}_x + \dot{\bar{x}})\dot{e}_{by}\Big] + I\ddot{\bar{\theta}} \tag{3.33}$$

where $(e_{bx}, e_{by})$ and $(\dot{e}_{bx}, \dot{e}_{by})$ are as defined previously. The second term in Equation (3.21),

$$-\frac{\partial L}{\partial \bar{\theta}} = -\frac{\partial T}{\partial \bar{\theta}} + \frac{\partial V}{\partial \bar{\theta}} = -m\dot{\bar{\theta}}\Big[(\dot{w}_y + \dot{\bar{y}})\frac{\partial e_{bx}}{\partial \bar{\theta}} - (\dot{w}_x + \dot{\bar{x}})\frac{\partial e_{by}}{\partial \bar{\theta}}\Big] + mg\sum_{i=1}^{4} u_i\frac{\partial h_i}{\partial \bar{\theta}} \tag{3.34}$$

for which

$$\frac{\partial h_i}{\partial \bar{\theta}} = \eta'(\|\mathbf{q}_i\|)\begin{bmatrix}a_i\\b_i\end{bmatrix}^{\mathsf{T}}\mathbf{R}_{\bar{\theta}}'^{\mathsf{T}}\hat{\mathbf{q}}_i\,. \tag{3.35}$$

However, we notice here that $\dot{\bar{\theta}}\,\partial e_{bx}/\partial\bar{\theta} = \dot{e}_{bx}$ and $\dot{\bar{\theta}}\,\partial e_{by}/\partial\bar{\theta} = \dot{e}_{by}$. Thus, Equation (3.34) reduces to

$$-\frac{\partial L}{\partial \bar{\theta}} = -m\Big[(\dot{w}_y + \dot{\bar{y}})\dot{e}_{bx} - (\dot{w}_x + \dot{\bar{x}})\dot{e}_{by}\Big] + mg\sum_{i=1}^{4} u_i\eta'(\|\mathbf{q}_i\|)\begin{bmatrix}a_i\\b_i\end{bmatrix}^{\mathsf{T}}\mathbf{R}_{\bar{\theta}}'^{\mathsf{T}}\hat{\mathbf{q}}_i\,. \tag{3.36}$$

The non-potential force is $Q^{\mathrm{D}}_{\bar{\theta}} = 0$ and the constraint force is

$$Q^{\mathrm{C}}_{\bar{\theta}} = -\sum_{i=1}^{4} \left( \left( \frac{\partial \varphi_i}{\partial \mathbf{v}_i} \frac{\partial \mathbf{v}_i}{\partial \dot{\bar{\theta}}} \right) \mathbf{v}_i + \varphi_i \frac{\partial \mathbf{v}_i}{\partial \dot{\bar{\theta}}} \right)^{\mathsf{T}} \boldsymbol{\lambda}_i \tag{3.37}$$

where

$$\frac{\partial \mathbf{v}_i}{\partial \dot{\bar{\theta}}} = \begin{bmatrix} 0 & -1 \\ 1 & 0 \end{bmatrix} \left( \begin{bmatrix} a_i \\ b_i \end{bmatrix} + \begin{bmatrix} r_{ix} \\ r_{iy} \end{bmatrix} - \begin{bmatrix} \bar{x} \\ \bar{y} \end{bmatrix} \right) = \begin{bmatrix} -y_{\mathrm{ball},i} \\ x_{\mathrm{ball},i} \end{bmatrix} .$$

*The case of the generalized coordinates $r_{ix}$ and $r_{iy}$:*

Referring to Equation (3.21), we notice that $T$ and $V$ are independent of $\dot{\mathbf{r}}_i = [\dot{r}_{ix}\ \dot{r}_{iy}]^{\mathsf{T}}$, and only $V$ depends on $\mathbf{r}_i = [r_{ix}\ r_{iy}]^{\mathsf{T}}$. Thus, the left-side of Equation (3.21) reduces to

$$\frac{\mathrm{d}}{\mathrm{d}t}\left( \frac{\partial L}{\partial \dot{\mathbf{r}}_i} \right) - \frac{\partial L}{\partial \mathbf{r}_i} = \frac{\partial V}{\partial \mathbf{r}_i} = mg \sum_{j=1}^{4} u_j \frac{\partial h_j}{\partial \mathbf{r}_i} = mgu_i \left( \eta'(\|\mathbf{r}_i\|)\, \hat{\mathbf{r}}_i - \eta'(\|\mathbf{q}_i\|)\, \hat{\mathbf{q}}_i \right)^{\mathsf{T}} \tag{3.38}$$

because the gradient $\partial h_j / \partial \mathbf{r}_i = \partial h_i / \partial \mathbf{r}_i$ for $j = i$ and zero otherwise, due to the decoupling of the bowl height $h_i$ and ball-bearing displacement $\mathbf{r}_i$. The gravitational restoring force is composed of two parts—contributions from the lower- and upper-bowls,

$$\mathbf{f}_{\mathcal{L}i} = mgu_i \eta'(\|\mathbf{r}_i\|)\, \hat{\mathbf{r}}_i \quad \text{and} \quad \mathbf{f}_{\mathcal{U}i} = mgu_i \eta'(\|\mathbf{q}_i\|)\, \hat{\mathbf{q}}_i \, . \tag{3.39}$$

Following from Equation (3.25), the constraint forces are $[Q^{\mathrm{C}}_{r_{ix}}\ Q^{\mathrm{C}}_{r_{iy}}] = \boldsymbol{\lambda}_i^{\mathsf{T}}$. Recall the damping forces are taken to be $Q^{\mathrm{D}}_{r_{ix}} = -C_{\mathrm{b}} \dot{r}_{ix}$ and $Q^{\mathrm{D}}_{r_{iy}} = -C_{\mathrm{b}} \dot{r}_{iy}$. By substituting these expressions into Equation (3.21), expressions for the multipliers $\boldsymbol{\lambda}_i$ are readily apparent:

$$\boldsymbol{\lambda}_i = C_{\mathrm{b}} \dot{\mathbf{r}}_i + \mathbf{f}_{\mathcal{L}i} - \mathbf{f}_{\mathcal{U}i} \, . \tag{3.40}$$

### *3.2.5 System dynamics*

The equations of state from the previous sections simplify to:

$$m(\ddot{\bar{x}} + \ddot{w}_x) - m(e_x \cos\bar{\theta} - e_y \sin\bar{\theta})\dot{\bar{\theta}}^2 - m(e_x \sin\bar{\theta} + e_y \cos\bar{\theta})\ddot{\bar{\theta}}$$

$$+\sum_{i=1}^{4}\mathbf{f}_{\mathcal{U}i}^{\mathsf{T}}\begin{bmatrix}1\\0\end{bmatrix}+\sum_{i=1}^{4}\left(\left(\frac{\partial\varphi_i}{\partial\mathbf{v}_i}\begin{bmatrix}1\\0\end{bmatrix}\right)\mathbf{v}_i+\varphi_i\begin{bmatrix}1\\0\end{bmatrix}\right)^{\mathsf{T}}(C_{\mathrm{b}}\dot{\mathbf{r}}_i+\mathbf{f}_{\mathcal{L}i}-\mathbf{f}_{\mathcal{U}i})=0 \quad (3.41a)$$

$$m(\ddot{\bar{y}}+\ddot{w}_y)-m(e_x\sin\bar{\theta}+e_y\cos\bar{\theta})\dot{\bar{\theta}}^2+\ m(e_x\cos\bar{\theta}-e_y\sin\bar{\theta})\ddot{\bar{\theta}}$$
$$+\sum_{i=1}^{4}\mathbf{f}_{\mathcal{U}i}^{\mathsf{T}}\begin{bmatrix}0\\1\end{bmatrix}+\sum_{i=1}^{4}\left(\left(\frac{\partial\varphi_i}{\partial\mathbf{v}_i}\begin{bmatrix}0\\1\end{bmatrix}\right)\mathbf{v}_i+\varphi_i\begin{bmatrix}0\\1\end{bmatrix}\right)^{\mathsf{T}}(C_{\mathrm{b}}\dot{\mathbf{r}}_i+\mathbf{f}_{\mathcal{L}i}-\mathbf{f}_{\mathcal{U}i})=0 \quad (3.41b)$$

$$m\Big[(e_x\cos\bar{\theta}-e_y\sin\bar{\theta})(\ddot{\bar{y}}+\ddot{w}_y)-(e_x\sin\bar{\theta}+e_y\cos\bar{\theta})(\ddot{\bar{x}}+\ddot{w}_x)\Big]+I\ddot{\bar{\theta}}$$
$$+\sum_{i=1}^{4}\mathbf{f}_{\mathcal{U}i}^{\mathsf{T}}\mathbf{R}'_{\bar{\theta}}\begin{bmatrix}a_i\\b_i\end{bmatrix}+\sum_{i=1}^{4}\left(\left(\frac{\partial\varphi_i}{\partial\mathbf{v}_i}\begin{bmatrix}-y_{\mathrm{ball},i}\\x_{\mathrm{ball},i}\end{bmatrix}\right)\mathbf{v}_i+\varphi_i\begin{bmatrix}-y_{\mathrm{ball},i}\\x_{\mathrm{ball},i}\end{bmatrix}\right)^{\mathsf{T}}(C_{\mathrm{b}}\dot{\mathbf{r}}_i+\mathbf{f}_{\mathcal{L}i}-\mathbf{f}_{\mathcal{U}i})=0 \quad (3.41c)$$

Note that these equations of state involve the ball-bearing locations $\mathbf{r}_i$ through the terms $\mathbf{f}_{\mathcal{L}i}$ and $\mathbf{f}_{\mathcal{U}i}$, which are evaluated at the ball-bearing locations $\mathbf{r}_i$. So far, $\eta(r)$ can represent any axisymmetric bowl profile. In the undamped case, the damping rate $C_{\mathrm{b}}$ is zero implying the non-potential forces $Q^{\mathrm{D}}_{r_{ix}}$ and $Q^{\mathrm{D}}_{r_{iy}}$ are equal to zero, as well.

The full set of system dynamics comprise Equations (3.17) and (3.41). Investigating Equations (3.41) further, we see that Equations (3.41a) and (3.41b) represent the force balance in the bottom-frame coordinates $X_{\mathrm{b}}$-$Y_{\mathrm{b}}$. Likewise, Equation (3.41c) is the moment balance about the centroid of the top-frame. Equations of state (Equations (3.41)) are highly nonlinear—the rotations are nonlinearly coupled with accelerations and rotational velocity. As previously noted, the ball-bearing motions $\dot{\mathbf{r}}_i$ are fully determined by the motion of the top-frame and must be simulated simultaneously with the platform motion.

## 3.3 Energy Conservation

The total energy of the system is

$$E(t)=T+V=\tfrac{1}{2}m(\dot{\bar{x}}^2+\dot{\bar{y}}^2)+m(\dot{\bar{y}}e_{\mathrm{b}x}-\dot{\bar{x}}e_{\mathrm{b}y})\dot{\bar{\theta}}+\tfrac{1}{2}I\dot{\bar{\theta}}^2+mg\boldsymbol{u}\boldsymbol{h} \quad (3.42)$$

when $\dot{w}_x(t) \equiv 0$ and $\dot{w}_y(t) \equiv 0$, i.e. in free response. Sufficient conditions for a conservative system having nonholonomic constraints are the following [67]: (i) the general form of Lagrange's equation (3.21) applies, (ii) the Lagrangian, Equation (3.20), is not an explicit function of time, and (iii) all constraints $\mathbf{g}_i$ are conservative. If these three criteria are satisfied, $\dot{E}(t) \equiv 0 \; \forall t$.

Criterion (i) is immediately satisfied from the development of Section 3.2. Criterion (ii) is satisfied if $\boldsymbol{w}(t) \equiv \mathbf{0}$. Criterion (iii) is proved by showing that

$$\sum_{z \in \mathcal{Z}} \frac{\partial \mathbf{g}_i}{\partial \dot{z}} \dot{z} = \mathbf{0}, \quad (i = 1, ...4) \,, \tag{3.43}$$

i.e. the constraint forces $Q_z^{\mathrm{C}}$ do no work, and the undamped, unforced system is indeed conservative. This result is numerically verified in Section 3.6.1.

**Theorem 1.** *The nonholonomic constraints, Equations* (3.19)*, restricting the motion of the ball-bearings, are conservative and satisfy the condition of Equation* (3.43)*.*

*Proof.* In order for a nonholonomic constraint, $\mathbf{g}_i = \mathbf{0}$, to be conservative, it must be work-less and satisfy Equation (3.43), which states the following: for $i = 1, ..., 4$,

$$\mathbf{0} = \sum_{z \in \mathcal{Z}} \frac{\partial \mathbf{g}_i}{\partial \dot{z}} \dot{z} = \frac{\partial \mathbf{g}_i}{\partial \dot{\tilde{x}}} \dot{\tilde{x}} + \frac{\partial \mathbf{g}_i}{\partial \dot{\tilde{y}}} \dot{\tilde{y}} + \frac{\partial \mathbf{g}_i}{\partial \dot{\tilde{\theta}}} \dot{\tilde{\theta}} + \sum_{j=1}^{4} \frac{\partial \mathbf{g}_i}{\partial \dot{\mathbf{r}}_j} \dot{\mathbf{r}}_j = \frac{\partial \mathbf{g}_i}{\partial \dot{\tilde{x}}} \dot{\tilde{x}} + \frac{\partial \mathbf{g}_i}{\partial \dot{\tilde{y}}} \dot{\tilde{y}} + \frac{\partial \mathbf{g}_i}{\partial \dot{\tilde{\theta}}} \dot{\tilde{\theta}} + \dot{\mathbf{r}}_i$$

$$= -\left( \frac{\partial \varphi_i}{\partial \mathbf{v}_i} \begin{bmatrix} \dot{\tilde{x}} - y_{\mathrm{ball},i} \dot{\tilde{\theta}} \\ \dot{\tilde{y}} + x_{\mathrm{ball},i} \dot{\tilde{\theta}} \end{bmatrix} \right) \mathbf{v}_i - \varphi_i \begin{bmatrix} \dot{\tilde{x}} - y_{\mathrm{ball},i} \dot{\tilde{\theta}} \\ \dot{\tilde{y}} + x_{\mathrm{ball},i} \dot{\tilde{\theta}} \end{bmatrix} + \dot{\mathbf{r}}_i = -\left( \frac{\partial \varphi_i}{\partial \mathbf{v}_i} \mathbf{v}_i \right) \mathbf{v}_i - \varphi_i \mathbf{v}_i + \dot{\mathbf{r}}_i = -\left( \frac{\partial \varphi_i}{\partial \mathbf{v}_i} \mathbf{v}_i \right) \mathbf{v}_i + \mathbf{g}_i \,.$$

The nonholonomic constraint $\mathbf{g}_i$ must equal zero by Equation (3.19). Therefore, all that remains is to prove the following:

$$\mathbf{0} = -\left( \frac{\partial \varphi_i}{\partial \mathbf{v}_i} \mathbf{v}_i \right) \mathbf{v}_i \,.$$

To this end, we work on the inner product, which by Equation (3.24),

$$\frac{\partial \varphi_i}{\partial \mathbf{v}_i} \mathbf{v}_i \propto \left( \frac{\mathbf{I} - \hat{\mathbf{v}}_i \hat{\mathbf{v}}_i^{\mathsf{T}}}{\|\mathbf{v}_i\|} \right) \mathbf{v}_i = \left( \mathbf{I} - \hat{\mathbf{v}}_i \hat{\mathbf{v}}_i^{\mathsf{T}} \right) \hat{\mathbf{v}}_i \equiv \mathbf{0} \,.$$

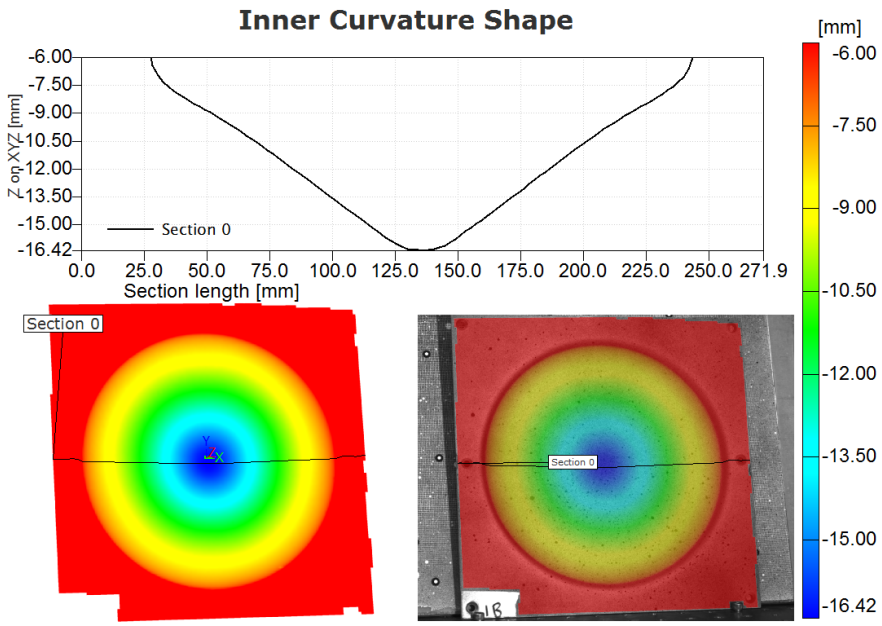


FIGURE 3.4: 3D bowl-shape measurement analysis.

Thus, $(\partial\varphi_i/\partial\mathbf{v}_i)\mathbf{v}_i = 0$, Equation (3.43) is satisfied, and the constraints (3.19) are conservative. □

## 3.4 Bowl Fitting

The bowls used in the platforms in this study (WorkSafe Iso-Base) were designed to have a conical radial profile. With this profile, the accelerations experienced by the isolated mass are bounded by the slope of the bowl profile ($\approx 0.1g$). However, due to the manufacturing process whereby thin stainless steel sheets are stamped in a mold, the bowls are not perfectly conical. Three-dimensional digital photogrammetry of sixteen bowl surfaces provided the data required to fit bowl profile models representative of the actual bowls used in practice. A representative bowl shape is provided in Figure 3.4. Figure 3.5(a) shows the resolution of the photogrammetry data: on the order of 13,500 points per bowl of which approximately 9,000 points are within the circular dished area.

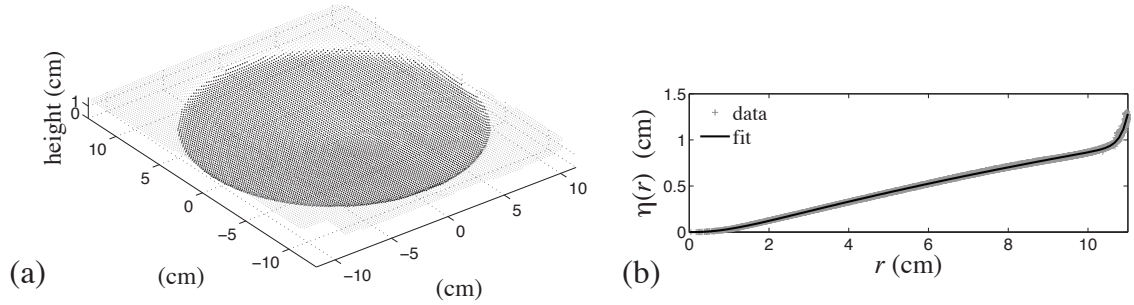


FIGURE 3.5: (a) Measured bowl shapes for a clamped bowl (•) and dished surface data (•). (b) Measured data for the bowl profile with nonlinear fitted bowl parameterization.

A proposed bowl profile parameterization is given as follows:

$$\eta(r) = \beta_1 \ln\left[\cosh\left(\frac{r}{\beta_2}\right)\right]\frac{\beta_2}{R} + \beta_3\left(\frac{r}{R}\right)^{\beta_4} + \beta_5\left(\frac{r}{R}\right)^{\beta_6} \tag{3.44}$$

where $R = 10$ cm. The first term accounts for the conical shape of the bowl with a rounded bottom, the second term accounts for the lip at the outer edge of the bowl where $r \approx 10$ cm, and the third term accounts for the negative curvature in the region $6 < r < 10$ cm.

Fit parameters $\beta_i$ are found for each of the sixteen bowls using a Levenberg-Marquardt algorithm [79, 80] to solve the nonlinear least-squares problem. The resulting parameter estimates are given in Table 3.1. Figure 3.5(b) shows the fit of Equation (3.44) to the photogrammetry data for a single bowl.

It is important to note that the bowl possesses regions of positive, negative and highly-positive curvature. The negative curvature at large radii (i.e. $6 < r < 10$ cm) introduces a softening effect, and the highly-positive curvature (or the lip) at the bowl extreme (i.e. $r > 10$ cm) acts as a hard displacement limit. Impacts of the ball-bearing with the lip

TABLE 3.1: Estimated mean and coefficient of variation (CV) for fit parameters $\beta_i$.

| $\beta_i$ | mean | CV | units | $\beta_i$ | mean | CV | units |
|---|---|---|---|---|---|---|---|
| $\beta_1$ | 1.4297 | 0.0434 | cm | $\beta_4$ | 59.0050 | 0.0616 | - |
| $\beta_2$ | 1.2717 | 0.0771 | cm | $\beta_5$ | -0.4501 | 0.1037 | cm |
| $\beta_3$ | 0.0013 | 0.4613 | cm | $\beta_6$ | 1.4357 | 0.0433 | - |

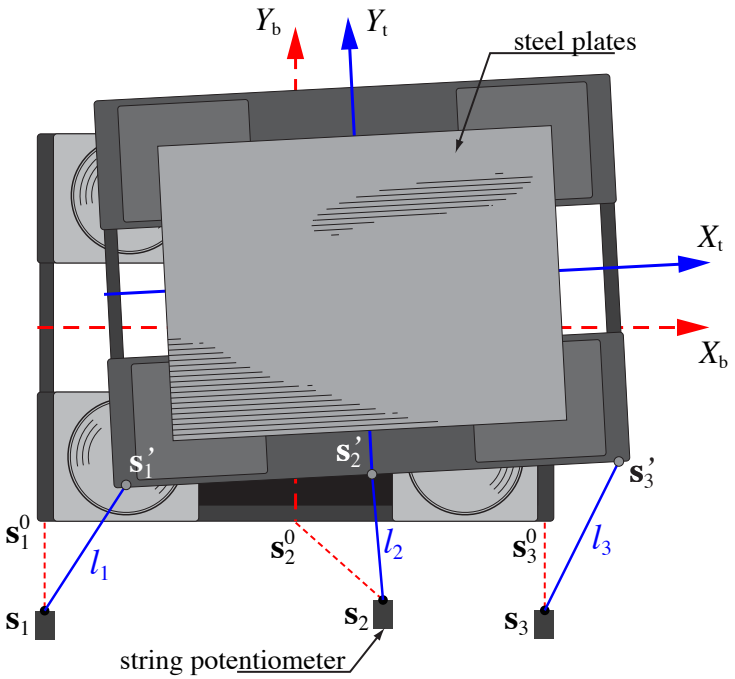


FIGURE 3.6: Experimental setup using three string potentiometers.

produce high accelerations that may be detrimental to isolated objects.

## 3.5 Energy Dissipation

In rolling platform systems, energy is dissipated at the interface between the ball-bearings and the steel bowls. Energy dissipation mechanisms can be uncovered through analyzing the energy content of experimental free responses. In these free-response experiments the platform position and velocity are determined through measurements of the distances between three points on the top-frame with respect to three fixed points in the bottom-frame coordinate system $X_b$-$Y_b$, as shown in Figure 3.6.

Three string potentiometers are attached to the top-frame at points $\mathbf{s}_i^0$ in the un-displaced configuration, i.e. $\bar{x}$, $\bar{y}$, and $\bar{\theta}$ are zero. When the top-frame is displaced $(\bar{x}, \bar{y}, \bar{\theta})$, the attachment points displace to coordinates $\mathbf{s}_i'$ as determined by Equation (3.2) to be

$$\mathbf{s}_i'(\bar{x}, \bar{y}, \bar{\theta}) = \begin{bmatrix} \bar{x} \\ \bar{y} \end{bmatrix} + \begin{bmatrix} \cos\bar{\theta} & -\sin\bar{\theta} \\ \sin\bar{\theta} & \cos\bar{\theta} \end{bmatrix} \mathbf{s}_i^0 \tag{3.45}$$

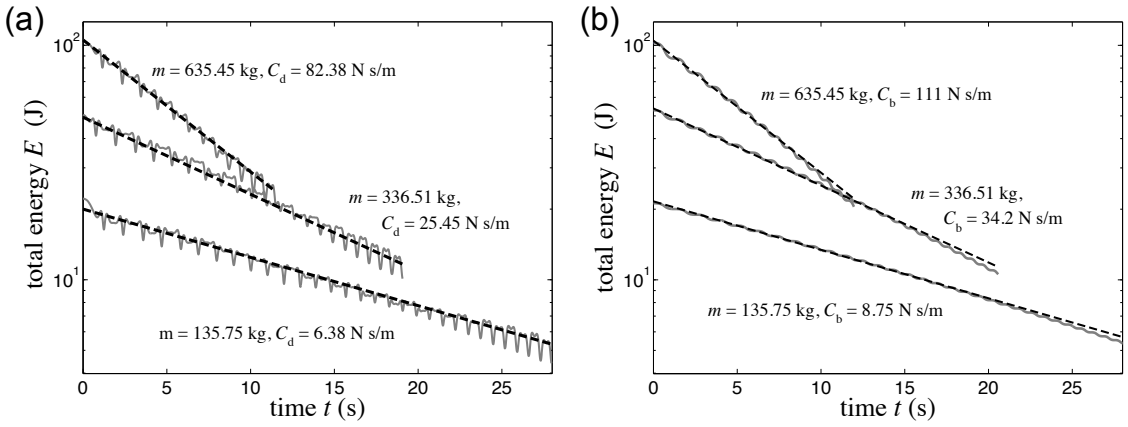


FIGURE 3.7: Energy dissipation histories for varying mass using three methods: (– – –) viscously damped SDOF oscillator with experimentally determined mean damping coefficient $C_d$; (a) (—) experimental; (b) (—) numerically simulated with fitted viscous ball-bearing damping coefficients $C_b$.

where $\mathbf{s}_i^0$ are known. The three string lengths $l_i$ were measured experimentally using string potentiometers (UniMeasure LX-PA) and recorded at 100 Hz. In order to find the top-frame's translations and rotation, the three nonlinear equations

$$l_i^2 = \left\| \mathbf{s}_i'(\bar{x}, \bar{y}, \bar{\theta}) - \mathbf{s}_i \right\|^2, \quad (i = 1, 2, 3) \tag{3.46}$$

are solved via Newton iterations for each measurement sample.

Having determined the platform positions $(\bar{x}, \bar{y}, \bar{\theta})$, the velocities $(\dot{\bar{x}}, \dot{\bar{y}}, \dot{\bar{\theta}})$ are found using central differences. Then, the kinetic and potential energies of the platform may be determined through Equations (3.5) and (3.9), respectively. The top-frame used in the experimental trials has the following geometric and inertial properties: $a$ = 44.6 cm, $b$ = 27.1 cm, $I$ = 71791 kg cm$^2$, and $m$ = 35.26 kg. The top-frame was loaded with rectangular steel plates of dimension 66 cm × 61 cm × 0.64 cm with primary axes in line with the $x$ axis of the top-frame. Each plate was approximately 20 kg with mass moment of inertia $I$ of 1346 kg cm$^2$. In all loading scenarios the masses were centered on the top-frame to have approximately zero eccentricity, i.e. $e_x$ and $e_y$ of zero. Six levels of mass were used: 135.75, 237.42, 336.51, 436.02, 535.70, and 635.45 kg.

For a single-degree-of-freedom oscillator in free response and having damping coefficient $c$, the energy of the system decays according to $\exp(-ct/m)$. Similarly, an equivalent,

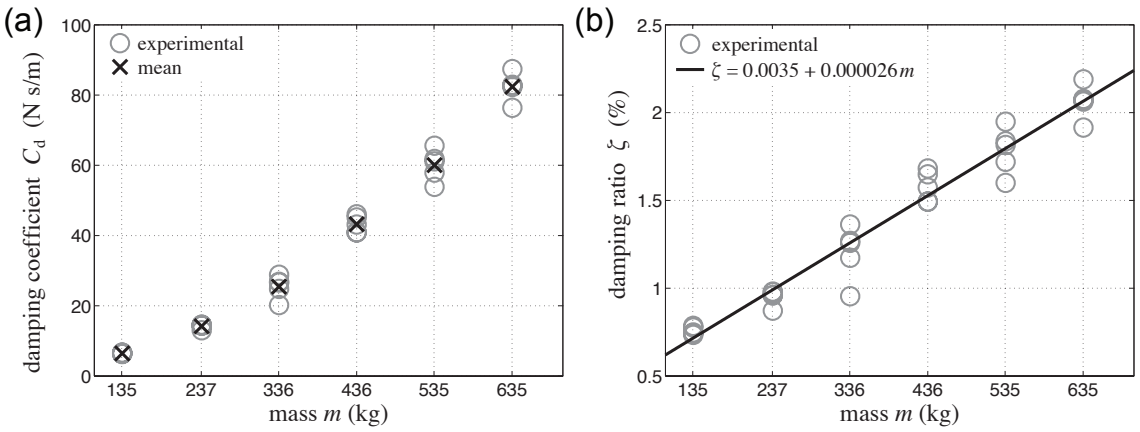


FIGURE 3.8: (a) Experimentally fitted damping parameter $C_d$ and (b) approximate damping ratio $\zeta$ for varying mass $m$.

viscous damping rate of the experimental system is found by performing a nonlinear, least-squares fit of the system's energy using the function

$$E(t) = E_0 \exp\left(-C_d t/m\right) \tag{3.47}$$

where $E = T + V$ which is determined from measurements. A Levenberg-Marquardt algorithm is used to fit parameters $E_0$ and $C_d$, knowing the mass $m$. Three experimental energy histories are shown for varying mass in Figure 3.7(a) with corresponding fitted damping rates $C_d$.

Five experimental tests were carried out for each level of mass. Tabulated fitted parameters $C_d$ for all thirty experimental runs are given in Table 3.2 and graphically in Figure 3.8(a). Note that $C_d/m \approx 2\zeta(2\pi/T_n)$ where $\zeta$ is the damping ratio and $T_n$ is the natural period of the system. Knowing $T_n \approx 2$ s, the approximate damping ratio of the system may be expressed as follows:

$$\zeta \approx \frac{C_d T_n}{4\pi m} \approx \frac{C_d}{2\pi m} \tag{3.48}$$

Using this expression, experimental $\zeta$ (in percent) are shown in Figure 3.8(b). Damping ratios range from about 0.75% at low mass (approximately 150 kg) and 2% at high mass

(approximately 650 kg). The expression

$$\zeta = 0.0035 + 0.000026\, m, \quad (m \text{ in kg}) \tag{3.49}$$

may be used to approximate the effect of equipment mass on the damping ratio for these rolling isolation platforms.

Because damping is low, it is convenient to assume that damping forces $Q^{\mathrm{D}}_{r_{ix}}$ and $Q^{\mathrm{D}}_{r_{iy}}$ are proportional to the velocity at the ball-bearing location with viscous damping coefficient $C_{\mathrm{b}}$ as described in the derivation of the equations of state. Values for $C_{\mathrm{b}}$ are determined by numerically simulating the model dynamics for varying $C_{\mathrm{b}}$ until equivalent energy dissipation is observed. Figure 3.7(b) graphically shows the fitted energy paths and the experimental energy paths for varying mass; good correspondence is seen between the experimental and numerical results. Table 3.5 gives the numerically-determined damping coefficients $C_{\mathrm{b}}$ for varying mass, and the following is the least-squares fit to the mass-dependent damping coefficient:

$$C_{\mathrm{b}}(m) = 0.000229\, m^2 + 0.02884\, m, \quad (m \text{ in kg}). \tag{3.50}$$

While this system is very lightly damped, damping may be increased by coating the steel bowls or steel ball-bearings with a viscoelastic layer. A model for such damping would be nonlinear in the rolling velocity [81].

TABLE 3.2: Experimentally fitted parameter $C_{\mathrm{d}}$ with mean and coefficient of variation (CV).

| mass | $C_{\mathrm{d}}$ (N s/m) for tests | | | | | mean | CV |
|---|---|---|---|---|---|---|---|
| $m$ (kg) | 1 | 2 | 3 | 4 | 5 | (N s/m) | (N s/m) |
| 135.75 | 6.62 | 6.70 | 6.38 | 6.34 | 6.26 | 6.46 | 0.029 |
| 237.42 | 14.57 | 13.00 | 14.64 | 14.31 | 14.33 | 14.17 | 0.047 |
| 336.51 | 28.82 | 26.83 | 20.18 | 26.60 | 24.82 | 25.45 | 0.129 |
| 436.02 | 45.17 | 46.09 | 43.10 | 40.93 | 40.88 | 43.23 | 0.055 |
| 535.70 | 65.55 | 61.13 | 61.81 | 57.90 | 53.86 | 60.05 | 0.073 |
| 635.45 | 87.43 | 82.94 | 82.33 | 82.76 | 76.42 | 82.38 | 0.048 |

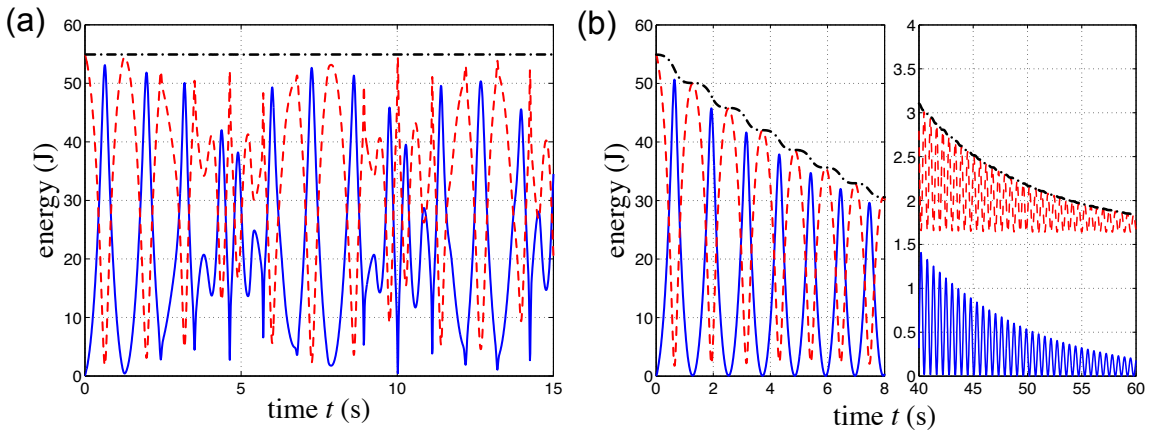


FIGURE 3.9: Numerically simulated free-vibration history for $m = 336.51$ kg: (a) no damping and (b) viscous damping. (—) kinetic energy $T$, (– – –) potential energy $V$, and (–·–) total system energy $E = T + V$.

## 3.6 Numerical Results

In the following sections, the proposed platform model is evaluated. Simulation results are found by numerically integrating the equations of state, Equations (3.41) and (3.17). First, as discussed in Section 3.3, the work done by the ball-bearings is analyzed for an undamped, free vibration. This simulation shows that the total energy of the model is conserved. Next, the chaotic nature of the system is analyzed incorporating the damping model determined in the previous section. Trajectories starting from nearly identical initial conditions follow qualitatively dissimilar paths demonstrating sensitivity to initial conditions; these sensitivities are quantified via Lyapunov exponents. Finally, we show the

TABLE 3.3: Numerically generated fitted damping coefficient $C_b$ for varying mass.

| mass $m$ (kg) | $C_b$ (N s/m) |
|---|---|
| 135.75 | 8.75 |
| 237.42 | 19.2 |
| 336.51 | 34.2 |
| 436.02 | 59.0 |
| 535.70 | 80.0 |
| 635.45 | 111 |

effect that the bowl profile has on the system response. As compared to parabolic bowls, the fitted bowl shapes show larger variations in platform responses.

### *3.6.1 Confirmation of energy conservation*

In the absence of damping, the total energy $E(t)$ of the system must be conserved. From the numerically simulated free responses of the undamped platform, the kinetic energy $T$ and potentially energy $V$ are calculated in accordance with Equations (3.5) and (3.9). Figure 3.9(a) shows the energy histories $T$, $V$, and $E = T + V$. As proven in Section 3.3 and the appendices, the total energy is constant for all time.

Next, we look at the same system but now with viscous damping included. Here the total energy should not be conserved due to the energy dissipated through the nonpotential forces $Q^{\mathrm{D}}_{r_{ix}}$ and $Q^{\mathrm{D}}_{r_{iy}}$. Figure 3.9(b) shows that the energy decays monotonically with time; energy cannot be injected into the system so $E(t)$ cannot increase with time. Because the ball-bearings are allowed to move off the center-lines, there exists an equilibrium with non-zero displacements. The ball-bearings impart forces that equilibrate the top platform in a displaced configuration. The right panel of Figure 3.9(b) exhibits this behavior—as the energy decays with time, the potential energy converges to a non-zero value.

### *3.6.2 Chaotic response*

Chaos is commonly characterized by deterministic state equations giving rise to aperiodic long-term behavior, and exhibiting strong sensitivity to initial conditions [82]. Lyapunov exponents (LEs) are commonly calculated to quantify the latter characteristic; LEs describe the exponential divergence rates of nearby trajectories [83]. Three experimental $\bar{x}$, $\bar{y}$, and $\bar{\theta}$ trajectories are shown in Figure 3.10(a). As can be seen in the figures, the initial conditions for all three trials are similar, but the trajectories diverge after a few cycles. Such behavior qualitatively exhibits the third characteristic of chaotic systems: sensitivity to initial conditions.

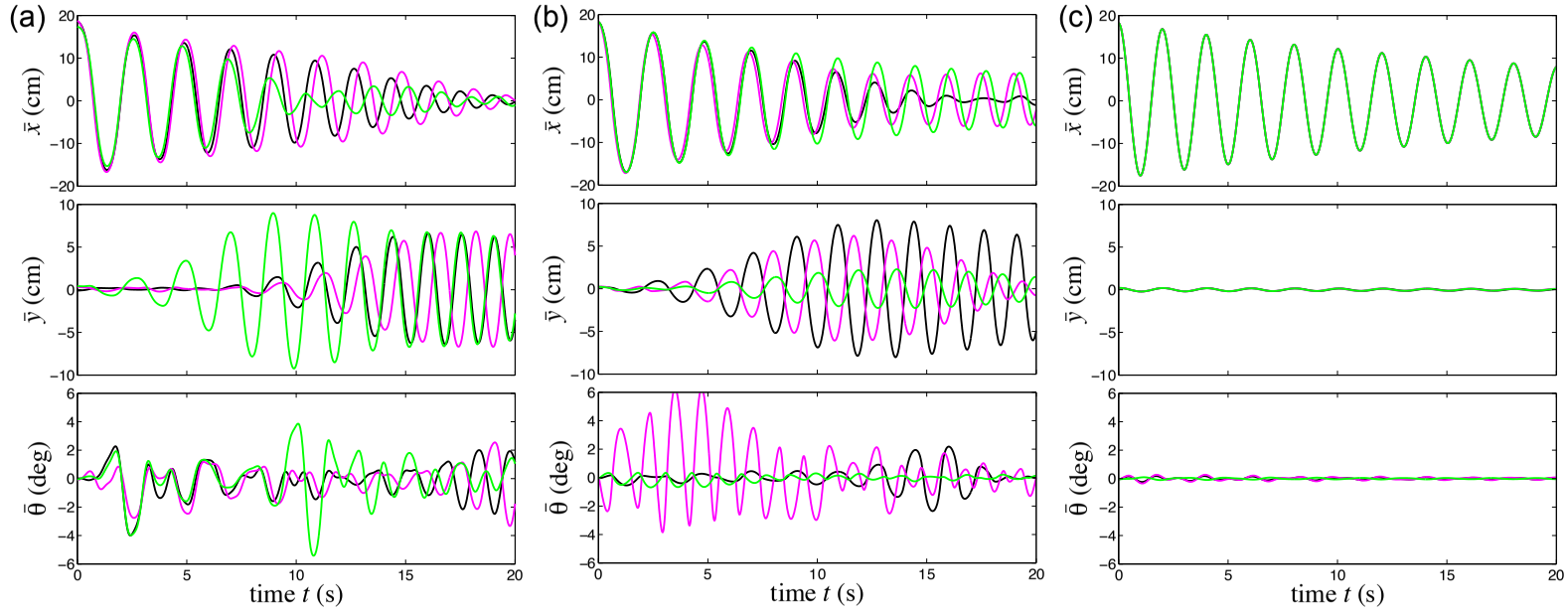


FIGURE 3.10: Comparison between the trajectories $\bar{x}(t)$, $\bar{y}(t)$, and $\bar{\theta}(t)$ for three initial conditions; $m = 237.42$ kg and $C_b = 19.2$ N s/m: (a) experiments, (b) predicted with fitted bowl profile, and (c) predicted with parabolic bowl profile.

The proposed model was used to generate trajectories from neighboring initial conditions. The initial platform configuration $(\bar{x}, \bar{y}, \bar{\theta})$ and velocities $(\dot{\bar{x}}, \dot{\bar{y}}, \dot{\bar{\theta}})$ were taken to be the mean of initial conditions from the three experimental trajectories. In order to initialize the eight ball-bearing positions $\mathbf{r}_i$, each ball-bearing was assumed to start on the center of the line connecting the lower- and upper-bowl centers (i.e. $\mathbf{p}_i/2$) plus some small random perturbation. Letting $(\bar{x}_0, \bar{y}_0, \bar{\theta}_0)$ denote the initial platform configuration, the initial ball-bearing positions are

$$\mathbf{r}_{i0} = \begin{bmatrix} \bar{x}_0 \\ \bar{y}_0 \end{bmatrix} + (\mathbf{R}(\bar{\theta}_0) - \mathbf{I}) \begin{bmatrix} a_i \\ b_i \end{bmatrix} + \begin{bmatrix} \varepsilon_{xi} \\ \varepsilon_{yi} \end{bmatrix}, \quad \varepsilon_{xi}, \varepsilon_{yi} \overset{iid}{\sim} \mathcal{N}(0, 5 \text{ mm}) \quad \forall\, i\,. \tag{3.51}$$

Perturbations $\varepsilon_{xi}$ and $\varepsilon_{yi}$ account for the inability to center perfectly the ball-bearings experimentally. Similar to the experimental trajectories, the numerically simulated trajectories produced by the proposed model with the fitted bowl profile exhibit strong sensitivity to initial conditions, see Figure 3.10(b).

In order to quantify chaos, we calculate LEs using the mathematical model. A powerful algorithm originally proposed by Wolf *et al.* [84] systematically measures all the LEs by tracking the evolution of a hyper-ellipsoid in state space about the trajectory. However, given that merely one positive LE implies chaos, only the largest LE needs to be calculated eliminating the need to perform Gram-Schmidt orthonormalization at each time step [83]. The process for calculating the principal LE is described below.

For the dynamical system

$$\dot{\mathbf{z}} = f(t, \mathbf{z}), \quad t \geq t_0 \tag{3.52}$$

where $\mathbf{z}(t) \in \mathbb{R}^n$ is the state vector, let $\mathbf{z}^{\mathrm{m}}(t)$ be the master trajectory with initial condition $\mathbf{z}^{\mathrm{m}}(t_0) = \mathbf{z}_0^{\mathrm{m}}$. At each time $t_k = k\Delta t$ the master trajectory is perturbed by $\mathbf{u}_k$ where $\|\mathbf{u}_k\| = \delta_0$ is a small enough to ensure linear response over $t \in [t_k, t_{k+1}]$; the perturbed state or slave trajectory is $\mathbf{z}_k^{\mathrm{s}} = \mathbf{z}_k^{\mathrm{m}} + \mathbf{u}_k$. The solution of Equations (3.52) is evaluated iteratively to obtain $\mathbf{z}_{k+1}^{\mathrm{m}}$ and $\mathbf{z}_{k+1}^{\mathrm{s}}$ whose difference is denoted $\boldsymbol{\Delta}_{k+1} = \mathbf{z}_{k+1}^{\mathrm{s}} - \mathbf{z}_{k+1}^{\mathrm{m}}$. The quantity $\ln \frac{\|\boldsymbol{\Delta}_{k+1}\|}{\delta_0}$ gives

a measure to the divergence/convergence of the master and slave trajectories. We repeat this procedure for all $k$ and renormalize the perturbation at each iteration $\mathbf{u}_k = \delta_0 \hat{\mathbf{\Delta}}_k$. The largest LE is defined to be

$$\lambda_{\max} = \lim_{K \to \infty} \frac{1}{t_K} \sum_{k=1}^{K} \ln \frac{\|\mathbf{\Delta}_k\|}{\delta_0} \,. \tag{3.53}$$

Allowing the simulation to run long enough, this algorithm approximates the average divergence rate of nearby trajectories. A system is said to be chaotic if $\lambda_{\max} > 0$ [83].

The free response of the numerical model was used to determine $\lambda_{max}$ for the RIS. Because the system is dissipative, state trajectories come to rest in a stable (potentially non-zero) state; hence, simulations cannot be run long enough to explore completely the state space before motion has stopped. Therefore, LEs were calculated over a shorter time period (e.g. 30 s) for a variety of initial conditions and an ensemble average was used to approximate $\lambda_{\max}$. In doing so for 150 initial conditions, $m = 237.42$ kg, the average $\lambda_{\max}$ was found to be **0.5068** indicating that this system is chaotic. Appendix A expands upon analysis of the chaotic response presented here.

### *3.6.3 Effect of the bowl profile on system responses*

The bowl profile plays an important role in the chaotic, non-repeatable response of the system. As described in Section 3.4, the experimental bowl profiles have a complex shape given by Equation (3.44) which possesses an inflection point. For a different system, the bowls may be modeled as paraboloids with a curvature $\alpha$ equal to 2 $\mathrm{m}^{-1}$ such that the predominant period of motion is approximately 2 s, as seen in the lab. Such an assumption simplifies the dynamics, i.e. $\eta'(r) \propto r$, but the chaotic platform motion seen in the lab was not captured by this model. Figure 3.10(c) shows three trajectories generated using the parabolic bowl model using the same initial conditions as in Figure 3.10(b). For an initial displacement primarily in $\bar{x}$, motion is rectilinear; transverse motion does not develop. The small amplitude oscillations seen in the $\bar{y}$ and $\bar{\theta}$ responses are remnants of the initial

ball-bearing perturbations $\varepsilon_{xi}$ and $\varepsilon_{yi}$. The largest LE for the system using a parabolic bowl was found to be **0.0391** using the previously described ensemble average method. The LE for the parabolic bowl system is positive, indicating the system may also be chaotic, but the smaller LE indicates that trajectories diverge at a slower rate as compared to the fitted model.

A parabolic bowl has no inflection point and does not exhibit the coupling between $\bar{x}$ and $\bar{y}$ motion as observed experimentally. In the experimental system and the associated model, displacement configurations exist where a ball-bearing becomes relatively confined in the stiffer center region of a bowl while the other three ball-bearings are in less stiff locations, further from the center. When this displacement configuration occurs, the top-frame rotates about the confined ball-bearing inducing large rotations and transverse displacements. Only with the model fit to the experimental system can such motion be captured.

## 3.7 Summary

Seismic isolation systems for light ($\approx$ 1 tonne) payloads are constructed from a pair of frames, each having four shallow steel dishes. The top-frame can roll in any horizontal direction on four steel ball-bearings which are located between pairs of dishes. RISs have kinematic constraints due to the slip-free condition of rolling spheres. In practice, the dish profiles are nearly parabolic near their centers and become conical further from the center. The dish profiles have an inflection point between the parabolic region and the conical region. The purpose of such a profile is to limit accelerations sustained by the payload under large input motions and to restrict isolator displacements at lower input levels. As a consequence of this bowl profile, lateral and rotational response motions are highly coupled, and the dynamic response of these isolation systems can not be predicted analytically or reproduced experimentally. Furthermore, uni-axial models can not capture the nonlinear

lateral-torsional coupling exhibited in these systems. A significantly positive Lyapunov exponent indicates that the isolation system is chaotic. Due to this nature of these RISs, uni-axial responses are not plausible, realistic response simulations must incorporate the coupling of the lateral and rotational responses, and the peak responses to deterministic loads must be evaluated statistically.

# 4

# A Simplified and Experimentally-Validated Predictive Model of a Rolling Isolation System

## 4.1 Background

In Chapter 3 we derived the nonholonomic equations of motion of the rolling isolation system (RIS), which consist of eleven coupled nonlinear differential equations. In this chapter we propose and validate a simplified mathematical model which preserves the complex nonlinear nature of the system.

Rolling equipment isolation systems [1] are widely used to isolate mainframes, LAN racks, electronics enclosures, telecommunications switches, as well as other mission-critical equipment and valuable property. Museums around the world have adopted isolation systems to protect objects (such as *The Statue of Hermes* and *The Gates of Hell*) from earthquake-induced floor motions [85]. Presently, the United States and Japan have hundreds of installations. Chang and Spencer [86] have recently implemented such a system in lab-scale tests of full-scale, actively-damped buildings. This study involved linear modeling because the focus of the work was for small displacements [34]. However, displacement demands for these systems in the field will be large enough (> 3 cm) to inval-

idate any linear approximation. The ability to predict the system's displacement demand associated with a particular hazard level or return period is of particular importance in the probabilistic seismic hazard analysis of contents protected by isolation. Estimating the displacement demand for an equipment isolation system corresponding to a specific installation, building site, and hazard level requires, in part, a predictive model of the isolation system behavior.

To date, researchers have primarily focused on the the single-axis behavior of equipment isolation systems, neglecting the coupling between transverse responses. Experimental tests on equipment isolation systems are sparse [4, 19, 40, 43], especially for multiaxis disturbances [36]. The prediction of the response of equipment isolation systems and their ability to protect building contents requires models that can capture the observed nonlinear behavior of actual isolation systems subjected to multiaxis shaking. Accordingly, the focus of this chapter is on the experimental validation of a multiaxial, nonlinear model of a rolling pendulum isolation system to further attenuate responses. An illustration of the RIS to be analyzed is shown in Figure 3.1.

This chapter presents the development and experimental validation of a simplified model of a rolling isolation system. First, a description of the RIS is provided, and the model is derived. Then, an experimental set-up is described, and a nonlinear bowl-shaped function is fit to measurements. A new idealized disturbance model intended to represent floor motions is then presented and used for the experimental and numerical trials. The set of disturbance scenarios is designed to cover a wide range of operating conditions of the isolator, and peak response quantities are computed. These computed responses are then compared to laboratory response measurements, validating that the model is predictive over a wide range of disturbance parameters. Finally, the experimentally-validated model is used to establish critical peak floor motions for an RIS.

## 4.2 Simplified Model of a Rolling Isolation System

The following development is a simplified version of the full model (3.41). Consider again the displaced configuration of a rolling isolation platform, illustrated in Figure 3.2. The bottom-frame is excited by translational disturbance $\boldsymbol{w}(t) = [w_x(t)\ w_y(t)]^\intercal$. Vibration-sensitive equipment is rigidly connected to the top-frame, and the total mass of the equipment and top-frame is $m$, with mass moment of inertia $I$; we assume that the equipment's mass is located *concentrically*. The top-frame undergoes rotation $\bar{\theta}(t)$ and translational displacements $\boldsymbol{d}_{\mathrm{R}}(t) = [\bar{x}(t)\ \bar{y}(t)]^\intercal$, relative to the bottom-frame.

### *4.2.1 Geometry and notation*

The top-frame and equipment are mechanically isolated from the bottom-frame via the rolling of large, steel ball-bearings between concave-up lower-bowls and concave-down upper-bowls at the four corners (Figure 3.1). The bowls and balls are numbered $i = 1,...,4$, as shown in Figure 3.2, with the coordinates of the bowl centers given by $\boldsymbol{c}_i = [a_i\ b_i]^\intercal$ where

$$\boldsymbol{a} = [a\ \ -a\ \ -a\ \ a]^\intercal \quad \text{and} \quad \boldsymbol{b} = [b\ \ b\ \ -b\ \ -b]^\intercal. \tag{4.1}$$

The gravitational restoring forces in the system are attributed to changes in the heights at the corners, which depend on the platform displacements $(\bar{x}, \bar{y}, \bar{\theta})$ and the ball-bearing locations. As seen in Figure 3.2, the ball-bearing locations with respect to the centers of the lower- and upper-bowls are $\mathbf{r}_i(t) = [r_{xi}(t)\ r_{yi}(t)]^\intercal$ and $\mathbf{q}_i(t) = [q_{xi}(t)\ q_{yi}(t)]^\intercal$, and the center-to-center displacement is

$$\mathbf{p}_i \equiv \mathbf{p}_i(\bar{x}, \bar{y}, \bar{\theta}; t) = \boldsymbol{d}_{\mathrm{R}} + (\mathbf{R}_{\bar{\theta}} - \mathbf{I})\boldsymbol{c}_i, \qquad (i = 1, ..., 4) \tag{4.2}$$

where $\mathbf{R}_{\bar{\theta}}$ is the rotation matrix. Using the relationship $\mathbf{p}_i = \mathbf{r}_i + \mathbf{q}_i$, it is straightforward to find $\mathbf{q}_i$ given the ball-bearing location $\mathbf{r}_i$. We assume all the bowls are axisymmetric with radius-dependent bowl-shape function $\eta(r)$. The height of the top-frame at the center of

the *i*th upper-bowl is the sum of contributions from the lower- and upper-bowls,

$$h_i(\bar{x}, \bar{y}, \bar{\theta}, \mathbf{r}_i) = \eta(\|\mathbf{r}_i\|) + \eta(\|\mathbf{q}_i\|). \tag{4.3}$$

For a mass eccentricity of zero ($e_x = e_y = 0$), the mass allocation vector simplifies to $\boldsymbol{u} = \frac{1}{4}\mathbf{1}_4$, and thus the potential energy (3.9) reduces to

$$V(\bar{x}, \bar{y}, \bar{\theta}, \mathbf{r}_1, ..., \mathbf{r}_4) = \tfrac{1}{4}\sum_{i=1}^{4} mgh_i \, . \tag{4.4}$$

The kinetic energy (3.5) simplifies to

$$T(\dot{\bar{x}}, \dot{\bar{y}}, \dot{\bar{\theta}}) = \tfrac{1}{2}m\Big[(\dot{w}_x + \dot{\bar{x}})^2 + (\dot{w}_y + \dot{\bar{y}})^2\Big] + \tfrac{1}{2}I\dot{\bar{\theta}}^2 \, . \tag{4.5}$$

### *4.2.2 Kinematics of rolling ball-bearings*

The ball-bearing coordinates $\mathbf{r}_i$ evolve according to a set of nonholonomic constraints prescribed by the condition of rolling without slipping between non-parallel surfaces (Section 3.2.3). The kinematic constraint, relating the the ball-bearing velocities $\dot{\mathbf{r}}_i$ to the relative velocities $\mathbf{v}_i$ of the upper-bowls at the ball-bearing locations, depends upon the slopes of the upper- and lower-bowls. For shallow bowls (i.e. $\eta'(r)$ small), the nonholonomic constraint can be approximated by the condition that the velocity of the ball-bearing center is half of the relative velocity across the isolation system and in the direction of this relative velocity,

$$\dot{\mathbf{r}}_i = \tfrac{1}{2}\mathbf{v}_i \equiv \tfrac{1}{2}\{\dot{\boldsymbol{d}}_{\mathrm{R}} + \dot{\bar{\theta}}\mathbf{D}(\boldsymbol{c}_i + \mathbf{r}_i - \boldsymbol{d}_{\mathrm{R}})\}, \qquad (i = 1, ..., 4) \tag{4.6}$$

where the matrix

$$\mathbf{D} = \begin{bmatrix} 0 & -1 \\ 1 & 0 \end{bmatrix}. \tag{4.7}$$

The eight nonlinear, first-order, ordinary differential equations (4.6) prescribe the evolution of the four ball-bearings in the $X_{\mathrm{b}}$-$Y_{\mathrm{b}}$ plane. Initial conditions $\mathbf{r}_{i0} = \mathbf{r}_i(0)$ must be specified.

### 4.2.3 *Equations of motion*

Applying the fundamental nonholonomic form of Lagrange's equation (3.21), the equations of motion of the centroidal coordinates, taking into account the constraints (4.6) are as follows:

$$m(\ddot{\boldsymbol{d}}_{\mathrm{R}} + \ddot{\boldsymbol{w}}) + \sum_{i=1}^{4} \mathbf{f}_{\mathcal{U}i} + \tfrac{1}{2}\sum_{i=1}^{4}(C_{\mathrm{b}}\dot{\mathbf{r}}_i + \mathbf{f}_{\mathcal{L}i} - \mathbf{f}_{\mathcal{U}i}) = \mathbf{0} \tag{4.8a}$$

$$I\ddot{\bar{\theta}} + \sum_{i=1}^{4} \mathbf{f}_{\mathcal{U}i}^{\mathsf{T}}\mathbf{D}\mathbf{R}_{\bar{\theta}}\boldsymbol{c}_i + \tfrac{1}{2}\sum_{i=1}^{4}(C_{\mathrm{b}}\dot{\mathbf{r}}_i + \mathbf{f}_{\mathcal{L}i} - \mathbf{f}_{\mathcal{U}i})^{\mathsf{T}}\mathbf{D}(\boldsymbol{c}_i + \mathbf{r}_i - \boldsymbol{d}_{\mathrm{R}}) = 0\,. \tag{4.8b}$$

The forces arising from the bowl gradient $\eta'(r)$ are

$$\mathbf{f}_{\mathcal{L}i} = \tfrac{1}{4}mg\eta'(\|\mathbf{r}_i\|)\hat{\mathbf{r}}_i \quad \text{and} \quad \mathbf{f}_{\mathcal{U}i} = \tfrac{1}{4}mg\eta'(\|\mathbf{q}_i\|)\hat{\mathbf{q}}_i, \tag{4.9}$$

where $\mathbf{q}_i = \mathbf{p}_i - \mathbf{r}_i$, as in Figure 3.2 and Equation (4.2). The damping is assumed to be linearly proportional to the ball-bearing velocities and the damping forces act at the ball-bearing locations; the experimentally-fitted mass-dependent damping rate $C_{\mathrm{b}}(m)$ is given by Equation (3.50). The full set of system dynamics comprises Equations (4.6) and (4.8), which must be integrated simultaneously.

## 4.3 Experimental Set-up

In order to assess the performance of the equipment isolation system and to validate the simplified model described above, experiments were conducted in which the system was excited uniaxially, and various response quantities were measured. Experiments were conducted on a single-axis servo-hydraulic shaking table. The table can achieve peak velocities of 50 cm/s and has a stroke of ±7.5 cm.

The RIS in this study, shown in Figure 4.1, has dimensions $a = 44.5$ cm and $b = 47$ cm. A 122 cm × 122 cm plywood board of mass 16 kg with moment of inertia 4.0 kg m$^2$ was placed on the top-frame to support rectangular steel plates of dimension 66 cm × 61 cm × 0.64 cm. Each plate has a mass of approximately 20 kg and a mass

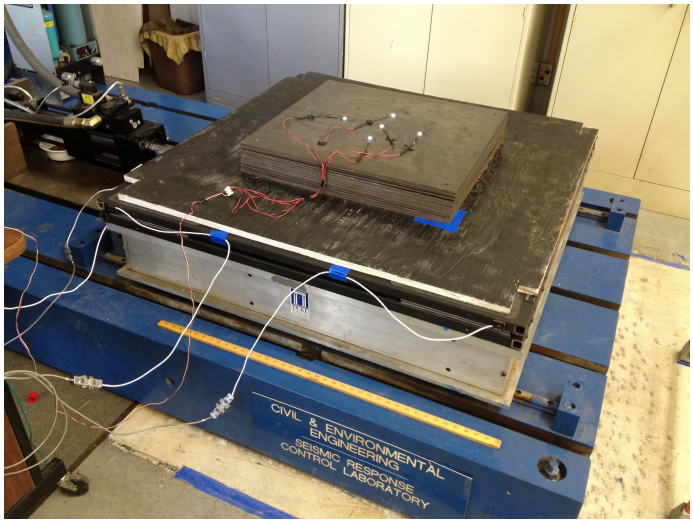


FIGURE 4.1: Experimental shaking table with rolling equipment isolation system.

moment of inertia of 1.346 kg m$^2$. Their primary axes were aligned with the $X_t$-axis of the top-frame. Two loading scenarios were investigated: *Light* (15 steel plates) and *Heavy* (30 steel plates).

An array of sensors was installed on the experimental system. Table displacement and acceleration responses were collected at a sample rate of 200 Hz. Silicon Design MEMS accelerometers were located on the shaking table and the top-frame: one measuring the shake table acceleration $\ddot{w}_x(t)$, and three measuring the the top-frame accelerations. The hydraulic actuator has a linear variable differential transformer (LVDT) to sense the table displacement $w_x(t)$.

The top-frame displacement was measured using a Flip MinoHD video camera at 30 fps. Five Oznium LEDs, located on the top of the steel plates, were controlled by the data acquisition to turn on and off precisely at the start and end of the test, allowing for exact synchronization between the digitized sensor records and the video. Figure 4.2 shows an example frame with the LEDs turned on and the top-frame in a displaced configuration. The video was post-processed using MATLAB's Image and Video Processing Toolbox [87]. Knowing the LED array geometry, a linear map was determined from pixel coordinates to physical coordinates. Note that the video displacement measurements represent total co-

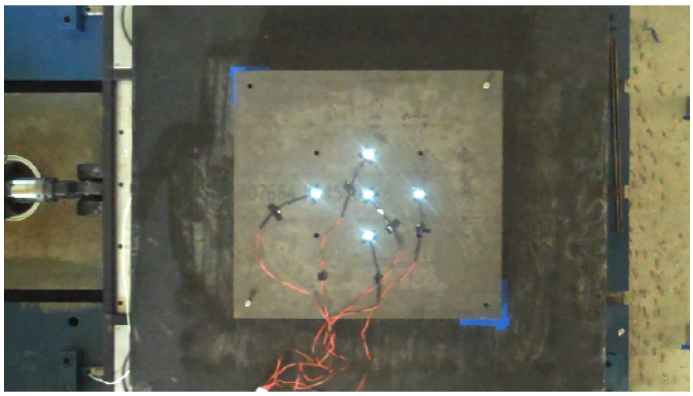

FIGURE 4.2: An example video frame used for the displacement measurements with five LEDs switched on.

ordinates. To find the relative displacement of the top-frame, displacement measurements from the actuators's LVDT are subtracted from the displacement measurements from the video. Appendix B gives an assessment of the vision-based system used here. In particular, the accuracy of acceleration measurements using the vision-based system is assessed by tracking a signal with time-dependent frequency and amplitude.

## 4.4 Bowl-shape Function

The potential energy, and hence the restoring forces, depend explicitly on the bowl-shape function $\eta(r)$. The bowls are intended to have conical radial profiles [37], but due to the manufacturing process the bowls are not perfectly conical. In Section 3.4 the following function was suggested [38]:

$$\eta(r) = \beta_1\beta_2 \ln\left[\cosh(r/\beta_2)\right]/10 + \beta_3(r/10)^{\beta_4} + \beta_5(r/10)^{\beta_6} \tag{4.10}$$

for which the six parameters $\beta_i$ were fit to high-resolution photogrammetry data. The numerically-fitted parameters are given in Table 3.1. However, the bowls were measured in an unloaded configuration, neglecting the *in situ* deformations produced by the installation. When installed, the bowls are clamped along two edges (see Figure 4.3) and a hard plastic puck is sandwiched within the platform to reduce elastic deformation in the bowls when loaded. Thus, the installed bowl shape is markedly different than the unloaded shape,

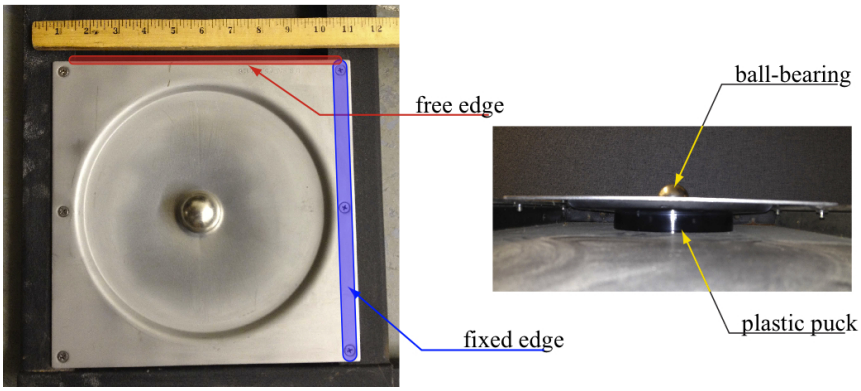


FIGURE 4.3: Installed bowl with clamped/free boundary conditions and plastic puck support.

requiring a new expression for $\eta(r)$. To determine the deformed shape, controlled free-response experiments were performed and the acceleration-displacement relationship was used to ascertain the bowl gradient $\eta'(r)$.

### *4.4.1 Experimental characterization*

For negligible rotations, the center-to-center displacements of the lower- and upper-bowls are approximately equal to the relative displacement of the top-frame's centroid ($\mathbf{p}_i \approx [\bar{x}\ \bar{y}]^\mathsf{T}$) and are equivalent at each corner ($\mathbf{p}_i = \mathbf{p}_j = \mathbf{p}$). The radial displacement of the centroid is

$$d_\mathrm{R}(t) = \left\|\boldsymbol{d}_\mathrm{R}(t)\right\| \equiv \sqrt{\bar{x}^2(t) + \bar{y}^2(t)} \approx \|\mathbf{p}(t)\|. \tag{4.11}$$

If we assume $\mathbf{r}_i = \mathbf{q}_i = \mathbf{p}/2$ (i.e. the ball-bearings are located halfway between the lower- and upper-bowl centers), then Equation (4.8a) states that the total acceleration $\boldsymbol{a}_\mathrm{T}$ is

$$\boldsymbol{a}_\mathrm{T}(t) = \ddot{\boldsymbol{d}}_\mathrm{R}(t) + \ddot{\boldsymbol{w}}(t) \approx -g\eta'(\|\mathbf{p}(t)/2\|)\,\hat{\mathbf{p}}_i(t) - C_\mathrm{b}\dot{\mathbf{p}}(t)/m\ . \tag{4.12}$$

Therefore, from Equations (4.11) and (4.12) we have the following approximation for the bowl gradient:

$$\eta'(d_\mathrm{R}(t)/2) \approx \left\|\boldsymbol{a}_\mathrm{T}(t) + C_\mathrm{b}\dot{\mathbf{p}}(t)/m\right\|/g. \tag{4.13}$$

Note $\eta'$ is strictly positive. A plot of the right-hand side of Equation (4.13) versus $d_\mathrm{R}(t)/2$ gives an approximation for the function $\eta'(r)$.

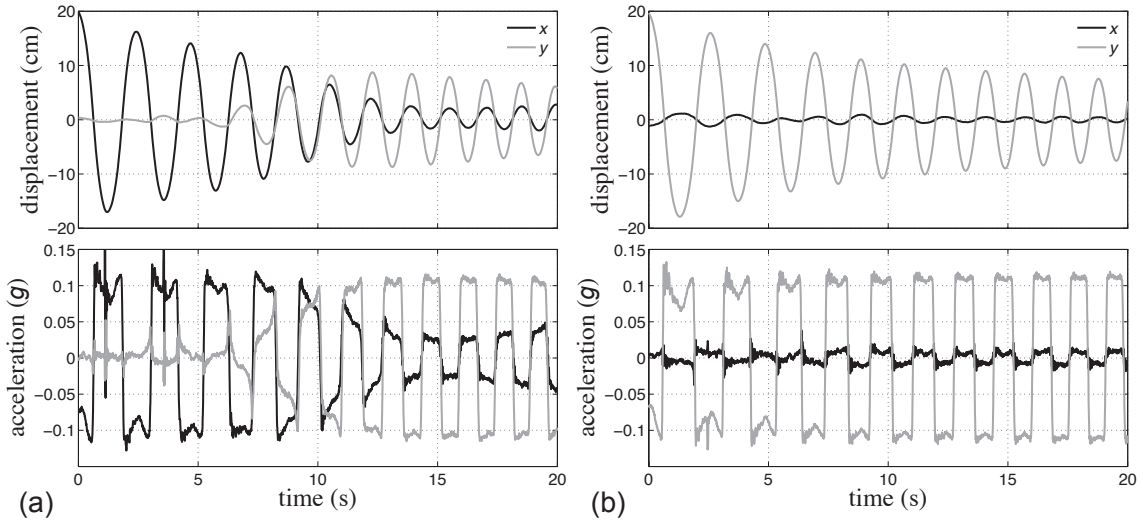


FIGURE 4.4: Experimental free-response displacement and acceleration trajectories: (a) $\bar{x}_0 = 19.5$ cm, $\bar{y}_0 = 0$ cm with a measured peak acceleration of impact 0.64 $g$ at $t = 1$ s and $t = 3.5$ s; and (b) $\bar{x}_0 = 0$ cm, $\bar{y}_0 = 19.5$ cm.

Four controlled free-response experiments were performed. The top-frame was displaced to its full capacity—twice in the $\bar{x}$-direction and twice in the $\bar{y}$-direction, denoted $\bar{x}_0$ and $\bar{y}_0$, respectively—and released from rest. Figure 4.4 shows experimental displacement and acceleration trajectories for two initial conditions—one in each direction. The large spikes in the acceleration records correspond to the ball-bearings colliding with the bowl lip.

The bowl gradient is computed from the measured free-response accelerations and displacements using Equation (4.13). For the simplified model, the following polynomial function was fit to the experimental data:

$$\eta'(r) = \sum_{i=1}^{6} \alpha_i (r/R)^i + \alpha_{50} (r/R)^{50} \tag{4.14}$$

where $R = 10$ cm. The term $\alpha_{50}(r/R)^{50}$ models the circumferential lip, which limits the displacement responses to about 22 cm. The estimated parameter values $\alpha_i$ and their asymptotic standard errors, are given in Table 4.1. Only the first quarter cycle of motion (~0.7 s) is used to ensure the approximations associated with Equation (4.13) are

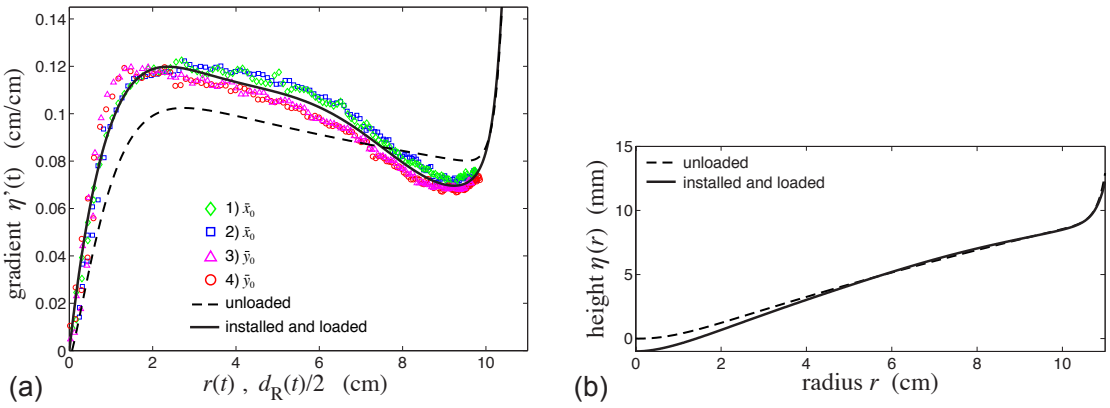


FIGURE 4.5: (a) Acceleration-displacement relationship of four free-response measurements—two with $\bar{x}_0$ = 19.5 cm (◇,□), and two with $\bar{y}_0$ = 19.5 cm (△,○)—with the fitted bowl-gradient function $\eta'$; and (b) the bowl height $\eta$ (not to scale): (– – –) unloaded and (——) installed and loaded.

warranted. Figure 4.5 shows the four normalized experimental total accelerations versus relative displacements. The dashed line is the unloaded bowl fit from Section 3.4, which shows poor correspondence with the experimental data. The fit of Equation (4.14) to the data is shown as a solid line in Figure 4.5.

Elementary plate theory indicates that dynamic vertical displacements of this system resulting from dynamic vertical loads are less than 0.1 mm. Even though the distortions are small to begin with, they are fully accounted for in the model since the model is developed from dynamic-response data.

It is interesting to observe from Figures 4.4 and 4.5 that the system has a preference to oscillate in the $\bar{y}$-direction as indicated by both the free-response trajectories and the stiffness relationship. When initially released in the $\bar{x}$-direction, lateral motion in the $\bar{y}$-direction develops within three cycles, whereas when initially released from the $\bar{y}$-direction, the system continues to oscillate in the $\bar{y}$-direction without significant lateral

TABLE 4.1: Parameter values and standard errors for the proposed bowl gradient function $\eta'(r)$.

| | $\alpha_1$ | $\alpha_2$ | $\alpha_3$ | $\alpha_4$ | $\alpha_5$ | $\alpha_6$ | $\alpha_{50}$ |
|---|---|---|---|---|---|---|---|
| $\alpha_i$ (cm) | 1.5768 | -7.9494 | 19.6698 | -25.6612 | 16.5632 | -4.1272 | 0.0134 |
| $\sigma_i$ (cm) | ±0.0227 | ±0.2641 | ±1.1177 | ±2.1694 | ±1.9630 | ±0.6714 | ±0.0008 |
| $\epsilon_i = \sigma_i/\alpha_i$ | 1.44% | 3.32% | 5.68% | 8.45% | 11.85% | 16.27% | 5.76% |

translation. This phenomenon can be explained by the acceleration-displacement relationship (Figure 4.5). The two responses starting from $\bar{x}_0 = 19$ cm (Figure 4.4(a)) exhibit larger accelerations than those starting from $\bar{y}_0 = 19.5$ cm. Due to the installation configuration, in which two edges of the dish are clamped and the other two edges are free, the free edges—corresponding to the $\bar{x}$-direction—bulge vertically, increasing the height (and stiffness) in that direction. This asymmetry is not part of the simplified model of this dissertation, but will be an extension of the present work.

## 4.5 Experimental Validation of the Predictive Model

We now validate the simplified mathematical model with experimental peak response spectra. The system is known to be chaotic [38, 63], and thus one cannot expect to match experimental and numerical trajectories. However, peak response quantities are more repeatable, in general. First, we develop a pulse disturbance model that is representative of floor responses in a structure and design a set of pulse periods and amplitudes to test. Next, we compare the analytical model to our experimental system by comparing peak response spectra.

### *4.5.1 Idealized floor motion model*

The motion of the shake table, $w(t)$, is controlled to represent an idealization of the motion of a floor of a building subjected to an earthquake ground motion. As such, it is dominated by a single frequency, the fundamental frequency of the building, $\omega_\mathrm{p} = 2\pi/T_\mathrm{p}$. The motion grows and decays in amplitude over time. This motion applies inertial loads to the isolated mass, and is therefore specified in terms of an acceleration,

$$\ddot{w}(t) = g(t)\cos(\omega_\mathrm{p} t - \phi),\ t \in [0, T] \tag{4.15}$$

for which $g(t)$ is the disturbance envelope. The envelope function is chosen to be strictly positive and unimodal with the following form:

$$g(t) = (t/\tau)^n \exp(-t/\tau) \tag{4.16}$$

where the rise-rate is determined by the exponent $n$. In order to contain approximately $N$ cycles of strong motion, the record must undergo $N/2$ cycles before $t = n\tau$ (i.e. the mode of $g(t)$). The period of the oscillations are $T_\mathrm{p}$, so the time-scale constant $\tau$ is determined from $n\tau = NT_\mathrm{p}/2$ or

$$\tau = NT_\mathrm{p}/(2n). \tag{4.17}$$

The disturbance record should have zero terminal velocity. The velocity record is found by integrating the acceleration record (4.15), and will tend to zero if the the phase angle $\phi$ is selected as follows:

$$\begin{aligned} \lim_{T\to\infty} \int_0^T \ddot{w}(t)\mathrm{d}t = 0 &\Rightarrow \cos\left[\phi - (n+1)\tan^{-1}(\tau\omega_\mathrm{p})\right] = 0 \\ &\Rightarrow \phi = (n+1)\tan^{-1}(\tau\omega_\mathrm{p}) \pm \pi/2. \end{aligned} \tag{4.18}$$

By selecting the parameters $\tau$, $\phi$, $n$, $N$ and $\omega$ as described above, the terminal displacement $w(T)$ will be non-zero, in general. Because $T \neq \infty$, the terminal velocity $\dot{w}(T)$ may be non-zero as well. Therefore, the acceleration waveform must be corrected in order to detrend the displacement and velocity histories. To correct the displacement and velocity records, the following iterative updates are used, respectively:

$$w(t) \leftarrow w(t) - G(t)w(T)/G(T) \tag{4.19a}$$

$$\dot{w}(t) \leftarrow \dot{w}(t) - G(t)\dot{w}(T)/G(T) \tag{4.19b}$$

which involve the cumulative function, $G(t) = \int_0^t g(s)\mathrm{d}s$. The normalized correction function $G(t)/G(T)$ has the useful properties of being zero at $t = 0$ and exactly unity at $t = T$, and has a majority of its support over the envelope region, which is desirable in the detrending process. Differentiating Equation (4.19a) twice and Equation (4.19b) once yields

the acceleration updates, which are simultaneously applied as follows:

$$\ddot{w}(t) \leftarrow \ddot{w}(t) - [\dot{g}(t)w(T) - g(t)\dot{w}(T)]/G(T) \; . \tag{4.20}$$

The acceleration update is iteratively performed until $w(T)$ and $\dot{w}(T)$ are close to zero; this procedure converges in two or three iterations.

### *4.5.2 Experiment design*

The shaking table disturbances used in this work were designed to represent *weak*, *moderate*, and *strong* motions over a range of periods. The disturbances are parameterized by the peak disturbance velocity $V_\mathrm{p}$ and the pulse period $T_\mathrm{p}$. Acceleration records were generated using the above procedure and scaled to match the prescribed peak velocity value $V_\mathrm{p}$ by scaling accelerations by a factor $V_\mathrm{p}/\max_t \dot{w}(t)$. For all records the exponent $n$ was taken to be 2, and the disturbance durations $T$ are given in Table 4.2. Table 4.2 also gives the experimental peak table velocities for weak, moderate, and strong cases in both the light and heavy system. The table velocity was calculated using the central difference of the LVDT table displacement measurements. The experiments were designed to have constant peak table velocities for the three disturbance strengths, but this was not precisely achieved in the laboratory implementation. Furthermore, two moderate and five strong scenarios cannot be performed due to the ±7.5 cm stroke limit of the actuator.

In order to draw a fair comparison between the experimental and numerical results, the shaking table acceleration records are applied to the numerical model. An example acceleration record is shown in Figure 4.6. The measured signal was low-pass filtered to reduce sensor noise without distorting the dominant waveform. The inputs to the mathematical model $\ddot{w}_x(t)$ and $\ddot{w}_y(t)$ were set to the low-pass-filtered measured acceleration records and zero, respectively, for all simulations. For the two moderate and five strong cases not experimentally performed, the input to the mathematical model $\ddot{w}_x(t)$ was set to the weak measured signal scaled to have peak velocities of $V_\mathrm{p}$ = 25 cm/s and 48 cm/s, respectively.

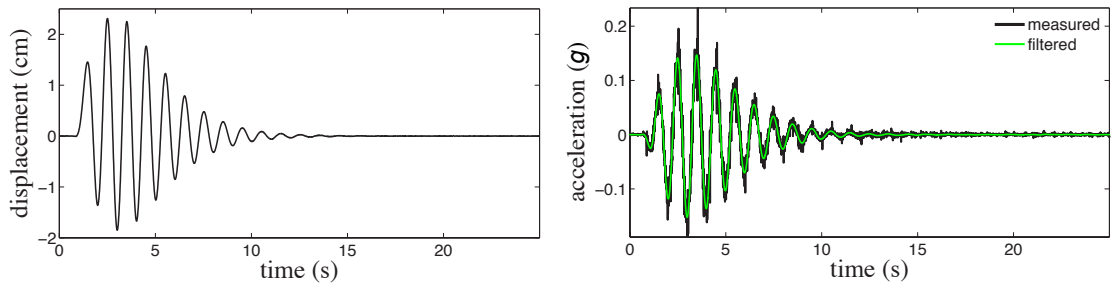


FIGURE 4.6: Displacement and acceleration input applied to shaking table table for the moderate disturbance with $T_p = 1$ s: (—) measured and (—) filtered records.

In practice one cannot ensure that the ball-bearings are perfectly centered in the lower- and upper-bowls at the beginning of the test. To account for the uncertainty in the initial ball-bearing locations in the numerical simulations, the initial ball-bearing locations $\mathbf{r}_{i0}$ are taken to be uniformly distributed within a circle with radius of 1 cm, i.e.

$$\mathbf{r}_{i0} = [\rho_i \cos\psi_i \;\; \rho_i \sin\psi_i]^\intercal \,, \quad \rho_i \overset{\text{iid}}{\sim} U(0,1) \text{ cm} \,, \quad \psi_i \overset{\text{iid}}{\sim} U(0,2\pi) \,. \tag{4.21}$$

Twenty different initial conditions are used to test the influence of the initial ball location on the peak responses.

The system is self-centering to within one or two millimeters. If, after a large shake,

TABLE 4.2: Peak experimental shake table velocities for single, undamped RIS experiments. The dashes (-) indicate experimental tests not performed due to the stroke limit of the shake table.

| | | Peak measured table velocity $V_p$ (cm/s) | | | | | |
|---|---|---|---|---|---|---|---|
| Pulse period | Duration | Light | | | Heavy | | |
| $T_p$ (s) | $T$ (s) | Weak | Moderate | Strong | Weak | Moderate | Strong |
| 0.20 | 10 | 7.44 | 11.71 | 32.95 | 8.17 | 12.00 | 32.77 |
| 0.35 | 10 | 10.45 | 16.31 | 42.11 | 10.43 | 16.55 | 41.83 |
| 0.50 | 10 | 11.55 | 18.85 | 45.57 | 11.56 | 18.69 | 46.05 |
| 0.67 | 15 | 12.35 | 19.95 | 47.21 | 12.30 | 23.38 | 48.09 |
| 0.85 | 20 | 12.87 | 23.45 | 47.48 | 12.98 | 23.45 | 47.40 |
| 1.00 | 25 | 13.07 | 23.14 | - | 13.26 | 23.35 | - |
| 1.25 | 30 | 13.43 | 23.29 | - | 13.29 | 23.19 | - |
| 1.60 | 35 | 14.39 | 22.86 | - | 14.49 | 23.11 | - |
| 2.20 | 45 | 14.28 | - | - | 14.24 | - | - |
| 3.00 | 60 | 13.95 | - | - | 14.13 | - | - |

a two-millimeter offset is not acceptable, the system can be quickly and easily re-centered without interrupting operation of the isolated equipment.

### *4.5.3 Peak response quantities*

The response quantities of interest are peak relative displacement and the peak total acceleration of the isolated mass. The peak relative displacement $d_{\mathrm{R}}^{\max}$ is given by

$$d_{\mathrm{R}}^{\max} = \max_{t} d_{\mathrm{R}}(t) = \max_{t} \sqrt{\bar{x}^2(t) + \bar{y}^2(t)}. \tag{4.22}$$

Two displacement measurements were acquired during the experiments; an LVDT measured the total displacement of the shaking table, and processed video recording gave the the total displacement of the equipment. By synchronizing these two measurements, the relative displacement of the top-frame was found by taking their difference. Two example experimental displacement records are shown in Figures 4.7(a) and 4.8(a) for two disturbance scenarios: moderate disturbance at $T_{\mathrm{p}} = 1.25$ s and strong disturbance at $T_{\mathrm{p}} = 0.85$ s, respectively. Figures 4.7(b) and 4.8(b) illustrate numerically-generated displacement records for the same disturbances. Response trajectories are not predictable due to the chaotic nature of this system [38], but as will be shown, the peak displacement responses are predictable with the simplified model.

The peak magnitude of the total acceleration $a_{\mathrm{T}}^{\max}$ is given by

$$a_{\mathrm{T}}^{\max} = \max_{t} a_{\mathrm{T}}(t) = \max_{t} \sqrt{\left(\ddot{\bar{x}}(t) + \ddot{w}_x(t)\right)^2 + \left(\ddot{\bar{y}}(t) + \ddot{w}_y(t)\right)^2}. \tag{4.23}$$

Three accelerometers—one in the $X_{\mathrm{t}}$-direction and two equally-spaced in the $Y_{\mathrm{t}}$-direction—measured two orthogonal accelerations of the top-frame. Figures 4.9(a) and 4.10(a) show two experimental acceleration records. Due to the top-frame's rotation $\bar{\theta}$, the measured accelerations are not in an absolute frame of reference. However, the magnitude of the total acceleration is rotationally-invariant and the norm of the recorded acceleration is equal to $a_{\mathrm{T}}(t)$. Figures 4.9(b) and 4.10(b) illustrate numerically-simulated acceleration histories.

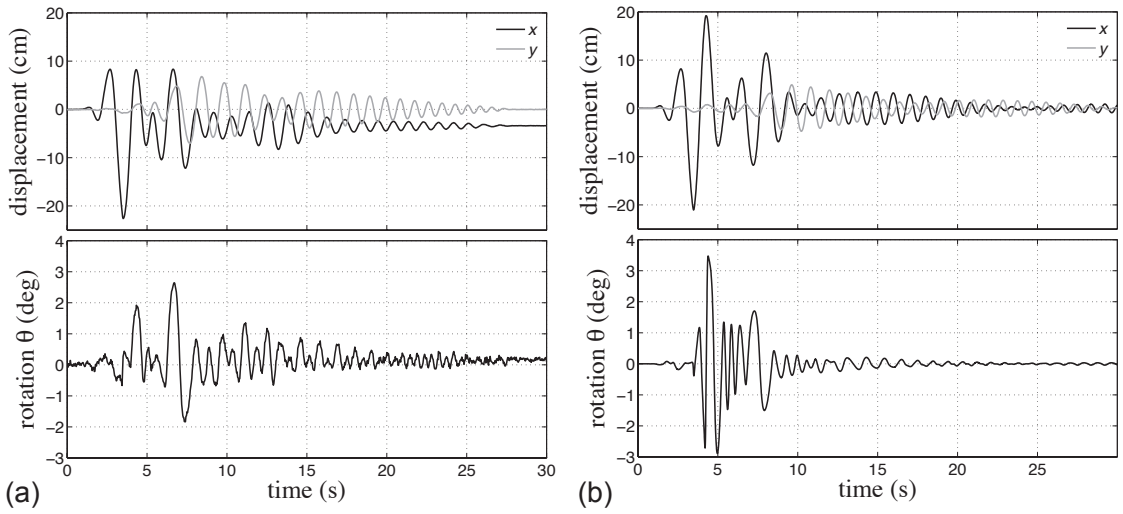


FIGURE 4.7: (a) Measured and (b) predicted displacement and rotation responses of the heavy system for the moderate disturbance at $T_p = 1.25$ s.

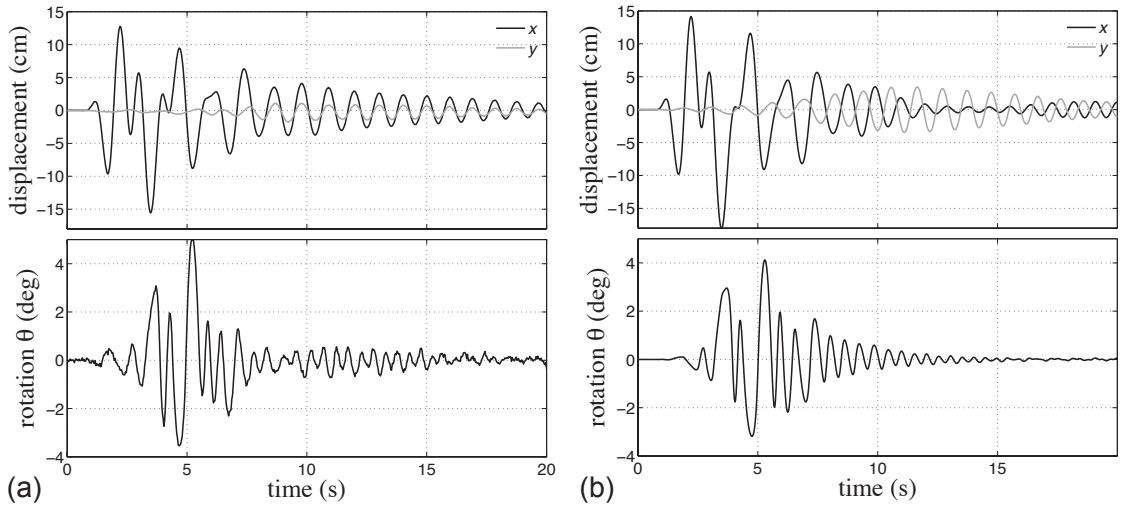


FIGURE 4.8: (a) Measured and (b) predicted displacement and rotation responses of the heavy system for the strong disturbance at $T_p = 0.85$ s.

### *4.5.4 Peak response spectra*

The experimental and numerical peak response spectra for the light and heavy systems can be seen in Figure 4.11. The pulse strengths are distinguished by the marker shape with the experimental response quantities in black and the numerical response quantities in gray. The experimental and numerical peak responses show excellent agreement.

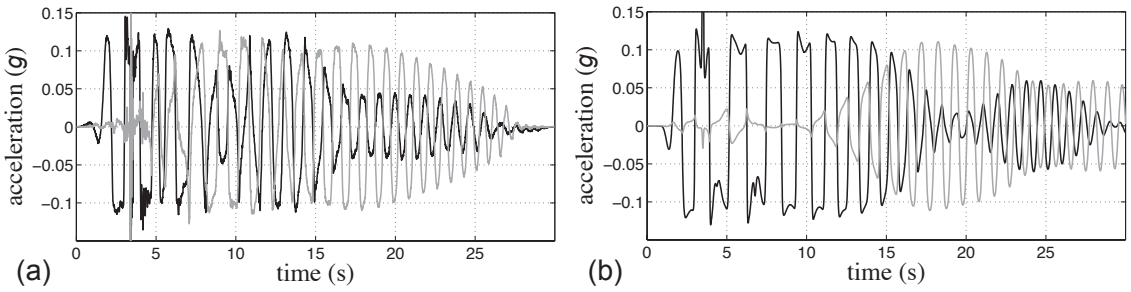


FIGURE 4.9: (a) Measured and (b) predicted acceleration responses of the heavy system for the moderate disturbance at $T_p$ = 1.25 s. Peak acceleration values (not shown): (a) 2.2 $g$ and (b) 0.6 $g$.

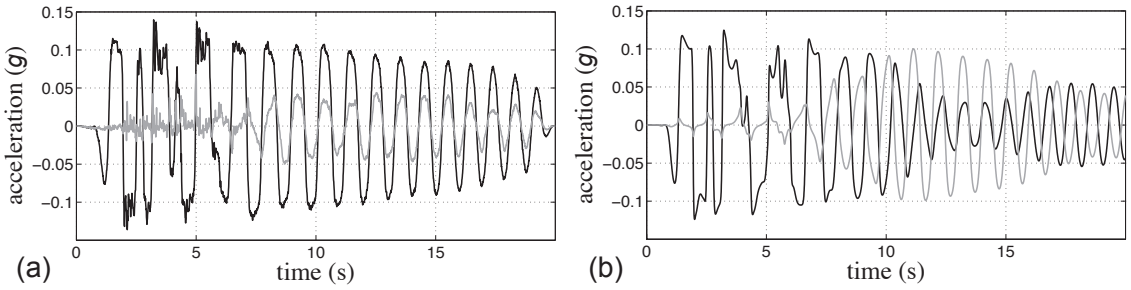


FIGURE 4.10: (a) Measured and (b) predicted acceleration responses of the heavy system for the strong disturbance at $T_p$ = 0.85 s.

For the light system in Figure 4.11(a-b), the peak displacements $d_R^{max}$ coincide for nearly all cases. Near resonance ($T_p \in [0.85,1.6]$ s), the numerically-determined displacements are more dispersed as compared to responses at off-resonant pulse periods. The experimental displacements fall within the numerically predicted spread except for the moderate cases at $T_p$ = 1.25 and 1.6 s. In these two cases, the experimental system displaces beyond 21 cm, the approximate theoretical limit at which the ball-bearings impact the bowl lip. In these experiments, when the ball-bearings collided with the bowl lip, the metal plates used to load the system slid and shifted. Because the LEDs used to measure the equipment displacement were attached to the top metal plate, the residual displacement in the plates were captured in the relative displacement measurement. An example of this can be seen in the displacement response illustrated in Figure 4.7(a). The residual displacements in the loading plates are on the order of 2–4 cm.

The numerical model predicts the peak acceleration $a_T^{max}$ well for cases without im-

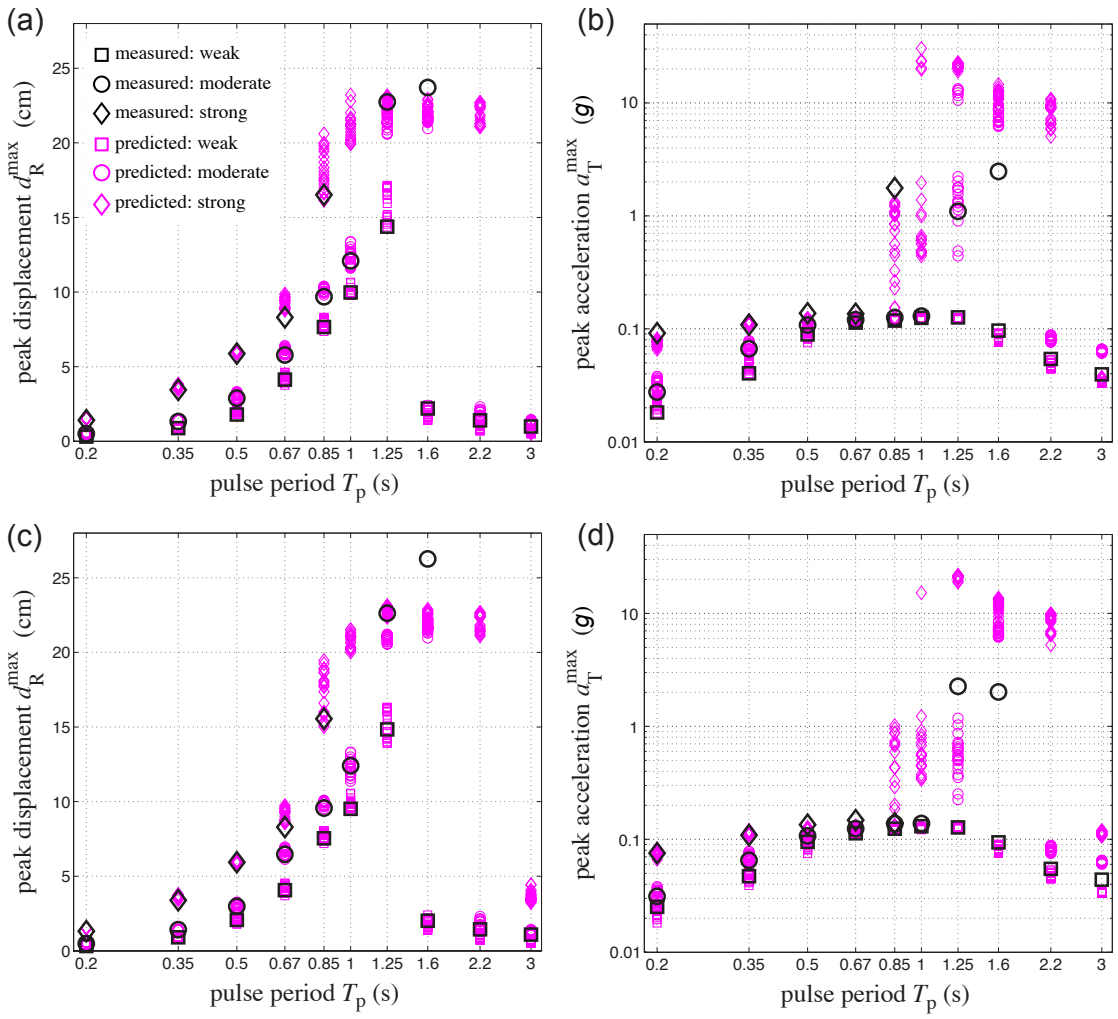


FIGURE 4.11: Peak displacement and acceleration pulse response spectra for (a-b) light system and (c-b) heavy system: weak (□), moderate (○), and strong (◇).

pacts, but differing results are seen for tests with impacts. The impacts of the ball-bearings with the bowl lips generate spikes in the acceleration. An example of an experimentally-measured acceleration spike is shown in Figure 4.9(a). These spikes can be hazardous to the operation of the isolated equipment and constitutes a failure of the isolation system. Elevated peak accelerations are observed in such impacting cases (e.g. moderate $T_p$ = 1.25 and 1.60 s). See Figure 4.11(b). Tests with impacts are easy to discern from tests without; in tests with impacts, the peak acceleration exceeds 0.13 $g$.

The disparity between the experimentally-measured and numerically-predicted accel-

erations in tests with impacts are due to saturation in the accelerometer measurements and/or poor approximations in the model. In cases with impacts, the acceleration measurements were clipped and were unable to record the true peak acceleration. Thus, the recorded and actual accelerations may differ. The model makes use of a shallow bowl approximation which does not hold when a ball-bearings come in contact with the bowl lip. In such instances, the model does not strictly correspond to the physics of the system and the calculated accelerations may be incorrect. Furthermore, in fitting the bowl-shape function, experimental data in the bowl lip region was limited and the numerical fit may not exactly capture the shape of the lip. Nevertheless, the model is able to accurately predict the occurrence of impacts, which is sufficient for failure prediction; impacts almost surely produce excessive inertial loads on the isolated object.

Similar results are observed for the heavy system in Figure 4.11(c-d)—excellent predictions of peak response quantities in cases without impacts and accurate prediction of the occurrence of impacts. One case requires further explanation: For the strong case at $T_{\mathrm{p}} = 0.85$ s, no impact was experimentally found whereas the numerical model predicts a range of responses, some including impacts. Figure 4.10(d) shows a simulated acceleration history without an impact. Qualitatively different responses are seen for varying initial conditions as the system undergoes a grazing bifurcation [88], for which the ball-bearings will collide, in only some cases.

The results presented in this section validate the predictive capabilities of the simplified model. Figure 4.11 demonstrates that the proposed simplified model successfully predicts the peak displacement and acceleration response under a variety of loading periods and amplitudes. In the next section, the predictive capability of this simplified and experimentally-validated model is used to assess the performance of the isolator.

## 4.6 Frontiers of Impact

In designing an isolation system, a designer would like to know at what disturbance amplitudes, over a range of periods, the displacement capacity would be exceeded. Due to the physical limitations of the shaking table (e.g. stroke and peak velocity), impacts could not be induced over all the pulse periods. However, this inverse problem can easily be solved using the experimentally-validated mathematical model.

We define $V_{\mathrm{p}}^{\mathrm{crit}}$ to be the smallest velocity amplitude at which the peak acceleration exceeds a critical threshold. For this example, we selected the light system ($m$ = 355 kg) with a threshold of $a_{\mathrm{T}} > 0.2\ g$ to indicate impacts. Using the bisection method, $V_{\mathrm{p}}^{\mathrm{crit}}$ was determined to the nearest 1 cm/s from twenty randomly generated initial conditions for a range of pulse periods $T_{\mathrm{p}}$. Table 4.3 gives the means and coefficients of variation (CV) of $V_{\mathrm{p}}^{\mathrm{crit}}$. In general, larger CVs are seen at or near resonance. The largest CVs in $V_{\mathrm{p}}^{\mathrm{crit}}$ are seen for $T_{\mathrm{p}}$ = 0.85 s. The distribution of $V_{\mathrm{p}}^{\mathrm{crit}}$ at this pulse period is bimodal, indicating a bifurcation in the response dependent on the ball-bearings' initial conditions, as was noted earlier. Figure 4.12 illustrates these critical amplitudes in a tripartite plot. Near resonance, the critical peak floor velocity is approximately 20 cm/s, whereas velocities 2–200 times larger are required at shorter periods ($T_{\mathrm{p}} \leq 1$ s). In the short-period range, the occurrence of impacts corresponds to a critical peak floor displacement level of 6–10 cm. The critical floor displacement drops to 4 cm near resonance and increases to nearly 25 cm for the longest pulse period ($T_{\mathrm{p}}$ = 3 s). In the long-period range, the system is acceleration

TABLE 4.3: Average and coefficient of variation (CV) of the critical disturbance amplitude $V_{\mathrm{p}}^{\mathrm{crit}}$ for an **undamped** rolling isolation system.

| | | Pulse period $T_{\mathrm{p}}$ (s) | | | | | | | | | | | |
|---|---|---|---|---|---|---|---|---|---|---|---|---|---|
| | | 0.20 | 0.35 | 0.50 | 0.67 | 0.85 | 1.0 | 1.25 | 1.6 | 2.2 | 3.0 | 4.0 | 5.0 |
| $V_{\mathrm{p}}^{\mathrm{crit}}$ (cm/s) | avg | 575 | 235 | 147 | 72 | 44 | 40 | 21 | 18 | 34 | 53 | 67 | 89 |
| | CV | 1.6 | 1.5 | 1.3 | 4.5 | 15.1 | 4.4 | 2.8 | 6.5 | 3.8 | 1.5 | 2.5 | 2.4 |

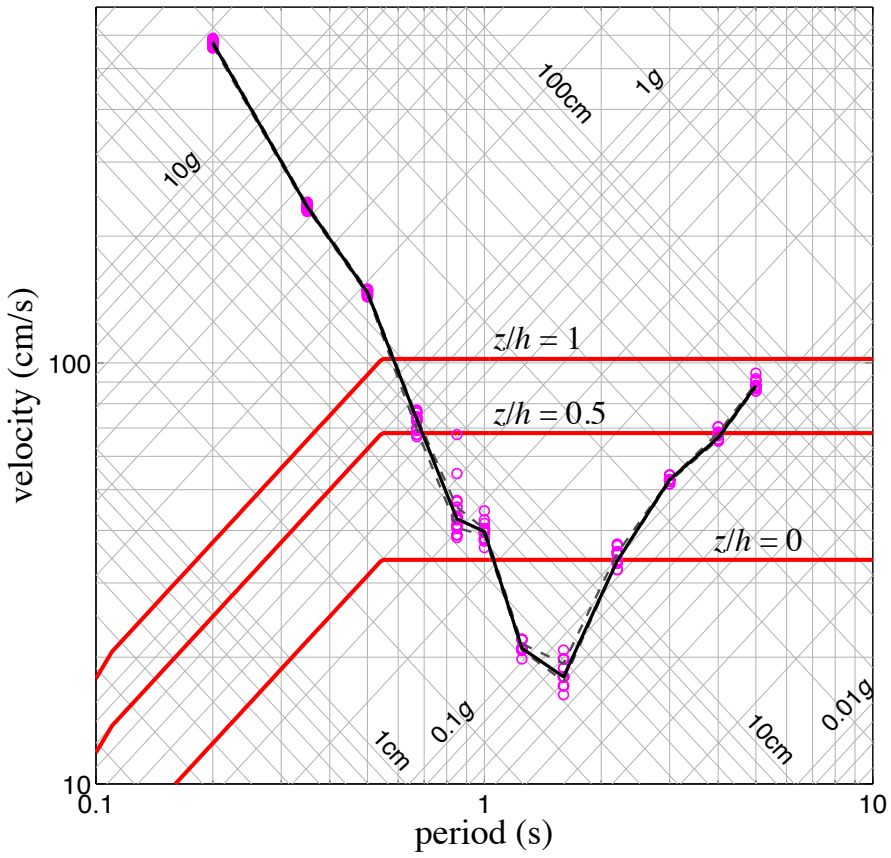


FIGURE 4.12: Seismic equipment isolation design spectrum. Critical disturbance velocity amplitude $V_{\mathrm{p}}^{\mathrm{crit}}$: twenty random initial conditions (○), median (—), and the 25th and 75th percentile (– – –). Seismic design spectra (—), as per ASCE 7-10, for a nonstructural component at three attachment heights: ground ($z/h = 0$), mid-height ($z/h = 0.5$), and roof ($z/h = 1$).

controlled—the impacts occur at a peak floor acceleration level of 0.12 $g$.

Finally, the sufficiency of the isolation system to protect equipment from design-level earthquakes is assessed. Valuable insight into the nature of the isolation system may be gleaned from threshold spectra such as Figure 4.12. Figure 4.12 also plots the seismic design spectra for nonstructural components, as per ASCE 7-10 [89]. These design spectra were generated for a vibration-isolated component located in a high seismicity area (San Francisco) with site class C. The equipment design spectral acceleration is as follows:

$$S_{a,\mathrm{equip}} = 0.4\frac{a_p S_a}{R_p/I_p}(1 + 2z/h) \tag{4.24}$$

where spectral acceleration $S_a$ is given by

$$S_a = \begin{cases} S_{DS}(0.4 + 0.6T/T_0): & T < T_0 \\ S_{DS}: & T_0 \leq T \leq T_S \\ S_{D1}/T: & T_S < T \leq T_L \\ S_{D1}T_L/T^2: & T > T_L \end{cases}. \tag{4.25}$$

Values for the design parameters are given in Table 4.4. Three component attachment levels were considered: ground ($z/h = 0$), mid-height ($z/h = 0.5$), and roof ($z/h = 1$).

From Figure 14, we see that the capacity of the system is sufficient at short periods (for lower floor levels). For structures responding to ground motions with near-fault pulse characteristics, displacement capacities of this lightly-damped system would not meet demands. Performance at longer periods and higher intensities could be enhanced in two ways: By increasing the displacement capacity of the system, larger floor velocities could be applied without inducing impacts. Alternately, additional damping would reduce responses near resonance ($T_{\mathrm{p}} \in$ [1,2] cm). Both of these approaches—implemented separately or in conjunction—would increase the system's isolation capacity and make the system better suited to protect vital payloads. Therefore, means of adding damping to the system and/or increasing the system's displacement capacity must be investigated.

## 4.7 Summary

This chapter presents an experimentally-validated and simplified model of a rolling equipment isolation system. The general problem formulation and modeling procedure are

TABLE 4.4: Parameter values for the ASCE 7-10 spectrum design representative of a site in San Francisco, CA with soil class C.

| Parameter | Value | Parameter | Value |
|---|---|---|---|
| $a_p$ | 2.5 | $S_S$ | 1.50 $g$ |
| $R_p$ | 2.5 | $T_0$ | 0.109 s |
| $I_p$ | 1.0 | $T_S$ | 0.545 s |
| $S_1$ | 0.629 $g$ | $T_L$ | 12 s |

described. Then, an experimental setup is presented, and the unique features of the experiment identified, including the *in situ* bowl deflections caused by the installation. An idealized floor-motion disturbance model is developed, and experimental data from tests on a single-axis shake table are used to asses peak responses. The proposed model was shown to effectively predict peak relative displacements, peak total accelerations, and the occurrence of impacts for a wide range of disturbance periods and amplitudes. Finally, this chapter demonstrates the risk-based design capabilities of the experimentally-validated model. Critical disturbance amplitudes were numerically evaluated for a range of pulse periods and ball perturbations; expanding the displacement capacity or reducing the displacement will enhance the behavior of this system for near-resonant excitations.

The mathematical model for the RIS validated in this study is parameterized for a system with a cone-like potential energy function. Notably, model parameters for the entire system can be determined from only a quarter-cycle of free-response measurements. Furthermore, parameterizations for any other RIS can be determined in this way and the resulting models should be equally valid.

### *4.7.1 Possible extensions*

The following are possible extensions of the model presented in this chapter for an undamped RIS and the system itself that need to be pursued further:

- The system has a preferential direction of motion in the free-response experiments, due in part to the deformed shape of the bowls when installed. This effect was seen in the acceleration-displacement relationship, as well. A model incorporating the non-symmetric bowl shape should be developed, and the effects on the performance of the system need to be assessed.

- When the system deflects in excess of 20 cm, the ball-bearings collide with the bowl lip, producing spikes in the equipment's total acceleration. These large accelerations

diminish the isolation performance of the system. The displacement capacity of the isolation system could be increased by stacking two systems on top of one another [53]. The potential benefits of a stacked isolation system should be analytically and experimentally analyzed, which is the topic of Chapters 5 and 6.

- RISs are designed to have very low damping (~1–2%), and the responses near the system's natural frequency can be large. To suppress resonant effects, additional damping may be introduced, e.g. by using rubber or polyurethane ball-bearings [43]. In a series of experiments, Tsai *et al.* [36] showed that by coating the steel ball-bearing of a similar RIS system with a damping material, the large displacement responses were reduced. Alternatively, the steel bowls could be covered with elastomeric sheets which would resist the rolling of the ball-bearings [90]. This additional rolling resistance may suppress resonant effects and improve the isolator's performance. In Chapter 9 we present and experimentally validate a model of a damped RIS, which is then used to assess the system's performance.

- In Chapter 10, a seismic hazard analysis of the in-building responses of RISs will be of use in loss-estimation of facilities protected with these systems.

# 5

# Vibration Suppression Using Double Rolling Isolation Systems: Theory

## 5.1 Background

Rolling pendulum isolation platforms (RISs) protect fragile building contents from earthquake hazards by decoupling horizontal floor motions from the horizontal responses of the isolated object. The suitability of RISs for shaking levels approaching a structure's design-basis earthquake depends substantially on the displacement demands of the motion. RISs can perform extremely well when their displacement capacities are not exceeded [41]. At the edge of the each bowl's rolling surface, a lip acts as a stiff limit on the ball-bearing's displacement. The isolation system's displacement capacity is determined by the contact of the ball-bearings with the bowl lips. The RISs in use today have displacement capacities of about 20 cm [1]. When the system deflects in excess of 20 cm, the ball-bearings collide with the bowl lip, producing spikes in the equipment's total acceleration. These large accelerations diminish the isolation performance of the system.

In Chapter 4 we showed that these systems' 20 cm displacement capacity might be deficient, especially near resonance. Therefore, we propose a novel *double* RIS (see Figure

5.1(a)), which comprises two ISO-Base platforms [1, 37] stacked one on top of the other. The displacement capacity of the stacked configuration is effectively double that of the individual subsystems.

This chapter presents and numerically evaluates a complete nonlinear model of the coupled dynamics of a double RIS. The derivation requires the use of two translating and rotating coordinate systems. The model is derived through the fundamental form of Lagrange's equation and involves the nonholonomic constraints of spheres rolling between non-parallel surfaces, a potential energy function calibrated to high-fidelity measurements of the platform geometry, and a damping model calibrated to free-response measurements. Free- and forced-response simulations provide some insight into the coupled nonlinear dynamics of this system.

The double RIS investigated in this chapter is depicted in depicted in Figure 5.1. It consists of eight large ball-bearings, and sixteen shallow radially-symmetric steel bowls fixed to three frames (bottom, middle, and top). The bottom-frame rests on the floor and holds four bowls concave-up. The middle-frame holds eight bowls, four concave-up and four concave-down. The top-frame holds four bowls, concave-down. A ball-bearing rolls between each pair of bowls in the bottom- and middle-frames and the middle- and top-frames. Large amplitude (translational and rotational) motions, non-quadratic bowl profiles, and the kinematics of spheres rolling between non-parallel surfaces give rise to nonlinear behavior. Further, under large displacements the ball-bearings may collide with the bowl lip, imparting impactive loads [91, 92].

The kinematics of rolling between non-parallel surfaces introduces nonholonomic constraints [38,93]. In order for the ball-bearings to roll without slipping, the equations of motion must be found using the appropriate form of Lagrange's equation [94]. The dynamical response of the system is investigated numerically through time-history simulation. The goal of these simulations is to provide the principal aspects of the system's nonlinear dynamics in free and forced responses.

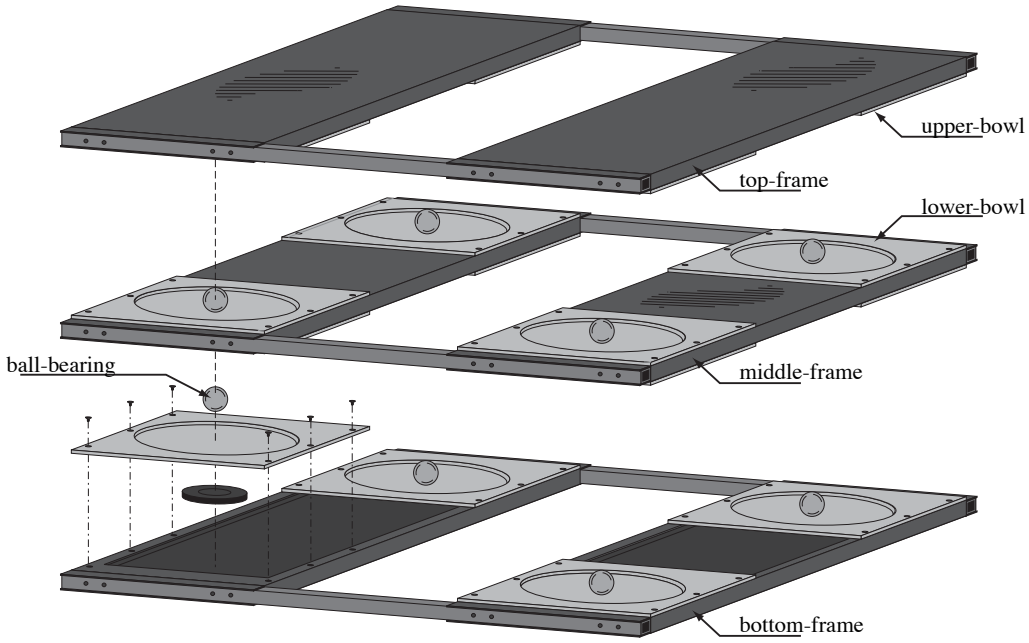


FIGURE 5.1: Exploded view of a double rolling isolation system.

## 5.2 Equations of Motion

The displaced configuration of a double RIS, depicted in Figure 5.1, is illustrated in Figure 5.2. The bottom-frame (- - -) has the $X_b$-$Y_b$ coordinate system, the middle-frame (-·-) has the $X_m$-$Y_m$ coordinate system, the top-frame (—) has the $X_t$-$Y_t$ coordinate system, and the location of two of the eight balls are shown as gray circles. The bottom-frame is excited by a disturbance that has $X_g$ and $Y_g$ translational components $w_x(t)$ and $w_y(t)$, and rotational component $w_\theta(t)$. With respect to the bottom-frame, the centroid of the middle-frame mass, $m_1$, is translated through displacements $\bar{x}_1(t)$ and $\bar{y}_1(t)$, and rotated by an angle $\bar{\theta}_1(t)$; with respect to the middle-frame, the centroid of the top-frame mass, $m_2$, is translated through displacements $\bar{x}_2(t)$, and $\bar{y}_2(t)$, and rotated by an angle $\bar{\theta}_2(t)$ The instantaneous centroidal velocities are $\dot{\bar{x}}_1(t)$, $\dot{\bar{y}}_1(t)$, $\dot{\bar{\theta}}_1(t)$, $\dot{\bar{x}}_2(t)$, $\dot{\bar{y}}_2(t)$, and $\dot{\bar{\theta}}_2(t)$.

Knowing the location and velocity of the centers of masses $m_1$ and $m_2$, expressions for the kinetic energy $T$ and potential energy $V$ of the system may be derived. Then applying the fundamental form of Lagrange's equation, the equations of state for the stacked seismic

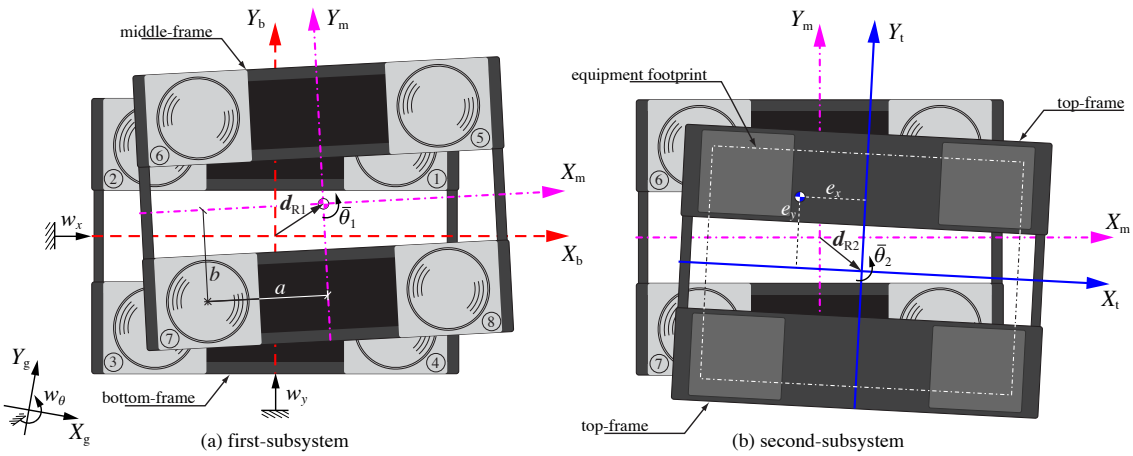


FIGURE 5.2: Double rolling isolation system geometry.

isolation platform are determined.

For the purpose of developing the model various engineering approximations are used to simplify the derivation. Assumptions include the following: (a) the ball-bearing mass is negligible with respect to the frame masses; (b) kinetic energy is modeled only in terms of the effect of the planar motion of the platforms—vertical velocity is not included in $T$; (c) the ball-bearings remain in contact throughout the platform's motion; (d) the equipment is rigidly-connected to the top-frame; and (e) linear-viscous damping represents energy dissipation in the system. Any further assumptions will be noted in the following discussion. Due to multiple rotating reference frames the equations of motion for the stacked isolation system are complicated—rotation matrices nonlinearly couple the dynamics of the two subsystems. The most concise notation, as selected by the author, is used to ease the comprehension of the equations of motion.

### *5.2.1 Kinetic energy*

The mass $m_1$ of the first-subsystem is attributed to the middle-frame, and the mass $m_2$ of the second-subsystems is attributed to the top-frame and equipment resting on the top-frame. In the top-frame's coordinates $X_t$-$Y_t$, the center of gravity of the isolated mass and equipment is located at $(e_x, e_y)$ with mass moment of inertia $I_2$. Whereas, in the middle-

frame's coordinates $X_{\mathrm{m}}$-$Y_{\mathrm{m}}$, the center of gravity coincides with the centroid at $(0, 0)$, with mass moment of inertia $I_1$. The kinetic energy $T$ of the system comes from the horizontal translational velocity and angular velocity of the center of masses with respect to an inertial reference, $X_{\mathrm{g}}$-$Y_{\mathrm{g}}$. The quadratic kinetic energy is given as follows:

$$T \equiv T(\bar{x}_1, \bar{y}_1, \bar{\theta}_1, \dot{\bar{x}}_1, \dot{\bar{y}}_1, \dot{\bar{\theta}}_1, \bar{x}_2, \bar{y}_2, \bar{\theta}_2, \dot{\bar{x}}_2, \dot{\bar{y}}_2, \dot{\bar{\theta}}_2) = \tfrac{1}{2} m_1 \boldsymbol{v}_1^{\mathsf{T}} \boldsymbol{v}_1 + \tfrac{1}{2} I_1 \omega_1^2 + \tfrac{1}{2} m_2 \boldsymbol{v}_2^{\mathsf{T}} \boldsymbol{v}_2 + \tfrac{1}{2} I_2 \omega_2^2 \quad (5.1)$$

where $\boldsymbol{v}_j = [v_{jx}\ v_{jy}]^{\mathsf{T}}$ is the global translational velocity vector and $\omega_j$ is the global angular velocity of the center of the $j$th mass. Expressions for the global velocities for the displaced configuration, Figure 5.2, need to be determined in order to apply Lagrange's equation.

For a fixed point in the middle-frame coordinates $X_{\mathrm{m}}$-$Y_{\mathrm{m}}$, define the local position vector to be $\boldsymbol{\xi}_{\mathrm{m}} = [x_{\mathrm{m}}\ y_{\mathrm{m}}]^{\mathsf{T}}$. The point's location in the bottom-frame coordinates $X_{\mathrm{b}}$-$Y_{\mathrm{b}}$, given middle-frame rotation $\bar{\theta}_1(t)$ and relative displacement $\boldsymbol{d}_{\mathrm{R1}}(t) = [\bar{x}_1(t)\ \ \bar{y}_1(t)]^{\mathsf{T}}$, is

$$\boldsymbol{\xi}_{\mathrm{b}} = \boldsymbol{d}_{\mathrm{R1}} + \mathbf{R}_{\bar{\theta}_1} \boldsymbol{\xi}_{\mathrm{m}} \quad (5.2)$$

where, in general, $\mathbf{R}_\theta$ is the rotation matrix through angle $\theta$. The corresponding velocity in the bottom-frame reference system is

$$\dot{\boldsymbol{\xi}}_{\mathrm{b}} = \dot{\boldsymbol{d}}_{\mathrm{R1}} + \dot{\bar{\theta}}_1 \mathbf{R}'_{\bar{\theta}_1} \boldsymbol{\xi}_{\mathrm{m}} \quad (5.3)$$

where the prime notation means differentiation with respect to the rotation angle, i.e. $\mathbf{R}'_\theta = \partial \mathbf{R}_\theta / \partial \theta$. Note that differentiation may be performed with the differentiation matrix, $\mathbf{R}'_\theta = \mathbf{D}\mathbf{R}_\theta = \mathbf{R}_\theta \mathbf{D}$, where

$$\mathbf{D} = \begin{bmatrix} 0 & -1 \\ 1 & 0 \end{bmatrix}.$$

That same point's location in the global (inertial) reference frame $X_{\mathrm{g}}$-$Y_{\mathrm{g}}$, given rotational disturbance $w_\theta(t)$ and translational disturbances $\boldsymbol{w}(t) = [w_x(t)\ \ w_y(t)]^{\mathsf{T}}$, is

$$\boldsymbol{\xi}_{\mathrm{g}} = \boldsymbol{w} + \mathbf{R}_{w_\theta} \boldsymbol{\xi}_{\mathrm{b}} = \boldsymbol{w} + \mathbf{R}_{w_\theta} (\boldsymbol{d}_{\mathrm{R1}} + \mathbf{R}_{\bar{\theta}_1} \boldsymbol{\xi}_{\mathrm{m}}) \quad (5.4)$$

with corresponding velocity

$$\dot{\boldsymbol{\xi}}_{\mathrm{g}} = \dot{\boldsymbol{w}} + \dot{w}_\theta \mathbf{R}_{w_\theta} \mathbf{D} \boldsymbol{\xi}_{\mathrm{b}} + \mathbf{R}_{w_\theta} \dot{\boldsymbol{\xi}}_{\mathrm{b}} \tag{5.5}$$

where $\dot{\boldsymbol{w}}$ is a vector of the translational base velocities and $\dot{w}_\theta$ is the rotational base velocity. Because the middle-frame's center of mass coincides with its centroid, the total translational velocity of the center of mass $m_1$ (i.e. $\boldsymbol{\xi}_{\mathrm{m}} = \mathbf{0}$), in the $X_{\mathrm{g}}$-$Y_{\mathrm{g}}$ coordinates, is

$$\boldsymbol{v}_1 = \dot{\boldsymbol{w}} + \dot{w}_\theta \mathbf{R}_{w_\theta} \mathbf{D} \boldsymbol{d}_{\mathrm{R1}} + \mathbf{R}_{w_\theta} \dot{\boldsymbol{d}}_{\mathrm{R1}} \ . \tag{5.6}$$

Notice $\boldsymbol{v}_1$ is linear in $\bar{x}_1$, $\bar{y}_1$, $\dot{\bar{x}}_1$, and $\dot{\bar{y}}_1$, while the centroidal rotation $\bar{\theta}_1$ and angular velocity $\dot{\bar{\theta}}_1$ do not enter the expression. The angular velocity of the middle-frame about its center of mass is the combination of that about the centroid and the base rotation, i.e.

$$\omega_1 = \dot{w}_\theta + \dot{\bar{\theta}}_1 \ . \tag{5.7}$$

For the second-subsystem we follow a procedure similar to the first-subsystem. Notice that mass $m_2$ may be eccentric, $\boldsymbol{\xi}_{\mathrm{t}} = \boldsymbol{e} = [e_x \ e_y]^{\mathsf{T}}$. The disturbance inputs to the second-system are the (global) centroidal displacements of the middle-frame, i.e. $\boldsymbol{w} + \mathbf{R}_{w_\theta} \boldsymbol{d}_{\mathrm{R1}}$ (translational) and $w_\theta + \bar{\theta}_1$ (rotational). The top-frame's center of mass velocities are as follows:

$$\boldsymbol{v}_2 = \boldsymbol{v}_1 + (\dot{w}_\theta + \dot{\bar{\theta}}_1) \mathbf{R}_{w_\theta} \mathbf{R}_{\bar{\theta}_1} \mathbf{D} (\boldsymbol{d}_{\mathrm{R2}} + \mathbf{R}_{\bar{\theta}_2} \boldsymbol{e}) + \mathbf{R}_{w_\theta} \mathbf{R}_{\bar{\theta}_1} (\dot{\boldsymbol{d}}_{\mathrm{R2}} + \dot{\bar{\theta}}_2 \mathbf{R}_{\bar{\theta}_2} \mathbf{D} \boldsymbol{e}) \tag{5.8a}$$

$$\omega_2 = \dot{w}_\theta + \dot{\bar{\theta}}_1 + \dot{\bar{\theta}}_2 \ . \tag{5.8b}$$

Unlike $\boldsymbol{v}_1$, the velocity $\boldsymbol{v}_2$ is a nonlinear function of $\bar{\theta}_1$, $\dot{\bar{\theta}}_1$, $\bar{\theta}_2$, and $\dot{\bar{\theta}}_2$.

The kinetic energy of the system in terms of the centroidal displacements and rotations is found from Equation (5.1) where the expressions for center of mass velocities—$\boldsymbol{v}_1$, $\omega_1$, $\boldsymbol{v}_2$ and $\omega_2$—are given in Equations (5.6), (5.7), (5.8a), and (5.8b), respectively, for each of the masses. As is common in rotating reference frames, as we have here, the kinetic energy is a function of not only velocities, but also the translations and rotations.

### 5.2.2 *Potential energy*

Next, the potential energy of the system is determined following a similar procedure as in Section 3.2.2. We assume the middle- and top-frames are flexible enough to accommodate out-of-plane deformation so that all eight balls are in contact for any platform displacement or rotation. It is also assumed that the out-of-plane deformation permits a small angle approximation, i.e. the bending of the top-frame corresponds only to vertical displacements at its corners. Under these conditions, the deformation of each frame will be approximately saddle-shaped $\tilde{h}(x, y)$.

The bottom-, middle-, and top-frames are rectangular of identical dimensions, as illustrated in Figure 5.2. The bowls and ball-bearings are numbered $i = 1, ..., 8$, in accordance with Figure 5.2, with the coordinates of the bowl centers given by $\boldsymbol{c}_i = [a_i \;\; b_i]^\intercal$ where

$$\boldsymbol{a} = [a \;\; -a \;\; -a \;\; a \;\;\; a \;\; -a \;\; -a \;\; a]^\intercal \quad \text{and} \quad \boldsymbol{b} = [b \;\; b \;\; -b \;\; -b \;\;\; b \;\; b \;\; -b \;\; -b]^\intercal. \tag{5.9}$$

As seen in Figure 5.3, the locations of the balls with respect to the centers of the lower- and upper-bowls are given by the vectors $\mathbf{p}_i(t) = [p_{ix} \; p_{iy}]^\intercal$, $\mathbf{q}_i = [q_{ix} \; q_{iy}]^\intercal$, and $\mathbf{r}_i(t) = [r_{ix} \; r_{iy}]^\intercal$. The vectors $\mathbf{p}_i(t)$ are the displacement of the center of the $i$th concave-down bowl with respect to the center of the $i$th concave-up bowl calculated as

$$\mathbf{p}_i \equiv \mathbf{p}_i(\bar{x}_j, \bar{y}_j, \bar{\theta}_j) = \boldsymbol{d}_{\mathrm{R}j}(t) + (\mathbf{R}_{\bar{\theta}_j(t)} - \mathbf{I})\boldsymbol{c}_i \; . \tag{5.10}$$

The vectors $\mathbf{r}_i(t)$ are additional coordinates that are governed by the kinematics of the rolling balls, but may be presumed to be known at this stage of the development. Using the relationship $\mathbf{p}_i = \mathbf{r}_i + \mathbf{q}_i$, we can now find $\mathbf{q}_i(t)$ as

$$\mathbf{q}_i \equiv \mathbf{q}_i(\bar{x}_j, \bar{y}_j, \bar{\theta}_j, \mathbf{r}_i) = \boldsymbol{d}_{\mathrm{R}j}(t) + (\mathbf{R}_{\bar{\theta}_j(t)} - \mathbf{I})\, \boldsymbol{c}_i - \mathbf{r}_i(t) \; . \tag{5.11}$$

Let the vector $\boldsymbol{h} = [h_1 \;\; \cdots \;\; h_8]^\intercal$, where $h_i$ are the relative height between the $i$th lower- and upper-bowl centers, given by

$$h_i \equiv h_i(\bar{x}_j, \bar{y}_j, \bar{\theta}_j, \mathbf{r}_i) = \eta(\|\mathbf{r}_i\|) + \eta(\|\mathbf{q}_i\|) \tag{5.12}$$

where $\eta(r)$ is the radial bowl-shape function.

The potential energy of the system comes from the changes in the total heights of the centers of masses $m_1$ and $m_2$, viz.

$$\tilde{h}_1 \equiv \tilde{h}(0,0) = [1 \;\; 0 \;\; 0 \;\; 0]([\mathbf{I}_{4\times4} \; \mathbf{0}_{4\times4}][\mathbf{1}_8 \;\; \boldsymbol{a} \;\; \boldsymbol{b} \;\; \boldsymbol{a}\circ\boldsymbol{b}])^{-1}[\mathbf{I}_{4\times4} \; \mathbf{0}_{4\times4}]\boldsymbol{h} \tag{5.13a}$$

$$\tilde{h}_2 \equiv \tilde{h}(e_x, e_y) = [1 \;\; e_x \;\; e_y \;\; e_x e_y]([\mathbf{0}_{4\times4} \; \mathbf{I}_{4\times4}][\mathbf{1}_8 \;\; \boldsymbol{a} \;\; \boldsymbol{b} \;\; \boldsymbol{a}\circ\boldsymbol{b}])^{-1}[\mathbf{I}_{4\times4} \; \mathbf{I}_{4\times4}]\boldsymbol{h} \tag{5.13b}$$

where $\boldsymbol{a}\circ\boldsymbol{b}$ is the element-wise multiplication of vectors $\boldsymbol{a}$ and $\boldsymbol{b}$, and $\mathbf{1}_8$ is the unit 8-vector. Equation (5.13a) reduces to $\tilde{h}_1 = \sum_{i=1}^{4} h_i/4$. Define

$$\mu_i = \begin{cases} m_1/4 + m_2 u_i, & i = 1, ..., 4 \\ m_2 u_{i-4}, & i = 5, ..., 8 \end{cases} \tag{5.14}$$

where $\boldsymbol{u} = [1 \;\; e_x \;\; e_y \;\; e_x e_y]([\mathbf{0}_{4\times4} \; \mathbf{I}_{4\times4}][\mathbf{1}_8 \;\; \boldsymbol{a} \;\; \boldsymbol{b} \;\; \boldsymbol{a}\circ\boldsymbol{b}])^{-1}$ allocates the mass $m_2$ to the four top-bowls and has the property $\sum_{i=1}^{4} u_i = 1$. The potential energy of the double RIS is

$$V = V(\bar{x}_1, \bar{y}_1, \bar{\theta}_1, \bar{x}_2, \bar{y}_2, \bar{\theta}_2, \mathbf{r}_1, ..., \mathbf{r}_8) = m_1 g\tilde{h}_1 + m_2 g\tilde{h}_2 = \sum_{i=1}^{8} \mu_i g h_i(\bar{x}_j, \bar{y}_j, \bar{\theta}_j, \mathbf{r}_i) \tag{5.15}$$

where the indices $j \in \{1, 2\}$ relate ball-bearing index $i$ to the appropriate subsystem via the map

$$j \equiv j(i) = \begin{cases} 1, & i = 1, ..., 4 \\ 2, & i = 5, ..., 8 \end{cases} . \tag{5.16}$$

Notice that $V$ depends on the system configuration and not its velocity.

It is important to note that the vectors $\mathbf{p}_i$, $\mathbf{q}_i$ and $\mathbf{r}_i$ ($i = 1, ..., 4$) are all relative to the bottom-frame coordinates $X_\mathrm{b}$-$Y_\mathrm{b}$; the vectors $\mathbf{p}_i$, $\mathbf{q}_i$ and $\mathbf{r}_i$ ($i = 5, ..., 8$) are all relative to the middle-frame coordinates $X_\mathrm{m}$-$Y_\mathrm{m}$. The potential energy of the system comes from the displacement of the middle- and top-frames with respect to the bottom- and middle-frames, respectively, and is independent of the motion of the bottom reference frame $X_\mathrm{b}$-$Y_\mathrm{b}$.

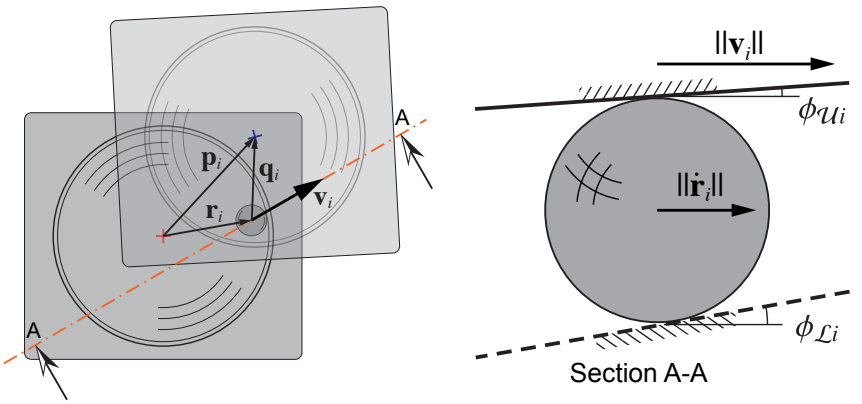


FIGURE 5.3: Geometry of a sphere rolling between two non-parallel surfaces: velocity $\mathbf{v}_i$ of the upper-bowl with respect to the lower-bowl at ball-bearing $i$ location, and relative velocity $\dot{\mathbf{r}}_i$ of $i$th ball-bearing rolling between rigid surfaces.

### *5.2.3 Kinematics of rolling ball-bearings*

The potential energy and the ensuing equations of state depend upon the locations of the ball-bearings $\mathbf{r}_i$. In Section 3.2.3, equations describing the evolution of a ball-bearing rolling, without slipping, between non-parallel surfaces were determined. These equations represent a set of nonholonomic constraints on the ball-bearing trajectories. The kinematic constraints relating the ball dynamics to the relative velocities of the platform are re-derived here.

Assuming slip-free rolling at the ball-bowl contact points, the ball-bearings roll in the direction of the velocity of the upper-bowl (at the ball-bearing location) with respect to the lower-bowl, denoted $\mathbf{v}_i$. See Figure 5.3(a). The velocity of the upper-bowl at the $i$th ball-bearing is found to be

$$\mathbf{v}_i = \dot{\boldsymbol{d}}_{\mathrm{R}j} + \dot{\theta}_j \mathbf{D}(\boldsymbol{c}_i + \mathbf{r}_i - \boldsymbol{d}_{\mathrm{R}j}) \,. \tag{5.17}$$

The nonholonomic constraints $\mathbf{g}_i$ for rolling without slipping of a ball-bearing is

$$\mathbf{0} = \mathbf{g}_i \equiv \dot{\mathbf{r}}_i - \varphi_i \mathbf{v}_i, \qquad (i = 1, ..., 8) \tag{5.18}$$

for which

$$\varphi_i \equiv \varphi_i(\bar{x}_j, \bar{y}_j, \bar{\theta}_j, \dot{\bar{x}}_j, \dot{\bar{y}}_j, \dot{\bar{\theta}}_j, \mathbf{r}_i) = \frac{\cos\phi_{\mathcal{L}i}}{\cos\phi_{\mathcal{L}i} + \cos\phi_{\mathcal{U}i}} \,. \tag{5.19}$$

Referring to Figure 5.3(b), the angles of the lower- and upper-surfaces in the rolling direction (i.e. parallel to $\mathbf{v}_i$) are

$$\phi_{\mathcal{L}i} = \tan^{-1}\left(\eta'(\|\mathbf{r}_i\|)\,\hat{\mathbf{v}}_i^{\mathsf{T}}\hat{\mathbf{r}}_i\right) \quad \text{and} \quad \phi_{\mathcal{U}i} = \tan^{-1}\left(\eta'(\|\mathbf{q}_i\|)\,\hat{\mathbf{v}}_i^{\mathsf{T}}\hat{\mathbf{q}}_i\right).$$

where $\hat{\mathbf{v}}_i = \mathbf{v}_i/\|\mathbf{v}_i\|$, $\hat{\mathbf{q}}_i = \mathbf{q}_i/\|\mathbf{q}_i\|$, and $\hat{\mathbf{r}}_i = \mathbf{r}_i/\|\mathbf{r}_i\|$, and $\eta'(r) = \mathrm{d}\eta(r)/\mathrm{d}r$.

Equation (5.18) represents sixteen nonlinear equations prescribing the evolution of the $x$ and $y$ locations of the eight ball-bearings. The evolution of ball-bearing positions $\mathbf{r}_i$ is nonlinear in the velocity and position of the upper-bowls, and is nonlinear in the position of the ball-bearing locations. This kind of kinematic condition is representative of generalized nonholonomic constraints.

### *5.2.4 Fundamental nonholonomic form of Lagrange's equation*

The set of twenty-two generalized coordinates

$$z \in \mathcal{Z} = \{\bar{x}_1, \bar{y}_1, \bar{\theta}_1, \bar{x}_2, \bar{y}_2, \bar{\theta}_2, r_{1x}, r_{1y}, ..., r_{8x}, r_{8y}\}$$

give the position and orientation of the centers of the middle- and top-frames and the ball-bearing locations. The fundamental nonholonomic form of Lagrange's equation [67] states that for any generalized coordinate $z$, the equation of state is given as follows:

$$\frac{\mathrm{d}}{\mathrm{d}t}\left(\frac{\partial T}{\partial \dot{z}}\right) - \frac{\partial T}{\partial z} + \frac{\partial V}{\partial z} = Q_z^{\mathrm{C}} + Q_z^{\mathrm{D}}\,. \tag{5.20}$$

Forces $Q_z^{\mathrm{C}}$ and $Q_z^{\mathrm{D}}$ are not derivable from potential energy functions. Forces $Q_z^{\mathrm{D}}$ are dissipative forces, corresponding to loss of energy, and are associated with micro-slip mechanisms over the finite contact surfaces between the ball-bearings and the steel bowls. These damping forces are relatively small and are determined from experimental data [38]. Dissipative forces acting on the frame centroids are assumed to be zero. The dissipative forces acting at the ball-bearing centers are modeled as linear-viscous damping [76]: $Q_{r_{ix}}^{\mathrm{D}} = -C_{\mathrm{b}}\dot{r}_{ix}$ and $Q_{r_{iy}}^{\mathrm{D}} = -C_{\mathrm{b}}\dot{r}_{iy}$.

The non-dissipative rolling contact forces $Q_z^{\mathrm{C}}$ enforce the constraints (5.18), are transverse to the paths of the ball-bearings, and are given by

$$Q_z^{\mathrm{C}} = \sum_{i=1}^{8} \left( \frac{\partial \mathbf{g}_i}{\partial \dot{z}} \right)^{\intercal} \boldsymbol{\lambda}_i \tag{5.21}$$

where multipliers $\boldsymbol{\lambda}_i$ enforce constraints $\mathbf{g}_i$ ($i = 1, ..., 8$) [78, 94]. For the centroidal coordinates $z \in \{\bar{x}_1, \bar{y}_1, \bar{\theta}_1, \bar{x}_2, \bar{y}_2, \bar{\theta}_2\}$, the constraints depend on $\dot{z}$ nonlinearly, though only through the vector $\mathbf{v}_i$, viz.

$$\frac{\partial \mathbf{g}_i}{\partial \dot{z}} = -\left( \frac{\partial \varphi_i}{\partial \mathbf{v}_i} \frac{\partial \mathbf{v}_i}{\partial \dot{z}} \right) \mathbf{v}_i - \varphi_i \frac{\partial \mathbf{v}_i}{\partial \dot{z}} \,. \tag{5.22}$$

The details of the gradient $\partial \varphi_i / \partial \mathbf{v}_i$ are given by Equation (3.24). Whereas, for the ball-bearing coordinates $z \in \{r_{1x}, r_{1y}, ..., r_{8x}, r_{8y}\}$, the constraints depend on $\dot{z}$ linearly, and the Jacobian matrix $\partial \mathbf{g}_i / \partial \mathbf{r}_k$ decouples as follows:

$$\frac{\partial \mathbf{g}_i}{\partial \dot{\mathbf{r}}_k} = \frac{\partial \dot{\mathbf{r}}_i}{\partial \dot{\mathbf{r}}_k} = \begin{cases} \mathbf{I}_{2\times 2}, & i = k \\ \mathbf{0}_{2\times 2}, & i \neq k \end{cases} \,. \tag{5.23}$$

The development of equations of state, for each $z \in \mathcal{Z}$, is derived from Lagrange's equation (5.20). The expressions in Equation (5.20), in general, are as follows:

$$\begin{aligned} \frac{\mathrm{d}}{\mathrm{d}t}\left( \frac{\partial T}{\partial \dot{z}} \right) = {} & m_1 \left( \frac{\partial \boldsymbol{v}_1}{\partial \dot{z}} \right)^{\intercal} \dot{\boldsymbol{v}}_1 + m_1 \frac{\mathrm{d}}{\mathrm{d}t}\left( \frac{\partial \boldsymbol{v}_1}{\partial \dot{z}} \right)^{\intercal} \boldsymbol{v}_1 + I_1 \frac{\partial \omega_1}{\partial \dot{z}} \dot{\omega}_1 + I_1 \frac{\mathrm{d}}{\mathrm{d}t}\left( \frac{\partial \omega_1}{\partial \dot{z}} \right) \omega_1 \\ & + m_2 \left( \frac{\partial \boldsymbol{v}_2}{\partial \dot{z}} \right)^{\intercal} \dot{\boldsymbol{v}}_2 + m_2 \frac{\mathrm{d}}{\mathrm{d}t}\left( \frac{\partial \boldsymbol{v}_2}{\partial \dot{z}} \right)^{\intercal} \boldsymbol{v}_2 + I_2 \frac{\partial \omega_2}{\partial \dot{z}} \dot{\omega}_2 + I_2 \frac{\mathrm{d}}{\mathrm{d}t}\left( \frac{\partial \omega_2}{\partial \dot{z}} \right) \omega_2 \end{aligned} \tag{5.24a}$$

$$\frac{\partial T}{\partial z} = m_1 \left( \frac{\partial \boldsymbol{v}_1}{\partial z} \right)^{\intercal} \boldsymbol{v}_1 + I_1 \frac{\partial \omega_1}{\partial z} \omega_1 + m_2 \left( \frac{\partial \boldsymbol{v}_2}{\partial z} \right)^{\intercal} \boldsymbol{v}_2 + I_2 \frac{\partial \omega_2}{\partial z} \omega_2 \tag{5.24b}$$

$$\frac{\partial V}{\partial z} = \sum_{i=1}^{8} \mu_i g \frac{\partial h_i}{\partial z} \,. \tag{5.24c}$$

Accelerations $\dot{\boldsymbol{v}}_1$ and $\dot{\boldsymbol{v}}_2$, appearing in Equation (5.24a), represent the *total* accelerations of masses $m_1$ and $m_2$, which we denote hereinafter as $\boldsymbol{a}_{\mathrm{T}1}$ and $\boldsymbol{a}_{\mathrm{T}2}$, respectively. Given here

are expressions for the total accelerations:

$$\boldsymbol{a}_{\mathrm{T}1} = \ddot{\boldsymbol{w}} + \mathbf{R}_{w_\theta}(\ddot{w}_\theta \mathbf{D} - \dot{w}_\theta^2 \mathbf{I})\boldsymbol{d}_{\mathrm{R}1} + 2\dot{w}_\theta \mathbf{R}_{w_\theta}\mathbf{D}\dot{\boldsymbol{d}}_{\mathrm{R}1} + \mathbf{R}_{w_\theta}\ddot{\boldsymbol{d}}_{\mathrm{R}1} \tag{5.25a}$$

$$\begin{aligned}\boldsymbol{a}_{\mathrm{T}2} = \boldsymbol{a}_{\mathrm{T}1} &+ \mathbf{R}_{w_\theta}\mathbf{R}_{\bar{\theta}_1}((\ddot{w}_\theta + \ddot{\bar{\theta}}_1)\mathbf{D} - (\dot{w}_\theta + \dot{\bar{\theta}}_1)^2\mathbf{I})(\boldsymbol{d}_{\mathrm{R}2} + \mathbf{R}_{\bar{\theta}_2}\boldsymbol{e}) \\ &+ 2(\dot{w}_\theta + \dot{\bar{\theta}}_1)\mathbf{R}_{w_\theta}\mathbf{R}_{\bar{\theta}_1}\mathbf{D}(\dot{\boldsymbol{d}}_{\mathrm{R}2} + \dot{\bar{\theta}}_2\mathbf{R}_{\bar{\theta}_2}\mathbf{D}\boldsymbol{e}) \\ &+ \mathbf{R}_{w_\theta}\mathbf{R}_{\bar{\theta}_1}(\ddot{\boldsymbol{d}}_{\mathrm{R}2} + \ddot{\bar{\theta}}_2\mathbf{R}_{\bar{\theta}_2}\mathbf{D}\boldsymbol{e} - \dot{\bar{\theta}}_2^2\mathbf{R}_{\bar{\theta}_2}\boldsymbol{e})\end{aligned} \tag{5.25b}$$

$$\dot{\omega}_1 = \ddot{w}_\theta + \ddot{\bar{\theta}}_1 \tag{5.25c}$$

$$\dot{\omega}_2 = \ddot{w}_\theta + \ddot{\bar{\theta}}_1 + \ddot{\bar{\theta}}_2\ . \tag{5.25d}$$

The total accelerations are of vital importance in the analysis and design of RISs.

The full set of equations of state is found by substituting Equations (5.24a)–(5.24c) into the fundamental form of Lagrange's equation (5.20) for each coordinate $z \in \mathcal{Z}$. It is straightforward to show, for this system, that $\partial \boldsymbol{v}_j/\partial z = \mathrm{d}(\partial \boldsymbol{v}_j/\partial \dot{z})/\mathrm{d}t$ for $j = 1, 2$. Thus, Equation (5.20) simplifies as follows:

$$m_1\left(\frac{\partial \boldsymbol{v}_1}{\partial \dot{z}}\right)^{\mathsf{T}}\boldsymbol{a}_{\mathrm{T}1} + I_1\frac{\partial \omega_1}{\partial \dot{z}}\dot{\omega}_1 + m_2\left(\frac{\partial \boldsymbol{v}_2}{\partial \dot{z}}\right)^{\mathsf{T}}\boldsymbol{a}_{\mathrm{T}2} + I_2\frac{\partial \omega_2}{\partial \dot{z}}\dot{\omega}_2 + \sum_{i=1}^{8}\mu_i g\frac{\partial h_i}{\partial z} = Q_z^{\mathrm{C}} + Q_z^{\mathrm{D}}\ . \tag{5.26}$$

The following subsections give a sketch of the derivation of the equations of state for the centroidal coordinates and the ball-bearing locations.

*The case of the first-subsystem coordinates*

For the first-subsystem's centroidal coordinates $z \in \{\bar{x}_1, \bar{y}_1, \bar{\theta}_1\}$, the details of the derivatives appearing in Equation (5.26) are given by

$$\partial \boldsymbol{v}_1/\partial \dot{\boldsymbol{d}}_{\mathrm{R}1} = \partial \boldsymbol{v}_2/\partial \dot{\boldsymbol{d}}_{\mathrm{R}1} = \mathbf{R}_{w_\theta}, \qquad \partial \boldsymbol{v}_1/\partial \dot{\bar{\theta}}_1 = [0\ \ 0]^{\mathsf{T}},\ \partial \boldsymbol{v}_2/\partial \dot{\bar{\theta}}_1 = \mathbf{R}_{w_\theta}\mathbf{R}_{\bar{\theta}_1}\mathbf{D}(\boldsymbol{d}_{\mathrm{R}2} + \mathbf{R}_{\bar{\theta}_2}\boldsymbol{e}),$$

$$\partial \omega_1/\partial \dot{\boldsymbol{d}}_{\mathrm{R}1} = \partial \omega_2/\partial \dot{\boldsymbol{d}}_{\mathrm{R}1} = [0\ \ 0], \quad \partial \omega_1/\partial \dot{\bar{\theta}}_1 = \partial \omega_2/\partial \dot{\bar{\theta}}_1 = 1.$$

The fifth term in Equation (5.26) involves the derivative of the corner heights of the form $\partial h_i/\partial z$. The first four heights ($i = 1, ..., 4$) depend the first-subsystems centroidal coordinates, but are independent of the second-subsystem's centroidal coordinates. Likewise, the

second four heights ($i = 5, ..., 8$) depend the second-subsystems centroidal coordinates, but are independent of the first-subsystem's centroidal coordinates. Thus, for $z \in \{\bar{x}_1, \bar{y}_1, \bar{\theta}_1\}$,

$$\frac{\partial h_i}{\partial z} = \begin{cases} \eta'(\|\mathbf{q}_i\|)\hat{\mathbf{q}}_i^{\mathsf{T}}(\partial \mathbf{q}_i/\partial z), & i = 1, ..., 4 \\ 0, & i = 5, ..., 8 \end{cases} \tag{5.27}$$

where

$$\partial \mathbf{q}_i/\partial \boldsymbol{d}_{\mathrm{R1}} = \mathbf{I}\,, \quad \partial \mathbf{q}_i/\partial \bar{\theta}_1 = \mathbf{R}_{\bar{\theta}_1}\mathbf{D}\boldsymbol{c}_i\,, \quad (i = 1, ..., 4).$$

As previously stated, $Q^{\mathrm{D}}_{\bar{x}_1}$, $Q^{\mathrm{D}}_{\bar{y}_1}$, and $Q^{\mathrm{D}}_{\bar{\theta}_1}$ are taken to be zero. All that is left is to determine $Q^{\mathrm{C}}_{\bar{x}_1}$, $Q^{\mathrm{C}}_{\bar{y}_1}$, and $Q^{\mathrm{C}}_{\bar{\theta}_1}$, which involve the derivative $\partial \mathbf{g}_i/\partial \dot{z}$:

$$\frac{\partial \mathbf{g}_i}{\partial \dot{z}} = \begin{cases} -(\frac{\partial \varphi_i}{\partial \mathbf{v}_i}\frac{\partial \mathbf{v}_i}{\partial \dot{z}})\mathbf{v}_i - \varphi_i \frac{\partial \mathbf{v}_i}{\partial \dot{z}}, & i = 1, ..., 4 \\ 0, & i = 5, ..., 8 \end{cases} \tag{5.28}$$

for which

$$\partial \mathbf{v}_i/\partial \dot{\boldsymbol{d}}_{\mathrm{R1}} = \mathbf{I}\,, \quad \partial \mathbf{v}_i/\partial \dot{\bar{\theta}}_1 = \mathbf{D}(\boldsymbol{c}_i + \mathbf{r}_i - \boldsymbol{d}_{\mathrm{R1}})\,, \quad (i = 1, ..., 4).$$

For $z \in \{\bar{x}_1, \bar{y}_1, \bar{\theta}_1\}$, the constraint forces are

$$Q^{\mathrm{C}}_z = \sum_{i=1}^{4} \Big[ -\Big(\frac{\partial \varphi_i}{\partial \mathbf{v}_i}\frac{\partial \mathbf{v}_i}{\partial \dot{z}}\Big)\mathbf{v}_i - \varphi_i \frac{\partial \mathbf{v}_i}{\partial \dot{z}}\Big]^{\mathsf{T}} \boldsymbol{\lambda}_i\,. \tag{5.29}$$

*The case of the second-subsystem coordinates*

For the second-subsystem's centroidal coordinates $z \in \{\bar{x}_2, \bar{y}_2, \bar{\theta}_2\}$, the details of the derivatives appearing in Equation (5.26) are given by

$$\partial \boldsymbol{v}_1/\partial \dot{\boldsymbol{d}}_{\mathrm{R2}} = \mathbf{0}_{2\times 2},\ \partial \boldsymbol{v}_2/\partial \dot{\boldsymbol{d}}_{\mathrm{R2}} = \mathbf{R}_{w_\theta}\mathbf{R}_{\bar{\theta}_1}, \quad \partial \boldsymbol{v}_1/\partial \dot{\bar{\theta}}_2 = [0\ \ 0]^{\mathsf{T}},\ \partial \boldsymbol{v}_2/\partial \dot{\bar{\theta}}_2 = \mathbf{R}_{w_\theta}\mathbf{R}_{\bar{\theta}_1}\mathbf{R}_{\bar{\theta}_2}\mathbf{D}\boldsymbol{e}$$

$$\partial \omega_1/\partial \dot{\boldsymbol{d}}_{\mathrm{R2}} = \partial \omega_2/\partial \dot{\boldsymbol{d}}_{\mathrm{R2}} = [0\ \ 0], \qquad \partial \omega_1/\partial \dot{\bar{\theta}}_2 = 0,\ \partial \omega_2/\partial \dot{\bar{\theta}}_2 = 1.$$

As previously mentioned, the bowl heights $h_i$ are dependent only on the subsystem coordinates. Thus, for $z \in \{\bar{x}_2, \bar{y}_2, \bar{\theta}_2\}$,

$$\frac{\partial h_i}{\partial z} = \begin{cases} 0, & i = 1, ..., 4 \\ \eta'(\|\mathbf{q}_i\|)\hat{\mathbf{q}}_i^{\mathsf{T}}(\partial \mathbf{q}_i/\partial z), & i = 5, ..., 8 \end{cases} \tag{5.30}$$

for which

$$\partial \mathbf{q}_i / \partial \boldsymbol{d}_{\mathrm{R}2} = \mathbf{I}\,, \quad \partial \mathbf{q}_i / \partial \bar{\theta}_2 = \mathbf{R}_{\bar{\theta}_2} \mathbf{D} \boldsymbol{c}_i, \quad (i = 5, ..., 8).$$

The non-potential forces $Q^{\mathrm{D}}_{\bar{x}_2}$, $Q^{\mathrm{D}}_{\bar{y}_2}$, and $Q^{\mathrm{D}}_{\bar{\theta}_2}$ are taken to be zero. Following a similar procedure as the first-subsystem dynamics, the constraint forces are

$$Q^{\mathrm{C}}_z = \sum_{i=5}^{8} \left[ -\left( \frac{\partial \varphi_i}{\partial \mathbf{v}_i} \frac{\partial \mathbf{v}_i}{\partial \dot{z}} \right) \mathbf{v}_i - \varphi_i \frac{\partial \mathbf{v}_i}{\partial \dot{z}} \right]^{\mathsf{T}} \boldsymbol{\lambda}_i \tag{5.31}$$

for $z \in \{\bar{x}_2, \bar{y}_2, \bar{\theta}_2\}$ where

$$\partial \mathbf{v}_i / \partial \dot{\boldsymbol{d}}_{\mathrm{R}2} = \mathbf{I}\,, \quad \partial \mathbf{v}_i / \partial \dot{\bar{\theta}}_2 = \mathbf{D}(\boldsymbol{c}_i + \mathbf{r}_i - \boldsymbol{d}_{\mathrm{R}2}), \quad (i = 5, ..., 8).$$

*The case of the generalized coordinates $r_{ix}$ and $r_{iy}$*

Referring to Equation (5.20), we notice that the kinetic energy of the system is independent of the ball-bearing coordinates $z \in \{r_{1x}, r_{1y}, ..., r_{8x}, r_{8y}\}$. Furthermore, the bowl-height gradients $\partial h_i / \partial \mathbf{r}_k$ $(k = 1, ..., 8)$ decouple because the $i$th height $h_i$ depends only on the $i$th ball-bearing displacement $\mathbf{r}_i$, i.e.

$$\frac{\partial V}{\partial \mathbf{r}_i} = \mu_i g \frac{\partial h_i}{\partial \mathbf{r}_i} = \mu_i g \left( \eta'(\|\mathbf{r}_i\|)\, \hat{\mathbf{r}}_i - \eta'(\|\mathbf{q}_i\|)\, \hat{\mathbf{q}}_i \right)^{\mathsf{T}}. \tag{5.32}$$

The gravitational restoring force is composed of two parts—a contribution from the lower-bowl and a contribution from the upper-bowl:

$$\mathbf{f}_{\mathcal{L}i} = \mu_i g \eta'(\|\mathbf{r}_i\|)\, \hat{\mathbf{r}}_i \quad \text{and} \quad \mathbf{f}_{\mathcal{U}i} = \mu_i g \eta'(\|\mathbf{q}_i\|)\, \hat{\mathbf{q}}_i\,. \tag{5.33}$$

By Equation (5.23), it follows that the constraint forces are $[Q^{\mathrm{C}}_{r_{ix}}\ Q^{\mathrm{C}}_{r_{iy}}]^{\mathsf{T}} = \boldsymbol{\lambda}_i$. Recall the damping forces are taken to be $Q^{\mathrm{D}}_{r_{ix}} = -C_{\mathrm{b}} \dot{r}_{ix}$ and $Q^{\mathrm{D}}_{r_{iy}} = -C_{\mathrm{b}} \dot{r}_{iy}$. By substituting these expressions into Equation (5.20), expressions for the multipliers are readily apparent:

$$\boldsymbol{\lambda}_i = C_{\mathrm{b}} \dot{\mathbf{r}}_i + \mathbf{f}_{\mathcal{L}i} - \mathbf{f}_{\mathcal{U}i}\,, \qquad (i = 1, ..., 8)\,. \tag{5.34}$$

We eliminate the multipliers $\boldsymbol{\lambda}_i$ by substituting them into Equations (5.29) and (5.31).

### 5.2.5 *System dynamics*

The centroidal equations of state are as follows:

$$\mathbf{R}_{w_\theta}^{\mathsf{T}}(m_1\boldsymbol{a}_{\mathrm{T}1} + m_2\boldsymbol{a}_{\mathrm{T}2}) + \sum_{i=1}^{4}\mathbf{f}_{\mathcal{U}i} = \sum_{i=1}^{4}(\partial\mathbf{g}_i/\partial\dot{\boldsymbol{d}}_{\mathrm{R}1})^{\mathsf{T}}\boldsymbol{\lambda}_i \tag{5.35a}$$

$$I_1\dot{\omega}_1 + m_2\boldsymbol{e}_{\mathrm{m}}^{\mathsf{T}}\mathbf{D}^{\mathsf{T}}\mathbf{R}_{\bar{\theta}_1}^{\mathsf{T}}\mathbf{R}_{w_\theta}^{\mathsf{T}}\boldsymbol{a}_{\mathrm{T}2} + I_2\dot{\omega}_2 + \sum_{i=1}^{4}\boldsymbol{c}_i^{\mathsf{T}}\mathbf{D}^{\mathsf{T}}\mathbf{R}_{\bar{\theta}_1}^{\mathsf{T}}\mathbf{f}_{\mathcal{U}i} = \sum_{i=1}^{4}(\partial\mathbf{g}_i/\partial\dot{\bar{\theta}}_1)^{\mathsf{T}}\boldsymbol{\lambda}_i \tag{5.35b}$$

$$m_2\mathbf{R}_{\bar{\theta}_1}^{\mathsf{T}}\mathbf{R}_{w_\theta}^{\mathsf{T}}\boldsymbol{a}_{\mathrm{T}2} + \sum_{i=5}^{8}\mathbf{f}_{\mathcal{U}i} = \sum_{i=5}^{8}(\partial\mathbf{g}_i/\partial\dot{\boldsymbol{d}}_{\mathrm{R}2})^{\mathsf{T}}\boldsymbol{\lambda}_i \tag{5.35c}$$

$$m_2\boldsymbol{e}^{\mathsf{T}}\mathbf{D}^{\mathsf{T}}\mathbf{R}_{\bar{\theta}_2}^{\mathsf{T}}\mathbf{R}_{\bar{\theta}_1}^{\mathsf{T}}\mathbf{R}_{w_\theta}^{\mathsf{T}}\boldsymbol{a}_{\mathrm{T}2} + I_2\dot{\omega}_2 + \sum_{i=5}^{8}\boldsymbol{c}_i^{\mathsf{T}}\mathbf{D}^{\mathsf{T}}\mathbf{R}_{\bar{\theta}_2}^{\mathsf{T}}\mathbf{f}_{\mathcal{U}i} = \sum_{i=5}^{8}(\partial\mathbf{g}_i/\partial\dot{\bar{\theta}}_2)^{\mathsf{T}}\boldsymbol{\lambda}_i \tag{5.35d}$$

where $\boldsymbol{a}_{\mathrm{T}1}$, $\boldsymbol{a}_{\mathrm{T}2}$, $\dot{\omega}_1$, and $\dot{\omega}_2$ are given by Equations (5.25), the Lagrange multipliers $\boldsymbol{\lambda}_i$ are given by Equation (5.34), and $\boldsymbol{e}_{\mathrm{m}} = \boldsymbol{d}_{\mathrm{R}2} + \mathbf{R}_{\bar{\theta}_2}\boldsymbol{e}$ is the $X_{\mathrm{m}}$-$Y_{\mathrm{m}}$ coordinates of the center of mass. Equations (5.35) are nonlinear, coupled, second-order ordinary differential equations, and they must be solved simultaneously with the ball-bearing kinematics (5.18). Investigating Equations (5.35) further, we see that Equations (5.35a) represent a force balance in the $X_{\mathrm{b}}$-$Y_{\mathrm{b}}$ coordinates, Equation (5.35b) is the moment balance about the centroid of $m_1$, Equation (5.35c) represent a force balance in the $X_{\mathrm{m}}$-$Y_{\mathrm{m}}$ coordinates, and Equation (5.35d) is the moment balance about the centroid of $m_2$.

## 5.3 Numerical Simulations

In this section, two series of numerical simulations are reported. In the first, we simulate the unforced response of the stacked platform and analyze the energy content of the system. Different values of the viscous damping coefficient $C_{\mathrm{b}}$ are considered: undamped ($C_{\mathrm{b}} = 0$) and damped ($C_{\mathrm{b}} > 0$). In the second, we consider the forced response under pulse-like base accelerations. Preliminary tests are performed to investigate the isolation capabilities of the system.

In both cases we set $m_1 = 70$ kg, $m_2 = 435$ kg, $I_1 = 23.0$ kg m$^2$, and $I_2 = 38.4$ kg m$^2$.

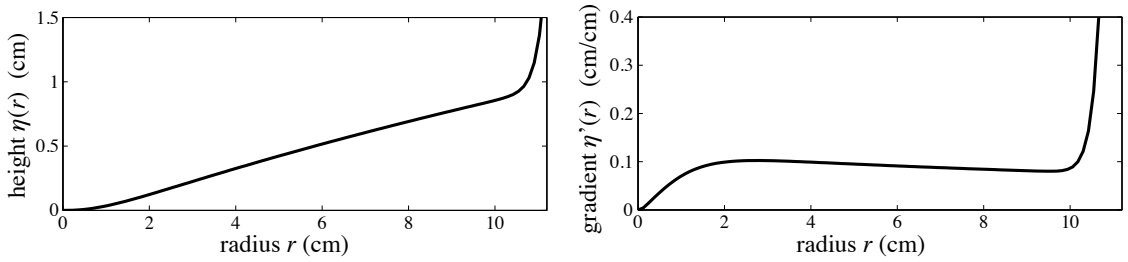


FIGURE 5.4: Bowl-shape height $\eta(r)$ and gradient $\eta'(r)$ used in the numerical simulations.

The geometric properties of the frames are as follows: $a = b = 0.45$ m and $e_x = e_y = 0$ m. As found in Section 3.5, the viscous damping rate $C_\mathrm{b}$ may be determined experimentally for different values of mass. However, only a single isolation system is modeled in Section 3.5. Here we assume that $C_\mathrm{b}$ is the same for the two subsystems and taken to be 56.0 N s/m, even though it would be slightly higher for the first-subsystem due to larger contact forces.

The experimentally-fitted bowl-shape function, as found in Section 3.4, is

$$\eta(r) = \beta_1\beta_2 \ln\left[\cosh(r/\beta_2)\right]/10 + \beta_3(r/10)^{\beta_4} + \beta_5(r/10)^{\beta_6}, \qquad (r \text{ in cm}) \,. \tag{5.36}$$

Table 3.1 gives the fitted model coefficients. The bowl shape function is shown in Figure 5.4 along with the gradient $\eta'(r)$ appearing in the system dynamics (5.24c). The profiles is roughly conical in the range $2 < r < 10$ cm and has a lip (with highly-positive curvature) where $r \approx 10$ cm. The potential restoring forces, which are roughly proportional to the bowl gradient, are nearly constant at small radii ($r < 10$ cm), but the bowl extreme ($r > 10$ cm) serves as a hard displacement limit. Collisions with the lip produce high accelerations that may be detrimental to isolated objects.

### *5.3.1 Unforced response*

We set the base excitations to be zero, $w_x(t) = w_y(t) = w_\theta(t) = 0, \ \forall t$, and start the system from a non-zero initial condition. The initial centroidal conditions are taken to be zero except for $\bar{x}_1(0) = \bar{x}_2(0) = 19$ cm, and the system is assumed to start from rest (zero velocity). The ball-bearings are assumed to start on the centerline connecting the lower- and

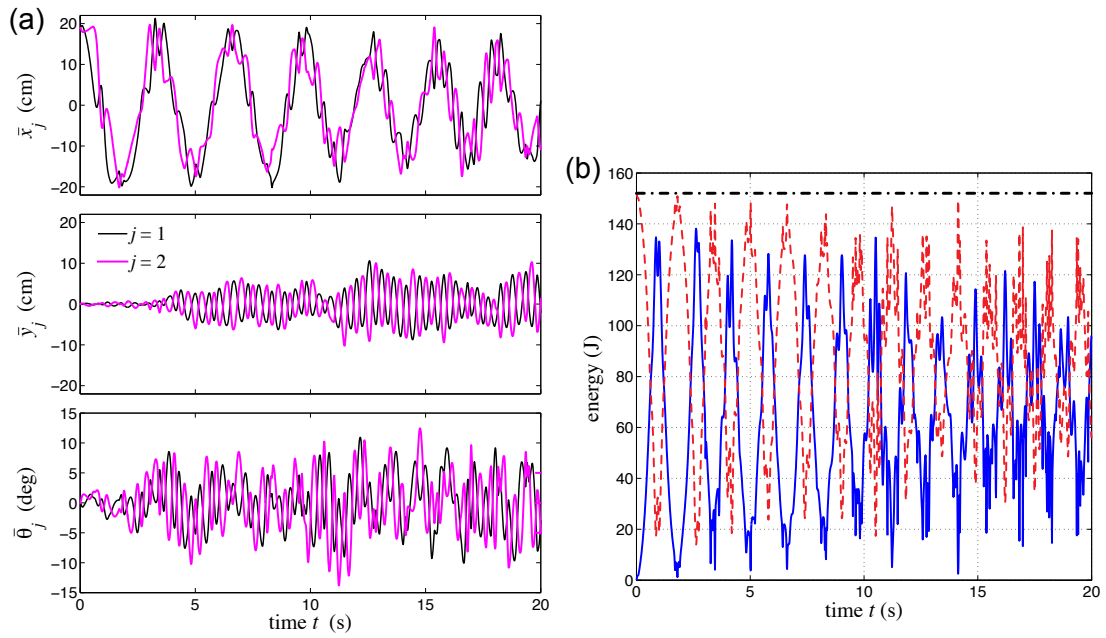


FIGURE 5.5: Unforced response of an undamped system. (a) Centroidal displacements: first-subsystem, $j = 1$ (——); second-subsystem, $j = 2$ (——). (b) Energy histories: kinetic energy $T$ (——), potential energy $V$ (– – –), and total energy $E$ (–·–).

upper-bowl centers, viz. $\mathbf{r}_i(0) = [0.095\text{ cm} + \varepsilon_{ix} \;\; \varepsilon_{iy}]^\mathsf{T}$, where small perturbations ($\varepsilon_{ix}$ and $\varepsilon_{iy} \approx 0.1$ cm) account for the inability to perfectly center the ball-bearings experimentally.

The total energy of the system ($E = T + V$) is

$$E(t) = \tfrac{1}{2}m_1\boldsymbol{v}_1^\mathsf{T}\boldsymbol{v}_1 + \tfrac{1}{2}I_1\omega_1^2 + \tfrac{1}{2}m_2\boldsymbol{v}_2^\mathsf{T}\boldsymbol{v}_2 + \tfrac{1}{2}I_2\omega_2^2 + \sum_{i=1}^{8}\mu_i g h_i(\bar{x}_j, \bar{y}_j, \bar{\theta}_j, \mathbf{r}_i)\,, \tag{5.37}$$

which should be conserved in an undamped system [38]. Two simulations are performed with different values of $C_\mathrm{b}$, representing an undamped system and a damped system.

*Undamped simulation*

First, we consider the undamped system with $C_\mathrm{b} = 0$. These simulations are not physical insofar as the damping in the system is generated by the rolling-friction of the ball-bearings and is governed by the compressive forces at the ball-bearings; no other forms of energy dissipation are treated. However, the following simulations serve as a test to confirm that the model is conservative in the absence of viscous damping, and to gain some insight into

the response of the system.

The centroidal displacement trajectories are given in Figure 5.5(a). Two predominant response frequencies are seen in the $\bar{x}_j$ history: a long-period motion (~3 s) and a short-period oscillation (~0.5 s). The former mode coincides with masses $m_1$ and $m_2$ moving in phase, whereas the latter mode corresponds to the two masses moving out-of-phase. The initial conditions used are such that the system undergoes larger displacements in the $\bar{x}_j$ direction, as compared to the $\bar{y}_j$ direction. However, due to the nonlinear coupling of the degrees of freedom, after very few oscillations, significant short-period displacements are seen in the $\bar{y}_j$ direction (~5–10 cm). Masses $m_1$ and $m_2$ experience high-frequency oscillations (~0.5 s) in the $\bar{y}_j$ direction, which are out of phase. This may be attributable to the range of the $\bar{y}_j$ direction displacements; for small oscillations (< 8 cm) the ball-bearings remain in the positive-curvature region of the bowls where higher resistive forces are produced. The rotational histories $\bar{\theta}_j(t)$ also have primarily short-period (0.5 s) responses, as is common in higher-mode responses, e.g. torsional modes.

Figure 5.5(b) shows the energy histories for the undamped free vibration. The kinetic and potential energies fluctuate with time, while the total energy $E$ is conserved as would be expected. This figure serves as a check of the numerical model—energy is conserved in the undamped case because the constraints (5.18) are conservative [38].

*Damped simulation*

We now fix $C_\mathrm{b} = 56$ N s/m and run an unforced response starting from the same initial conditions as in the previous section. The results are shown in Figure 5.6. Once again, the nonlinear coupling between translational and rotational degrees of freedom induces transverse displacements after few oscillations. This numerical test reveals that the high-frequency oscillations are suppressed in the damped case. However, some of the out-of-phase, high-frequency vibrations are still visible, especially in the small displacement range of the $\bar{y}_j(t)$ history. After the transient response decays (~12–15 s), only the low-

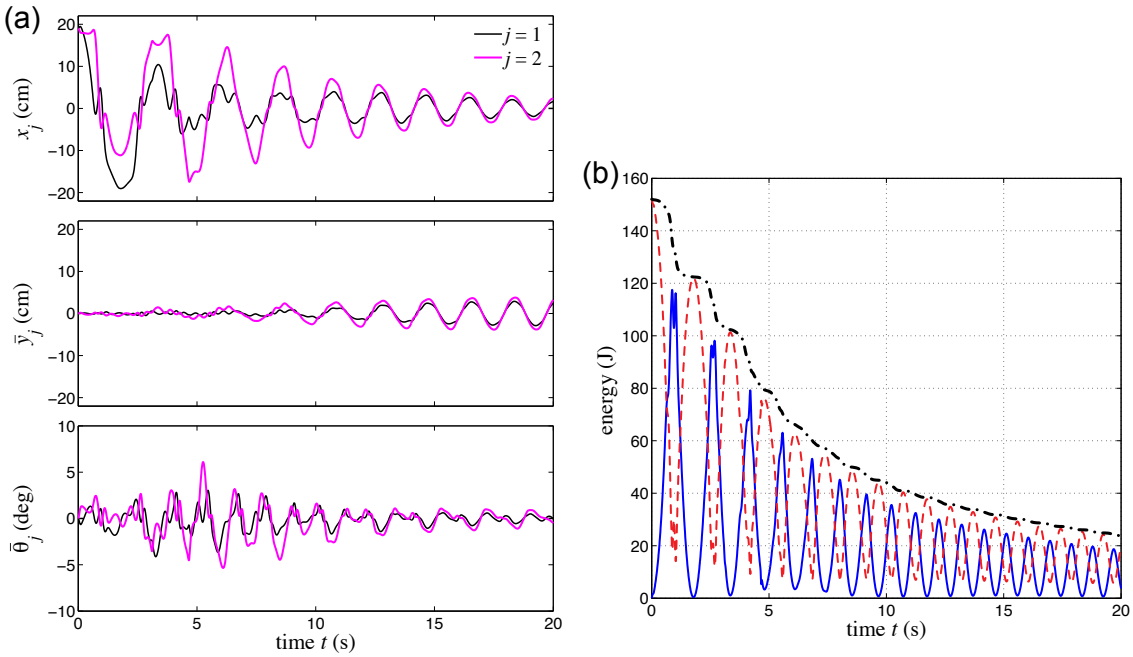


FIGURE 5.6: Unforced response of a damped system. (a) Centroidal displacements: first-subsystem, $j = 1$ (——); second-subsystem, $j = 2$ (——). (b) Energy histories: kinetic energy $T$ (——), potential energy $V$ (– – –), and total energy $E$ (–·–).

frequency oscillation remains and is nearly periodic.

Through the introduction of damping, the total energy of the system is no longer conserved. See Figure 5.6(b). Because energy is not injected by any means in the free response, the total energy decays monotonically with time. The kinetic and potential energies are oscillatory. If the simulation is allowed to run long enough, the system comes to rest at a non-zero displaced condition. This phenomenon appears because the ball-bearings are allowed to move off the center-lines, and hence, the ball-bearings impart forces that self-equilibrate the middle- and top-frames in a displaced configuration.

### *5.3.2 Forced response*

In this subsection we assume pulse-like disturbances [39], which are parameterized by the pulse period $T_{\mathrm{p}}$ and peak velocity $V_{\mathrm{p}}$ in each direction, i.e. $x$, $y$, and $\theta$. We fix the pulse periods to be $T_{\mathrm{p}x} = T_{\mathrm{p}y} = 1.2$ s and $T_{\mathrm{p}\theta} = 0.6$ s, and investigate two levels of peak velocity: *moderate* and *strong*. The moderate disturbance acceleration records are shown in

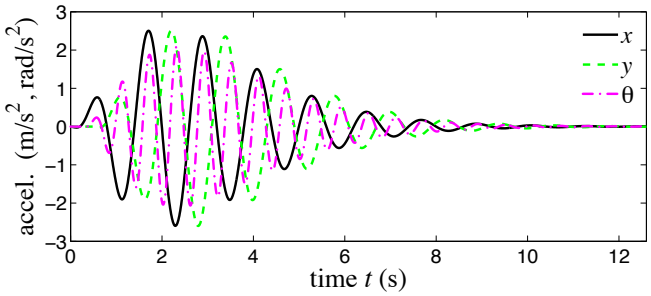


FIGURE 5.7: Moderate pulse-like disturbances $w_x(t)$, $w_y(t)$, and $w_\theta(t)$ used in the forced response.

Figure 5.7. These disturbances are representative of an earthquake filtered through a structure, and are fundamentally similar to the floor responses this system would experience within a building.

In these tests we vary the values of the pulse strength to see its effect on the dynamics. In particular, we analyze the influence of the pulse parameter $V_{\mathrm{p}}$, focusing on the impact phenomenon. For later use, we also define the relative radial displacement of the $j$th frame centroid to be

$$d_{\mathrm{R}j}(t) = \sqrt{\bar{x}_j^2(t) + \bar{y}_j^2(t)}$$

and the total acceleration of the $j$th frame centroid to be

$$a_{\mathrm{T}j}(t) = \|\ddot{\boldsymbol{a}}_{\mathrm{T}j}(t)\|.$$

*Moderate disturbance*

First, we analyze the response to a moderate disturbance for which we fix $V_{\mathrm{p}x} = V_{\mathrm{p}y} = 0.5$ m/s and $V_{\mathrm{p}\theta} = 0.2$ rad/s. Figure 5.8 shows the displacement and total acceleration responses for the moderate disturbance. From the relative centroidal displacement histories $d_{\mathrm{R}j}(t)$, we see at $t = 2$ s mass $m_2$ ($j = 2$) experiences a hard displacement limit. When $d_{\mathrm{R}j} > 20$ cm, the ball-bearings in the $j$th subsystem collide with the bowl lip (i.e. $r \simeq \|\mathbf{q}_j\| \simeq \|\mathbf{r}_j\| \simeq 10$ cm), and induce large restoring forces, countering further displacement in that direction. Hence, a plateau is seen in the displacement trajectory at the instance of the collision. Note that only the second-subsystem collides; the first-subsystem

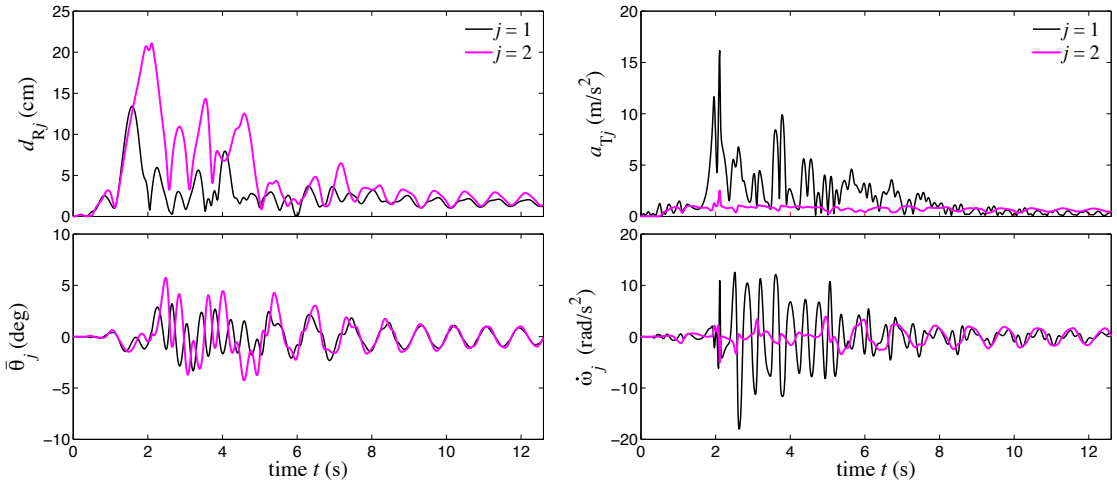


FIGURE 5.8: Moderate disturbance. Numerically simulated forced response histories: first-subsystem, $j = 1$ (—); second-subsystem, $j = 2$ (—).

has a maximum radial displacement of 13.4 cm, well below the collision threshold.

In the aseismic design of an equipment isolation system, peak accelerations are of paramount concern. As seen in Figure 5.8, mass $m_2$ experiences larger total accelerations (~5-15 m/s$^2$) than mass $m_2$ throughout the response. However, mass $m_1$ is not acceleration sensitive, being simply a frame, and large accelerations are not a concern. Conversely, mass $m_2$ represents the payload to be isolated, and its total acceleration needs to be closely monitored. Due to the large reaction forces at impact ($t = 2$ s), an impulsive response is seen in the total acceleration response $a_{T2}(t)$ with a peak value of 2.52 m/s$^2$. When a collision occurs in the second-subsystem, the top-frame and middle-frame act as if rigidly connected, moving as one, and the inertial forces acting on mass $m_2$ are transmitted to mass $m_1$. Because the first-subsystem possesses additional displacement capacity at $t = 2$ s, i.e. $d_{R1} < 20$ cm, mass $m_2$ is free to continue to globally displace. If both subsystems were to collide simultaneously, mass $m_2$ would reach an absolute displacement boundary, and we would expect to see much larger total accelerations.

After the main disturbance has passed ($t > 6$ s), the displacements and rotations decay to a periodic oscillation, as in the unforced response case. Similar to the total translational

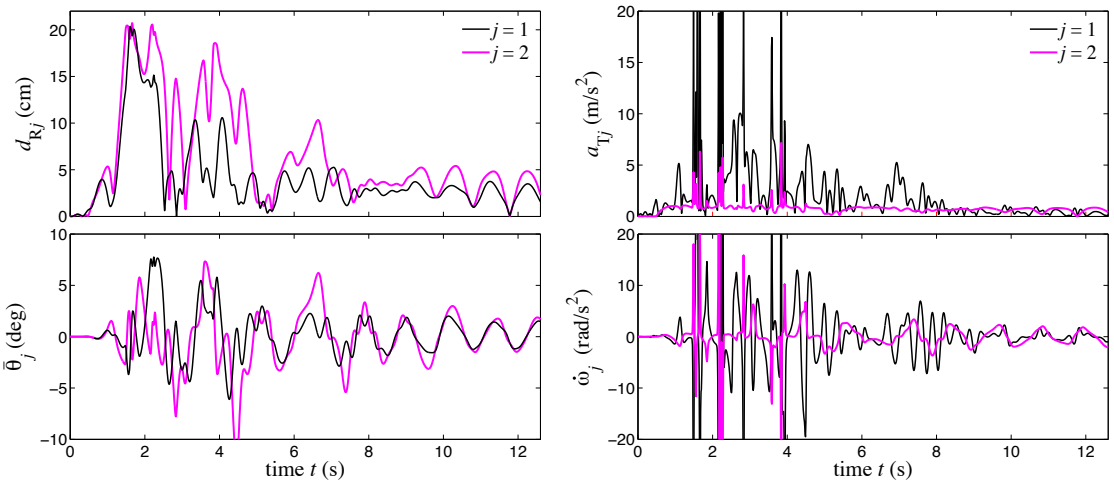


FIGURE 5.9: Strong disturbance. Numerically simulated forced response histories: first-subsystem, $j = 1$ (—); second-subsystem, $j = 2$ (—).

acceleration response, the total azimuthal response $\dot{w}_j(t)$ experiences a spike at the time of collision. This may be due to not all the ball-bearings colliding simultaneously, causing a whipping action in which the frame pivots about one of the constrained ball-bearings. Once again, the first-subsystem undergoes larger total rotational accelerations than the second-subsystem.

*Strong disturbance*

In the next simulations we test the system subject to a strong disturbance—50% stronger than the moderate case: $V_{px} = V_{py} = 0.75$ m/s and $V_{p\theta} = 0.3$ rad/s. Figure 5.9 represents the motions in the case of a strong disturbance. Immediately we see the displacements and rotations are higher than for the moderate disturbance. Furthermore, the two subsystems spend more time in a collided or nearly collided state. Correspondingly, larger total accelerations are seen in both subsystems, e.g. the first-subsystem's total accelerations are ~10-42 m/s$^2$. Three major peaks in $a_{T2}(t)$ are seen, with a maximum value of 7.16 m/s$^2$, nearly three times as large as the moderate case. The first peak at $t = 1.5$ s corresponds to a collision in which the two subsystems collide simultaneously.

## 5.4 Summary

In the protection of vibration-sensitive equipment from harsh floor motions, the displacement capacity of an isolation system must be sufficient to assure that impacts are not realized. Toward this end, this chapter proposed and investigated a double RIS affected by nonholonomic constraints and geometric nonlinearity. This chapter highlights the development of a twenty-two degree-of-freedom nonlinear model, which possesses hard displacement limits and experiences coupling between translational and rotation oscillations. Furthermore, both the experimentally-fitted bowl profile and rolling-ball dynamics have been shown to play a key role in the system response.

Numerical simulations are performed to gain insight into the main dynamical phenomena. It is shown that the system is conservative in the unforced response when the damping rate is zero. When the damping rate is non-zero, energy is no longer conserved and the higher modes are suppressed. In both cases, rotations and translations are coupled, and after a few oscillations, transverse displacements and significant rotations develop.

Next, forced response simulations are carried out to investigate the influence of impacts on the system's behavior. In the case of a pulse-like disturbance, the system dynamics are investigated for varying disturbance strengths by varying the pulse velocity. When the ball-bearings collide with the bowl lips, the total acceleration of the isolated mass increase sharply at the time of impact. So long as only the first- or second-subsystem collides, the accelerations remain within an acceptable range. Whereas, when the disturbance was strong enough to produce simultaneous impacts in both subsystems, significantly (approximately 3 times) higher accelerations were seen.

The proposed stacked system possesses double the displacement capacity of its constituent subsystems alone. Thus, potentially-damaging impacts may be avoided, decreasing the occurrence of equipment failures and the related costs. In the next chapter, we will simplify the full model presented here and experimentally validate the double RIS model.

# 6

# Vibration Suppression Using Double Rolling Isolation Systems: Experimental Validation

## 6.1 Background

In Chapter 4, an experimental and numerical assessment of the single, undamped rolling isolation system (RIS) showed the displacement capacity was deficient under various loading regimes [52]. The following two strategies were proposed to prevent impacts and improve isolation performance: (a) Decrease the displacement demands on the isolator by introducing additional energy dissipation—passive [65, 95], semi-active [39, 96] or active [97]. (b) Increase the isolator's displacement capacity. The latter was addressed in Chapter 5. We proposed stacking two isolation platforms, one on top of the other, to effectively double the displacement capacity [53]. This chapter serves as an extension of Chapter 5, which primarily focused on modeling and evaluating a high-fidelity model of the double vibration isolation system. In this chapter, we propose and experimentally validate a simplified model of the stacked system, which retains the complex nonlinear nature of the system. A simplification procedure, similar to the one used for the single RIS (Chapter 4), is followed.

## 6.2 Simplified Model of a Double Rolling Isolation System

The double RIS investigated in this chapter is depicted in Figure 5.1. It consists of eight large ball-bearings, and sixteen shallow radially-symmetric steel bowls fixed to three frames (bottom, middle, and top). The bottom-frame rests on the floor and holds four concave-up bowls. The middle-frame holds eight bowls—four concave-up and four concave-down. The top-frame holds four concave-down bowls. A ball-bearing rolls between each pair of bowls in the bottom- and middle-frames and the middle- and top-frames. Large amplitude (translational and rotational) motions, non-quadratic bowl profiles, and the kinematics of spheres rolling between non-parallel surfaces give rise to complex, nonlinear behavior. Further, under large displacements the ball-bearings may collide with the bowl lip, imparting impactive loads [91, 92], which may be detrimental to the performance of the system.

### *6.2.1 Geometry and notation*

The displaced configuration of a double RIS is illustrated in Figure 5.2. The bottom-frame has the $X_{\mathrm{b}}$-$Y_{\mathrm{b}}$ coordinate system (- - -), the middle-frame has the $X_{\mathrm{m}}$-$Y_{\mathrm{m}}$ coordinate system (-·-), and the top-frame has the $X_{\mathrm{t}}$-$Y_{\mathrm{t}}$ coordinate system (—). The bottom-frame is excited by translational disturbance $\boldsymbol{w}(t) = [w_x(t)\ w_y(t)]^{\mathsf{T}}$ that has $X_{\mathrm{g}}$ and $Y_{\mathrm{g}}$ translational components. In the applications for which RISs are used, significant base rotations are not typically observed. Therefore, rotational base-excitation $w_\theta(t)$ is neglected in the simplified model. The total mass of the middle-frame $m_1$ is concentrically located about the frame's centroid, which undergoes rotation $\bar{\theta}_1(t)$ and translational displacement $\boldsymbol{d}_{\mathrm{R1}}(t) = [\bar{x}_1(t)\ \bar{y}_1(t)]^{\mathsf{T}}$, relative to the bottom-frame. Vibration-sensitive equipment is rigidly connected to the top-frame, and the total mass of the equipment and top-frame is $m_2$, which is assumed to be concentrically located. The top-frame undergoes rotations $\bar{\theta}_2(t)$ and translational displacement $\boldsymbol{d}_{\mathrm{R2}}(t) = [\bar{x}_2(t)\ \bar{y}_2(t)]^{\mathsf{T}}$, relative to the middle-frame.

Masses $m_1$ and $m_2$ have mass moments of inertia $I_1$ and $I_2$, respectively.

The top-frame and equipment are mechanically isolated from the bottom-frame via the rolling of large, steel ball-bearings between concave-up lower-bowls and concave-down upper-bowls at the four corners (Figure 5.1). The bowls and ball-bearings are numbered $i = 1, ..., 8$, as shown in Figure 5.2, with the coordinates of the bowl centers given by $\boldsymbol{c}_i = [a_i \; b_i]^\mathsf{T}$ where

$$\boldsymbol{a} = [a \;\; -a \;\; -a \;\; a \;\;\; a \;\; -a \;\; -a \;\; a]^\mathsf{T} \quad \text{and} \quad \boldsymbol{b} = [b \;\; b \;\; -b \;\; -b \;\;\; b \;\; b \;\; -b \;\; -b]^\mathsf{T} . \tag{6.1}$$

As seen in Figure 5.3, the ball-bearing locations with respect to the centers of the lower- and upper-bowls are, respectively, $\mathbf{r}_i(t) = [r_{ix}(t) \; r_{iy}(t)]^\mathsf{T}$ and $\mathbf{q}_i(t) = [q_{ix}(t) \; q_{iy}(t)]^\mathsf{T}$ where

$$\mathbf{q}_i \equiv \mathbf{q}_i(\bar{x}_j, \bar{y}_j, \bar{\theta}_j, \mathbf{r}_i) = \boldsymbol{d}_{\mathrm{R}j}(t) + (\mathbf{R}_{\bar{\theta}_j(t)} - \mathbf{I})\boldsymbol{c}_i - \mathbf{r}_i(t) \tag{6.2}$$

where $\mathbf{R}_{\bar{\theta}_j(t)} = \mathbf{R}(\bar{\theta}_j(t))$ is the rotation matrix, $\mathbf{I}$ is identity, and the map

$$j \equiv j(i) = \begin{cases} 1, & i = 1, ..., 4 \\ 2, & i = 5, ..., 8 \end{cases} \tag{6.3}$$

relates the ball-bearing index $i$ to the appropriate subsystem $j \in \{1, 2\}$; .

The gravitational restoring forces in the system are attributed to the changes in heights at the corners, which depend on the frame configurations $(\bar{x}_1, \bar{y}_1, \bar{\theta}_1, \bar{x}_2, \bar{y}_2, \bar{\theta}_2)$ and the ball-bearing locations $\mathbf{r}_i$. The height at the center of the $i$th bowl is the sum of the contribution from the lower- and upper-bowls, viz.

$$h_i(\bar{x}_j, \bar{y}_j, \bar{\theta}_j, \mathbf{r}_i) = \eta(\|\mathbf{r}_i\|) + \eta(\|\mathbf{q}_i\|) \tag{6.4}$$

where we assume all the bowls are axisymmetric with radius-dependent bowl-shape function $\eta(r)$. The gravitational restoring forces arising from the bowl gradient $\eta'(r) = \mathrm{d}\eta(r)/\mathrm{d}r$ are [38]

$$\mathbf{f}_{\mathcal{L}i} = \mu_i g \eta'(\|\mathbf{r}_i\|)\hat{\mathbf{r}}_i \quad \text{and} \quad \mathbf{f}_{\mathcal{U}i} = \mu_i g \eta'(\|\mathbf{q}_i\|)\hat{\mathbf{q}}_i \; . \tag{6.5}$$

For zero mass eccentricity, the allocated mass at each corner $\mu_i$, given by Equation (5.14), simplifies to

$$\mu_i = \begin{cases} (m_1 + m_2)/4, & i = 1, ..., 4 \\ m_2/4, & i = 5, ..., 8 \end{cases}. \tag{6.6}$$

The forces $\mathbf{f}_{\mathcal{L}i}$ and $\mathbf{f}_{\mathcal{U}i}$ act in the direction of the normalized vectors $\hat{\mathbf{r}}_i = \mathbf{r}_i/\|\mathbf{r}_i\|$ and $\hat{\mathbf{q}}_i = \mathbf{q}_i/\|\mathbf{q}_i\|$, respectively.

### *6.2.2 Kinematics of rolling ball-bearings*

The ball-bearing coordinates $\mathbf{r}_i(t)$ evolve according to a set of nonholonomic constraints prescribed by the condition of rolling without slipping between non-parallel surfaces, which for shallow bowls (Section 4.2.2) can be approximated as follows [52]:

$$\dot{\mathbf{r}}_i(t) = \tfrac{1}{2}\{\dot{\boldsymbol{d}}_{\mathrm{R}j}(t) + \dot{\bar{\theta}}_j(t)\mathbf{D}\left(\boldsymbol{c}_i + \mathbf{r}_i(t) - \boldsymbol{d}_{\mathrm{R}j}(t)\right)\}, \quad (i = 1, ..., 8) \tag{6.7}$$

where the term in braces is equivalent to $\mathbf{v}_i$, the relative velocity of the upper-bowls at the ball-bearing locations, and

$$\mathbf{D} = \begin{bmatrix} 0 & -1 \\ 1 & 0 \end{bmatrix}.$$

The sixteen nonlinear first-order ordinary differential equations (6.7) prescribe the evolution of the first-subsystem's four ball-bearings ($i = 1, ..., 4$) in the $X_\mathrm{b}$-$Y_\mathrm{b}$ plane and the second-subsystem's four ball-bearings ($i = 5, ..., 8$) in the $X_\mathrm{m}$-$Y_\mathrm{m}$ plane. Initial conditions $\mathbf{r}_{i0} = \mathbf{r}_i(0)$ must be specified. However, in practice one cannot ensure that the ball-bearings are perfectly centered in the lower- and upper-bowls at the beginning of the test. To account for the uncertainty in the initial ball-bearing locations in the numerical simulations, the initial ball-bearing locations $\mathbf{r}_{i0}$ are taken to be

$$\mathbf{r}_{i0} = [\rho_i \cos\psi_i \;\; \rho_i \sin\psi_i]^\mathsf{T}, \quad \rho_i \overset{\text{iid}}{\sim} U(0, 1) \text{ cm}, \quad \psi_i \overset{\text{iid}}{\sim} U(0, 2\pi). \tag{6.8}$$

### 6.2.3 *Equations of motion*

In the absence of mass eccentricity ($\boldsymbol{e} \equiv \mathbf{0}$) and rotational disturbance ($w_\theta(t) \equiv 0$), the total accelerations of centers of masses $m_1$ and $m_2$ (Equation (5.25)) are, respectively,

$$\boldsymbol{a}_{\mathrm{T}1} = \ddot{\boldsymbol{w}} + \ddot{\boldsymbol{d}}_{\mathrm{R}1} \tag{6.9a}$$

$$\boldsymbol{a}_{\mathrm{T}2} = \ddot{\boldsymbol{w}} + \ddot{\boldsymbol{d}}_{\mathrm{R}1} + \ddot{\bar{\theta}}_1 \mathbf{R}_{\bar{\theta}_1} \mathbf{D} \boldsymbol{d}_{\mathrm{R}2} - \dot{\bar{\theta}}_1^2 \mathbf{R}_{\bar{\theta}_1} \boldsymbol{d}_{\mathrm{R}2} + 2\dot{\bar{\theta}}_1 \mathbf{R}_{\bar{\theta}_1} \mathbf{D} \dot{\boldsymbol{d}}_{\mathrm{R}2} + \mathbf{R}_{\bar{\theta}_1} \ddot{\boldsymbol{d}}_{\mathrm{R}2} \,. \tag{6.9b}$$

Applying the fundamental nonholonomic form of Lagrange's equation, the equations of motion of the centroidal coordinates, taking into account the constraints (6.7), are as follows [53]:

$$m_1 \boldsymbol{a}_{\mathrm{T}1} + m_2 \boldsymbol{a}_{\mathrm{T}2} + \sum_{i=1}^{4} \mathbf{f}_{\mathcal{U}i} + \tfrac{1}{2} \sum_{i=1}^{4} (C_{\mathrm{b}} \dot{\mathbf{r}}_i + \mathbf{f}_{\mathcal{L}i} - \mathbf{f}_{\mathcal{U}i}) = \mathbf{0} \tag{6.10a}$$

$$\begin{aligned} I_1 \ddot{\bar{\theta}}_1 + m_2 \boldsymbol{d}_{\mathrm{D}2}^{\mathsf{T}} \mathbf{D}^{\mathsf{T}} \mathbf{R}_{\bar{\theta}_1}^{\mathsf{T}} \boldsymbol{a}_{\mathrm{T}2} + I_2 (\ddot{\bar{\theta}}_1 + \ddot{\bar{\theta}}_2) + \sum_{i=1}^{4} \mathbf{f}_{\mathcal{U}i}^{\mathsf{T}} \mathbf{R}_{\bar{\theta}_1} \mathbf{D} \boldsymbol{c}_i \\ + \tfrac{1}{2} \sum_{i=1}^{4} (C_{\mathrm{b}} \dot{\mathbf{r}}_i + \mathbf{f}_{\mathcal{L}i} - \mathbf{f}_{\mathcal{U}i})^{\mathsf{T}} \mathbf{D} (\boldsymbol{c}_i + \mathbf{r}_i - \boldsymbol{d}_{\mathrm{R}1}) = 0 \end{aligned} \tag{6.10b}$$

$$m_2 \mathbf{R}_{\bar{\theta}_1}^{\mathsf{T}} \boldsymbol{a}_{\mathrm{T}2} + \sum_{i=5}^{8} \mathbf{f}_{\mathcal{U}i} + \tfrac{1}{2} \sum_{i=5}^{8} (C_{\mathrm{b}} \dot{\mathbf{r}}_i + \mathbf{f}_{\mathcal{L}i} - \mathbf{f}_{\mathcal{U}i}) = \mathbf{0} \tag{6.10c}$$

$$I_2 (\ddot{\bar{\theta}}_1 + \ddot{\bar{\theta}}_2) + \sum_{i=5}^{8} \mathbf{f}_{\mathcal{U}i}^{T} \mathbf{R}_{\bar{\theta}_2} \mathbf{D} \boldsymbol{c}_i + \tfrac{1}{2} \sum_{i=5}^{8} (C_{\mathrm{b}} \dot{\mathbf{r}}_i + \mathbf{f}_{\mathcal{L}i} - \mathbf{f}_{\mathcal{U}i})^{T} \mathbf{D} (\boldsymbol{c}_i + \mathbf{r}_i - \boldsymbol{d}_{\mathrm{R}2}) = 0. \tag{6.10d}$$

The full set of system dynamics comprises Equations (6.7) and (6.10), which must be integrated simultaneously.

Damping in the system is assumed to be linearly proportional to the ball-bearing velocities and the damping forces act at the ball-bearing locations (Section 3.5). The mass-dependent damping rate $C_{\mathrm{b}}(m)$ is taken to be equal in the first- and second-subsystems [38]:

$$C_{\mathrm{b}}(m) = 0.000229\, m^2 + 0.02884\, m \tag{6.11}$$

where $m = m_1 + m_2$ has units of kg and $C_{\mathrm{b}}$ has units of N s/m.

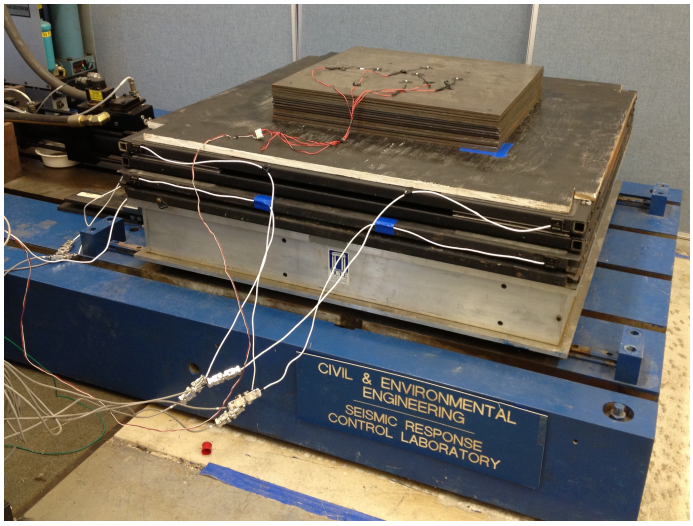


FIGURE 6.1: Experimental shaking table with a double rolling isolation system.

The gravitational restoring forces $\mathbf{f}_{\mathcal{L}i}$ and $\mathbf{f}_{\mathcal{U}i}$ depend explicitly on the bowl-shape gradient $\eta'(r)$. In Chapter 4, we experimentally characterized the the bowl-shape function in its installed and loaded configuration for the single RIS by analyzing the acceleration-displacement relationship in controlled free-response experiments. The following polynomial function was fit to experimental data [52]:

$$\eta'(r) = \sum_{i=1}^{6} \alpha_i (r/R)^i + \alpha_{50} (r/R)^{50} \tag{6.12}$$

where $R = 10$ cm and the fit parameters are given in Table 4.1. The bowl-shape function $\eta(r)$ and gradient $\eta'(r)$ are shown in Figure 4.5.

## 6.3 Experimental Set-up

In order to validate the simplified model described above and to assess the performance of the double isolation system, experiments were conducted in which the system was excited uni-axially, and various response quantities were measured. The experiments were performed in conjunction with those of Chapter 4, in which a single rolling platform was modeled and tested. A more detailed description of the experimental setup may be found therein. A brief description of the experimental double RIS follows.

The double RIS in this study, shown in Figure 6.1, has dimensions $a = 44.5$ cm and $b = 47$ cm. The middle-frame mass is 76.5 kg with moment of inertia 26.85 kg m$^2$, and the top-frame mass is 37.5 kg with moment of inertia 13.16 kg m$^2$. A 122 cm $\times$ 122 cm plywood board of mass 16 kg with moment of inertia 4.0 kg m$^2$ was placed on the top-frame to support rectangular steel plates of dimension 66 cm $\times$ 61 cm $\times$ 0.64 cm. Each plate has a mass of approximately 20 kg and a mass moment of inertia of 1.346 kg cm$^2$. Their primary axes were aligned with the $X_t$-axis of the top-frame. Two loading scenarios were investigated: *Light* (15 steel plates) and *Heavy* (30 steel plates). An array of sensors was installed on the experimental system measuring the table displacement and acceleration, three accelerations of the middle-frame, and three accelerations of the top-frame. The top-frame's total displacement was measured using image processing of video taken from an aerial camera.

TABLE 6.1: Peak experimental shake table velocities for double, undamped rolling isolation system experiments.

| Pulse period | Duration | Peak measured table velocity $V_p$ (cm/s) | | | | | |
|---|---|---|---|---|---|---|---|
| | | Light | | | Heavy | | |
| $T_p$ (s) | $T$ (s) | Weak | Moderate | Strong | Weak | Moderate | Strong |
| 0.20 | 10 | 7.59 | 11.80 | 23.46 | 8.13 | 11.70 | 23.23 |
| 0.35 | 10 | 10.43 | 16.44 | 28.62 | 10.30 | 16.28 | 28.78 |
| 0.50 | 10 | 11.55 | 18.57 | 46.15 | 11.67 | 18.80 | 28.98 |
| 0.67 | 15 | 12.26 | 19.97 | 46.69 | 12.39 | 19.80 | 47.76 |
| 0.85 | 20 | 12.76 | 20.68 | 47.11 | 12.72 | 23.30 | 47.90 |
| 1.00 | 25 | 13.04 | 23.70 | - | 12.91 | 23.17 | - |
| 1.25 | 30 | 13.20 | 23.25 | - | 13.40 | 23.21 | - |
| 1.60 | 35 | 14.32 | 23.22 | - | 14.38 | 23.23 | - |
| 2.20 | 45 | 15.61 | - | - | 15.62 | - | - |
| 3.00 | 60 | 13.96 | - | - | 14.02 | - | - |

The dashes (-) indicate experimental tests not performed due to the stroke limit of the shake table.

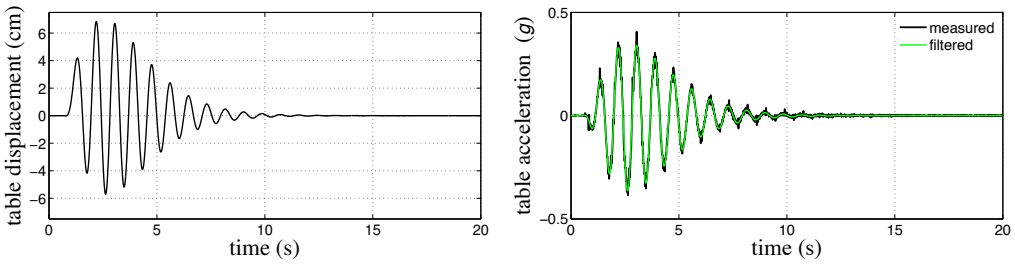


FIGURE 6.2: Displacement and acceleration input applied to shaking table table for the strong disturbance with $T_\mathrm{p} = 0.85$ s: measured (—) and filtered (—) records.

## 6.4 Experiment Design

The motion of the shake table $w(t)$ is controlled to represent the enveloped-harmonic function described in Section 4.5.1 and is briefly described herein. The table acceleration is specified to be

$$\ddot{w}(t) = g(t)\cos(\omega_\mathrm{p} t - \phi),\ t \in [0, T] \tag{6.13}$$

for which the disturbance envelope $g(t) = (t/\tau)^2 \exp(-t/\tau)$ and the frequency of the harmonic $\omega_\mathrm{p} = 2\pi/T_\mathrm{p}$. The disturbance parameters are chosen to be

$$\tau = 5T_\mathrm{p}/4 \qquad \text{(time-scale constant)}$$

$$\phi = 3\tan^{-1}(\tau\omega_\mathrm{p}) \pm \pi/2 \qquad \text{(phase angle).}$$

The acceleration record is detrended to ensure nearly zero terminal velocity and displacement using the following update:

$$\ddot{w}(t) \leftarrow \ddot{w}(t) - \left[\dot{g}(t)w(T) - g(t)\dot{w}(T)\right] \Big/ \int_0^T g(s)\mathrm{d}s\ . \tag{6.14}$$

The acceleration update is iteratively performed until $w(T)$ and $\dot{w}(T)$ are close to zero.

The shaking table disturbances used in this work were designed to represent *weak*, *moderate*, and *strong* motions over a range of periods. The disturbances are parameterized by the peak disturbance velocity $V_\mathrm{p}$ and the pulse period $T_\mathrm{p}$. Acceleration records were generated using the above procedure and scaled to match the prescribed peak velocity value $V_\mathrm{p}$ by scaling accelerations by a factor $V_\mathrm{p}/\max_t \dot{w}(t)$. Table 6.1 gives disturbance

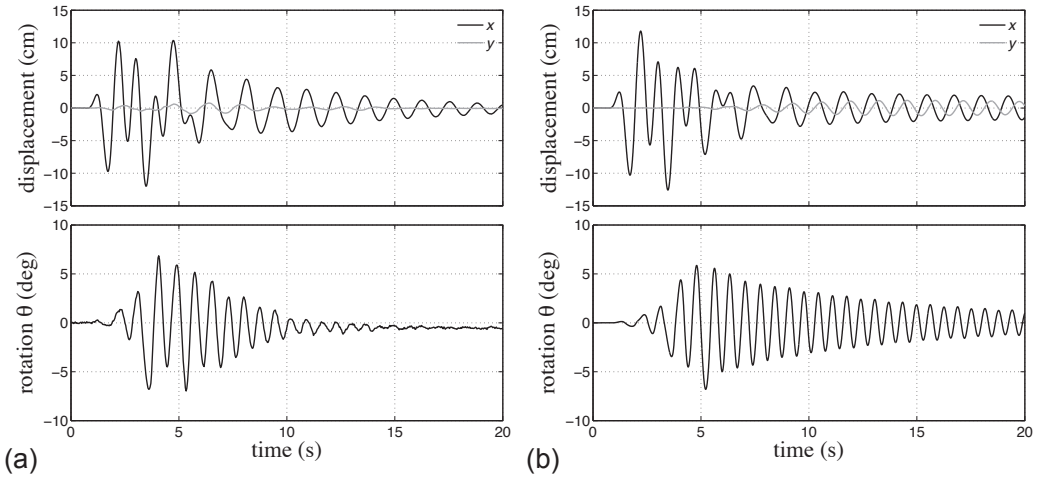


FIGURE 6.3: (a) Measured and (b) predicted displacement and rotation responses of the heavy system for the strong disturbance at $T_p = 0.85$ s.

durations $T$ and the experimental peak table velocities for weak, moderate, and strong cases in both the light and heavy systems. The table velocity was calculated using the central difference of the LVDT table displacement measurements. The experiments were designed to have constant peak table velocities for the three disturbance strengths, but this was not precisely achieved in the laboratory implementation. Furthermore, two moderate and five strong scenarios cannot be performed due to the ±75 mm stroke limit of the actuator. An example acceleration record is shown in Figure 6.2. The measured signal was low-pass filtered to reduce sensor noise without distorting the dominant waveform.

## 6.5 Experimental Validation of the Predictive Model

We now experimentally validate the simplified mathematical model. The inputs to the mathematical model $\ddot{w}_x(t)$ and $\ddot{w}_y(t)$ were set to low-pass-filtered measured acceleration records and zero, respectively, for all simulations. For the two moderate and five strong cases not experimentally performed, the input to the mathematical model $\ddot{w}_x(t)$ was set to the weak measured signal scaled to have peak velocities of $V_p = 25$ cm/s and 48 cm/s, respectively.

Two displacement measurements were acquired during the experiments; an LVDT

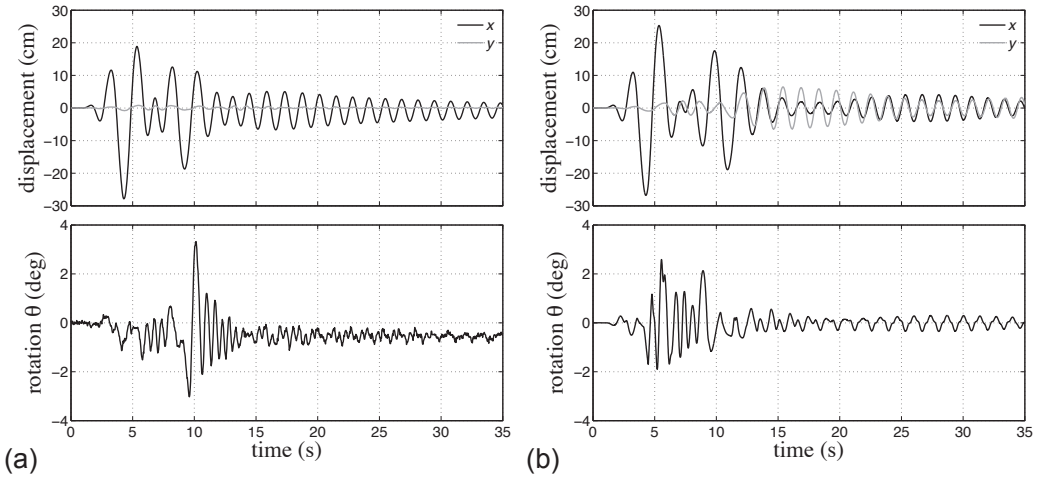


FIGURE 6.4: (a) Measured and (b) predicted displacement and rotation responses of the heavy system for the moderate disturbance at $T_{\mathrm{p}} = 1.60$ s.

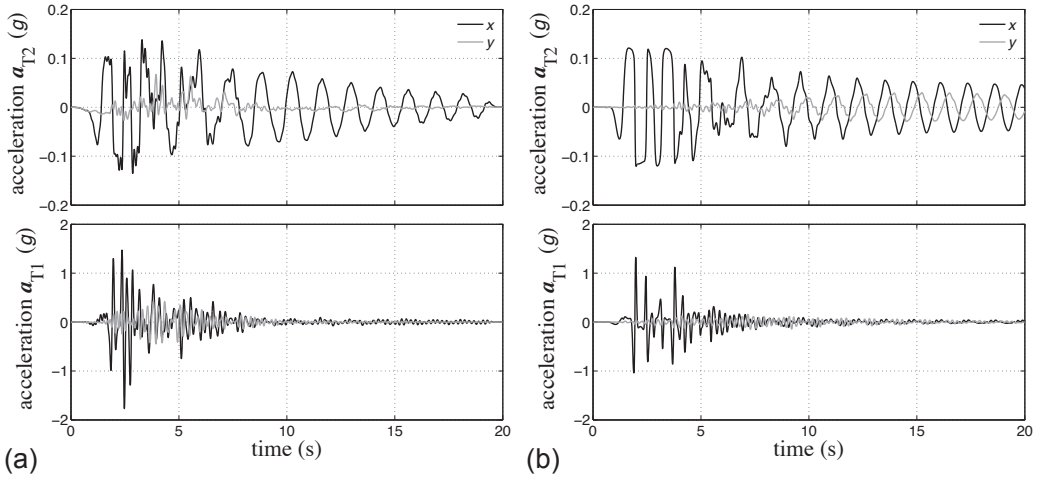


FIGURE 6.5: (a) Measured and (b) predicted acceleration responses of the heavy system for the strong disturbance at $T_{\mathrm{p}} = 0.85$ s.

measured the displacement of the shaking table, and processed video recording gave the the total displacement of the equipment. By synchronizing these two measurements, the displacement of the top-frame, relative to the shaking table, was found by taking their difference. Two experimentally-measured displacement records are shown in Figures 6.3(a) and 6.4(a) for two disturbance scenarios: a strong disturbance at $T_{\mathrm{p}} = 0.85$ s and a moderate disturbance at $T_{\mathrm{p}} = 1.60$ s, respectively. Figures 6.3(b) and 6.4(b) illustrate numerically-predicted displacement records for the same disturbances for one set of ran-

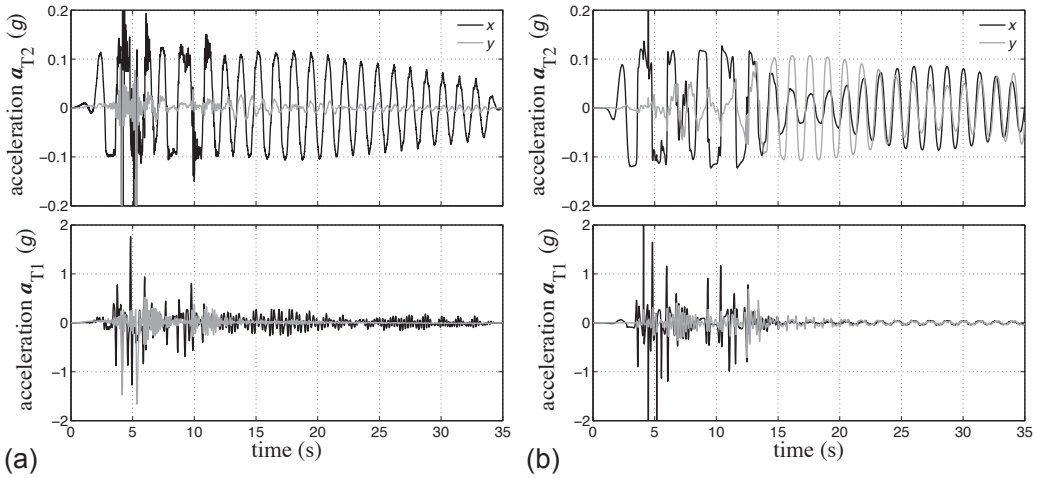


FIGURE 6.6: (a) Measured and (b) predicted acceleration responses of the heavy system for the moderate disturbance at $T_p$ = 1.60 s. Peak acceleration values (not shown): (a) 1.5 $g$ and (b) 0.55 $g$.

dom initial ball-bearing locations $\mathbf{r}_{i0}$. RISs are known to be chaotic [38, 63], and thus one cannot expect to match measured and predicted trajectories exactly. However, in both cases the trajectories are qualitatively similar.

Three accelerometers, one in the $X_t$-direction and two equally-spaced in the $Y_t$-direction, measured two orthogonal accelerations of the middle- and top-frames. Figures 6.5(a) and 6.6(a) show experimentally-measured acceleration records, $\boldsymbol{a}_{T1}(t)$ and $\boldsymbol{a}_{T2}(t)$, for the middle- and top-frames. Figures 6.5(b) and 6.6(b) illustrate numerically-simulated acceleration histories. Once again the numerically-predicted trajectories show good correspondence to the experimental histories. For the moderate disturbance at $T_p$ = 1.60 s, the experimental system experiences an impact of a ball-bearing with one of the bowl lips, which produces a spike in the top-frame's acceleration record; the impact is successfully captured by the numerical model. From Figures 6.5 and 6.6, the middle-frame experiences an order of magnitude higher acceleration than the top-frame. High accelerations in the middle-frame are not detrimental because the isolated object is rigidly connected to the top-frame and experiences the same acceleration as the top-frame. In fact, the middle-frame acts as an energy absorber, diverting the energy that would otherwise be imparted to the equipment.

### 6.5.1 *Peak response spectra*

As previously noted, the system is chaotic and we cannot expect to exactly match response histories. However, peak response quantities are more repeatable, in general. The response quantities of interest for a vibration isolator are the peak relative displacement and the peak total acceleration of the isolated mass. The peak displacement of the top-frame relative to the ground, denoted $d_{\mathrm{R}}^{\max}$, is given by

$$d_{\mathrm{R}}^{\max} = \max_{t} \left\| \boldsymbol{d}_{\mathrm{R}1}(t) + \mathbf{R}_{\bar{\theta}_1(t)} \boldsymbol{d}_{\mathrm{R}2}(t) \right\|. \tag{6.15}$$

For a single RIS, $d_{\mathrm{R}}^{\max}$ is constrained to be less than 22 cm, but by stacking two systems, the largest permissible displacement $d_{\mathrm{R}}^{\max}$ is doubled to 44 cm. The peak total acceleration experienced by the isolated mass, denoted $a_{\mathrm{T}}^{\max}$, is given by

$$a_{\mathrm{T}}^{\max} = \max_{t} \left\| \boldsymbol{a}_{\mathrm{T}2}(t) \right\|. \tag{6.16}$$

Due to the top- and middle-frames' rotations, the measured accelerations are not in an absolute frame of reference. However, the magnitude of the total acceleration is rotationally-invariant and the norm of the recorded acceleration is equivalent to $\|\boldsymbol{a}_{\mathrm{T}2}(t)\|$.

Next, peak response spectra are generated for the selected pulse periods and velocities given in Table 6.1. Figure 6.7 shows the experimentally-measured (black) and numerically-predicted (gray) peak response spectra for the light (a-b) and heavy (c-d) systems. The pulse strengths are distinguished by the marker shapes. Twenty random initial ball conditions $\mathbf{r}_{i0}$ are used in the numerically predicted responses, producing a spread in the peak responses. In general, the variance of the peak responses is larger for the light system; the light system shows a greater sensitivity to the initial ball-bearing locations. The experimental peak displacements $d_{\mathrm{R}}^{\max}$ fall within the numerically predicted spread, signifying successful peak response prediction with the numerical model. The full displacement capacity of the double isolation system ($\approx$ 44 cm) could not be realized experimentally due

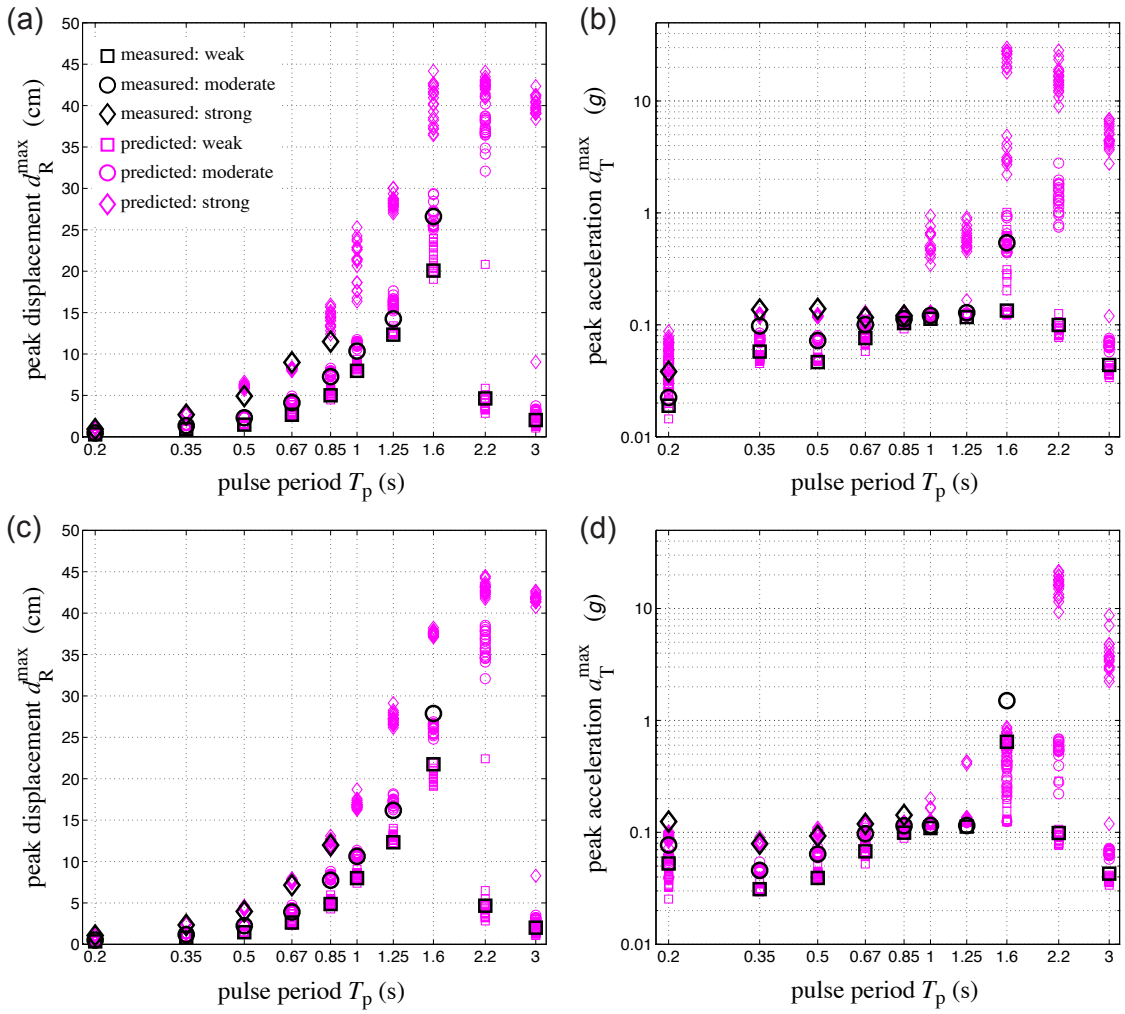


FIGURE 6.7: Peak displacement and acceleration pulse response spectra for (a-b) light system and (c-d) heavy system: weak (□), moderate (○), and strong (◇).

to the shake table's limitations, but the numerical model shows that the light system exhibits larger peak displacement responses. Correspondingly, larger accelerations are seen, indicating the double isolation system performs better for more massive equipment.

Slightly elevated accelerations, representing a second mode response, can be seen in the both the experimental and numerical acceleration spectra. The second mode resonance occurs at $0.35 < T_p < 0.67$ s for the light system, and is shifted to $T_p = 0.20$ s for the heavy system. These accelerations are not large enough to cause a failure in the vibration-sensitive equipment being isolated. However, three experimentally-measured accelera-

tions exhibit appreciably higher values: the light system under moderate disturbance at $T_p$ = 1.6 s, and the heavy system under weak and moderate disturbances at $T_p$ = 1.6 s. In these three instances, a ball-bearing in the second-subsystem impacts with the bowl lip, generating spikes in the acceleration record. An example of an experimentally-measured acceleration spike is shown in Figure 6.6(a). Overall, the proposed model successfully predicts the peak responses of the double RIS.

## 6.6 Summary

The purpose of this chapter has been to derive a simplified model of a double RIS that can be used to simulate the system's response to external disturbances. By comparing experimentally-measured time histories and peak response spectra with numerically-predicted results, the proposed model is successfully validated. The numerical model is successfully able to capture and predict vibration suppression quantities of interest, such as peak displacement, peak acceleration, and the occurrence of impacts. The experimentally-validated model can now be used to evaluate the stacked system's performance for a broader range of disturbances (e.g. earthquake-induced floor responses), without the limitations of experiments (e.g. equipment and time constraints).

There are two drawbacks to the double RIS tested in this chapter. The first drawback relates to the bowls used in the experimental set-up. Because the double RIS was constructed from two *identical* single RISs stacked one on top of the other, the bowl profiles in the first- and second-subsystems are identical. Future work should look at optimizing the bowl-shape functions in the first- and second subsystems in order to reduce the occurrence of impacts and improve the system's performance. The simplified model presented in this chapter can serve as a useful tool for the design of high-performance isolation systems because, in the derivation of the equations of motion, no assumptions were made about the bowl-shape function.

Second, the double RIS is very lightly damped because its constituent subsystems are themselves lightly damped. The high acceleration response in the middle-frame, though not detrimental to the overall system performance, may be reduced with additional damping. Another design innovation, which is the topic of Chapter 9, is the inclusion of supplemental damping by introducing additional rolling resistance via elastomeric sheets on which the ball-bearings would roll, decreasing the displacement demand on the isolator. Future work should investigate the inclusion of supplemental damping in the first-subsystem, the second-subsystem, or both to increase the double RIS's performance.

# 7

# Optimal Performance of Constrained Control Systems

## 7.1 Background

In Chapter 2 the calculus of variations was used to derive the necessary conditions for extremizing an integral function (2.1). From this result, Lagrange's equations of motion for holonomic systems were deduced. The next useful extension of Section 2.2 is to derive the necessary conditions for optimality of the constrained control problem, with particular interest in semi-actively constrained systems.

Over the last several decades a large number of semi-active control devices have been developed for a broad range of applications. Since the publication of review articles on semi-active control [98, 99], research has progressed on semi-active stiffness devices [100–104], semi-active damping devices [105–107], and semi-active friction devices [108, 109]. Models for these devices involve constraints, either directly on device forces, or indirectly on an internal variable such as a valve position, a solenoid voltage, or an electrical resistance.

There are two principal advantages of implementing semi-active control. The first is

that the power a semi-active device may regulate within the structure can be orders of magnitude greater than the power required to regulate the device properties (e.g. damping and/or stiffness). The second is that the controlled system is unconditionally stable in a bounded-input, bounded-output sense *regardless* of the feedback law implemented. A potential disadvantage of semi-active control systems is that, for some applications, closed-loop semi-active performance may be only marginally better than that of simpler passive control systems [98]. Additionally, actuation constraints of semi-active control systems render the system nonlinear and performance can be assessed and optimized only through transient response simulations. It is common practice to evaluate the performance of semi-actively controlled systems for a particular feedback law and compare the result to a passively controlled system. This method of performance evaluation may be used to assess the potential performance of a semi-active control system subject to the constraint of the feedback control rule, which can be overly restrictive.

A more complete evaluation of the potential benefit of a semi-active control system eliminates the restriction of the feedback control rule. Methods of trajectory optimization may be used to determine the best possible performance, as defined by a particular objective function, and strictly adhering to the constraints of a particular semi-active device, the structural system into which it is applied, and the external forcing. This optimization enables a rigorous evaluation of new semi-active devices and a meaningful comparison with existing semi-active devices and passive devices. Semi-active devices that can achieve performance levels sufficiently better than those of existing passive devices or alternative semi-active devices merit the development of control hardware and feedback control rules.

The correct formulation, and importance, of constrained control problems have been known for decades. Kirk emphasizes that "the optimal [constrained] control history ... *cannot* be determined, in general, by calculating the optimal [unconstrained] control history and allowing it to saturate whenever the stipulated boundaries are violated." [110] (p. 236). Further, Tseng and Hedrick prove that "clipped-optimal is sub-optimal in the

sense that it minimizes only the instantaneous performance index difference [and] does not guarantee optimality in minimizing [an integral] performance index." [111] (p. 556).

We note here that in a dynamical control system, $\dot{\mathbf{x}} = \mathbf{f}(\mathbf{x}, \mathbf{u}; t)$, changing the controls $\mathbf{u}$ at time $t$ changes $\dot{\mathbf{x}}$ (but not $\mathbf{x}$) at time $t$. So any state-dependent performance index can not be instantaneously improved by changing the controls at time $t$. It is therefore rational to minimize integral cost functions. The choice of the objective function is subjective, and reflects the control engineer's best judgment regarding the purpose of the control system.

Following the work of Tseng and Hedrick [111], we state the semi-active control optimization problem as a constrained two-point boundary value problem (TPBVP), and gives a solution procedure by which the constraints are eliminated, reducing the problem to an unconstrained TPBVP. The method is illustrated on a simplified tuned-mass-damper (TMD) with a supplemental semi-active damper, in which the dynamics are linear (except for the actuation constraints) and the Lagrangian of the cost function is quadratic. The purpose of this chapter is to provide a concise tutorial on semi-active performance optimization that illustrates, in detail, just how easy it is to setup and solve such problems.

The method for optimizing semi-active control trajectories illustrated in this chapter is fundamentally distinct from feedback control methods such as clipped optimal or Lyapunov-based controls. The motivation for the use of such techniques is for the design of real-time feedback laws that are straight-forward to compute in closed form, easy to implement, and feasible under semi-active constraints. However, such approaches are always sub-optimal; i.e., they leave open the possibility that there may be some *other* feedback law that, if implemented, could have led to a much more favorable dynamic response. Indeed, irrespective of the measure of optimality chosen, the optimal feedback problem for semi-actively constrained systems remains an open problem.

By contrast, techniques exist for the rigorous computation of the optimal *physically achievable* performance of a semi-actively constrained system, given precise models of the system and disturbance. Such techniques do not result in an optimal feedback law, and

the optimized control inputs are anticipatory; i.e., they presume knowledge of the entire disturbance trajectory. These solutions are highly valuable in the context of semi-active control system analysis, for several reasons:

- First, they can be used to assess the ultimate viability of semi-active control for a given application. More specifically, they determine whether a given semi-active device, embedded within a given structure, and subjected to a given disturbance, can *possibly* achieve a level of performance the designer requires. This effectively enables the hardware of an application to be assessed prior to the design of a feedback law. This observation was a significant motivation for investigations in this area in automotive suspensions applications, by Hrovat *et al.* [112], as well as Tseng and Hedrick [111].

- Second, the nature of the optimized trajectory for the control input can be used to gain significant intuition regarding the mathematical structure a semi-active feedback law should have. For example, in Ref. [113], Leavitt *et al.* used optimal control techniques to infer heuristic switching rules for a semi-active variable-stiffness device under harmonic excitation. Likewise, in Ref. [39], Harvey *et al.* examined optimal control trajectories for a semi-actively controlled isolation system subjected to a near-field earthquake pulse record, and showed that the qualitative nature of the optimized semi-active force depends on the specific parameters of the pulse record as well as the performance measure. For some parameter combinations, it resembles a "pseudo-negative stiffness" damping force. For others, it is more reminiscent of nonlinear viscous damping.

- Third, the optimal control techniques discussed in this paper are directly applicable to model predictive control (MPC) synthesis [114]. This is a feedback control technique in which the optimal control trajectory is periodically solved in real-time from the present time over a receding horizon, using an iteratively-updated forecast of the

future disturbance trajectory. Such techniques have recently been investigated for semi-active applications by Giorgetti *et al.* [115].

Section 7.2 rigorously defines semi-active optimization as a constrained two-point boundary value problem, provides optimality conditions, and presents a solution methodology for this class of problems. In Section 7.5 the performance of an optimal semi-active control system is illustrated in the context of a semi-active TMD application, and is compared to performance achieved via clipped LQR.

The primary objective of this chapter is to provide a tutorial on how to solve the optimal semi-active control problem, and to illustrate the method with a simple example. As such, emphasis is placed on the application to a relatively simple system and on providing detailed information on how the method can be implemented. MATLAB code is provided in Appendix C.

## 7.2 Necessary Conditions for Optimality

In the context of optimal control, the interpretation of generalized coordinates $\mathbf{z}$ is different than in Section 2.3. The coordinate vector $\mathbf{z}(t)$ is a collection of states $\mathbf{x}(t) \in \mathbb{R}^n$ and controls $\mathbf{u}(t) \in \mathbb{R}^m$, i.e. $\mathbf{z} = [\mathbf{x}^\mathsf{T}\ \mathbf{u}^\mathsf{T}]^\mathsf{T}$. The equality constraint (2.2) is derived from the system's differential equation,

$$\dot{\mathbf{x}}(t) = \mathbf{f}(\mathbf{x}(t), \mathbf{u}(t), t)\ , \quad \mathbf{x}(t_0) = \mathbf{x}_0\ , \quad t \in [t_0, t_\mathrm{f}]\ . \tag{7.1}$$

The equivalent constraint,

$$\mathbf{g}(\mathbf{z}, \dot{\mathbf{z}}, t) = \mathbf{g}(\mathbf{x}, \dot{\mathbf{x}}, \mathbf{u}, t) = \mathbf{f}(\mathbf{x}, \mathbf{u}, t) - \dot{\mathbf{x}} = 0 \tag{7.2}$$

is time varying and, hereinafter, assumed to be deterministic—stochastic disturbances will not be addressed in this dissertation.

The optimal constrained control problem is stated as follows: an admissible control trajectory $\mathbf{u}(t) \in \mathbb{R}^m$ is to be applied to a non-autonomous system $\mathbf{f}(\mathbf{x}, \mathbf{u}, t)$ over a finite-

horizon $t \in [t_0, t_f]$ in order to minimize a Lagrange-type cost function $J$ of the states and controls subject to an $\ell$-component state-control inequality constraint $\mathbf{c}(\mathbf{x}, \mathbf{u}, t)$. More concisely, the problem may be stated as follows:

$$\min_{\mathbf{x}(t)\in\mathbb{R}^n} \min_{\mathbf{u}(t)\in\mathbb{R}^m} J = \int_{t_0}^{t_f} L(\mathbf{x}(t), \mathbf{u}(t))\, \mathrm{d}t \tag{7.3a}$$

$$\text{subject to} \quad \dot{\mathbf{x}}(t) = \mathbf{f}(\mathbf{x}(t), \mathbf{u}(t), t), \quad t \in [t_0, t_f] \tag{7.3b}$$

$$\mathbf{x}(t_0) = \mathbf{x}_0 \tag{7.3c}$$

$$\mathbf{c}(\mathbf{x}(t), \mathbf{u}(t), t) \leq \mathbf{0}\ . \tag{7.3d}$$

Notice the Lagrangian $L(\cdot)$ is taken to be independent of $\dot{\mathbf{x}}$ and $\dot{\mathbf{u}}$.

The necessary conditions for optimality were derived in Chapter 2 using the calculus of variations. To recapitulate, the augmented Lagrangian $\Lambda$ is given as follows:

$$\Lambda(\mathbf{x}, \mathbf{u}, \boldsymbol{\lambda}, \boldsymbol{\mu}, t) \equiv L(\mathbf{x}, \mathbf{u}, t) + \boldsymbol{\lambda}^\mathsf{T}(\mathbf{f}(\mathbf{x}, \mathbf{u}, t) - \dot{\mathbf{x}}) + \boldsymbol{\mu}^\mathsf{T}\mathbf{c}(\mathbf{x}, \mathbf{u}, t) \tag{7.4}$$

where $\boldsymbol{\lambda}(t) \in \mathbb{R}^n$ is the Lagrange multiplier vector or *costate* vector for the dynamic constraint (7.3b), and $\boldsymbol{\mu}(t) \in \mathbb{R}^\ell$ are Lagrange multipliers for the inequality constraint (7.3d). Note that all $\mu_i(t) \geq 0,\ \forall t$. Classically, the Hamiltonian $H$ is defined to be

$$H(\mathbf{x}, \mathbf{u}, \boldsymbol{\lambda}, \boldsymbol{\mu}, t) \equiv L(\mathbf{x}, \mathbf{u}, t) + \boldsymbol{\lambda}^\mathsf{T}\mathbf{f}(\mathbf{x}, \mathbf{u}, t) + \boldsymbol{\mu}^\mathsf{T}\mathbf{c}(\mathbf{x}, \mathbf{u}, t) \tag{7.5}$$

such that $\Lambda = H - \boldsymbol{\lambda}^\mathsf{T}\dot{\mathbf{x}}$. In the usual way, the constraints were then adjoined with multipliers to the performance index $J$, the augmented cost was defined to be

$$J_\mathrm{A} = \int_0^{t_f} (H - \boldsymbol{\lambda}^\mathsf{T}\dot{\mathbf{x}})\, \mathrm{d}t\ . \tag{7.6}$$

Setting the variation of $J_\mathrm{A}$ with respect to independent increments $\delta\mathbf{x}$, $\delta\mathbf{u}$, $\delta\boldsymbol{\lambda}$, and $\delta\boldsymbol{\mu}$, equal to zero, i.e. $\delta J_\mathrm{A} = 0$, we obtain the necessary conditions for optimality. Note that perturbations $\delta\boldsymbol{\mu}$ about the optimum $\boldsymbol{\mu}^*$ are constrained: if $\mu_i^*(t) = 0$, then $\delta\mu_i(t)$ must be greater than or equal to zero, otherwise $\delta\mu_i(t)$ is unconstrained. The corresponding variation in the cost $\delta J_\mathrm{A}(\delta\boldsymbol{\mu}) \leq 0$, i.e. perturbations in $\boldsymbol{\mu}$ reduce the cost at (local) maxima.

Seeing as the augmented Lagrangian $\Lambda$ is independent of the control rate $\dot{\mathbf{u}}$, Equation (2.7a) decouples as follows:

$$\mathbf{0} = \frac{\partial \Lambda}{\partial \mathbf{x}} - \frac{\mathrm{d}}{\mathrm{d}t}\left(\frac{\partial \Lambda}{\partial \dot{\mathbf{x}}}\right) \equiv \frac{\partial H}{\partial \mathbf{x}} + \dot{\boldsymbol{\lambda}} \tag{7.7a}$$

$$\mathbf{0} = \frac{\partial \Lambda}{\partial \mathbf{u}} \equiv \frac{\partial H}{\partial \mathbf{u}} \, . \tag{7.7b}$$

The time interval $t \in [t_0, t_\mathrm{f}]$ is fixed, but unlike the Lagrange's principle formulation, the states and controls are not fixed at $t_\mathrm{f}$, so $\delta\mathbf{x}(t_\mathrm{f})$ and $\delta\mathbf{u}(t_\mathrm{f})$ are free. Therefore, the boundary conditions (2.6c) are

$$\left(\frac{\partial \Lambda}{\partial \dot{\mathbf{x}}}\delta\mathbf{x} + \frac{\partial \Lambda}{\partial \dot{\mathbf{u}}}\delta\mathbf{u}\right)\Bigg|_{t_0}^{t_\mathrm{f}} = -\boldsymbol{\lambda}^\mathsf{T}\delta\mathbf{x}\Big|_{t_\mathrm{f}} = 0 \, . \tag{7.8}$$

For arbitrary $\delta\mathbf{x}(t_\mathrm{f})$ the terminal costate condition $\boldsymbol{\lambda}(t_\mathrm{f}) = \mathbf{0}$ results. This dissertation only treats the finite-horizon open-loop control problem and will not discuss the infinite-horizon problem in which $t_\mathrm{f} \to \infty$.

Now we are ready to state the full necessary conditions for the constrained optimal control problem as follows:

$$\dot{\mathbf{x}} = \frac{\partial H}{\partial \boldsymbol{\lambda}} = \mathbf{f}(\mathbf{x}, \mathbf{u}, t), \qquad \mathbf{x}(0) = \mathbf{x}_0 \tag{7.9a}$$

$$-\dot{\boldsymbol{\lambda}} = \frac{\partial H}{\partial \mathbf{x}} = \frac{\partial L}{\partial \mathbf{x}} + \frac{\partial \mathbf{f}^\mathsf{T}}{\partial \mathbf{x}}\boldsymbol{\lambda} + \frac{\partial \mathbf{c}^\mathsf{T}}{\partial \mathbf{x}}\boldsymbol{\mu}, \qquad \boldsymbol{\lambda}(t_\mathrm{f}) = \mathbf{0} \tag{7.9b}$$

$$\mathbf{0} = \frac{\partial H}{\partial \mathbf{u}} = \frac{\partial L}{\partial \mathbf{u}} + \frac{\partial \mathbf{f}^\mathsf{T}}{\partial \mathbf{u}}\boldsymbol{\lambda} + \frac{\partial \mathbf{c}^\mathsf{T}}{\partial \mathbf{u}}\boldsymbol{\mu} \tag{7.9c}$$

$$\mathbf{0} \geq \frac{\partial H}{\partial \boldsymbol{\mu}} = \mathbf{c}(\mathbf{x}, \mathbf{u}, t) \, . \tag{7.9d}$$

The necessary conditions (7.9) are differential-algebraic equations with the differential equations, (7.9a) and (7.9b), constituting a TPBVP—initial states and terminal costates are known.

Though these necessary conditions are well-known, methods to find solutions are not well represented for complex constraints $\mathbf{c}(\cdot)$, i.e. nonlinear and/or state constraints. Here,

we present a saturation method in which knowledge of the decentralized structure of the constraint boundaries allows for closed-form expressions for the optimal Lagrange multiplier values. This is an extension of Butsuen's work [116] which involved linear constraints on the a single actuator system with only state weight in the cost. The extensions presented here allow for exogenous disturbances and multiple controls subject to a much broader class of constraints involving controls and states. By recognizing that control constraints are decentralized, i.e. each constraint equation involves only one control input, it will become evident in the following that optimal values of the constraint Lagrange multipliers may be found in closed form from $\partial H/\partial \mathbf{u} = \mathbf{0}$.

This chapter presents the formulation and solution to optimal control problems with nonlinear decentralized constraints. The solution to the unconstrained finite-horizon linear-quadratic (LQ) problem is found by solving a TPBVP [59]. Numerical methods to solve unconstrained TPBVPs are well established, e.g. shooting methods, finite-differences, finite-elements. The method applied here is a collocation with a piecewise cubic polynomial function, which satisfies the boundary conditions for each subinterval, and is implemented by the MATLAB function `bvp4c.m` [117]. This method requires an initial guess for the trajectories—states and costates—from which the nonlinear algebraic equations for the coefficients of the cubic polynomial solution are solved iteratively by linearization [118]. The contribution of this chapter is to show that systems in which controls are individually constrained can be cast as an unconstrained TPBVP. In the method introduced here the constraints are enforced through Lagrange multipliers. Because controls are individually constrained, the Lagrange multipliers required to enforce constraints may be determined individually.

### 7.2.1 Linear-quadratic constrained control

Equation (7.9) provides the optimal controller for general nonlinear systems, but this section considers the linear, time-invariant (LTI) plant

$$\dot{\mathbf{x}}(t) = \mathbf{f}(\mathbf{x}, \mathbf{u}, t) = \mathbf{A}\mathbf{x}(t) + \mathbf{B}\mathbf{u}(t) + \mathbf{B}_w\mathbf{w}(t), \quad \mathbf{x}(t_0) = \mathbf{x}_0, \quad \mathbf{x}(t) \in \mathbb{R}^n \ . \tag{7.10}$$

Equation (7.10) is parameterized as follows: $\mathbf{A} \in \mathbb{R}^{n\times n}$ is the dynamics matrix, $\mathbf{B} \in \mathbb{R}^{n\times m}$ is the control input matrix, and $\mathbf{B}_w \in \mathbb{R}^{n\times s}$ is the input matrix associated with the known, deterministic exogenous disturbance $\mathbf{w}(t) \in \mathbb{R}^s$. The Lagrangian $L(\cdot)$ is quadratic with state weighting matrix $\mathbf{Q} \in \mathbb{R}^{n\times n}$, control weighting matrix $\mathbf{R} \in \mathbb{R}^{m\times m}$, and bilinear state-control weighting matrix $\mathbf{S} \in \mathbb{R}^{n\times m}$, viz.

$$L(\mathbf{x}, \mathbf{u}; t) = \frac{1}{2}\begin{bmatrix}\mathbf{x}(t)\\ \mathbf{u}(t)\end{bmatrix}^\mathsf{T}\begin{bmatrix}\mathbf{Q} & \mathbf{S}\\ \mathbf{S}^T & \mathbf{R}\end{bmatrix}\begin{bmatrix}\mathbf{x}(t)\\ \mathbf{u}(t)\end{bmatrix} \ . \tag{7.11}$$

Weighting matrices $\mathbf{Q}$ and $\mathbf{R}$ are symmetric.

Using the necessary conditions (7.9), the solution to the LQ constrained control problem is as follows:

$$\dot{\mathbf{x}} = \frac{\partial H}{\partial \boldsymbol{\lambda}} = \mathbf{A}\mathbf{x} + \mathbf{B}\mathbf{u} + \mathbf{B}_w\mathbf{w}, \qquad \mathbf{x}(t_0) = \mathbf{x}_0 \tag{7.12a}$$

$$-\dot{\boldsymbol{\lambda}} = \frac{\partial H}{\partial \mathbf{x}} = \mathbf{Q}\mathbf{x} + \mathbf{S}\mathbf{u} + \mathbf{A}^\mathsf{T}\boldsymbol{\lambda} + \frac{\partial \mathbf{c}^\mathsf{T}}{\partial \mathbf{x}}\boldsymbol{\mu}, \qquad \boldsymbol{\lambda}(t_\mathrm{f}) = \mathbf{0} \tag{7.12b}$$

$$\mathbf{0} = \frac{\partial H}{\partial \mathbf{u}} = \mathbf{R}\mathbf{u} + \mathbf{S}^\mathsf{T}\mathbf{x} + \mathbf{B}^\mathsf{T}\boldsymbol{\lambda} + \frac{\partial \mathbf{c}^\mathsf{T}}{\partial \mathbf{u}}\boldsymbol{\mu} \tag{7.12c}$$

$$\mathbf{0} \geq \frac{\partial H}{\partial \boldsymbol{\mu}} = \mathbf{c}(\mathbf{x}, \mathbf{u}, t) \ . \tag{7.12d}$$

Henceforth, the LQ problem will be handled, but the proposed methods are viable for nonlinear dynamics and arbitrary Lagrangians.

## 7.3 Optimal Constrained Control Law

Numerical solutions to Equations (7.12a)–(7.12d) are represented by four trajectories—$\mathbf{u}(t)$, $\mathbf{x}(t)$, $\boldsymbol{\lambda}(t)$, and $\boldsymbol{\mu}(t)$. Controls and Lagrange multipliers that satisfy the stationarity condition (7.12c) and control constraints (7.12d) may be evaluated for each time step and inserted into the state and costate dynamics, Equations (7.12a) and (7.12b), thereby resulting in an unconstrained TPBVP. This method involves a saturation procedure described below.

At the optimal solution, the complementary slackness condition

$$\mu_j(t) \begin{cases} = 0, & c_j(\mathbf{x}, u_j, t) < 0 \\ \geq 0, & c_j(\mathbf{x}, u_j, t) = 0 \end{cases} \tag{7.13}$$

must hold, i.e. improvements can only come by violating the constraint. Pontryagin's Minimum Principle [119] states the optimal control $\mathbf{u}^*(t)$ is the one that minimizes the value of the Hamiltonian $H(\cdot)$ at any particular instant. To solve the necessary conditions (7.12), the following quadratic program is solved at each time $t$:

$$\min_{\mathbf{u}(t)} \max_{\boldsymbol{\mu}(t) \geq \mathbf{0}} H(\mathbf{x}, \mathbf{u}, \boldsymbol{\lambda}, \boldsymbol{\mu}; t). \tag{7.14}$$

This minimization must respect the constraint of Equation (7.12d), but is essentially an algebraic problem at each instant in time [120]. The difficulty arrises in computing the solution to the state/costate system of equations in the form of a TPBVP.

The optimal control $\mathbf{u}(t)$ and inequality constraint multiplier $\boldsymbol{\mu}(t)$ are found from Equation (7.12c) as follows: define the proposed control to be

$$\mathbf{u}_{\text{active}}(t) \equiv -\mathbf{R}^{-1} \left( \mathbf{S}^{\mathsf{T}} \mathbf{x}(t) + \mathbf{B}^{\mathsf{T}} \boldsymbol{\lambda}(t) \right) . \tag{7.15}$$

This is the optimal 'active' (or unconstrained) control given by Equation (7.12c) where $\boldsymbol{\mu}(t) \equiv \mathbf{0}$. The subscript 'active' is used here to represent the finite-horizon unconstrained optimal control input, not an LQR or LQG feedback controller. Unless constraints are

redundant or over-specified, no more than one constraint per control input is invoked at any point in time; we saturate the control to the most restrictive constraint. Furthermore, each constraint is assumed to be decentralized with respect to its control, i.e. $\mathbf{c}(\mathbf{x}, \mathbf{u}, t) = \left[\mathbf{c}^{(1)^\intercal}(\mathbf{x}, u_1, t) \ \cdots \ \mathbf{c}^{(m)^\intercal}(\mathbf{x}, u_m, t)\right]^\intercal$ where $\mathbf{c}^{(k)}(\cdot) \in \mathbb{R}^{\ell_k}$ and $\sum_k \ell_k = \ell$. Similarly, the inequality constraint Lagrange multipliers can be partitioned as follows: $\boldsymbol{\mu}(t) = [\boldsymbol{\mu}^{(1)^\intercal}(t) \ \cdots \ \boldsymbol{\mu}^{(m)^\intercal}(t)]^\intercal$. This allows for determination of each optimal control $u_k(t)$ independently of the other controls. So at most, only one multiplier $\mu_j^{(k)}(t)$ will be activated at any time for a given control $u_k(t)$. If $\mathbf{c}^{(k)}(\mathbf{x}, u_{k,\text{active}}, t) \leq \mathbf{0}$, accept $u_k^*(t) = u_{k,\text{active}}(t)$; otherwise, $\mu_j^{(k)}(t)$ must be determined such that the violated constraint $c_j^{(k)}(\mathbf{x}, u_k, t) = 0$. To this end, we define the saturation function as follows:

$$\text{sat}(\mathbf{x}, u_k; t) = \begin{cases} u_k, & \mathbf{c}^{(k)}(\mathbf{x}, u_k, t) \leq 0 \\ \underset{u(t)}{\arg}\left\{c_j^{(k)}(\boldsymbol{x}, u; t) = 0\right\}, & c_j^{(k)}(\mathbf{x}, u_k, t) > 0 \end{cases} . \tag{7.16}$$

The instantaneous optimal control is found from enforcing the constraints on the 'active' control, namely

$$u_k^*(t) \equiv \text{sat}(\mathbf{x}, u_{k,\text{active}}; t) \ . \tag{7.17}$$

A visualization of the saturation function is given in Figure 7.1. The leftmost figure, Figure 7.1(a), shows a feasible proposed control, i.e. $\mathbf{c}^{(k)}(\mathbf{x}, u_{k,\text{active}}, t) \leq \mathbf{0}$; therefore, we accept $u_k(t) = u_{k,\text{active}}(t)$. Next, Figure 7.1(b) depicts a simple saturation of an infeasible proposal constraint, $c_2^{(k)}(\mathbf{x}, u_{k,\text{active}}, t) > 0$; $u_{k,\text{active}}(t)$ is saturated to $u_k^*$ such that $c_2^{(k)}(\mathbf{x}, u_k^*, t) = 0$. Finally, Figure 7.1(c) shows a scenario where two constraints are not satisfied; in this case, we saturate to the most restrictive constraint, $c_1^{(k)}(\mathbf{x}, u_k^*, t) = 0$.

Once all optimal $u_k(t)$ have been determined, it's a matter of finding the corresponding optimal $\mu_j^{(k)}(t)$ from Equation (7.12c) such that the Hamiltonian has a saddle point at the constraint boundary. Note that because the constraints are decentralized and each control will adhere to at most one active constraint, at most $m$ Lagrange multipliers $\mu_j^{(k)}(t)$ need to be determined. In the case where $u_{k,\text{active}}(t)$ is feasible, Lagrange multipliers $\boldsymbol{\mu}^{(k)}(t) = \mathbf{0}$; if

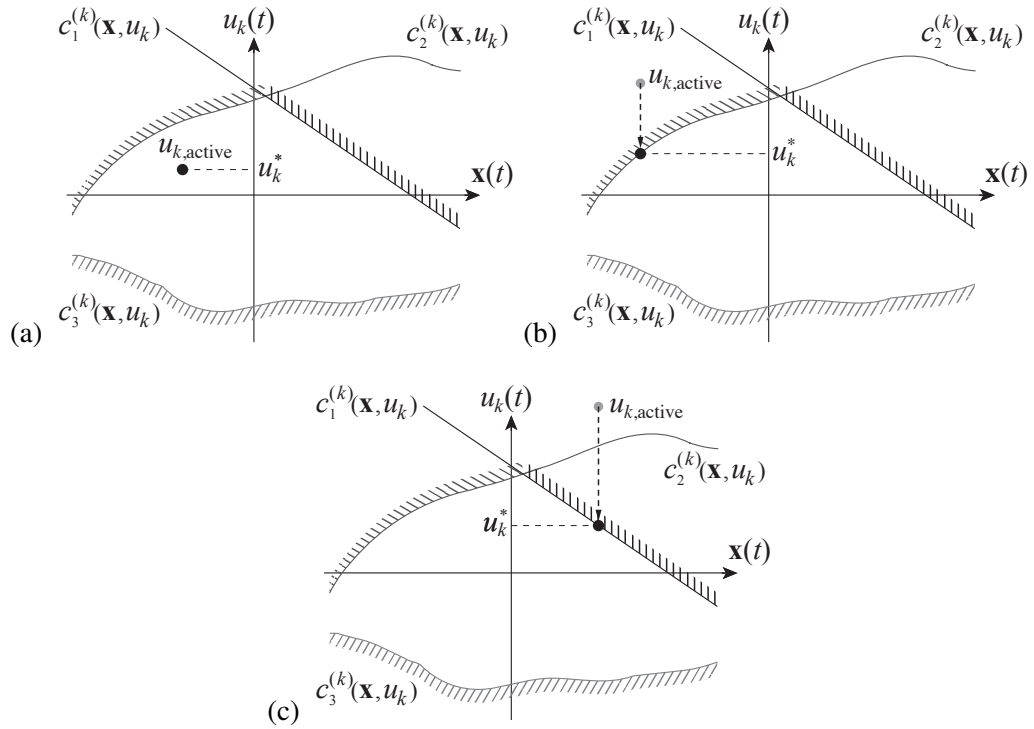


FIGURE 7.1: Saturation function visualization in extended state space. (a) Accept $u_k^* = u_{k,\text{active}}$; (b) saturate $u_{k,\text{active}}$ to nearest constraint boundary, $c_2^{(k)}(\mathbf{x}, u_k^*) = 0$; and (c) saturate $u_{k,\text{active}}$ to most restrictive constraint, $c_1^{(k)}(\mathbf{x}, u_k^*) = 0$.

$u_{k,\text{active}}(t)$ violates constraint $c_j^{(k)}(\mathbf{x}, u_k, t)$, then Lagrange multiplier $\mu_j^{(k)}(t)$ is found from the $k$th equality in Equation (7.12c) with all other $\mu_l^{(k)}(t) = 0,\ l \neq i$.

## 7.4 Semi-Active Control

### *7.4.1 Semi-active force constraint*

Typically, controllable dampers have performance limitations described by a maximum achievable control force amplitude $u_{\max}$, a maximum achievable damping coefficient $c_{k,\max}$, and a dissipative force-velocity relation. So, for semi-active damping, feasible control forces are bounded by sectors shown in Figure 1, where $v_k(t) \equiv v_k(\mathbf{x}(t))$ is the velocity across the $k$th actuator. The former limitation implies $|u_k(t)| < u_{k,\max}$ and the latter implies $|u_k(t)| \in [0, c_{k,\max}|v(t)|]$. Such constraints may be expressed by the following nonlinear

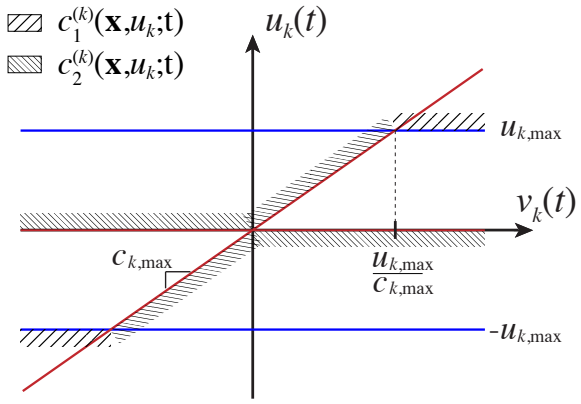


FIGURE 7.2: Sector-bound constraint for semi-active damping device, where $v_k(t)$ is the velocity across the $k$th actuator.

inequality constraint equations:

$$\mathbf{c}^{(k)}(\mathbf{x}, u_k; t) = \begin{bmatrix} (u_k(t) + u_{k,\max})(u_k(t) - u_{k,\max}) \\ u_k(t)(u_k(t) - c_{k,\max} v_k(t)) \end{bmatrix} \leq \mathbf{0} \,. \tag{7.18}$$

For other semi-active device models, the feasible region may take other forms, as described in Section 7.6.1. The following section gives the solution procedure proposed by Harvey *et al.* [39], which is an extension of the work of Tseng and Hedrick [111].

### *7.4.2 Implementation of saturation function for semi-active systems*

For a linear system (7.10) with quadratic Lagrangian (7.11) subject to semi-active constraints of the form given by Equation (7.18) on each control $u_k(t)$ ($k = 1, ..., m$), the saturation function (7.16) can be implemented numerically as follows [39]:

1. At time $t$, find optimal unconstrained control $\mathbf{u}_{\text{active}}(t)$ from Equation (7.15).

2. For $k = 1, ..., m$, find the velocity across $k$th actuator $v_k(t)$ and perform the following checks:

   (a) if $\mathbf{c}^{(k)}(\mathbf{x}, u_{k,\text{active}}; t) \leq \mathbf{0}$, then set $u_k^*(t) = u_{k,\text{active}}(t)$, set $\mu_1^{(k)}(t) = 0$, set $\mu_2^{(k)}(t) = 0$, and break;

(b) if $u_{k,\text{active}}(t) \cdot v_k(t) < 0$, then set $u_k^*(t) = 0$, set $\mu_1^{(k)}(t) = 0$, $\mu_2^{(k)}(t) \neq 0$ is yet to be determined, and break;

(c) if $|v_k(t)| > u_{k,\max}/c_{k,\max}$, then set $u_k^*(t) = u_{k,\max}\,\text{sign}(u_{k,\text{active}}(t))$ where sign$(\cdot)$ is the signum function, $\mu_1^{(k)}(t) \neq 0$ is yet to be determined, set $\mu_2^{(k)}(t) = 0$, and break;

(d) if $v_k(t) = 0$, then set $u_k^*(t) = 0$, set $\mu_1^{(k)}(t) = 0$, set $\mu_2^{(k)}(t) = 0$, and break;

(e) otherwise, set $u_k^*(t) = c_{k,\max} v_k(t)$, set $\mu_1^{(k)}(t) = 0$, $\mu_2^{(k)}(t) \neq 0$ is yet to be determined.

3. With optimal, saturated controls $\mathbf{u}^*(t)$, solve for the corresponding optimal, non-zero $\boldsymbol{\mu}^*(t)$ from

$$\mathbf{0} = \mathbf{R}\mathbf{u}^*(t) + \mathbf{S}^\mathsf{T}\mathbf{x}(t) + \mathbf{B}^\mathsf{T}\boldsymbol{\lambda}(t) + (\partial \mathbf{c}^\mathsf{T}/\partial \mathbf{u})\big|_{\mathbf{u}^*(t)}\boldsymbol{\mu}(t)\,.$$

Note that step 2(d) is in place to handle the singularity in Equation (7.12c) at $v_k(t) = 0$; i.e. for $v_k(t) = 0$, the equality constraint $u_k(t) = 0$ must be satisfied, thus making $\mu_2^{(k)}(t)$ arbitrary, for which we have chosen $\mu_2^{(k)}(t) = 0$. The above procedure is a means of determining the optimal control and inequality constraint Lagrange multiplier instantaneously. In MATLAB the saturation function can be implemented by calling a function such as `sat(x,uactive,p)` given in Appendix C.

In solving for $\mathbf{u}^*(t)$ and $\boldsymbol{\mu}^*(t)$ and substituting them into Equations (7.12a) and (7.12b), the TPBVP is now *unconstrained*, as given by

$$\frac{\mathrm{d}}{\mathrm{d}t}\begin{bmatrix}\mathbf{x}(t)\\ \boldsymbol{\lambda}(t)\end{bmatrix} = \begin{bmatrix}\mathbf{A} & \mathbf{0}\\ -\mathbf{Q} & -\mathbf{A}^\mathsf{T}\end{bmatrix}\begin{bmatrix}\mathbf{x}(t)\\ \boldsymbol{\lambda}(t)\end{bmatrix} + \begin{bmatrix}\mathbf{B}\\ -\mathbf{S}\end{bmatrix}\mathbf{u}^*(t) + \begin{bmatrix}\mathbf{0}\\ (\partial \mathbf{c}^\mathsf{T}/\partial \mathbf{x})\big|_{\mathbf{u}^*(t)}\end{bmatrix}\boldsymbol{\mu}^*(t) + \begin{bmatrix}\mathbf{B}_w\\ \mathbf{0}\end{bmatrix}\mathbf{w}(t) \tag{7.19}$$

with boundary conditions

$$\begin{bmatrix}\mathbf{x}(t_0)\\ \boldsymbol{\lambda}(t_f)\end{bmatrix} = \begin{bmatrix}\mathbf{x}_0\\ \mathbf{0}\end{bmatrix}\,. \tag{7.20}$$

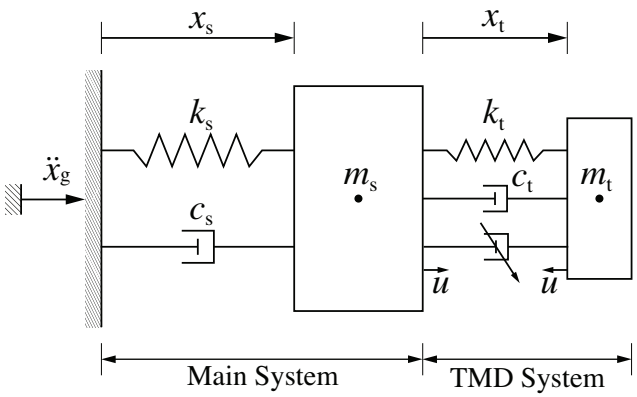


FIGURE 7.3: Structural model of a single-degree-of-freedom structure with TMD.

Note, however, that the saturation operation makes the TPBVP nonlinear for the LQ problem. To ensure that the necessary conditions (7.12) are satisfied, the states $\mathbf{x}(t)$ and costates $\boldsymbol{\lambda}(t)$ must be determined by numerically solving Equation (7.19). Numerical methods to solve unconstrained TPBVPs are well established, e.g. shooting methods, finite differences, and finite elements. In this study, the unconstrained TPBVP is solved with the MATLAB function `bvp4c.m`, which implements a collocation method with piecewise cubic interpolation satisfying the boundary conditions over each time step [117]. The following section gives a numerical demonstration of how to implement `bvp4c` to solve Equation (7.19) and determine optimal control trajectories that adhere to semi-active constraints.

## 7.5 Numerical Example

### *7.5.1 Tuned-mass-damper system*

To illustrate the performance optimization of a semi-active system, the semi-active performance of a simple semi-active TMD model is optimized to suppress seismic responses. The model is very similar to the system studied by Hrovat *et al.* [121], except that in this study the system is subjected to base acceleration $\ddot{x}_g$, as shown in Figure 7.3. The mass-normalized equations of motion which model the vibration of the system are

$$(1+\bar{m})\ddot{x}_s(t) + \bar{m}\ddot{x}_t(t) + 2\zeta_s\omega_s\dot{x}_s(t) + \omega_s^2 x_s(t) = -(1+\bar{m})\ddot{x}_g(t) \tag{7.21a}$$

$$\ddot{x}_s(t) + \ddot{x}_t(t) + 2\zeta_t\omega_t\dot{x}_t(t) + \omega_t^2 x_t(t) + u(t)/m_t = -\ddot{x}_g(t) \tag{7.21b}$$

with the following parameters defined [121]:

$$\bar{m} = \frac{m_\mathrm{t}}{m_\mathrm{s}}, \qquad \omega_\mathrm{s} = \sqrt{\frac{k_\mathrm{s}}{m_\mathrm{s}}}, \qquad \omega_\mathrm{t} = \sqrt{\frac{k_\mathrm{t}}{m_\mathrm{t}}}, \qquad \zeta_\mathrm{s} = \frac{c_\mathrm{s}}{2m_\mathrm{s}\omega_\mathrm{s}}, \qquad \zeta_\mathrm{t} = \frac{c_\mathrm{t}}{2m_\mathrm{t}\omega_\mathrm{t}}. \tag{7.22}$$

Equations (7.21) can be represented in state-space form (7.10) where $w(t) = \ddot{x}_g(t)$,

$$x(t) = [x_\mathrm{s}(t)\ x_\mathrm{t}(t)\ \dot{x}_\mathrm{s}(t)\ \dot{x}_\mathrm{t}(t)]^\mathsf{T},$$

$$\mathbf{A} = \begin{bmatrix} 0 & 0 & 1 & 0 \\ 0 & 0 & 0 & 1 \\ -\omega_\mathrm{s}^2 & \bar{m}\omega_\mathrm{t}^2 & -2\zeta_\mathrm{s}\omega_\mathrm{s} & \bar{m}2\zeta_\mathrm{t}\omega_\mathrm{t} \\ \omega_\mathrm{s}^2 & -(1+\bar{m})\omega_\mathrm{t}^2 & 2\zeta_\mathrm{s}\omega_\mathrm{s} & -(1+\bar{m})2\zeta_\mathrm{t}\omega_\mathrm{t} \end{bmatrix}, \ \mathbf{B} = \begin{bmatrix} 0 \\ 0 \\ \bar{m}/m_\mathrm{t} \\ -(1+\bar{m})/m_\mathrm{t} \end{bmatrix}, \ \mathbf{B}_w = \begin{bmatrix} 0 \\ 0 \\ -1 \\ 0 \end{bmatrix}.$$

The mass ratio $\bar{m} = 0.10$, and the TMD natural frequency $\omega_\mathrm{t}$ is the optimum tuning frequency $\omega_\mathrm{t}^*$ discussed in the next subsection. Table 7.1 gives numerical values for the system parameters. As a benchmark for comparison, the optimal performance will be compared to the following three cases.

*Optimized passive TMD*

A passive TMD with optimized parameters is used as the first benchmark for comparison. Parameter optimization of the passive TMD results in the following expressions for $\omega_\mathrm{t}^*$ and $\zeta_\mathrm{t}^*$ [122]:

$$\text{optimum tuning frequency:} \qquad \omega_\mathrm{t}^* = \frac{\omega_\mathrm{s}}{1+\bar{m}}, \tag{7.23a}$$

$$\text{optimum passive damping ratio:} \qquad \zeta_\mathrm{t}^* = \sqrt{\frac{3\bar{m}}{8(1+\bar{m})}}. \tag{7.23b}$$

Table 7.1 gives numerical values for the passive TMD system parameters. Note the passive damping force, $c_\mathrm{t}^* v(t)$, is to be clipped at the same level $u_\mathrm{max}$ as the semi-active device to ensure a fair comparison.

TABLE 7.1: Parameter values used in simulation.

| Building data | Semi-Active TMD data | Passive TMD data [122] |
|---|---|---|
| $m_s = 1 \times 10^6$ kg | $m_t = 1 \times 10^5$ kg | $m_t = 1 \times 10^5$ kg |
| $k_s = 1 \times 10^6$ N/m | $k_t^* = 8.26 \times 10^4$ N/m | $k_t^* = 8.26 \times 10^4$ N/m |
| $c_s = 2 \times 10^4$ N s/m | $c_t = 1.82 \times 10^3$ N s/m | $c_t^* = 3.36 \times 10^4$ N s/m |
| $\zeta_s = 0.01$ | $\zeta_t = 0.01$ | $\zeta_t^* = 0.185$ |
| $\omega_s = 1.0$ rad/s | $\omega_t^* = 0.909$ rad/s | $\omega_t^* = 0.909$ rad/s |

*Clipped LQR*

The second control scheme—clipped LQR—is a somewhat *ad hoc* yet prevalent sub-optimal scheme, based on linear quadratic regulator (LQR) theory. Define the linear feedback control $u_{\text{LQR}}(t) = -\mathbf{R}^{-1}(\mathbf{PB} + \mathbf{S})^{\mathsf{T}}\mathbf{x}(t)$, where $\mathbf{P}$ is found by solving the algebraic Riccati equation

$$\mathbf{0} = \mathbf{A}^{\mathsf{T}}\mathbf{P} + \boldsymbol{P}\mathbf{A} - (\mathbf{PB} + \mathbf{S})\mathbf{R}^{-1}(\mathbf{PB} + \mathbf{S})^{\mathsf{T}} + \mathbf{Q}. \tag{7.24}$$

In order to be able to be implemented $u_{\text{LQR}}$ directly in the compliant damper model, feedback controls are *clipped* when the prescribed forces is infeasible.

*Uncontrolled*

Finally, the performance of the optimal control trajectory is juxtaposed against an uncontrolled structure with no TMD, which is essentially the response of a SDOF system with parameters given in the first column of Table 7.1.

### *7.5.2 Pulse-like disturbance model*

Two types of ground motions are considered in this study: an idealized pulse and a historical ground motion record. Analytical pulse models are useful in the systematic design and assessment of seismic protective systems. Furthermore, due to the smooth nature of the disturbance and responses, simulations are less computationally demanding, which can accelerate parameter tuning, e.g. determining weighting matrices $\mathbf{Q}$, $\mathbf{R}$, and $\mathbf{S}$.

The pulse acceleration in this study is given by [39]

$$\ddot{x}_g(t) = \left[(t - t_0)/\tau\right]^{\eta} \exp\left[-(t - t_0)/\tau\right] \cos\left[\omega_p(t - t_0) - \phi\right] . \tag{7.25}$$

Accelerations are zero for $t < t_0$ and have a predominant period $T_p = 2\pi/\omega_p$. In order for the record to contain $N$ cycles of strong motion, the decay time constant $\tau$ is set to $NT_p/4$. Ground acceleration records should have negligibly small velocity and small displacement at the end of the record. For a zero terminal velocity, the phase constant $\phi$ should be [39]

$$\tan\phi = \left[3(\tau\omega_p)^2 - 1\right]/\left[3(\tau\omega_p) - (\tau\omega_p)^3\right] . \tag{7.26}$$

To enforce small residual displacements the second derivative of a scaled logistic is iteratively subtracted from the acceleration record until the displacement at the end of the record is close to zero. The associated fixed-point map is

$$\ddot{x}_g(t) \leftarrow \ddot{x}_g(t) - x_g(t_f) \exp(-s)[1 + \exp(-s)]^3[\exp(-s) - 1]/(\tau/2)^2 , \tag{7.27}$$

where $x_g(t_f)$ is the displacement at the end of the record, and $s$ is a scaled time variable equal to $(t - t_0 - \eta\tau)/(\tau/2)$. In applying the fixed-point-map (7.27), accelerations should not be reset to zero for $t < t_0$. For $\eta = 2$, $1 < N < 5$, and $0.5 < T_p < 4$ s, peak velocities scale with $T_p$ and are approximately given by

$$\dot{x}_g^{\max} = \max\left[4.063N^{-2.165}\exp(-4.403/N), 2.329N^{-1.336}\exp(-5.693/N)\right]T_p \pm 0.5\% .$$

He and Agrawal [123] validated a similar pulse model through comparison with numerous ground motions, corresponding response spectra, and the performance of passive energy dissipation systems. The pulse model used in the present work has a terminal velocity of zero (from Equation (7.26)) and a terminal displacement of zero (from Equation (7.27)). In this study, disturbance waveforms were scaled to match prescribed peak velocity values $V_p$ by scaling accelerations by a factor of $V_p/\dot{x}_g^{\max}$. Figure 3(a) illustrates a sample disturbance record using the following disturbance parameters: $\omega_p = 1.0$ rad/s, $V_p = 0.8$ m/s, $t_0 = 2.0$ s, $\eta = 2$, and $N = 2.0$.

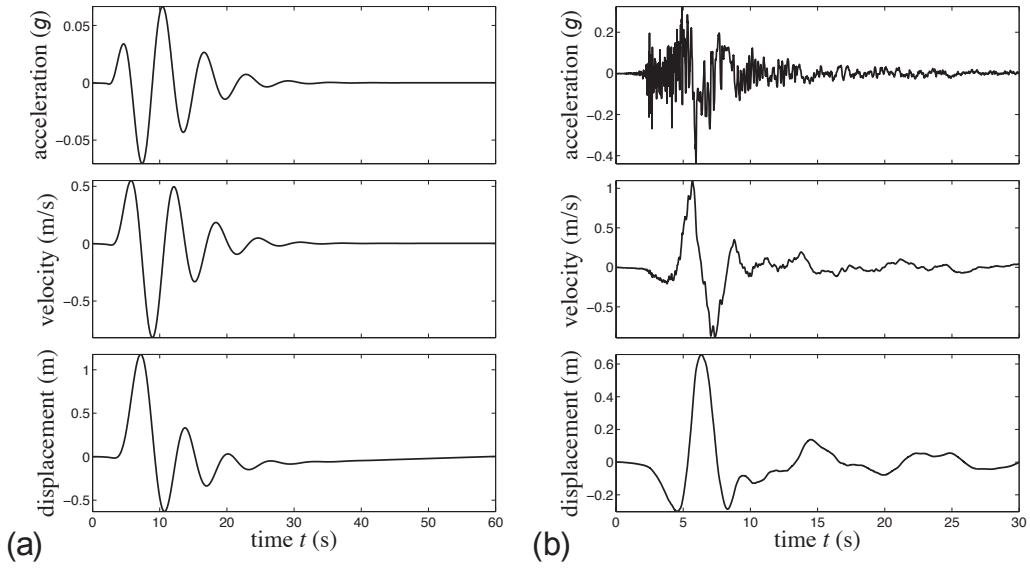


FIGURE 7.4: Acceleration, velocity, and displacement time histories of a pulse-like ground motion and a recorded ground motion. (a) Pulse-like ground motion for parameter values given in Section 7.5.2; (b) 1979 Imperial Valley earthquake, El Centro Array #6 -230°.

### *7.5.3 Performance index and numerical values*

In this example the Lagrangian $L(\cdot)$ is selected as the square of the total acceleration of the primary structure:

$$L(\boldsymbol{x}, u; t) = \tfrac{1}{2}[\ddot{x}_{\mathrm{g}}(t) + \ddot{x}_{\mathrm{s}}(t)]^2 \equiv \tfrac{1}{2}[\mathbf{A}_{(3,:)}\mathbf{x}(t) + \mathbf{B}_{(3)}u(t)]^2 \tag{7.28}$$

where $\mathbf{A}_{(3,:)}$ is the third row of the dynamics matrix and $\mathbf{B}_{(3)}$ is the third entry of the control input vector. The state, control input, and cross weighting matrices are thus $\mathbf{Q} = \mathbf{A}_{(3,:)}^{\mathsf{T}}\mathbf{A}_{(3,:)}$, $R = \mathbf{B}_{(3)}\mathbf{B}_{(3)}$, and $\mathbf{S} = \mathbf{A}_{(3,:)}^{\mathsf{T}}\mathbf{B}_{(3)}$.

We consider only adjustable control forces $u(t)$ that are constrained by Equation (9.20). For the constraint $g_1(\mathbf{x}, u; t)$, the maximum semi-active force $u_{\max} = 5 \times 10^4$ N is used in simulation. For the maximum dissipating constraint $g_2(\mathbf{x}, u; t)$, the velocity across the actuator is $\dot{x}_{\mathrm{t}} = \mathbf{T}^{\mathsf{T}}\mathbf{x}$ for which $\mathbf{T}^{\mathsf{T}} = [0\ 0\ 0\ 1]$. The maximum damping coefficient is taken to be $c_{\max} = 2\zeta_{\max}\omega_{\mathrm{t}}m_{\mathrm{t}}$, with $\zeta_{\max} = 18$ percent.

### *7.5.4* MATLAB *procedure*

Appendix C gives sample code for this example. The procedure involves first initializing the model parameters (line 2). The variables `dt` and `nT` are the time step and length of the time vector `t`, respectively, used to linearly interpolate the disturbance history `w` at intermediate times. The initial states `x0` and terminal costates `lf` must also be specified. Concatenating the state and costate into a single vector, define `z=[x;l]`. Specify global variables (line 1), which are accessed by the ODE function `zdot(t,z,w)`, the boundary condition (BC) function `bcfun(z0,zf,x0,lf)`, and the saturation function `sat(x,uactive,l)`.

In line 4, the `options` are specified using `bvpset`. The maximum mesh discretization (the maximum number of time steps) `NMax` is increased to avoid premature termination of `bvp4c`; because `bvp4c` uses an adaptive mesh, with `NMax` too small the evaluation may be terminated before convergence is met. By setting `Stats` to `on`, the simulation results are displayed, e.g. number of ODE calls, number of BC calls.

`bvp4c` requires an initial guess for the trajectories, for which a constant initialization of 5×`eps` is selected for this example using the function `bvpinit`. An initial guess of zero is not permitted because the BCs would be automatically satisfied and `bvp4c` would fail to run.

In line 6, `bvp4c` is called. The four arguments to `bvp4c` are the ODE function `zdot(t,z,w)` given in Appendix C which represents Equation (7.19); the BC function in Equation (7.20), given in Appendix C by the function `bcfun(z0,zf,z0,lf)`; the initial guess for the solution `solinit`; and the previously defined `options`. The output `sol` of `bvp4c` must then be evaluated using the command `z = deval(sol,t)` for the time series `t`. Finally, the state and costate histories may be extracted from `z`.

### 7.5.5 *Optimized semi-active control trajectories*

The proposed method is now applied to the previously described TMD model under two loading scenarios. First, a pulse-like disturbance is used to validate that the optimized trajectories satisfy the necessary conditions. Then, optimal semi-active trajectories are computed for a recorded earthquake ground motion. In both cases, a comparison is make between the optimal semi-active controller, the optimized passive TMD, the clipped LQR controller, and the uncontrolled system.

*Pulse-like ground motion*

The converged optimal semi-active trajectory, the passive trajectory, the clipped LQR trajectory, and uncontrolled trajectory are given in Figure 7.5, along with the primary structure total acceleration ($\ddot{x}_g + \ddot{x}_s$) history and the cumulative objective function $J$. The control force $u(t)$ versus the velocity across the actuator $v(t)$ shows that the semi-active constraint is strictly satisfied. As evident from the control force history, the optimal trajectory requires less energy than the clipped LQR and passive controllers (in an $L_1$ sense). As observed from Figure 7.5, the optimal control significantly reduces the mean-square acceleration (i.e. $J$), as compared to the passive, clipped LQR, and uncontrolled systems—approximately 33%, 47%, and 89%, respectively.

Figure 7.6 shows the constraint time histories and the corresponding Lagrange multiplier. We see that the complementary slackness condition (7.13) is strictly satisfied by the optimal trajectory. That is to say, the Lagrange multiplier is turned on when the control input desires to be infeasible, pinning the trajectory to the associated constraint boundary. It is clear that the term $\boldsymbol{\mu}^\intercal(t)\mathbf{c}(\mathbf{x}, u; t) \equiv 0, \forall t$.

Figure 6 shows converged control histories from three initial guesses: constant at `5*eps*ones(8,1)`, constant at `10*ones(8,1)`, and the active solution. The number of ODE calls to reach convergence varies: approximately $5.4 \times 10^5$, $3.6 \times 10^5$, and $5.5 \times 10^5$

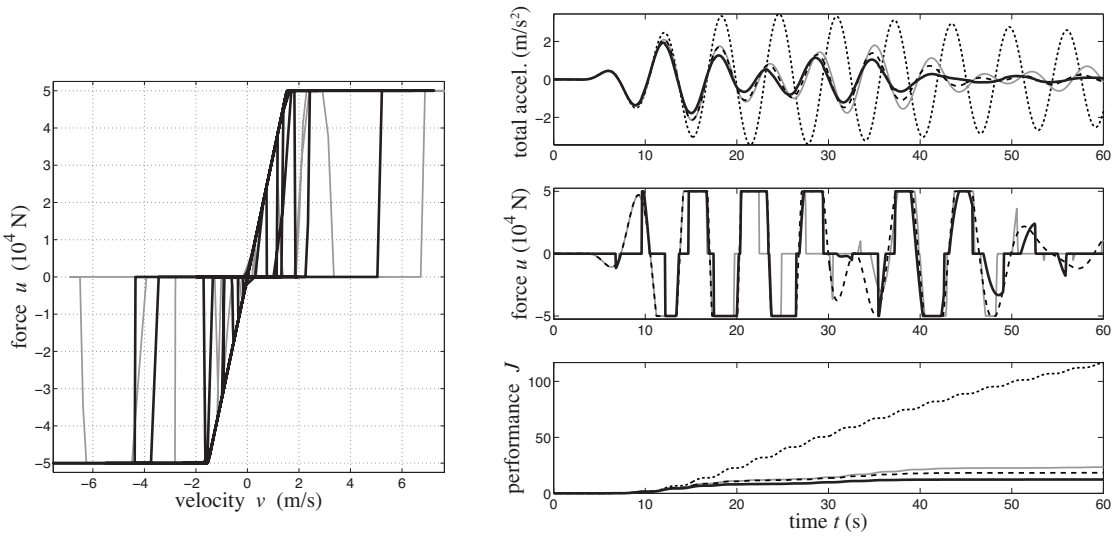


FIGURE 7.5: Responses to a pulse-like disturbance: comparison of optimal (thick) with passive (dashed), clipped LQR (gray), and uncontrolled (dotted).

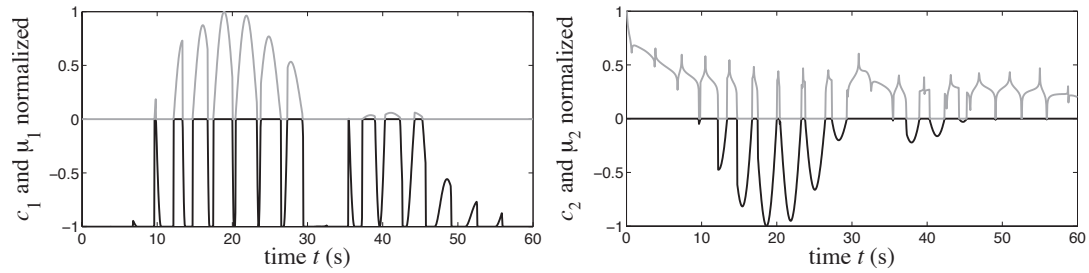


FIGURE 7.6: Normalized constraint $c_i(\mathbf{x}, u; t)$ and normalized Lagrange multiplier $\mu_i(t)$ time histories (black: constraint $c_i(\mathbf{x}, u; t)$; gray: Lagrange multiplier $\mu_i(t)$).

ODE calls, respectively. The speed of convergence is dependent on the initial guess; with a bad initial guess convergence may be very slow. Nonetheless, for all three initial guesses, the method converges to the same optimal trajectories.

*Earthquake ground motion*

Now we consider a recorded earthquake ground motion. The recorded ground motion is the E06230 component of the 1979 Imperial Valley earthquake [124]. Figure 3(b) illustrates the disturbance record. The optimal control force trajectory is illustrated in Figure 7, along with the structure's total acceleration and the performance history. Once again, the optimal control significantly outperforms the uncontrolled system (68%) and marginally

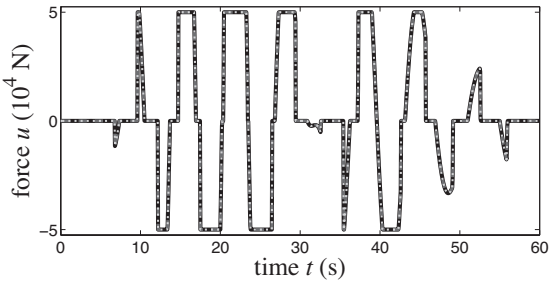


FIGURE 7.7: Converged control force histories from three initial guesses (black: 5×`eps`; dashed dark gray: 10; dotted light gray: active solution).

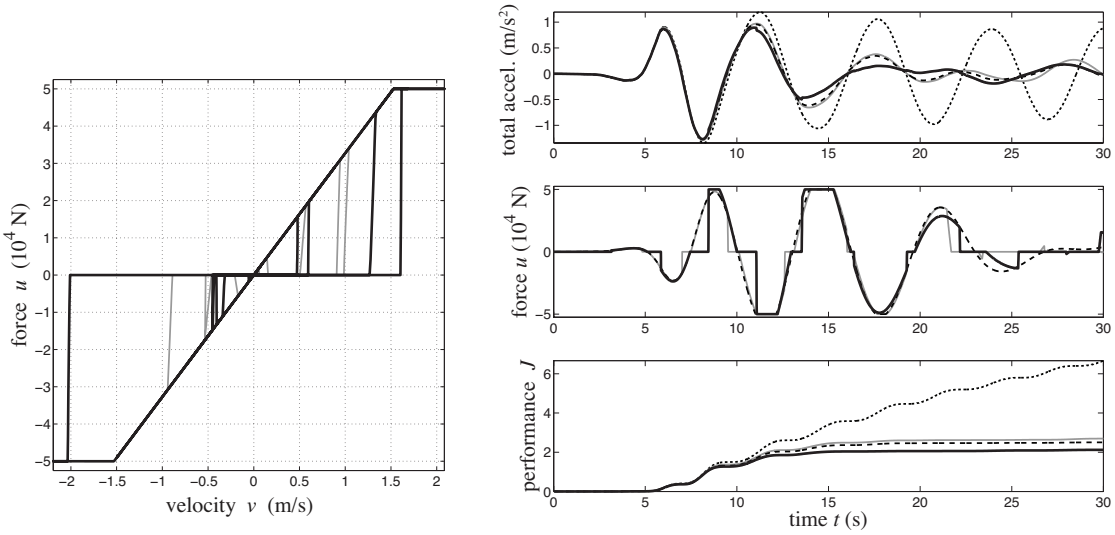


FIGURE 7.8: Recorded ground motion test: comparison of optimal (thick) with passive (dashed), clipped LQR (gray), and uncontrolled (dotted).

outperforms the passive and clipped LQR controllers (15% and 21%, respectively). The proposed method is robust enough to handle non-smooth ground motions such as recorded earthquake records. However, convergence required approximately $1.4 \times 10^6$ ODE evaluations.

## 7.6 Summary

The ability to answer the question "How much could semi-active control improve performance in this application?" can be powerful in establishing the potential for a new semi-active control device or a new semi-active control application. Methods of constrained

optimal control, as outlined in this chapter, provide an easy and ready means to generate such answers. In this chapter a general approach to inequality constrained optimal control problems was presented. The method determines controls and Lagrange multipliers to enforce inequality state and/or control constraints while satisfying the stationarity condition. Inserting these controls and Lagrange multipliers into the state and costate equations results in an unconstrained TPBVP.

An easily implementable saturation procedure is described for a semi-active device with damping-rate and force-saturation constraints. The illustrative example presented is meant to serve as a guide and is therefore intentionally simple. The proposed procedure will be applied in Chapter 8 to the optimal semi-active control of a rolling isolation system.

### *7.6.1 Possible extensions*

This chapter is intended to encourage the application of optimal semi-active control to answer many important questions. The list of topics below are a sample of studies that could be performed with the methods outlined in this chapter.

- Time-lag in semi-active control systems can certainly affect the best achievable performance. By applying optimal semi-active control analysis to systems with a time-lag will show how important the time-lag effects can be. Incorporating time-lag into the semi-active damper, where the semi-active damping force is given by $\dot{f}(t) = (u(t) - f(t))/T$ and $T$ is the time-lag, typically 0.02 to 0.10 seconds, would add realism to the simulation results. The state equations would remain linear.

- Different semi-active devices have different behavior. By applying optimal semi-active control analysis to systems controlled by different semi-active devices, the relative potential of different devices can be assessed.

- Semi-active control may potentially provide greater performance for linear structural systems than for nonlinear or hysteretic structural systems. Application of op-

timal semi-active control analysis to structures with different nonlinearities would show how semi-active control would benefit the behavior of one type of structure as compared to another.

- This study addresses a system with a single semi-active device. Extension to systems with multiple semi-active devices may be studied. In doing so, care must be taken in the saturation function so that coupling between devices is properly accounted for.

- The constraints imposed upon the optimization in this study pertain only to the semi-active device. The constrained optimization methods described in this paper can also be applied to constrain peak responses. For example, in earthquake engineering, peak responses are typically of greater interest than mean squared responses [124]. Extending this method to suppress peak response is a matter of removing the quadratic state cost, so that

$$J = \int_0^{t_f} \tfrac{1}{2} R u^2(t)\, \mathrm{d}t,$$

and adding a constraint on the peak response, for example,

$$c_x = \max |x_s(t)| - x_{\text{allow}} \leq 0.$$

The method here would be to iteratively reduce $x_{\text{allow}}$ until no feasible solution can be found.

- The methodology presented in this paper can be extended to minimizing peak responses by changing the quadratic integrand to a fourth or higher (even) order, and by reducing the time horizon to the first few large cycles of response. Doing so would result in nonlinear costate dynamics.

- Optimal control trajectories could be investigated and parameterized in order to develop a class of nonlinear feedback control rules inspired by these optimal performance studies.

# 8

# Assessment of a Semi-Active Rolling Isolation System

## 8.1 Background

As pointed out in Chapters 3 and 4, rolling isolation systems (RISs) are lightly damped, and supplemental damping or intelligent control may be beneficial to the systems' performances. During low-level seismic events, passive isolation systems perform extremely well [2, 13, 125, 126]. Whereas, when subjected to earthquakes with high-amplitude near-fault ground motions, considerable amplification will produce excessive isolator displacements endangering the isolated object [125]. Passive damping is effective in reducing isolator drifts but at the expense of increasing equipment accelerations at high frequencies [56]. Another drawback of passive damping is the inability to adjust system parameters to achieve the desired performance objectives without *a priori* knowledge of the external excitation. Therefore, it would be desirable to be able to adaptively adjust system parameters in order to optimize the performance of RISs for both near- and far-field ground motions. To this end, smart isolation systems have been proposed. In particular semi-active control systems are attractive due to their guaranteed stability and low power

consumption [41, 57, 58].

In this chapter we optimize open-loop controls for a vibration isolation system controlled via variable damping forces, using the method of Chapter 7. Control trajectories are optimized to minimize peak total response accelerations when the system is excited by a pulse-like acceleration at the base. Pulse response spectra are compiled and compared to passive linear viscous damping for the SDOF system. Potential parameterized feedback control laws are deduced from optimal control trajectories for different excitation frequencies. Performance metrics for a multi-degree-of-freedom isolation system are compared between the proposed method, the clipped linear-quadratic regulator (LQR) feedback control [127], and a passively-damped system.

## 8.2 Linear Model of an Isolation System

This section describes a linear time-invariant (LTI) model of a semi-actively controlled isolation system. Consider the semi-active isolation system shown in Figure 8.1 being exogenously excited by base accelerations $\ddot{w}_x$, $\ddot{w}_y$, and $\ddot{w}_\theta$. Equations of state for this system considering the kinematics of large rotations and rolling contacts were derived in Chapter 3. Equations (3.41) can be linearized in displacements $\{\bar{x}, \bar{y}, \bar{\theta}\}$, velocities $\{\dot{\bar{x}}, \dot{\bar{y}}, \dot{\bar{\theta}}\}$, and disturbance $w_\theta$, resulting in the following equations of motion:

$$m[\ddot{w}_x + \ddot{\bar{x}} - e_y(\ddot{\bar{\theta}} + \ddot{w}_\theta)] + C_\mathrm{b}\dot{\bar{x}} + \tfrac{1}{2}mg\alpha(\bar{x} - e_y\bar{\theta}) + F_{\mathrm{s}1} = 0 \tag{8.1a}$$

$$m[\ddot{w}_y + \ddot{\bar{y}} + e_x(\ddot{\bar{\theta}} + \ddot{w}_\theta)] + C_\mathrm{b}\dot{\bar{y}} + \tfrac{1}{2}mg\alpha(\bar{y} + e_x\bar{\theta}) + F_{\mathrm{s}2} + F_{\mathrm{s}3} = 0 \tag{8.1b}$$

$$\begin{aligned} me_x(\ddot{w}_y + \ddot{\bar{y}}) - me_y(\ddot{w}_x + \ddot{\bar{x}}) + I(\ddot{w}_\theta + \ddot{\bar{\theta}}) + C_\mathrm{b}\dot{\bar{\theta}}(b^2 + a^2) \\ + \tfrac{1}{2}mg\alpha(e_x\bar{y} - e_y\bar{x} + (a^2 + b^2)\bar{\theta}) - aF_{\mathrm{s}2} + aF_{\mathrm{s}3} = 0 \end{aligned} \tag{8.1c}$$

for parabolic bowls of curvature $\alpha$, gravitational acceleration $g = 9.81$ m/s$^2$, and equipment mass $m$ taken to be 500 kg. Inherent damping is treated through dissipative forces acting at the ball location with damping rate $C_\mathrm{b}$; as discussed previously, the systems is very lightly damped (~2%).

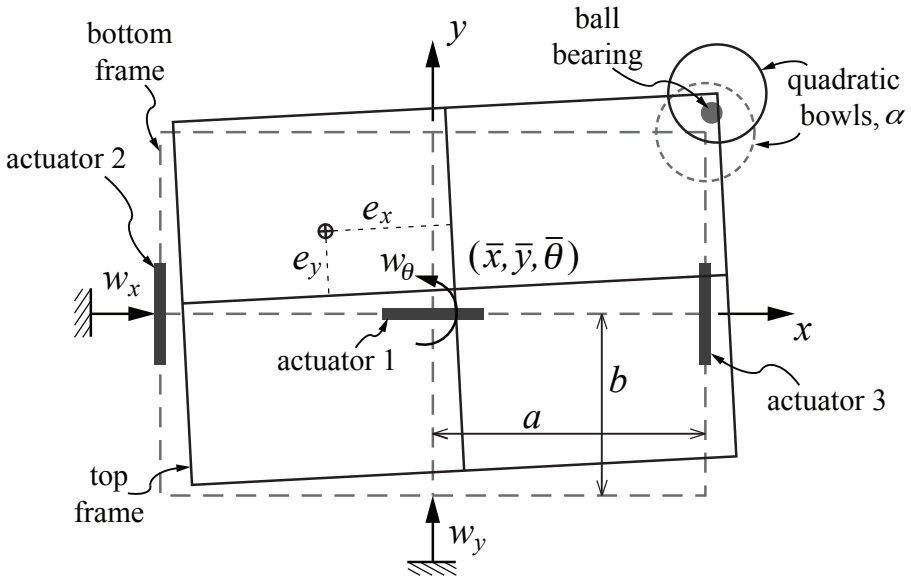


FIGURE 8.1: Semi-active actuator configuration and platform geometry.

The system is actuated by semi-active forces $F_{sk}$ $(k = 1, 2, 3)$. In this application the damping force is modeled as a controllable internal force and may be interpreted as a friction coefficient acting with time lag $T_u$. The response of the semi-active force may be approximated as a first-order dynamic equation as follows:

$$\dot{F}_{sk}(t) = (u_k(t) - F_{sk}(t))/T_u \tag{8.2}$$

where $u_k(t)$ is a target control force, and $T_u$ is between 0.02 s and 0.05 s.

Equations (8.1) may alternately be written in matrix form as follows:

$$\mathbf{M}\begin{bmatrix}\ddot{\bar{x}}\\ \ddot{\bar{y}}\\ \ddot{\bar{\theta}}\end{bmatrix} + \mathbf{C}\begin{bmatrix}\dot{\bar{x}}\\ \dot{\bar{y}}\\ \dot{\bar{\theta}}\end{bmatrix} + \mathbf{K}\begin{bmatrix}\bar{x}\\ \bar{y}\\ \bar{\theta}\end{bmatrix} + \mathbf{F}\begin{bmatrix}F_{s1}\\ F_{s2}\\ F_{s3}\end{bmatrix} = -\mathbf{M}\begin{bmatrix}\ddot{w}_x\\ \ddot{w}_y\\ \ddot{w}_\theta\end{bmatrix} \tag{8.3}$$

where

$$\mathbf{M} \equiv \begin{bmatrix} m & 0 & -me_y \\ 0 & m & me_x \\ -me_y & me_x & I \end{bmatrix}, \qquad \mathbf{C} \equiv \begin{bmatrix} C_b & 0 & 0 \\ 0 & C_b & 0 \\ 0 & 0 & C_b(a^2+b^2) \end{bmatrix},$$

$$\mathbf{K} \equiv \tfrac{1}{2}mg\alpha \begin{bmatrix} 1 & 0 & -e_y \\ 0 & 1 & e_x \\ -e_y & e_x & a^2+b^2 \end{bmatrix}, \qquad \mathbf{F} \equiv \begin{bmatrix} 1 & 0 & 0 \\ 0 & 1 & 1 \\ 0 & -a & a \end{bmatrix}.$$

By defining the state variables for this system $\mathbf{x} = [\bar{x}\ \bar{y}\ \bar{\theta}\ \dot{\bar{x}}\ \dot{\bar{y}}\ \dot{\bar{\theta}}\ F_{s1}\ F_{s2}\ F_{s3}]^\intercal$ we can rewrite Equation (8.3) in LTI form (7.10) where

$$\mathbf{A} = \begin{bmatrix} \mathbf{0} & \mathbf{I} & \mathbf{0} \\ -\mathbf{M}^{-1}\mathbf{K} & -\mathbf{M}^{-1}\mathbf{C} & -\mathbf{M}^{-1}\mathbf{F} \\ \mathbf{0} & \mathbf{0} & -\frac{1}{T_u}\mathbf{I} \end{bmatrix}, \qquad \mathbf{B} = \begin{bmatrix} \mathbf{0} \\ \mathbf{0} \\ \frac{1}{T_u}\mathbf{I} \end{bmatrix}, \qquad \mathbf{B}_w = \begin{bmatrix} \mathbf{0} \\ -\mathbf{I} \\ \mathbf{0} \end{bmatrix}, \qquad \mathbf{w} = \begin{bmatrix} \ddot{w}_x \\ \ddot{w}_y \\ \ddot{w}_\theta \end{bmatrix}$$

and $\mathbf{I}$ is the identity matrix.

### *8.2.1 Semi-active force constraints*

Other treatments of the semi-active vibration suppression problem [111, 127, 128] have formulated the problem as a damping rate control. In doing so, the state dynamics are bilinear in states and controls, and subsequently the costate dynamics (7.9b) and stationarity condition (7.9c) are bilinear as well [120]. The advantage of damping rate control is a simplified control constraint, i.e. $u(t) \in [u_{\min}, u_{\max}]$. Using a force control approach simplifies the dynamics, i.e. linear state dynamics, but at the expense of a more complex (quadratic, mixed-type) state-control constraint. Unlike previous papers, we include an additional force saturation constraint—the proposed device has a maximum damping rate as well as a peak device force [129]. In the force control framework, such a constraint is a function of the control only while in the bilinear model, such a constraint would be a mixed-type state-control constraint.

Feasible control forces are bounded by sectors shown in Figure 7.2. Constraining the control $u_k$ consequently constrains the damping force $F_{sk}$. The controllable damper has the performance limitations described by a maximum achievable damping coefficient $c_{k,\max} > 0$ and control force amplitude $u_{k,\max}$. The former limitation may be expressed by the nonlinear constraint

$$u_k(t)\big(u_k(t) - c_{k,\max} v_k(t)\big) \le 0, \ \forall\ k \tag{8.4}$$

where $v_k(t)$ is the velocity across the $k$th actuator as given by

$$v_1 = \dot{\bar{x}}, \quad v_2 = \dot{\bar{y}} - a\dot{\bar{\theta}}, \quad v_3 = \dot{\bar{y}} + a\dot{\bar{\theta}}\ .$$

A passivity constraint is a limiting case of Equation (8.4) whereby the damping force is merely dissipative, i.e. $-u_k(t)\, v_k(t) \leq 0$. In the unsaturated passive case, an arbitrarily large force $u_k$ can be applied independent of the magnitude of the velocity. However, the device is further constrained by the force saturation limit $u_k \in [-u_{k,\max}, u_{k,\max}]$; such a constraint is given by the following inequality:

$$(u_k(t) + u_{k,\max})(u_k(t) - u_{k,\max}) \leq 0, \ \forall\, k\,. \tag{8.5}$$

Thus, the quadratic state-control constraint is

$$\mathbf{c}(\mathbf{x}, \mathbf{u}; t) = \begin{bmatrix} \mathbf{c}^{(1)}(\mathbf{x}, u_1; t) \\ \mathbf{c}^{(2)}(\mathbf{x}, u_2; t) \\ \mathbf{c}^{(3)}(\mathbf{x}, u_3; t) \end{bmatrix} \leq \mathbf{0} \tag{8.6}$$

where

$$\mathbf{c}^{(k)}(\mathbf{x}, u_k; t) \equiv \begin{bmatrix} (u_k(t) + u_{k,\max})(u_k(t) - u_{k,\max}) \\ u_k(t)(u_k(t) - c_{k,\max} v_k(t)) \end{bmatrix}. \tag{8.7}$$

### *8.2.2 Semi-active control to reduce accelerations*

Consider the controlled isolation system shown in Figure 8.1. The equation of motion of this system is represented by an LTI form (7.10) with state matrices given above. In this application, the desired forces $u_k(t)$ are sought to decrease the total acceleration experienced by the isolated mass without using too much control effort. Thus the quadratic Lagrangian $L(\cdot)$ is given by

$$L(\mathbf{x}, \mathbf{u}, t) = \tfrac{1}{2}\Big[q_x(\ddot{\tilde{x}} + \ddot{w}_x)^2 + q_y(\ddot{\tilde{y}} + \ddot{w}_y)^2 + q_\theta(\ddot{\tilde{\theta}} + \ddot{w}_\theta)^2 + \rho_1 u_1^2 + \rho_2 u_2^2 + \rho_3 u_3^2\Big]. \tag{8.8}$$

Letting $\mathbf{N} = [-\mathbf{M}^{-1}\mathbf{K} \ \ -\mathbf{M}^{-1}\mathbf{C} \ \ -\mathbf{M}^{-1}\mathbf{F}]$, the total accelerations are equal to $\mathbf{N}\mathbf{x}$ and the state weight matrix is $\mathbf{Q} = \mathbf{N}^\intercal \mathrm{diag}(q_x, q_y, q_\theta)\mathbf{N}$. There is no cross weight, thus, $\mathbf{S} = \mathbf{0}$. The control weight matrix is $\mathbf{R} = \mathrm{diag}(\rho_1, \rho_2, \rho_3)$. Weights $(q_x, q_y, q_\theta)$ are chosen such that the total acceleration is dominant in the cost as opposed to the control effort; this is done because the controls constrained by Equation (8.6) are inexpensive and, therefore,

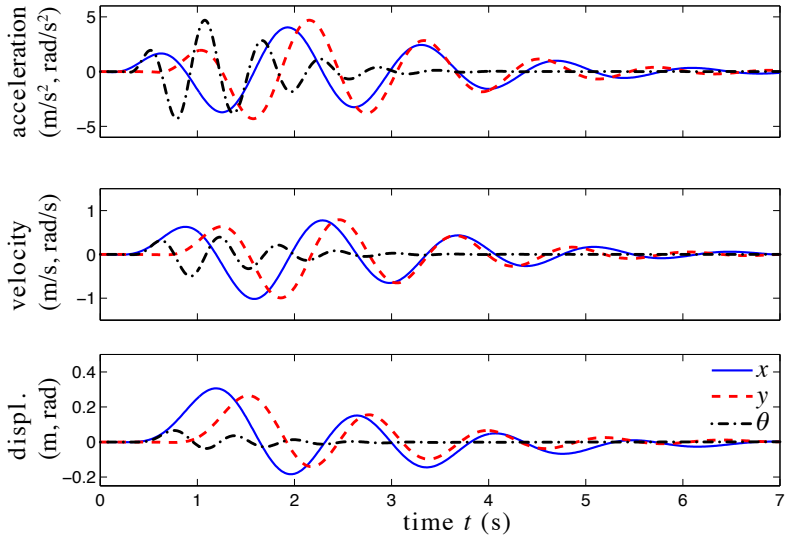


FIGURE 8.2: Disturbance records for $V_{px} = V_{py} = 1$ m/s, $V_{p\theta} = 0.5$ rad/s, $T_{px} = 1.4$ s, $T_{py} = 1.2$ s, $T_{p\theta} = 0.6$ s, $N = 2.5$, and $\eta = 2$: $x$ (——); $y$ (– – –); $\theta$ (–·–).

need not be overly-weighted. For a linear system (7.10) with quadratic Lagrangian (7.11) subject to semi-active constraints of the form given by Equation (8.7) on each control $u_k(t)$ ($k = 1, ..., m$), the saturation function sat($\cdot$) can be implemented as described in Section 7.4.2.

### *8.2.3 Disturbance Model*

External disturbances $\ddot{w}_x$, $\ddot{w}_y$ and $\ddot{w}_\theta$ represent an idealization of the motions of a floor of a building subjected to an earthquake ground motion. As such, it is dominated by a single frequency, $2\pi/T_p$, and grows and decays in amplitude over time. The pulse-like acceleration model, detailed in Section 7.5.2, is used to represent the floor motions. The disturbance applies inertial loads to the isolated mass, and is therefore specified in terms of an acceleration record (7.25). In this study $t_{0x} = 0$ s, $t_{0y} = 0.5$ s, $t_{0\theta} = 0.25$ s, $N = 2.5$ and $\eta = 2$. In this study disturbance waveforms were scaled to match prescribed peak velocity values, $V_p$, by scaling accelerations with a factor $V_p/\dot{w}_{max}$. Figure 8.2 illustrates a sample of disturbance records.

The disturbance duration $t_f$ is selected such that the peak response is captured without

accumulating too much additional cost from transient responses. The controller we desire suppresses peak responses, and with too long of a disturbance record the optimal control may gain performance by simply damping the transient response. In all simulations, duration $t_\mathrm{f}$ is found from the expression $t_\mathrm{f} = 2N \max\{T_{\mathrm{p}x}, T_{\mathrm{p}y}, T_{\mathrm{p}\theta}\}$.

## 8.3 Simulation Results

The solution method proposed in Chapter 7 is now applied to the semi-active isolation system previously described. Values for constants are given in Table 8.1 unless otherwise stated. All three devices are assumed to be identical: $u_{k,\max} = 981$ N and $c_{k,\max} = 1566$ N s/m ($k = 1, 2, 3$). These values correspond to 20 percent self-weight ($m = 500$ kg) and 50 percent damping in the first mode of vibration.

First, a SDOF system is assessed. Control trajectories are found for a range of pulse periods. At shorter period pulses ($T_{\mathrm{p}x} \in [0.4, T_{\mathrm{n}x}]$ where $T_{\mathrm{n}x} \approx 2$ s) "pseudo-negative stiffness" [130] appears to be nearly optimal whereas, at longer period pulses ($T_{\mathrm{p}x} > T_{\mathrm{n}x}$), viscous damping is optimal. Pulse response spectra are constructed to demonstrate the performance of the optimally controlled system over a clipped LQR control and two passively controlled systems with respect to four metrics: cost, $J$; peak control forces, $\max|u_1|$; peak total acceleration, $\max|\ddot{\bar{x}} + \ddot{w}_x|$; and peak relative displacement, $\max|\bar{x}|$.

Table 8.1: Semi-active control simulation parameters.

| | | | |
|---|---|---|---|
| bowl curvature | $\alpha$ | 2.0 | 1/m |
| control lag | $T_u$ | 0.05 | sec |
| ball friction damping rate | $C_\mathrm{b}$ | 62.6 | N s/m |
| mass eccentricity, $x$ | $e_x$ | 0.2 | m |
| mass eccentricity, $y$ | $e_y$ | 0.1 | m |
| frame $x$-dimension | $a$ | 0.45 | m |
| frame $y$-dimension | $b$ | 0.25 | m |
| mass moment of inertia | $I$ | 44.2 | kg m$^2$ |
| translational state weights | $q_x$, $q_y$ | $m^2$ | |
| rotational state weight | $q_\theta$ | $I^2$ | |
| control weights | $\rho_1, \rho_2, \rho_3$ | 1.0 | |

Next, the full three-degree-of-freedom system is analyzed. Twelve cases are investigated for a range of pulse periods and pulse velocities. Comparisons are made between trajectories found using the proposed optimal method and the clipped LQR method. Performance metrics are defined and compared for the optimal method and a clipped LQR scheme which are juxtaposed with a linear-viscous, passively damped system as outlined in the following section.

### *8.3.1 Isolation Control Schemes*

Here we define three control schemes, and investigate the corresponding system behaviors in Sections 8.3.2 and 8.3.3. They are now described.

*Scheme 1—optimal*

This uses the full dynamic optimization outlined in Section 7.3, finding the numerical solution of the state/costate TPBVP (7.19). The MATLAB function `bvp4c.m` [117] is used to integrate Equation (7.19).

*Scheme 2—clipped LQR*

This is a somewhat *ad hoc* yet prevalent sub-optimal scheme, based on LQR theory. In the simpler case of a linear *active* system model with quadratic cost, the optimal control equations can reduce to a simpler problem, involving the solution of the algebraic Riccati equation (ARE) given by Equation (7.24)—see for example Refs. [121, 127]. The optimal infinite-horizon controller (assuming no exogenous disturbance) can be given by a simple feedback form $\mathbf{u}_{\mathrm{LQR}}(t) = -\mathbf{R}^{-1}(\mathbf{PB} + \mathbf{S})^{\mathsf{T}}\mathbf{x}(t)$ where $\mathbf{P}$ is found from solving the ARE. In order to be able to implement directly in the compliant damper model, feedback controls $\mathbf{u}_{\mathrm{ARE}}(t)$ are *clipped* when the prescribed force is infeasible.

The shortcoming of this method arises from the infinite-horizon assumption and neglecting the disturbance $\mathbf{w}(t)$. However, it does permit a feedback controller which may be implemented in real time.

*Scheme 3—passive*

This is simple passive damper regulation. The controller is linear viscous damping, i.e. $u_k(t) = c_{\text{pass}} v_k(t)$. Two levels of damping are considered: (a) $c_{\text{pass}} = c_{\max} = 1566$ N s/m and (b) $c_{\text{pass}} = 3c_{\max}/5 = 940$ N s/m. In both cases, the passive control force is subject to saturation limit $u_{\max} = 981$ N to make a fair comparison with the semi-active controller.

Note schemes 1 and 2 are centralized control algorithms which need the full state of the system. In the case of scheme 1, the costates are required, as well. Whereas, scheme 3 is a decentralized control algorithm which needs only the states at the actuators' locations. A decentralized control algorithm is preferable in large-scale structures where a dense sensor array becomes necessary [131]. Otherwise a nonlinear observer, e.g. classical Kalman estimator, is required to approximate the full system state. However, the goal of this project is to determine the optimal performance of a semi-active isolation system, not the most practically implementable controller.

### *8.3.2 Single-degree-of-freedom system*

For the case in which the isolated mass has zero eccentricity and is excited uniaxially, i.e. $w_y(t) \equiv 0$ and $w_\theta(t) \equiv 0 \; \forall \; t$, the system's dynamics (8.1) decouple. If initial $\bar{y}$ displacement and $\bar{\theta}$ rotation are zero, the SDOF equation of motion is

$$m\ddot{\bar{x}} + C_{\text{b}}\dot{\bar{x}} + \tfrac{1}{2}mg\alpha\bar{x} + F_{\text{s1}} = -m\ddot{w}_x \; . \tag{8.9}$$

Control trajectories are found for this SDOF system when subjected to the pulse base excitation. Figure 8.3 shows the control force $u_1(t)$ versus the velocities across the actuator, $v_1(t) = \dot{\bar{x}}$. Three pulse periods are shown—1.4 s, 2.0 s, and 2.6 s—which are shorter than, at, and longer than, respectively, the natural period of the system, $T_{\text{n}x} = 2.01$ seconds. Also, two levels of excitation—$V_{\text{p}x} = 0.5$ and 1.0 m/s, termed *weak* and *strong*,

respectively—are investigated. "Pseudo-negative stiffness" [130] appears to be optimal at short pulse periods ($T_{px} < T_{nx}$) when subjected to a weak excitation, whereas for a stronger excitation, the actuator is saturated, effectively squashing the "pseudo-negative stiffness" effect. At longer periods ($T_{px} > T_{nx}$), linear viscous damping is optimal regardless of the input strength. Near resonance, a transition in optimality between "pseudo-negative stiffness" and linear viscous damping occurs.

Figure 8.4 shows four pulse-response spectra for moderate-strength excitations, $V_{px} = 1.0$ m/s. Define the ratio of the pulse period to natural period to be $\Pi_{px} \equiv T_{px}/T_{nx}$. The proposed control (scheme 1) outperforms the three other schemes in terms of cost $J$, as expected; of all admissible controls satisfying Equation (8.6), scheme 1 is optimal. We note that at short-period excitations ($\Pi_{px} < 1$) the clipped LQR control performs better than both the passive controls. However, beyond resonance ($\Pi_{px} > 1$) the passive controls perform better than the clipped LQR controller. Also, at long period where linear-viscous damping was seen to be optimal, the passive control with $c_{pass} = c_{max}$ performs equivalently to the optimal control.

Smaller device forces are necessary in the short-period regime ($\Pi_{px} < 0.4$); all four control schemes saturate the device for intermediate- to resonant-period excitations ($0.4 < \Pi_{px} < 1.3$); and at long-period excitations ($\Pi_{px} \geq 1.3$), the clipped LQR solution requires larger device forces than both passive and optimal.

In terms of peak accelerations, the optimal and clipped LQR solutions perform best at shorter pulse periods while passive and optimal perform better at longer periods. The optimal controller performs well in terms of peak acceleration because the time horizons were selected such that the peak absolute accelerations are captured but transient responses do not contribute significantly to the integral cost $J$. Because we use a quadratic cost, peak absolute accelerations weigh heavily on the cost.

Finally, the fourth spectrum shows the peak displacement of the isolated mass. Recall that displacement weight was not included in the cost, see Section 8.2.2, and thus the

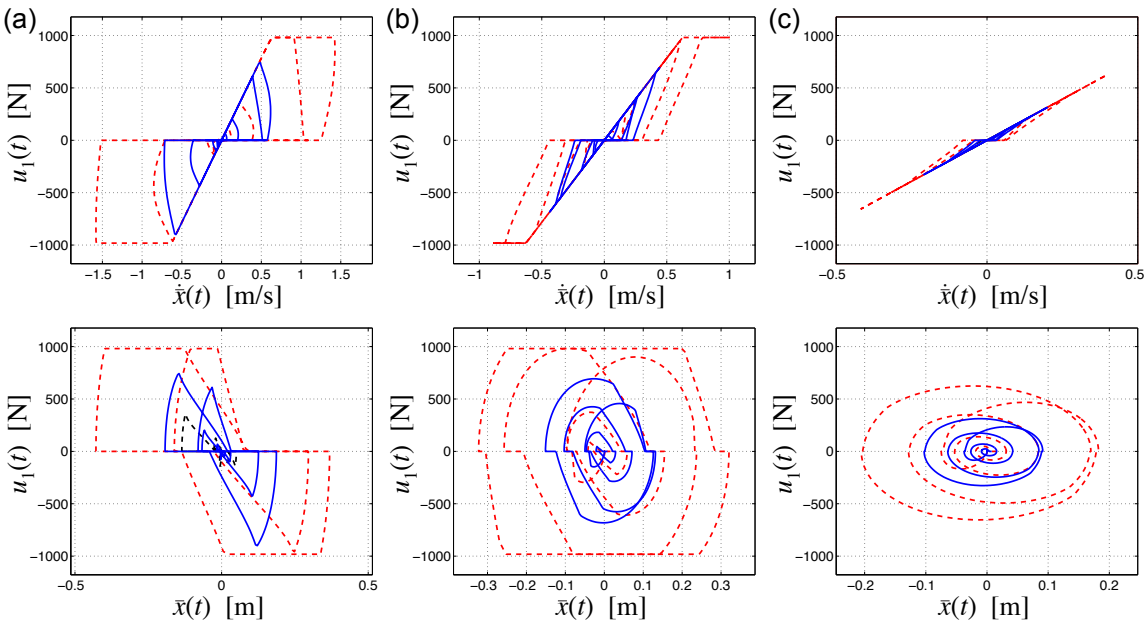


FIGURE 8.3: Single-degree-of-freedom optimal control trajectories. Control force $u_1$ versus (top) velocity $\dot{\bar{x}}$ and (bottom) displacement $\bar{x}$ across actuator 1. (a) $T_{px} = 1.4$ s; (b) $T_p = 2.0$ s; (c) $T_p = 3.0$ s. Legend: (——) $V_{px} = 0.5$ m/s and (– – –) $V_{px} = 1.0$ m/s.

optimal control will not necessarily perform well in terms of max $|\bar{x}|$. In the short-period range ($\Pi_{px} < 1$), clipped LQR performs relatively well but not in the long-period range ($\Pi_{px} > 1$) where the optimal control and passive control ($c_{pass} = c_{max}$) do exceedingly well.

### *8.3.3 Three-degree-of-freedom system*

For the full three-degree-of-freedom isolation platform with three actuators, twelve cases are investigated for varying pulse strengths and fundamental periods by varying the disturbance parameters peak-velocities $V_{px}$, $V_{py}$, and $V_{p\theta}$ and pulse-periods $T_{px}$, $T_{py}$, and $T_{p\theta}$, respectively. The three pulse strengths (*weak*, *moderate*, and *strong*) and the four pulse periods (*short*, *intermediate*, *resonant*, and *long*) are given in Table 8.2 where the natural periods of the system are $T_{nx} = 2.01$ s, $T_{ny} = 2.01$ s, and $T_{n\theta} = 0.85$ s.

Figure 8.5 shows control $u_k(t)$ trajectories versus the velocity $v_k(t)$ across actuator $k$ for four pulse period scenarios for a moderate strength excitation. The optimal trajectory is shown along with the clipped LQR solution. These two solutions are qualitatively different

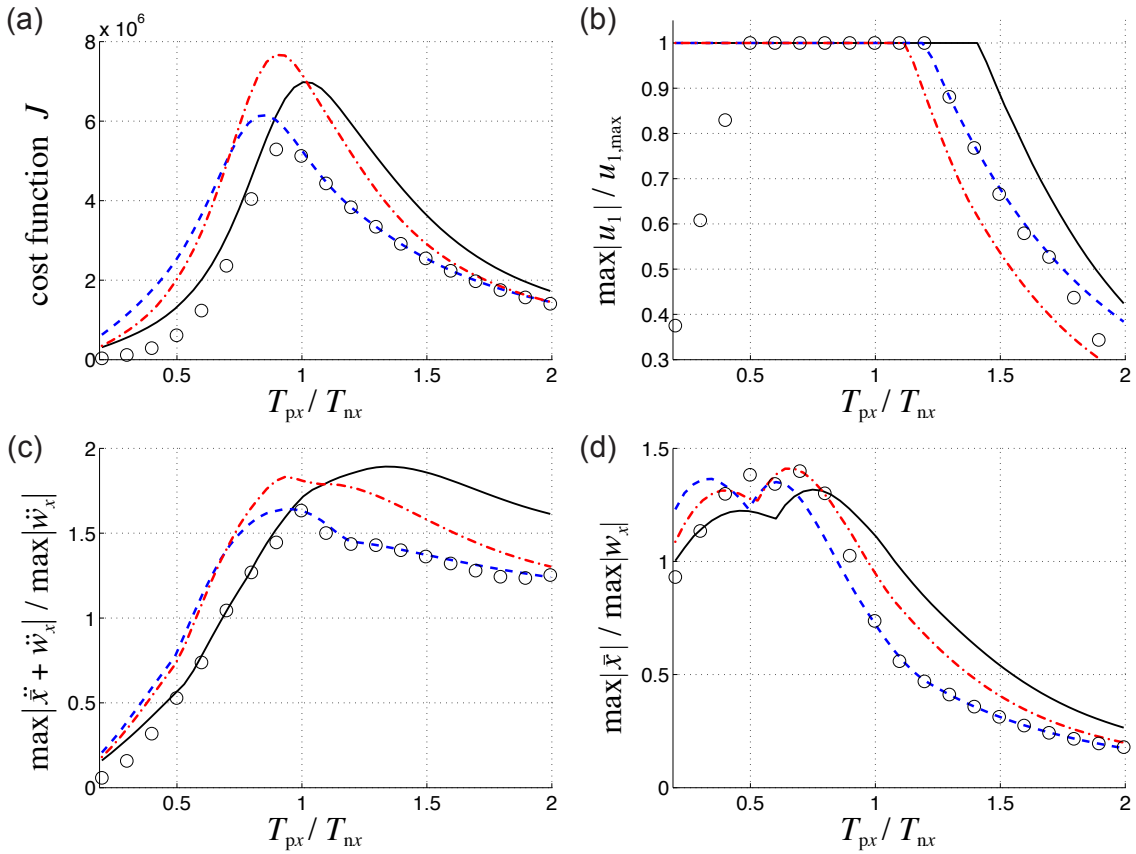


FIGURE 8.4: Single-degree-of-freedom pulse-response spectra: (a) cost function, $J$; (b) peak control force normalized, $\max|u_1|/u_{1,\max}$; (c) peak total acceleration normalized, $\max|\ddot{\bar{x}} + \ddot{w}_x|/\max|\ddot{w}_x|$; and (d) peak displacement normalized, $\max|\bar{x}|/\max|w_x|$ over a range of pulse periods $T_{px}$. Legend: (○) optimal; (—) clipped LQR; (– – –) passive $c_{\text{pass}} = 1566$ N s/m; and (–·–) passive $c_{\text{pass}} = 940$ N s/m.

especially in the longer period regimes—resonant and long period—where the optimal control trajectory mimics linear viscous damping whereas the clipped LQR solution does not. Also, velocities $v_k(t)$ are seen to be larger in the clipped LQR scheme. For shorter period excitations—short and intermediate periods—trajectories are more similar; both

TABLE 8.2: Simulated pulse strengths and periods.

| | Pulse strength | | | | Pulse period | | |
|---|---|---|---|---|---|---|---|
| | $V_{px}$ (m/s) | $V_{py}$ (m/s) | $V_{p\theta}$ (rad/s) | | $T_{px}$ (s) | $T_{py}$ (s) | $T_{p\theta}$ (s) |
| *Weak* | 0.5 | 0.5 | 0.3 | *Short* | 0.8 | 0.6 | 0.3 |
| *Moderate* | 1.0 | 1.0 | 0.5 | *Intermediate* | 1.4 | 1.2 | 0.6 |
| *Strong* | 1.2 | 1.2 | 0.6 | *Resonant* | 2.0 | 2.2 | 0.8 |
| | | | | *Long* | 3.0 | 3.2 | 1.3 |

controls reside within the feasible domain and not only on the boundary.

The five additional normalized performance metrics are defined as follows:

$$\Pi_1 \equiv \frac{\max_{t,k} \left|u_k(t)\right|}{\max_k u_{k,\max}} \qquad \text{(peak control force)} \tag{8.10a}$$

$$\Pi_2 \equiv \frac{\max_t \left|\ddot{\boldsymbol{d}}_{\mathrm{R}}(t) + \ddot{\boldsymbol{w}}(t)\right|}{\max_t \left|\ddot{\boldsymbol{w}}(t)\right|} \qquad \text{(peak total translational acceleration)} \tag{8.10b}$$

$$\Pi_3 \equiv \frac{\max_t \left|\ddot{\bar{\theta}}(t) + \ddot{w}_\theta(t)\right|}{\max_t \left|\ddot{w}_\theta(t)\right|} \qquad \text{(peak total rotational acceleration)} \tag{8.10c}$$

$$\Pi_4 \equiv \frac{\max_t \left|\boldsymbol{d}_{\mathrm{R}}(t)\right|}{\max_t \left|\boldsymbol{w}(t)\right|} \qquad \text{(peak relative radial displacement)} \tag{8.10d}$$

$$\Pi_5 \equiv \frac{\max_t \left|\bar{\theta}(t)\right|}{\max_t \left|w_\theta(t)\right|} \qquad \text{(peak relative rotation)} \tag{8.10e}$$

where $\boldsymbol{d}_{\mathrm{R}}(t) \equiv [\bar{x}\ \bar{y}]^{\mathsf{T}}$ is the relative, translational displacement of the top-frame and $\boldsymbol{w}(t) \equiv [w_x\ w_y]^{\mathsf{T}}$ is the translational base displacement vector. These five metrics along with the cost $J$ are compared in Table 8.3 for four control schemes: (1) optimal, (2) clipped LQR, and the two aforementioned clipped-passive damping schemes (3a) $c_{\mathrm{pass}} = 1566$ N s/m and (3b) $c_{\mathrm{pass}} = 940$ N s/m. From the table, the following conclusions could be drawn:

- At short period excitations, the optimal controller drastically outperforms linear-viscous passive systems in terms of $J$ and peak accelerations, $\Pi_2$ and $\Pi_3$. Clipped LQR also does well at short periods, with performance metrics 50% to 80% larger than optimal control.

- At longer period excitations, the optimal controller performs approximately equivalent to a linear-viscous passive device with the same maximum damping rate, $c_{\mathrm{pass}} = c_{\max}$. This is due to linear-viscous damping being nearly optimal in the long-period regime. Clipped LQR responses are notably larger than passive responses in these cases.

- In almost all cases, clipped LQR uses larger device forces than the optimal solution as well as the two passive schemes. This means that implementing the clipped LQR control in practice may require larger devices to achieve equivalent performance as a passive damper, especially in the long-pulse regime.

## 8.4 Summary

In this chapter the general approach to inequality constrained optimal control problems, presented in Chapter 7, is applied to the *semi-active* control of a rolling isolation system. We seek to determine whether *intelligent* damping, as opposed to passive control, is a worthwhile pursuit. Applying the open-loop trajectory optimization, the optimal performance of a semi-active rolling isolation system is determined, which tells an engineer the *best possible* performance one could hope to achieve. Two cases were investigated: single-degree-of-freedom isolator with one actuator and the full three-degree-of-freedom system actuated by three devices. In both cases, the complex nonlinear dynamics of the rolling isolation system are linearized to ease the computation of the optimal trajectories. The control force experiences a time lag arising from the modeled devices, thus raising the order of the system.

Comparisons are made between the responses of the optimal, clipped LQR, and passive controlled isolation systems. The results show that the responses of the optimal controller are 50% to 60% of those of the clipped LQR controlled system in the short period regime, and better than those of the passive controlled system. In the long-period range, the optimal solution is comparable to the passive viscous scheme and substantially outperforms the clipped LQR controlled system.

Semi-active control systems have the potential for far-better performance than achievable using clipped LQR feedback control rules. However, the marginal improvement over a passively damped system are not substantial enough to further pursue this technology at

this time. Passive damping devices are more affordable, in general, and thus more likely to be purchased by the consumer. Furthermore, the installation of semi-active dampers would be difficult due to the low clearance between the top- and bottom-frames of the rolling isolation system; modifications to the current system would need to be investigated. Therefore, passive damping via a rolling rubber layer will be pursued henceforth.

Though the major conclusions of this chapter do not lend to pursuing semi-active control in rolling isolation systems, the approach to determining optimal constrained trajectories is valuable. The major contribution of this chapter is to demonstrate the use of the method of Chapter 7 to a complex system, which permits a systematic comparison of various control methodologies.

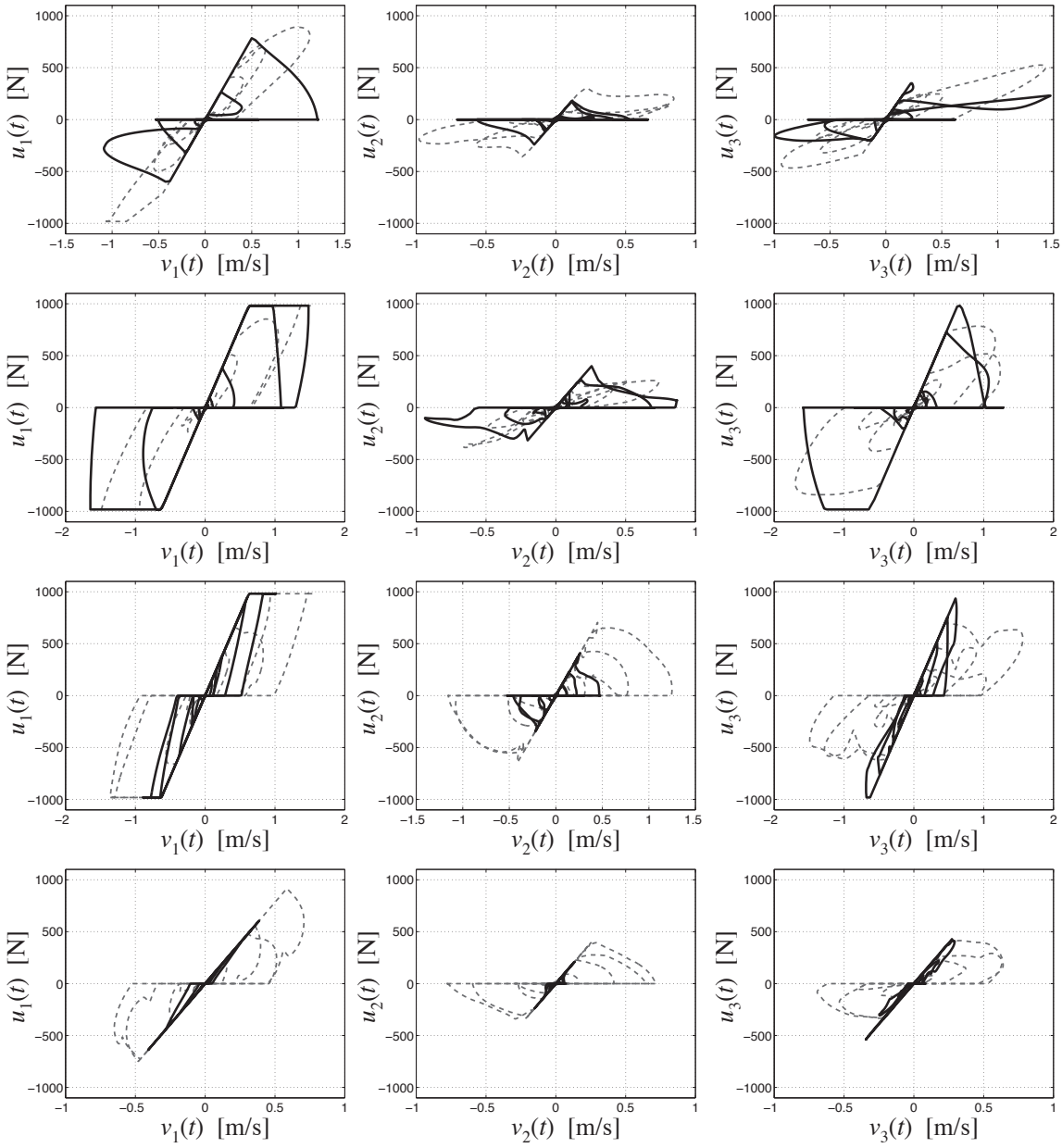


FIGURE 8.5: Three-degree-of-freedom control $u_k(t)$ versus velocity $v_k(t)$ for Moderate strength excitation: (1st row) Short period, (2nd row) Intermediate period, (3rd row) Resonant period, and (4th row) Long period. Legend: (—) *scheme 1*, optimal; (– – –) *scheme 2*, clipped LQR.

TABLE 8.3: Performance objectives evaluated using schemes 1, 2, 3a, and 3b for twelve cases of pulse-period and pulse-velocity. Bold, italicized values are at least 10% better than the next best control result.

| | **Weak**: $V_{px}, V_{py}$ = 0.5 m/s, $V_{p\theta}$ = 0.3 rad/s | | | | | | **Moderate**: $V_{px}, V_{py}$ = 1.0 m/s, $V_{p\theta}$ = 0.5 rad/s | | | | | | **Strong**: $V_{px}, V_{py}$ = 1.2 m/s, $V_{p\theta}$ = 0.6 rad/s | | | | | |
|---|---|---|---|---|---|---|---|---|---|---|---|---|---|---|---|---|---|---|
| | **Short period:** $T_p \ll T_n$ | | | | | | **Short period:** $T_p \ll T_n$ | | | | | | **Short period:** $T_p \ll T_n$ | | | | | |
| *Scheme* | $J$ [$10^6$] | $\Pi_1$ | $\Pi_2$ | $\Pi_3$ | $\Pi_4$ | $\Pi_5$ | $J$ [$10^6$] | $\Pi_1$ | $\Pi_2$ | $\Pi_3$ | $\Pi_4$ | $\Pi_5$ | $J$ [$10^6$] | $\Pi_1$ | $\Pi_2$ | $\Pi_3$ | $\Pi_4$ | $\Pi_5$ |
| 1 | ***0.08*** | ***0.40*** | ***0.18*** | ***0.53*** | 1.34 | ***2.51*** | ***0.30*** | ***0.80*** | ***0.18*** | ***0.60*** | 1.32 | ***3.01*** | ***0.44*** | 0.96 | ***0.18*** | ***0.60*** | 1.32 | ***3.01*** |
| 2 | 0.30 | 0.55 | 0.28 | 0.69 | 1.20 | 3.22 | 1.20 | 1.00 | 0.28 | 0.81 | 1.21 | 3.90 | 1.67 | 1.00 | 0.28 | 0.81 | 1.21 | 3.89 |
| 3a | 1.49 | 1.00 | 0.68 | 1.49 | 1.11 | 2.93 | 3.73 | 1.00 | 0.57 | 1.53 | 1.31 | 5.63 | 4.72 | 1.00 | 0.55 | 1.52 | 1.40 | 6.22 |
| 3b | 0.72 | 0.70 | 0.56 | 1.50 | 1.25 | 3.12 | 2.54 | 1.00 | 0.51 | 1.64 | 1.27 | 4.47 | 3.34 | 1.00 | 0.49 | 1.60 | 1.32 | 4.98 |
| | **Intermediate period:** $T_p < T_n$ | | | | | | **Intermediate period:** $T_p < T_n$ | | | | | | **Intermediate period:** $T_p < T_n$ | | | | | |
| 1 | ***0.73*** | 0.91 | 0.78 | 2.13 | 1.24 | 3.02 | ***3.10*** | 1.00 | 0.86 | 2.26 | 1.37 | 2.82 | ***4.80*** | 1.00 | 0.92 | 2.09 | 1.46 | ***2.56*** |
| 2 | 1.08 | 0.74 | 0.84 | 1.48 | 1.13 | 3.44 | 4.48 | 1.00 | 0.93 | 1.73 | 1.30 | 4.07 | 6.74 | 1.00 | 0.99 | 1.86 | 1.40 | 4.09 |
| 3a | 2.43 | 0.94 | 1.24 | 1.00 | ***0.87*** | ***1.40*** | 9.24 | 1.00 | 1.34 | 1.33 | 1.32 | 3.03 | 13.02 | 1.00 | 1.39 | 1.75 | 1.51 | 4.14 |
| 3b | 2.16 | 0.75 | 1.28 | 1.05 | 1.25 | 1.82 | 8.51 | 1.00 | 1.33 | 1.33 | 1.44 | 2.72 | 12.18 | 1.00 | 1.37 | ***1.44*** | 1.57 | 3.44 |
| | **Resonant period:** $T_p \approx T_n$ | | | | | | **Resonant period:** $T_p \approx T_n$ | | | | | | **Resonant period:** $T_p \approx T_n$ | | | | | |
| 1 | 1.86 | 0.70 | ***1.21*** | 1.62 | 0.65 | 2.03 | 7.84 | 1.00 | 1.44 | 1.72 | 0.78 | 2.68 | 12.68 | 1.00 | 1.68 | 1.58 | 0.91 | 2.96 |
| 2 | 2.67 | 0.73 | 1.96 | 2.19 | 1.14 | 4.87 | 11.76 | 1.00 | 2.16 | 2.73 | 1.27 | 6.43 | 19.53 | 1.00 | 2.33 | 2.75 | 1.40 | 6.86 |
| 3a | 1.97 | 0.67 | 1.34 | 0.95 | ***0.59*** | ***1.57*** | 8.27 | 1.00 | 1.43 | 0.95 | ***0.68*** | ***1.83*** | 13.31 | 1.00 | 1.60 | 0.95 | ***0.82*** | ***1.85*** |
| 3b | 2.63 | ***0.59*** | 1.57 | 0.98 | 0.87 | 2.07 | 10.75 | 1.00 | 1.67 | 0.99 | 0.91 | 2.41 | 17.01 | 1.00 | 1.84 | 0.99 | 1.04 | 2.32 |
| | **Long period:** $T_p > T_n$ | | | | | | **Long period:** $T_p > T_n$ | | | | | | **Long period:** $T_p > T_n$ | | | | | |
| 1 | 1.07 | 0.33 | 1.40 | 1.24 | 0.25 | 0.64 | 4.26 | 0.65 | 1.39 | 1.11 | 0.25 | 0.75 | 6.12 | 0.78 | 1.38 | 1.08 | 0.25 | 0.74 |
| 2 | 1.63 | 0.47 | 2.35 | 2.70 | 0.44 | 1.68 | 6.47 | 0.94 | 2.34 | 3.19 | 0.44 | 1.98 | 9.31 | 1.00 | 2.34 | 3.16 | 0.44 | 1.98 |
| 3a | 1.08 | 0.34 | 1.42 | 1.08 | 0.25 | 0.62 | 4.29 | 0.68 | 1.41 | 1.08 | 0.25 | 0.75 | 6.17 | 0.82 | 1.41 | 1.08 | 0.25 | 0.75 |
| 3b | 1.22 | ***0.26*** | 1.59 | 1.13 | 0.32 | 0.72 | 4.83 | ***0.52*** | 1.59 | 1.14 | 0.32 | 0.85 | 6.95 | ***0.63*** | 1.59 | 1.14 | 0.32 | 0.85 |

# 9

# Vibration Suppression Using Damped Rolling Isolation Systems: Theory and Experimental Validation

## 9.1 Background

Rolling pendulum isolation platforms decouple the motion of isolated objects from the motion of the supporting floor via a rolling interface [37]. Such systems can reduce accelerations transmitted to the object considerably by allowing for large displacements between the object and the floor, and shifting the natural period to a range longer than the floor motion period. The prediction of the response of rolling isolation systems (RISs) and their ability to protect building components from seismically-induced floor responses requires validated models that can capture the observed nonlinear behavior of actual isolation systems subjected to multiaxial shaking. The dynamic behavior of RISs involves nonholonomic constraints, non-quadratic potential energy functions, strong nonlinear coupling of lateral and rotational responses, and chaotic regimes [38, 63]. Many existing models for these systems are limited to uniaxial behavior, neglecting most, if not all, of these complexities [28–33]. Furthermore, experimental assessment of existing models is sparse [33–35],

especially for multiaxial disturbances.

Sliding pendulum isolation platforms function on the same principle as rolling pendulum systems, but provide damping through sliding Polytetrafluoroethylene (PTFE) interfaces [132, 133]. Increasing the frictional force reduces displacements across the isolators at the expense of higher accelerations in the isolated object, because of the already-high level of the frictional forces [55, 133]. Because rolling resistance is normally much smaller than PTFE friction, rolling pendulum systems are amenable to designs requiring lower levels of damping.

Lightly-damped RISs perform extremely well when their displacement capacities are not exceeded. When the isolator's displacement capacity is insufficient to meet the demands of a disturbance, the performance of the isolator is diminished due to impacts, giving rise to high acceleration responses in the isolated object. In Chapter 4 an experimental and numerical assessment of an undamped RIS showed the challenges of implementing lightly-damped RISs for high-intensity motions [52]. An RIS designed for strong (infrequent) floor motions would either have (i) a larger displacement capacity [53], or (ii) supplemental damping to reduce displacement demands. Two methods for adding damping to RISs have been investigated: (i) encasing the ball-bearing with a damping material (e.g. rubber) [36] or (ii) bonding viscoelastic layers to the counter-facing surfaces [33, 47]. Both approaches act to increase the rolling resistance and thus increase energy dissipation, decrease isolator displacements, and improve performance over undamped RISs. The latter approach is the focus of this chapter.

In prior investigations into bonding viscoelastic sheets to RISs [33, 47], the rolling surfaces were flat, and elastic re-centering forces were provided via springs. Rolling *pendulum* isolation systems provide re-centering via gravitational potential energy and have dynamics independent of the mass of the isolated object. An illustration of the damped RIS to be analyzed in this chapter is shown in Figure 9.1. This system comprises a pair of rectangular frames, four pairs of shallow bowls bonded with rubber sheets, and four rigid

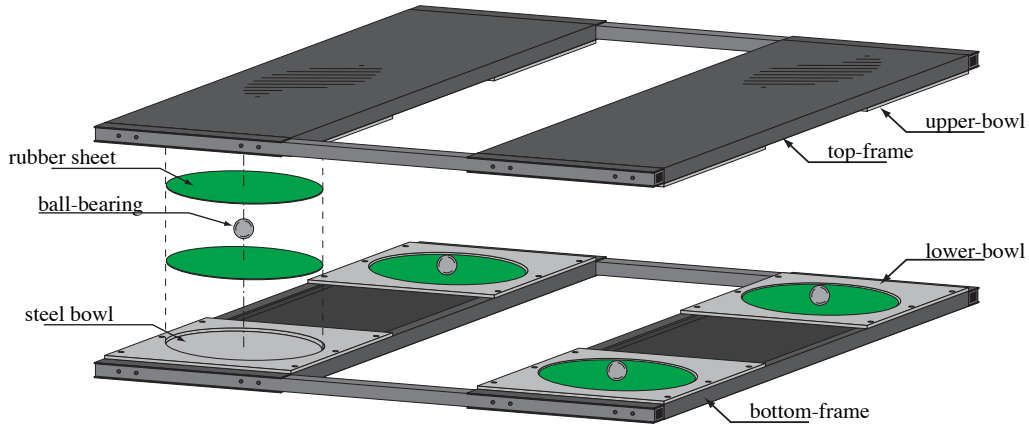


FIGURE 9.1: Exploded view of a damped rolling isolation system.

steel ball-bearings. The object resting on the top-frame is isolated from the floor motion applied to the bottom-frame through a rolling pendulum mechanism. The bottom- and top-frames contain four concave-up bowls and four concave-down bowls, respectively, at their corners. Four ball-bearings roll between the rubber-coated lower- and upper-bowls (Figure 9.1) allowing for the top-frame to displace with respect to the bottom-frame. At the edge of the bowl's rolling surface, a lip acts as a hard limit on the ball-bearing's displacement. The isolation system's displacement capacity is defined by the contact of the ball-bearing with the bowl lip. Concave steel dishes are bonded with a rubber layer which supplies the desired energy dissipation. Because both the gravitational restoring forces and the damping forces increase with the isolated mass, base-excited responses of rolling pendulum isolation platforms damped with viscoelastic sheets are nearly independent of the amount of mass being isolated.

This chapter concerns the development and experimental validation of a model of a damped RIS. First, descriptions of the damped RIS and its geometry are provided, and the model is derived. Next, a rolling resistance model is proposed and fit to experimental data. Then, free- and forced-response experiments are performed on the damped RIS, to which numerical predictions using the proposed model are compared. The set of disturbance scenarios is designed to cover a wide range of operating conditions of the isolator, and peak

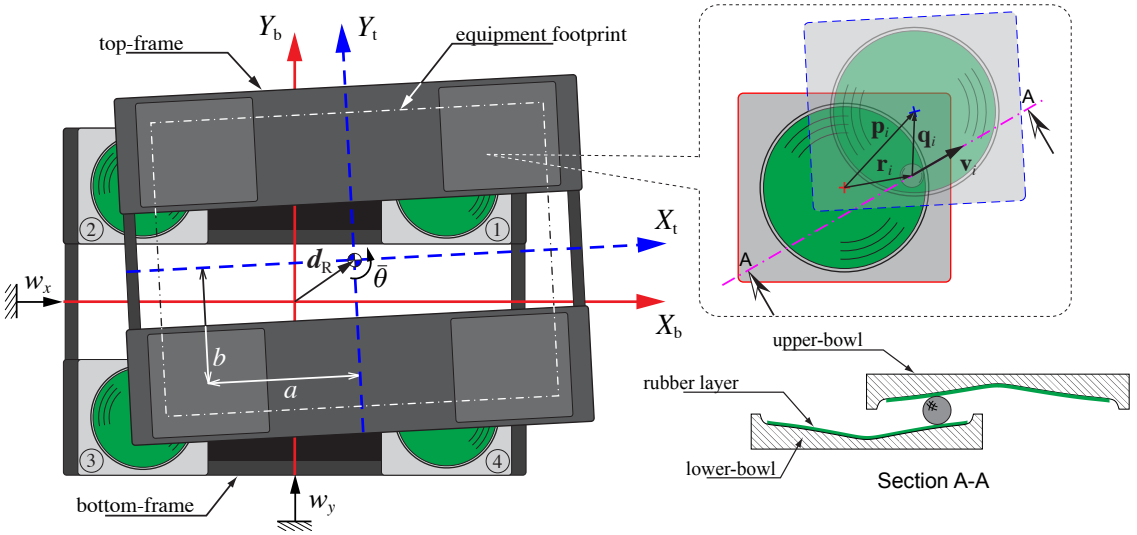


FIGURE 9.2: Damped rolling isolation system geometry.

response quantities are computed. Finally, the experimentally-measured responses and numerically-computed predictions are compared, validating that the model is *predictive* over a wide range of disturbance parameters.

## 9.2 Simplified Model of a Damped Rolling Isolation System

### *9.2.1 Geometry and notation*

Consider the displaced configuration of a damped RIS illustrated in Figure 9.2. The bottom-frame is excited by translational disturbance $\boldsymbol{w}(t) = [w_x(t)\ w_y(t)]^\mathsf{T}$. Vibration-sensitive equipment is rigidly connected to the top-frame, and the total mass of the equipment and top-frame is $m$ with mass moment of inertia $I$; we assume that the equipment's mass is concentrically located. The top-frame undergoes rotation $\bar{\theta}(t)$ and translational displacements $\boldsymbol{d}_R(t) = [\bar{x}(t)\ \bar{y}(t)]^\mathsf{T}$, relative to the bottom-frame.

The top-frame and equipment are mechanically isolated from the bottom-frame via the rolling of large, steel ball-bearings between concave-up lower-bowls and concave-down upper-bowls at the four corners (Figure 9.1). The bowls and balls are numbered $i = 1,...,4$, as shown in Figure 9.2, with the coordinates of the bowl centers given by $\boldsymbol{c}_i = [a_i\ b_i]^\mathsf{T}$

where

$$\boldsymbol{a} = [a \;\; -a \;\; -a \;\; a]^\intercal \quad \text{and} \quad \boldsymbol{b} = [b \;\; b \;\; -b \;\; -b]^\intercal. \tag{9.1}$$

The gravitational potential energy in the system is attributed to the changes in the heights at the corners, which depend on the platform displacements $(\bar{x}, \bar{y}, \bar{\theta})$ and the ball-bearing locations. As seen in Figure 9.2, the ball-bearing locations with respect to the centers of the lower- and upper-bowls are $\mathbf{r}_i(t) = [r_{xi}(t) \; r_{yi}(t)]^\intercal$ and $\mathbf{q}_i(t) = [q_{xi}(t) \; q_{yi}(t)]^\intercal$, and the center-to-center displacement $\mathbf{p}_i(t) = [p_{xi}(t) \; p_{yi}(t)]^\intercal$ is

$$\mathbf{p}_i \equiv \mathbf{p}_i(\bar{x}, \bar{y}, \bar{\theta}; t) = \boldsymbol{d}_\mathrm{R} + (\mathbf{R}_{\bar{\theta}} - \mathbf{I})\, \boldsymbol{c}_i \tag{9.2}$$

where $\mathbf{R}_{\bar{\theta}}$ is the rotation matrix. Using the relationship $\mathbf{p}_i = \mathbf{r}_i + \mathbf{q}_i$, it is now straightforward to find $\mathbf{q}_i$ given the ball-bearing location $\mathbf{r}_i$. We assume all the bowls are axisymmetric with radius-dependent bowl-shape function $\eta(r)$. The height at the center of the $i$th bowl is the sum of contributions from the lower- and upper-bowls,

$$h_i(\bar{x}, \bar{y}, \bar{\theta}, \mathbf{r}_i) = \eta(\|\mathbf{r}_i\|) + \eta(\|\mathbf{q}_i\|). \tag{9.3}$$

### *9.2.2 Kinematics of rolling ball-bearings*

The ball-bearing coordinates $\mathbf{r}_i$ evolve according to a set of nonholonomic constraints prescribed by the condition of rolling without slipping between non-parallel surfaces [38]. The kinematic constraint, relating the ball-bearing velocities $\dot{\mathbf{r}}_i(t) = [\dot{r}_{xi}(t) \; \dot{r}_{yi}(t)]^\intercal$ to the relative velocities $\mathbf{v}_i(t) = [v_{xi}(t) \; v_{yi}(t)]^\intercal$ of the upper-bowls at the ball-bearing locations, depends upon the slopes of the upper- and lower-bowls. For shallow bowls (i.e. $\eta'(r) < 0.15$), the nonholonomic constraint is approximated here by the condition that the velocity of the ball-bearing center is half of the relative velocity across the isolation system. The ball-bearing velocity is in the direction of this relative velocity,

$$\dot{\mathbf{r}}_i = \tfrac{1}{2}\mathbf{v}_i = \tfrac{1}{2}\{\dot{\boldsymbol{d}}_\mathrm{R} + \dot{\bar{\theta}}\,\mathbf{D}\,(\boldsymbol{c}_i + \mathbf{r}_i - \boldsymbol{d}_\mathrm{R})\}\,, \qquad (i = 1, ..., 4) \tag{9.4}$$

where the differentiation matrix

$$\mathbf{D} = \begin{bmatrix} 0 & -1 \\ 1 & 0 \end{bmatrix} .$$

The eight nonlinear first-order ordinary differential equations (9.4) prescribe the evolution of the four ball-bearings in the $X_\mathrm{b}$-$Y_\mathrm{b}$ plane. Initial conditions $\mathbf{r}_{i0} = \mathbf{r}_i(0)$ must be specified.

### *9.2.3 Equations of motion*

Applying the fundamental nonholonomic form of Lagrange's equation, the equations of motion of the centroidal coordinates, taking into account the constraints prescribed in Equation (9.4), are as follows [38]:

$$m\left(\ddot{\boldsymbol{d}}_\mathrm{R} + \ddot{\boldsymbol{w}}\right) + \sum_{i=1}^{4}\left(\mathbf{f}_{\mathrm{D}i} + \tfrac{1}{2}\mathbf{f}_{\mathcal{U}i} + \tfrac{1}{2}\mathbf{f}_{\mathcal{L}i}\right) = \mathbf{0} \tag{9.5a}$$

$$I\ddot{\bar{\theta}} + \sum_{i=1}^{4}\left(\mathbf{f}_{\mathrm{D}i} + \tfrac{1}{2}\mathbf{f}_{\mathcal{L}i} - \tfrac{1}{2}\mathbf{f}_{\mathcal{U}i}\right)^\mathsf{T}\mathbf{D}\left(\boldsymbol{c}_i + \mathbf{r}_i - \boldsymbol{d}_\mathrm{R}\right) + \sum_{i=1}^{4}\mathbf{f}_{\mathcal{U}i}^\mathsf{T}\mathbf{D}\mathbf{R}_{\bar{\theta}}\boldsymbol{c}_i = 0 \, . \tag{9.5b}$$

where $\mathbf{f}_{\mathrm{D}i}$ are the dissipative forces, which will be defined and parameterized later. The gravitational forces arising from the bowl gradient $\eta'(r)$ are

$$\mathbf{f}_{\mathcal{L}i} = \tfrac{1}{4}mg\eta'(\|\mathbf{r}_i\|)\,\hat{\mathbf{r}}_i \quad \text{and} \quad \mathbf{f}_{\mathcal{U}i} = \tfrac{1}{4}mg\eta'(\|\mathbf{q}_i\|)\,\hat{\mathbf{q}}_i, \tag{9.6}$$

where $g = 9.81$ m/s$^2$; and the over-hat indicates the unit vector, e.g. $\hat{\mathbf{r}}_i \equiv \mathbf{r}_i/\|\mathbf{r}_i\|$. The system dynamics comprise Equations (9.4) and (9.5), which must be integrated simultaneously.

### *9.2.4 Bowl-shape function*

In Chapter 4 we experimentally characterized the undamped, or "nominal", bowl slope $\eta_0'(r)$ in its installed and loaded configuration [52]. The following polynomial function was fit to experimental free responses:

$$\eta_0'(r) = \sum_{i=1}^{6}\alpha_i(r/R)^i + \alpha_{50}(r/R)^{50} \tag{9.7}$$

where $R = 10$ cm; and values for the estimated parameters $\alpha_i$ are given in Table 4.1. The nominal height can be found by integrating Equation (9.7), viz.

$$\eta_0(r) = \int_0^r \eta_0'(\rho)\,\mathrm{d}\rho \tag{9.8}$$

In the damped RIS, rubber sheets are glued to the surfaces of the eight bowls. The rubber sheets are uniformly 1.58 mm thick and do not affect the nominal bowl shape (or gradient) function. Over time, creep in the rubber sheets results in a 'divot' at the center of each bowl, approximately equal to the compressed deformation of the rubber sheet under load, 0.95 mm. This divot increases the resistance to initial motion. Since motion trajectories are not likely to return to the center of the dish during a transient response, this modification usually affects just the initial motion of the system. The following function is proposed to model the divot slope:

$$\eta_{\text{divot}}'(r) = \sigma\,(r/r_{\text{divot}})\ \exp(-r/r_{\text{divot}}) \tag{9.9}$$

where $\sigma$ is a scaling parameter, and $r_{\text{divot}}$ is the radial distance to the edge of the divot (i.e. the mode of $\eta_{\text{divot}}'(r)$), which is measured to be 3.5 mm. The divot height function is

$$\eta_{\text{divot}}(r) = \int_0^r \eta_{\text{divot}}'(\rho)\,\mathrm{d}\rho = \sigma\, r_{\text{divot}}\,\left[1 - (1 + r/r_{\text{divot}})\exp(-r/r_{\text{divot}})\right] - \eta_{\text{divot},0} \tag{9.10}$$

where $\eta_{\text{divot},0}$ is the divot depth, which is measured to be 0.95 mm. The scaling parameter $\sigma$ is chosen such that $\eta_{\text{divot}}(r)$ is zero for large $r$, i.e. the divot is localized at $r = 0$. Namely, $\eta_{\text{divot}}(\infty) = 0 \ \Rightarrow\ \sigma \equiv \eta_{\text{divot},0}/r_{\text{divot}}$.

The total bowl-shape function $\eta(r)$ is the sum of the contributions from the nominal function $\eta_0(r)$ and the divot function $\eta_{\text{divot}}(t)$:

$$\eta(r) = \eta_0(r) + \eta_{\text{divot}}(r)\ . \tag{9.11}$$

The nominal, the divot and the total bowl-height functions are shown in Figure 9.3(a). Figure 9.3(b) gives the bowl-slope functions. The influence of the divot on the height appears to be small, whereas for the slope, the effect is pronounced near $r = 0$, acting to increase the resistance when the system starts from rest.

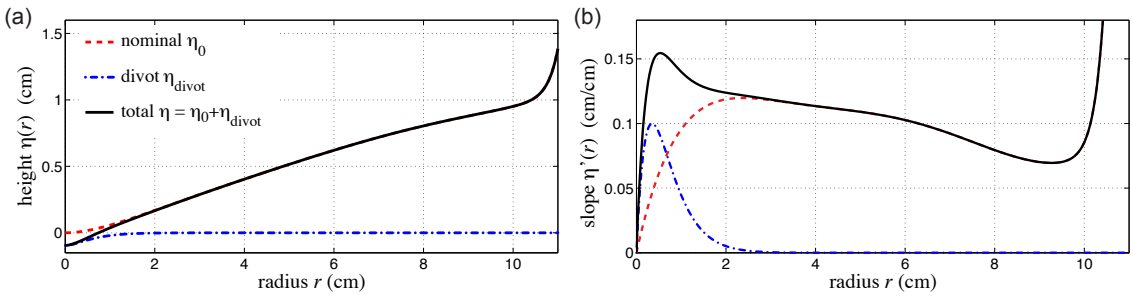


FIGURE 9.3: Nominal, total, and divot (a) bowl-height $\eta$ and (b) bowl-slope $\eta'$ functions versus bowl radius $r$. Not to scale.

## 9.3 Experimental Characterization of Rolling Resistance

Damping forces in the system are modeled to act at the ball-bearing locations and in the direction of the velocity,

$$\mathbf{f}_{\mathrm{D}i} = R_{\mathrm{r}}(\mathbf{v}_i, P)\,\hat{\mathbf{v}}_i\,, \tag{9.12}$$

where the rolling resistance $R_{\mathrm{r}} \equiv R_{\mathrm{r}}(\mathbf{v}_i, P)$ is a nonlinear function of the velocity of the top-frame across the $i$th ball-bearing $\mathbf{v}_i$ and the vertical, compressive load $P$. The relationship for the rolling resistance is given by the sigmoid

$$R_{\mathrm{r}}(\mathbf{v}_i, P) = \mu(P)\,\tanh\left(\|\mathbf{v}_i\|/v_{\mathrm{s}}\right) \tag{9.13}$$

where $\mu(P)$ is a load-dependent force level and $v_{\mathrm{s}}$ is a velocity scaling constant.

### *9.3.1 Experimental set-up*

An experimental set-up—originally constructed for the purposes of a related study on rolling resistance—was used to independently evaluate the rolling resistance of the elastomeric sheet used in the damped RIS. Figure 9.4 shows the experimental set-up. The set-up comprises two horizontal plates—one attached to the shaking table and another attached to the non-moving bed-plate. Counter-facing rubber sheets are attached to the lower- and upper-plates and a 38.1 mm steel ball-bearing is situated therebetween. By moving the shaking table, the lower-plate moves with respect to the stationary upper-plate, and the ball-bearing rolls between the two surfaces. A constant vertical load is applied to

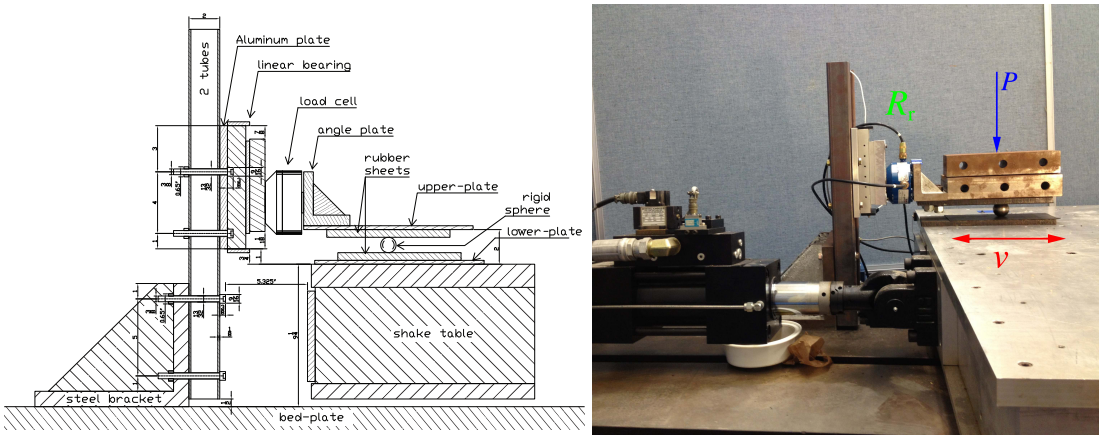


FIGURE 9.4: Schematic and photograph of the rolling resistance experimental set-up.

the upper-plate by adding masses on top of the upper-plate, which is permitted to translate vertically via a linear bearing. Thus, all of the applied weight is carried by the single ball-bearing. Eight load levels were used to investigate the effect of vertical load on rolling resistance: $P$ = 86, 226, 297, 509, 649, 720, 901, and 1083 N.

An array of sensors was installed on the experimental system. The hydraulic actuator has a linear variable differential transformer (LVDT) to sense the table displacement. The table velocity was calculated using the central difference of the LVDT table displacement measurements. A load cell situated between the upper-plate and the linear bearing measures the horizontal force which is equivalent to the rolling resistance. Table displacement and rolling resistance measurements were collected at 400 samples per second.

The shaking table was driven using a chirp-up signal with a frequency range of 0.2 to 2 Hz; thus, a range of amplitudes and frequencies is explored with a single experiment. A representative table velocity history is shown in Figure 9.5(a). The hydraulic actuator can achieve a peak velocity of 29 cm/s at the low-pressure setting used in these experiments.

### *9.3.2 Hierarchical modeling*

For the rolling-resistance experimental system described in the previous section, only one ball is used, so the index $i$ in Equation (9.13) can be ignored for now. Further, the velocity is rectilinear and can be treated as a scalar. Thus, for the following analysis, Equation

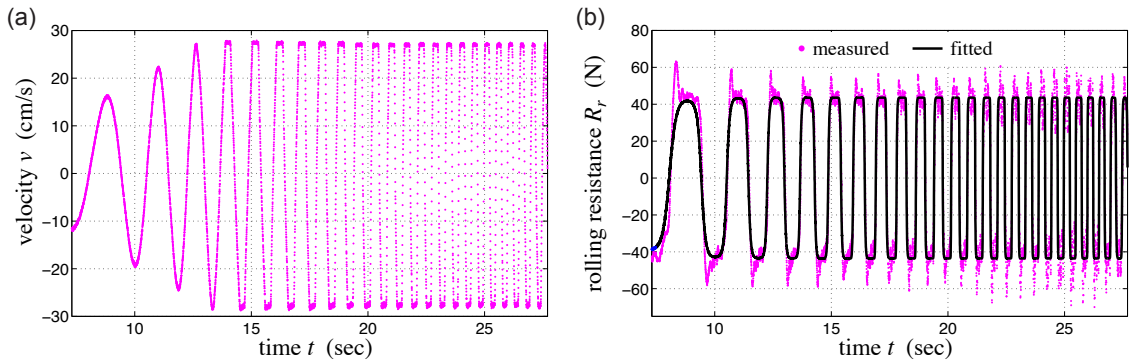


FIGURE 9.5: (a) Measured shaking table velocity; (b) measured and fitted rolling resistance $R_r$ time histories: $P = 901$ N.

(9.13) is considered to be

$$R_r(v\,|\,\mu(P_k)) = \mu(P_k)\,\tanh\left(v/v_s\right) \tag{9.14}$$

where $v$ is the velocity across the rolling interface, i.e. the shake table velocity. The rolling resistance model is fit using a multilevel or hierarchical approach, in which the levels are as follows. *Level 1*: Regress the rolling resistance $R_r(v\,|\,\mu(P_k))$ on the velocity $v$ for a given compressive load $P_k$ ($k = 1, ..., 8$). *Level 2*: Regress the force amplitude $\mu(P)$ on the compressive load $P$. In all analyses, the estimate of the velocity scaling parameter is taken to be $v_s = 8.5$ cm/s.

*Level 1: Rolling resistance $R_r$ regression*

In the first level of the hierarchical model, the rolling resistance $R_r$ is regressed on the velocity $v$, for a constant load level $P_k$. That is, the level 1 regression equation is

$$R_r(v\,|\,\mu(P_k)) = \mu(P_k)\,\tanh\left(v/v_s\right) \tag{9.15}$$

where the regression coefficients $\mu(P_k)$ are fit independently for the eight ($k = 1, ..., 8$) experimental trials ($P_k = 86$, 226, 297, 509, 649, 720, 901, and 1083 N). At each load level, the root mean square error is calculated.

$$s_{R_r} \equiv s_{R_r}(P_k) = \sqrt{\frac{1}{N-1}\sum_{i=0}^{N}\Big(R_{ri} - R_r(v_i\,|\,\hat{\mu}(P_k))\Big)^2} \tag{9.16}$$

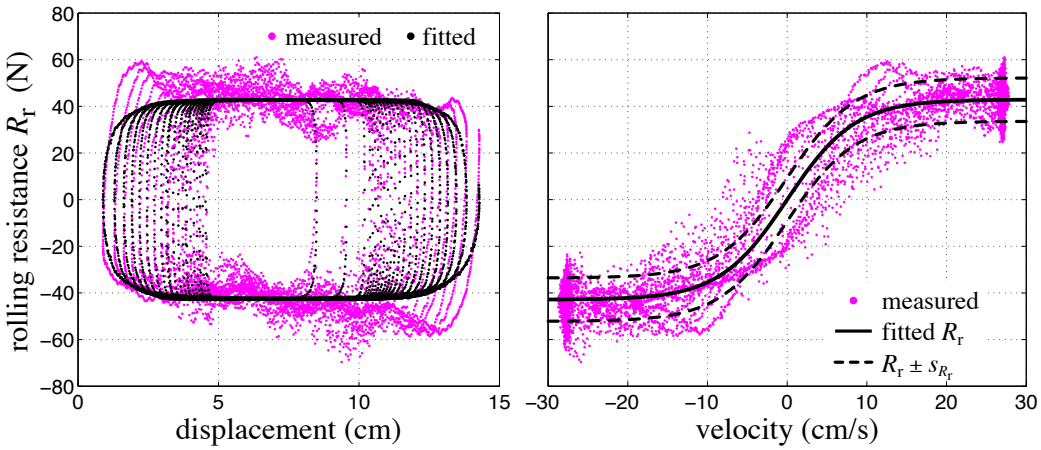


FIGURE 9.6: Fitted and measured rolling resistance $R_r$ versus displacement and velocity for a load of $P_k$ = 901 N.

in which $R_{ri}$ is a measured force at time $t_i$ ($i = 0, ..., N$); and $R_r(v_i \,|\, \hat{\mu}(P_k))$ is the estimate of the force corresponding to the measured velocity $v_i$ at time $t_i$ and the estimates of the force level $\hat{\mu}(P_k)$ and velocity parameter $v_s$. Figure 9.5(b) shows measured and fit rolling-resistance time histories for $P$ = 901 N. For the same load level, the left frame of Figure 9.6 shows the experimental and fit rolling resistance versus displacement. In the right frame, the rolling resistance is plotted versus the velocity. The fit rolling resistance for $P$ = 901 N and the approximately 70% confidence interval $R_r \pm s_{R_r}$ are overlaid on the experimental $R_r$.

*Level 2: Force amplitude μ regression*

In the second level of the hierarchical model, the force amplitude $\mu$ is regressed on the applied load $P$. The level 2 regression equation is given by the power law

$$\mu(P) = \alpha P^{\beta} \tag{9.17}$$

The model parameters $\alpha$ and $\beta$ are fit to the force amplitude $\hat{\mu}(P)$ from the previous section (Level 1). The nonlinear least-squares problem is solved using the Levenberg-Marquardt algorithm, which yields fit parameters $\hat{\alpha} = 0.008226$ and $\hat{\beta} = 1.26343$ with asymptotic standard errors $\sigma_\alpha = 0.0022$ and $\sigma_\beta = 0.0391$. The fitted power $\hat{\beta}$ matches closely the

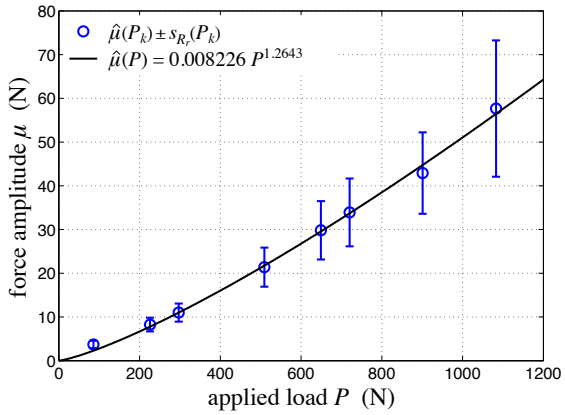


FIGURE 9.7: Fitted and measured force amplitude $\mu$ versus the applied load $P$. The error bars represent the combination of unmodeled variability in rolling resistance and measurement error.

values suggested by classical theory [134] and boundary element computations [135]. The fitted function (9.17) is shown in Figure 9.7. In Figure 9.7, the fitted force amplitudes $\hat{\mu}(P_k)$ are plotted, with $\pm s_{R_r}$ error bars, versus the eight levels of load $P_k$. The prediction error $s_{R_r}$ increases monotonically with the load.

*Implementation*

The rolling resistance model to be implemented in all subsequent simulations is given by Equation (9.13), and depends upon the applied load $P$. The top-frame of the damped RIS is supported at each of its four corners by a ball-bearing which carries approximately one quarter the total mass $m$. Thus, the applied load to each ball-bearing is $P \approx mg/4$. Incorporating the fitted model-parameters, the rolling resistance is modeled as follows:

$$\mathbf{f}_{\mathrm{D}i}(\mathbf{v}_i, m) = 0.008226\,(mg/4)^{1.26343}\ \tanh\left(\|\mathbf{v}_i\|/8.5\right)\hat{\mathbf{v}}_i \tag{9.18}$$

where the units of $\mathbf{f}_{\mathrm{D}i}$, $\mathbf{v}_i$ and $m$ are N, cm/s and kg, respectively.

The rolling resistance model is arguably over-simplified—it neglects hysteresis and transients involved in rolling resistance phenomena. Nevertheless, as will be shown in the next section, for the purpose of predicting free responses, pulse responses, and peak responses, this model is able to capture all the fundamental behavior of the damped RIS.

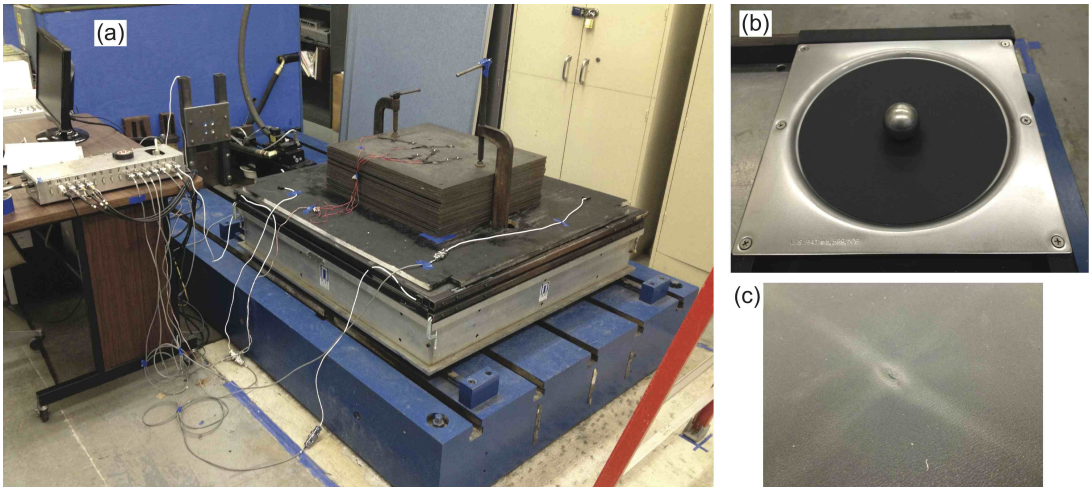


FIGURE 9.8: (a) Experimental shaking table with damped RIS. (b) Steel ball-bearing resting on ("virgin") rubber sheet which has been glued to the underlying steel bowl. (c) Divot formed at the center of the rubber sheet. This photo was taken after all experiments were performed.

## 9.4 Experimental Validation of the Predictive Model

We now validate the mathematical model with experimental response histories and peak response spectra. First, we analyze experimental free-response histories and compare predictions made with our analytical model to the experimental system. Next, we develop a pulse disturbance model and design a set of pulse periods and amplitudes to test. Experimental and predicted time-histories are compared for a few cases. Finally, peak response spectra demonstrate the model is predictive over broad range of amplitudes and periods.

### *9.4.1 Experimental set-up*

In order to assess the performance of the damped isolation system and to validate the model described above, experiments were conducted in which the system was excited uniaxially, and various response quantities were measured. Experiments were conducted on a single-axis servo-hydraulic shaking table. The table can achieve peak velocities of 50 cm/s and has a stroke of ±7.5 cm.

The damped RIS in this study, shown in Figure 9.8, has dimensions $a = 44.5$ cm and $b = 47$ cm. A 122 cm × 122 cm plywood board of mass 16 kg with moment of inertia

4.0 kg m$^2$ was placed on the top-frame to support rectangular steel plates of dimension 66 cm × 61 cm × 0.64 cm. Each plate has a mass of approximately 20 kg and a mass moment of inertia of 1.346 kg cm$^2$. Their primary axes were aligned with the $X_t$-axis of the top-frame, and the plates were rigidly connected to the plywood with C-clamps. Two loading scenarios were investigated: *Light* (15 steel plates ≈ 300 kg) and *Heavy* (30 steel plates ≈ 600 kg).

An array of sensors was installed on the experimental system. Silicon Design MEMS accelerometers were located on the shaking table and the top-frame: one measuring the shake table acceleration $\ddot{w}_x(t)$, and three measuring the the top-frame accelerations. The hydraulic actuator has a linear variable differential transformer (LVDT) to sense the table displacement $w_x(t)$. Table displacement and acceleration responses were collected at a sample rate of 200 Hz.

The top-frame displacement was measured using a Flip MinoHD video camera at 30 fps. Five Oznium LEDs, located on the top of the steel plates, were controlled by the data acquisition to turn on and off precisely at the start and end of the test, allowing for exact synchronization between the digitized sensor records and the video. The video was post-processed using MATLAB's Image and Video Processing Toolbox [87, 136] in order to extract the top-frame's absolute displacement. To find the relative displacement of the top-frame $(\bar{x}, \bar{y}, \bar{\theta})$, displacement measurements from the actuators's LVDT are subtracted from the displacement measurements from the video.

### *9.4.2 Prediction of free responses*

Six free-response experiments—three in the $x$-direction and three in the $y$-direction—were performed with the light system. Figures 9.9 and 9.10 give the free-response histories when the system is initially displaced to $\bar{x}_0$ and $\bar{y}_0$, respectively. The measured responses (Tests #1-6) exhibit repeatability—three tests performed from nearly identical initial conditions respond nearly identically, without diverging. Unlike the undamped sys-

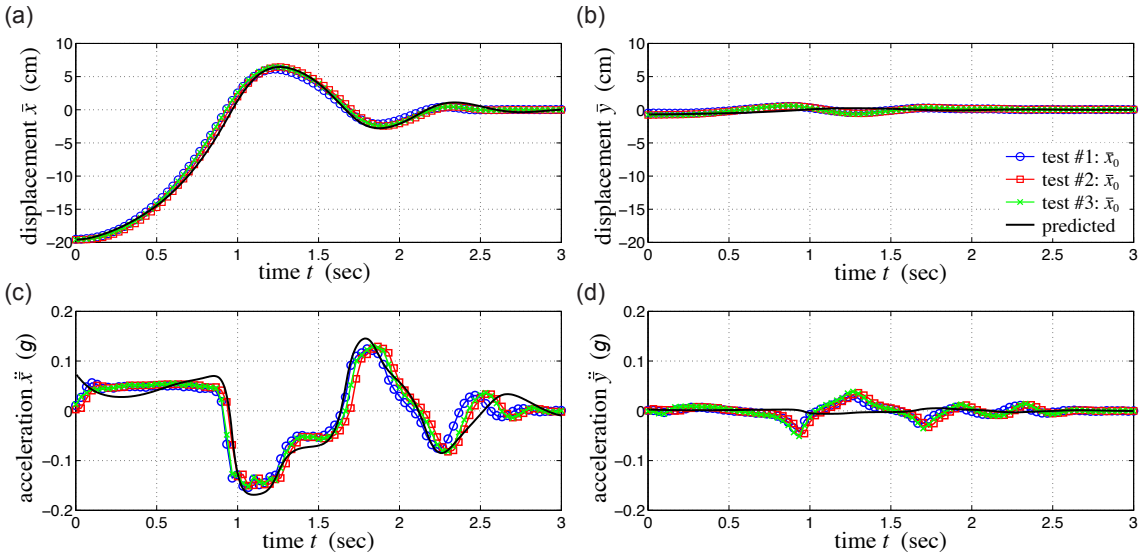


FIGURE 9.9: Measured and predicted free-response histories with initial displacement $\bar{x}_0$: (a) displacement $\bar{x}(t)$, (b) displacement $\bar{y}(t)$, (c) acceleration $\ddot{\bar{x}}(t)$, and (d) acceleration $\ddot{\bar{y}}(t)$.

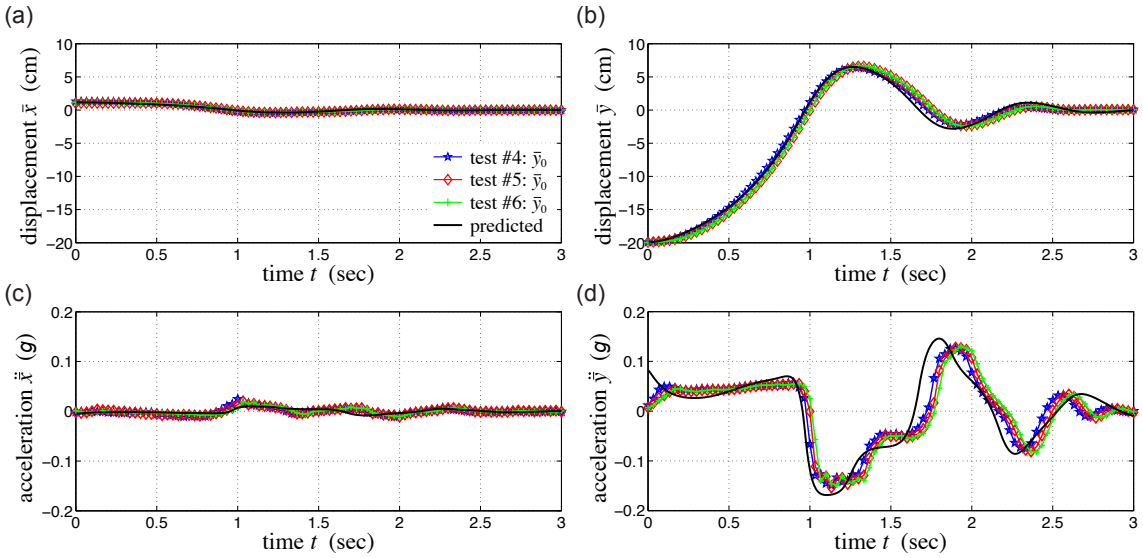


FIGURE 9.10: Measured and predicted free-response histories with initial displacement $\bar{y}_0$: (a) displacement $\bar{x}(t)$, (b) displacement $\bar{y}(t)$, (c) acceleration $\ddot{\bar{x}}(t)$, and (d) acceleration $\ddot{\bar{y}}(t)$.

tem [38, 63], the damped RIS is insensitive to initial conditions. Furthermore, lateral translations do not develop as they do in the undamped system [38].

Numerical simulations using the proposed model were performed for both cases: $\bar{x}_0$ and $\bar{y}_0$. In each case, the model was initialized to the mean initial conditions of the three experiments, and the ball-bearing locations were taken to be $\mathbf{r}_i(0) = \mathbf{p}_i(0)/2$. The pre-

dicted histories are shown in Figures 9.9 and 9.10 by the black line. In both cases, the model predicts the displacement with very little error; the acceleration trajectories match closely, as well. This demonstrates that the model is able to predict free displacement and acceleration responses.

### *9.4.3 Disturbance model for forced-response tests*

The rectilinear motion of the shake table $w_x(t)$ is controlled to represent a monotone ($\omega_\mathrm{p} = 2\pi/T_\mathrm{p}$) disturbance, which grows and decays in amplitude over time [52]. This motion applies inertial loads to the isolated mass, and is therefore specified in terms of an acceleration,

$$\ddot{w}_x(t) = g(t)\cos(\omega_\mathrm{p} t - \phi),\ t \in [0, T] \tag{9.19}$$

for which the strictly-positive, unimodal disturbance envelope is

$$g(t) = (t/\tau)^2 \exp(-t/\tau)\ . \tag{9.20}$$

The time-scale constant $\tau$ is taken to be $5T_\mathrm{p}/4$ such that each record contains five cycles of strong motion. By selecting $\phi = 3\tan^{-1}(\tau\omega_\mathrm{p}) \pm \pi/2$, the disturbance record has nearly zero terminal velocity. The acceleration waveform is corrected in order to detrend the displacement and velocity histories as follows:

$$\ddot{w}_x(t) \leftarrow \ddot{w}_x(t) - [\dot{g}(t)w_x(T) - g(t)\dot{w}_x(T)]/G(T)\ . \tag{9.21}$$

which involves the cumulative function, $G(t) = \int_0^t g(\tau)\mathrm{d}\tau$. The acceleration update is iteratively performed until $w_x(T)$ and $\dot{w}_x(T)$ are close to zero; this procedure converges in two or three iterations. The $y$-direction disturbance $w_y(t)$ is zero for all experiments.

### *9.4.4 Experiment design*

The shaking table disturbances used in this work were designed to represent *weak*, *moderate*, and *strong* motions over a range of periods. The disturbances are parameterized by the

peak disturbance velocity $V_{\mathrm{p}}$ and the pulse period $T_{\mathrm{p}}$. Acceleration records were generated using the above procedure and were scaled to match the prescribed peak velocity value $V_{\mathrm{p}}$ by scaling accelerations by a factor $V_{\mathrm{p}}/\max_t \dot{w}(t)$. Table 9.1 gives the disturbance durations $T$ and the experimental peak table velocities for weak, moderate, and strong cases in both the light and heavy system. The table velocity was calculated using the central difference of the LVDT table displacement measurements. The experiments were designed to have constant peak table velocities for the three disturbance strengths, but this was not precisely achieved in the laboratory implementation. Furthermore, two moderate and five strong scenarios cannot be performed due to the ±7.5 cm stroke limit of the actuator.

### *9.4.5 Prediction of forced-response time histories*

In order to draw a fair comparison between the experimental and numerical results, the shaking table acceleration records are applied to the numerical model. An example acceleration record is shown in Figure 9.11. The measured signal was low-pass filtered, with a cut-off frequency of 2.5 times the pulse frequency, to remove some sensor noise without distorting the dominant waveform. The inputs to the mathematical model $\ddot{w}_x(t)$ and $\ddot{w}_y(t)$

TABLE 9.1: Peak experimental shake table velocities for damped rolling pendulum isolator experiments.

| Pulse period | Duration | Peak measured table velocity $V_{\mathrm{p}}$ (cm/s) | | | | | |
|---|---|---|---|---|---|---|---|
| | | Light | | | Heavy | | |
| $T_{\mathrm{p}}$ (s) | $T$ (s) | Weak | Moderate | Strong | Weak | Moderate | Strong |
| 0.20 | 10 | 9.68 | 16.63 | 33.02 | 10.14 | 16.69 | 32.14 |
| 0.35 | 10 | 12.94 | 20.96 | 41.53 | 13.54 | 20.85 | 41.76 |
| 0.50 | 10 | 13.90 | 22.39 | 45.49 | 14.05 | 22.39 | 46.56 |
| 0.67 | 15 | 14.55 | 23.12 | 46.50 | 14.46 | 22.79 | 46.97 |
| 0.85 | 20 | 14.63 | 23.30 | 46.25 | 14.91 | 23.35 | 47.20 |
| 1.00 | 25 | 14.62 | 23.27 | - | 14.56 | 23.18 | - |
| 1.25 | 30 | 14.36 | 22.93 | - | 14.46 | 23.05 | - |
| 1.60 | 35 | 14.17 | 22.54 | - | 14.19 | 22.71 | - |
| 2.20 | 45 | 13.98 | - | - | 13.92 | - | - |
| 3.00 | 60 | 13.82 | - | - | 13.83 | - | - |

The dashes (-) indicate experimental tests not performed due to the stroke limit of the shake table.

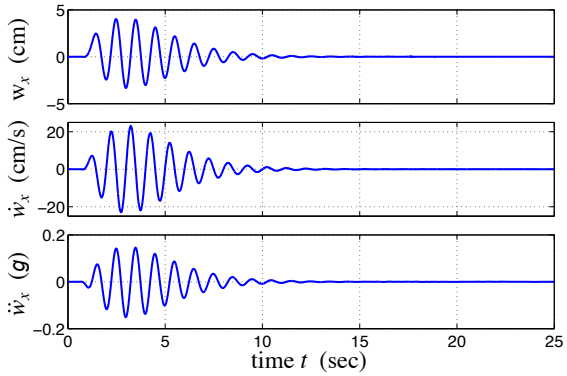


FIGURE 9.11: Measured displacement, velocity and (filtered) acceleration input applied to shaking table table: moderate disturbance with $T_{\rm p} = 1$ s.

were set to the low-pass-filtered measured acceleration records and zero, respectively, for all simulations. For the two moderate and five strong cases not experimentally performed, the input to the mathematical model $\ddot{w}_x(t)$ was set to the weak measured signal scaled to have peak velocities of $V_{\rm p} = 25$ cm/s and 48 cm/s, respectively.

In practice one cannot ensure that each ball-bearing is perfectly centered in the lower- and upper-bowls at the beginning of a test. To account for the uncertainty in the initial ball-bearing locations in the numerical simulations, the initial ball-bearing locations $\mathbf{r}_{i0}$ are taken to be uniformly distributed within a circle with radius of 0.5 cm, i.e.

$$\mathbf{r}_{i0} = [\rho_i \cos\psi_i \;\; \rho_i \sin\psi_i]^{\mathsf{T}} \;, \quad \rho_i \overset{\text{iid}}{\sim} U(0, 0.5) \text{ cm} \;, \quad \psi_i \overset{\text{iid}}{\sim} U(0, 2\pi) \;. \tag{9.22}$$

Twenty different initial conditions are used to test the influence of the initial ball location on the peak responses.

Two displacement measurements were acquired during the experiments; an LVDT measured the total displacement of the shaking table, and processed video recording gave the the total displacement of the equipment. By synchronizing these two measurements, the relative displacement of the top-frame was found by taking their difference. Two example experimental displacement records are shown in Figures 9.12(a-b) and 9.13(a-b) for two disturbance scenarios: strong disturbance at $T_{\rm p} = 0.50$ s and moderate disturbance at $T_{\rm p} = 1.00$ s, respectively. Figures 9.12(a-b) and 9.13(a-b) illustrate displacement records

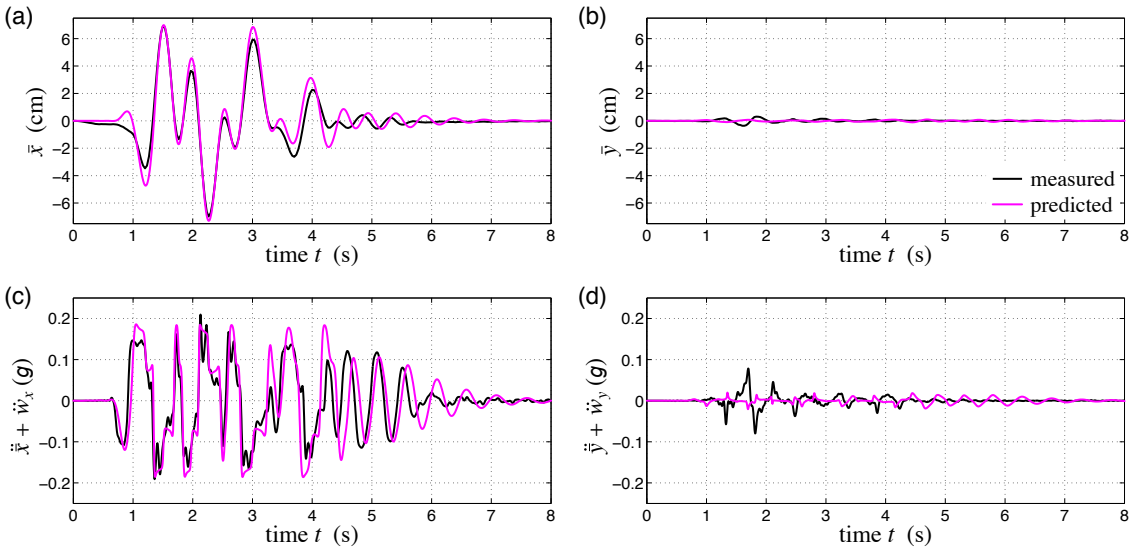


FIGURE 9.12: Measured (—) and predicted (—) displacement and acceleration responses of the light system: strong disturbance at $T_p = 0.50$ s.

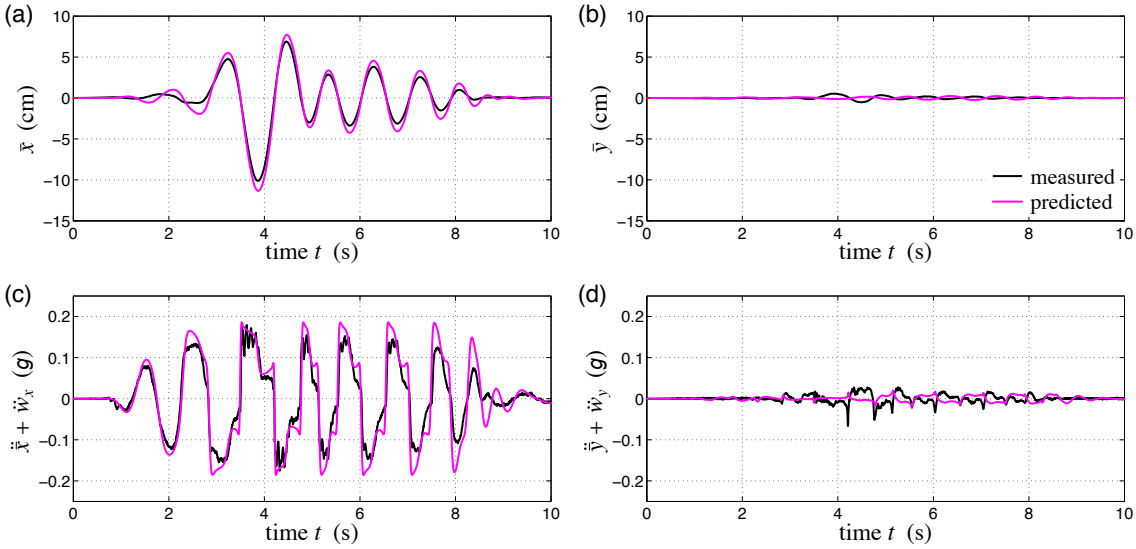


FIGURE 9.13: Measured (—) and predicted (—) displacement and acceleration responses of the light system: moderate disturbance at $T_p = 1.00$ s.

predicted by the model using the same disturbances. In both cases, the predicted displacement trajectories match the experimental displacement responses closely.

One accelerometer in the $X_t$-direction and two accelerometers equally-spaced in the $Y_t$-direction measured two orthogonal accelerations of the top-frame. For two disturbance scenarios, Figures 9.12(c-d) and 9.13(c-d) illustrate experimental acceleration records and

numerically-generated predictions of the acceleration histories. This demonstrates that the model is able to predict forced displacement and acceleration responses.

### *9.4.6 Prediction of peak response spectra*

The response quantities of interest are peak relative displacement and the peak total acceleration of the isolated mass. The peak relative displacement $d_{\mathrm{R}}^{\max}$ is defined as

$$d_{\mathrm{R}}^{\max} = \max_{t} \sqrt{\bar{x}^2(t) + \bar{y}^2(t)}. \tag{9.23}$$

The peak magnitude of the total acceleration $a_{\mathrm{T}}^{\max}$ is defined as

$$a_{\mathrm{T}}^{\max} = \max_{t} \sqrt{\left(\ddot{\bar{x}}(t) + \ddot{w}_x(t)\right)^2 + \left(\ddot{\bar{y}}(t) + \ddot{w}_y(t)\right)^2}. \tag{9.24}$$

Due to the top-frame's rotation $\bar{\theta}$, the measured accelerations are not in an absolute frame of reference. However, the magnitude of the total acceleration is rotationally-invariant and the norm of the recorded acceleration is equal to $a_{\mathrm{T}}(t)$.

The experimental and numerical peak response spectra for the light and heavy systems can be seen in Figure 9.14. The pulse strengths are distinguished by the marker shape, and the measured and predicted response quantities are distinguished by color. The measured and predicted peak responses show excellent agreement. For the light system in Figure 9.14(a), the peak displacements $d_{\mathrm{R}}^{\max}$ coincide in nearly all cases, with the numerical prediction being slightly high near resonance ($T_{\mathrm{p}} \in [0.67,1.0]$ s).

The model predicts the peak acceleration $a_{\mathrm{T}}^{\max}$ well in most cases. In no experimental test did the isolation system reach its maximum displacement capacity (20 cm); the largest peak displacement was 12.5 cm for the strong $T_{\mathrm{p}} = 0.85$ s. The model predicted excessively-large displacements (> 20 cm) in three loading scenarios—strong $T_{\mathrm{p}} = 1.00$, 1.25, and 1.6 s—which could not be tested experimentally due to the stroke limit of the actuator. In these cases, one or more ball-bearings impacted with the bowl lip, generating spikes in the acceleration response, which can be hazardous to isolated objects and

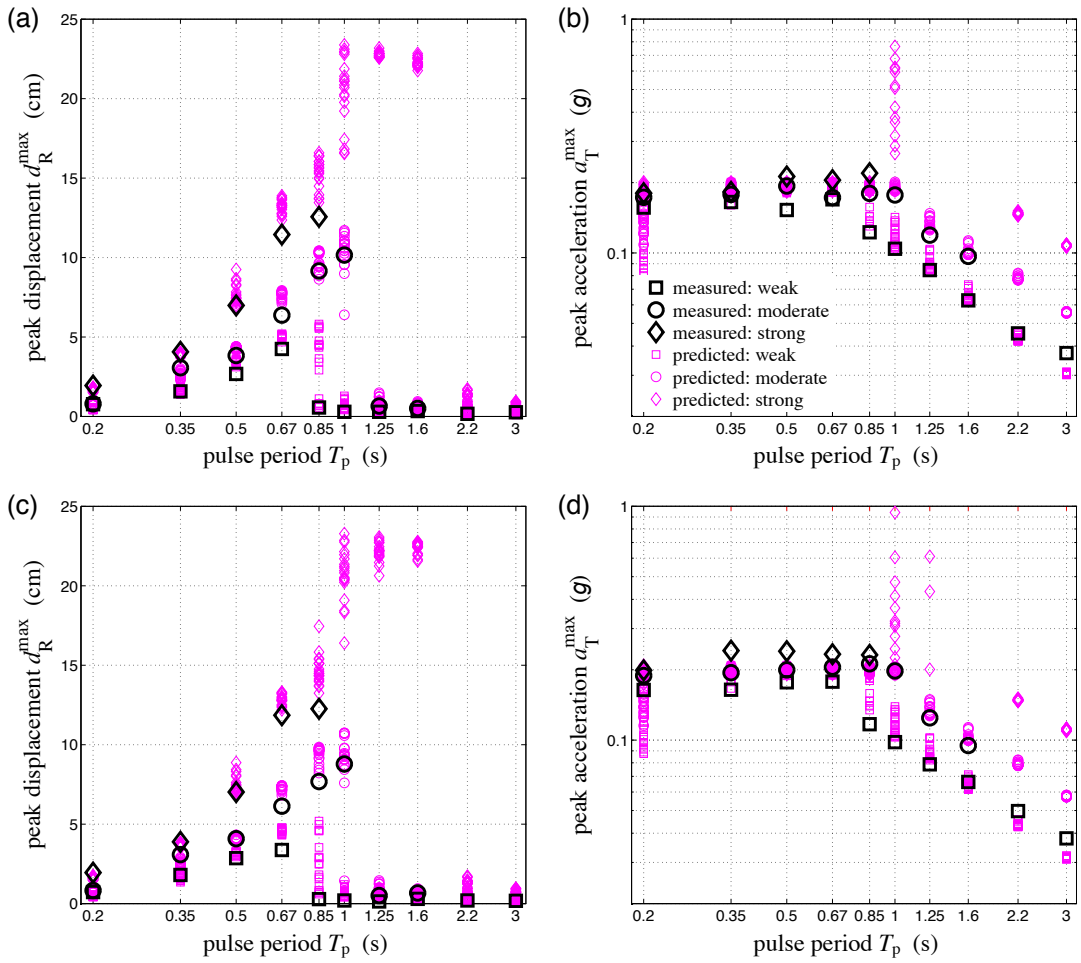


FIGURE 9.14: Measured and predicted peak displacement and acceleration pulse response spectra for (a-b) light system and (c-d) heavy system: weak (□), moderate (○), and strong (◇). No spikes in acceleration due to impacts were seen experimentally. Large (greater than 1 $g$) accelerations are predicted for cases not experimentally tested (i.e. strong motions at $T_p$ = 1, 1.25, and 1.6 s), but are not shown in the acceleration spectra; these points corresponds to peak displacements greater than 20 cm.

can constitute a failure of the isolation system. Elevated peak accelerations are observed when the ball-bearing impacts the lip, but for clarity are not shown in Figures 9.14(b) and 9.14(d).

Nearly identical results are observed for the light and heavy systems. Rolling pendulum isolation platforms have mass-independent behavior—the natural period is independent of the mass of the isolated equipment. Damped RISs, as we have shown, exhibit mass-dependent (i.e. load-dependent) rolling resistance, which scales nearly linearly (to

the power 1.25) with mass. Thus, the damped isolation behavior is approximately mass-independent, as shown experimentally and numerically.

Figure 9.14 demonstrates that the proposed simplified model successfully predicts the peak displacement and acceleration response under a variety of loading periods and amplitudes, and the results presented in this section validate the predictive capabilities of the simplified model.

## 9.5 Frontiers of Impact Revisited

In designing an isolation system, it is useful to know at what disturbance amplitudes, over a range of periods, the displacement capacity would be exceeded. Due to the physical limitations of the shaking table (e.g. stroke and peak velocity), impacts could not be induced. However, this inverse problem can be solved easily using the experimentally-validated mathematical model.

Define $V_{\mathrm{p}}^{\mathrm{crit}}$ to be the smallest velocity amplitude at which the peak acceleration exceeds a *critical* threshold. For this example we selected the light system ($m = 355$ kg) with threshold criterion of $a_{\mathrm{T}}^{\max} > 0.2\ g$ to indicate impacts. Using the bisection method, $V_{\mathrm{p}}^{\mathrm{crit}}$ was determined to the nearest 1 cm/s from twenty randomly generated initial conditions for a range of pulse periods $T_{\mathrm{p}}$. Table 9.2 gives the means and coefficients of variation (CV) of $V_{\mathrm{p}}^{\mathrm{crit}}$. Figure 9.15 illustrates these critical amplitudes in a tripartite plot. Near resonance ($T_{\mathrm{p}} = 1.25$ s), the critical peak floor velocity is approximately 34 cm/s, whereas velocities 3–15 times larger are required at shorter periods ($T_{\mathrm{p}} \leq 1$ s). In the short-period

TABLE 9.2: Average and coefficient of variation (CV) of the critical disturbance amplitude $V_{\mathrm{p}}^{\mathrm{crit}}$ for a damped rolling pendulum isolator.

| | | Pulse period $T_{\mathrm{p}}$ (s) | | | | | | | | | | | |
|---|---|---|---|---|---|---|---|---|---|---|---|---|---|
| | | 0.20 | 0.35 | 0.50 | 0.67 | 0.85 | 1.0 | 1.25 | 1.6 | 2.2 | 3.0 | 4.0 | 5.0 |
| $V_{\mathrm{p}}^{\mathrm{crit}}$ (cm/s) | avg | 486 | 197 | 136 | 94 | 54 | 41 | 34 | 40 | 57 | 78 | 105 | 132 |
| | CV | 0.6 | 0.9 | 10 | 21.8 | 4.4 | 4.5 | 3.9 | 4.2 | 2.2 | 1.8 | 2.2 | 1.5 |

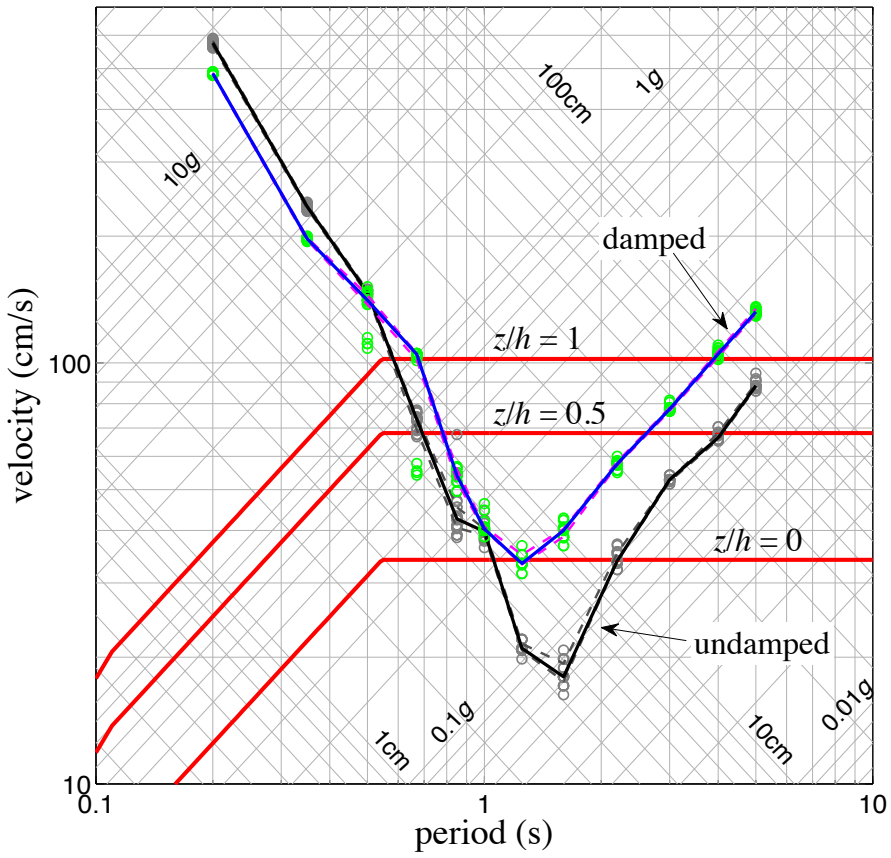


FIGURE 9.15: Seismic equipment isolation design spectrum. Critical disturbance velocity amplitude $V_{\mathrm{p}}^{\mathrm{crit}}$ for damped and undamped RISs: twenty random initial conditions (○), median (—), and the 25th and 75th percentile (– – –). Seismic design spectra (—), as per ASCE 7-10, for a nonstructural component at three attachment heights: ground ($z/h = 0$), mid-height ($z/h = 0.5$), and roof ($z/h = 1$).

range, the occurrence of impacts corresponds to a critical peak floor displacement level of approximately 10 cm. The critical floor displacement drops to 7 cm near resonance and increases to 100 cm for the longest pulse period ($T_{\mathrm{p}} = 5$ s). In the long-period range, the system is acceleration controlled—the impacts occur at a peak floor acceleration level of 0.18 $g$.

Figure 9.15 also illustrates the critical amplitude of an undamped RIS [52] at the same critical acceleration threshold. Up to periods of $T_{\mathrm{p}} = 1$ s, the two systems are displacement-controlled and have nearly the same critical velocity $V_{\mathrm{p}}^{\mathrm{crit}}$. Whereas, at or above the systems' resonant periods ($T_{\mathrm{p}} \geq 1.25$ s), the damped system significantly outper-

formed the undamped system. Near resonance ($T_{\mathrm{p}} \in [1.25, 1.6]$ *s*), the damped system's critical velocity is 50 to 100 percent *higher* than the undamped system. At longer-than-resonant periods ($T_{\mathrm{p}} > 1.6$ s), the damped and undamped systems are both acceleration controlled with acceleration thresholds of 0.18 $g$ and 0.12 $g$, respectively. These values correspond to the gravitational-plus-damping restoring force levels in each system, which relate to the necessary inertial force to 'escape' from the potential well. Upon doing so, the top-frame and equipment impact, violently in some cases, with the bowl lip.

Finally, the sufficiency of the damped and undamped isolation systems to protect equipment from design-level earthquakes is assessed. The seismic design spectra for non-structural components, as per ASCE 7-10 [89], are also plotted in Figure 9.15. These design spectra were generated for a vibration-isolated component located in a high seismicity area (San Francisco) with site class C. The equipment design spectral acceleration is given by Equations (4.24) and (4.25), where values for the design parameters are given in Table 4.4. Three component attachment levels were considered: ground ($z/h = 0$), mid-height ($z/h = 0.5$), and roof ($z/h = 1$).

From Figure 14, we see that the capacity of both the damped and the undamped systems is sufficient at short periods, for lower floor levels. At near-resonant excitations (periods from 1 s to 2 s), the undamped RIS would not meet demands at *any* floor level. The damped system is able to meet the seismic demands for lower floor levels at all periods. At period longer than 2 s, the capacity of the undamped system is sufficient for low to intermediate floor levels, and is sufficient throughout the structure's height only at periods greater than 5 s. The damped RIS's capacity is sufficient at mid-height and roof attachment heights for periods greater than 2.5 s and 4 s, respectively.

The following design recommendations are supported by the foregoing analyses and discussion:

- Supplemental damping via rubber coated rolling surfaces is capable of decreasing

the displacement demands on RISs, and thus increase the performance of such systems for high-intensity motions.

- The improvement of isolation performance through added damping is more pronounced at longer period excitations.

- A 22 cm displacement capacity for damped rolling pendulum isolators is sufficient to prevent impacts in installations at lower floor levels in regions with high probability of strong ground motion.

## 9.6 Summary

This chapter presents a simple and experimentally-validated model of a damped rolling pendulum isolation system. The general problem formulation and modeling procedure are described. An experimental set-up is presented, and the unique features of the experiment are identified, including the deformations ('divot') in the rubber layer and the load-dependent rolling-resistance of a rigid steel ball-bearing rolling between rubber sheets. Experimental data from tests on a single-axis shake table are used to assess peak responses. The proposed model was shown to effectively predict both free- and forced-response histories and peak responses in terms of both relative displacements and total accelerations. Finally, the paper demonstrates the capabilities of the system in meeting design criteria. Critical disturbance amplitudes were numerically evaluated for a range of pulse periods. Decreasing the displacement demand via supplemental damping was shown to enhance the behavior of this rolling isolation system for near-resonant excitations.

# 10

# Assessment of the Seismic Performance of Undamped and Damped Rolling Isolation Systems

## 10.1 Background

This chapter serves as a culmination of findings from the preceding chapters. In Chapter 3 a model for a rolling isolation system (RIS) was developed which respected the nonholonomic constraints associated with the rolling of rigid steel balls between rigid steel bowls. Then, in Chapter 4 this model was simplified and experimentally validated using an idealized disturbance model. It was shown that an undamped RIS's displacement capacity might not be sufficient, so two approaches were proposed: increase the system's displacement capacity (Chapters 5 and 6) or decrease the displacement demand (Chapters 8 and 9). A double RIS was modelled and validated in Chapters 5 and 6, and Chapter 8 focused on evaluating optimal semi-active control of an RIS. These two approaches can potentially improve the performance of RISs, but are currently underdeveloped—future work should address these shortcomings. Finally, Chapter 9 modelled and validated a damped RIS, and showed improved performance over the undamped system.

This chapter builds upon the comparison presented in Chapter 9 by examining the

performances of a damped RIS and an undamped RIS located within earthquake-excited structures. Six structures of varying height and stiffness [137] are chosen to represent a range of potential RIS installations. Finite element models of the six structures are first derived for representative planar frames, then reduced through dynamic condensation, and finally incorporated into three-dimensional (3D) models with hysteretic coupling in orthogonal directions. The structural models are orthotropic in plan and uniform along the height. Three suites of recorded ground-motion records are scaled and inputted into these reduced, hysteretic models. The bidirectional floor responses at varying heights are applied to the undamped and damped experimentally-validated RIS models (Chapters 4 and 9). Empirical cumulative distribution functions (CDFs) of peak isolator response for the two systems are compared.

## 10.2 Structural Systems Considered

The buildings considered in this study are six steel moment-resisting frame building with 4, 8, and 12 stories designed and previously studied by Santa-Anna and Miranda [137]. As indicated in Figure 10.1, these building have three bays at 7.32 m with uniform mass distribution over their height. For each of the aforementioned heights, two different buildings are considered: one is designed to be relatively *flexible* and the other to be relatively *rigid*. All are designed using the lateral load distribution specified in the 1994 Uniform Building Code for Zone IV. The rigidities of their beams and columns were tuned to obtain fundamental periods of vibration that are representative of existing steel building in California.

FRAME3DD [139] was used to generate mass matrices $\boldsymbol{M}$ and stiffness matrices $\boldsymbol{K}$ for the six planar frames. The $i$th node possesses three degrees of freedom—lateral displacement $x_i$, vertical displacement $z_i$, and rotation $\phi_i$—resulting in $3 \cdot 4 \cdot n$ total degrees of freedom, where $n$ is the number of stories. Therefore, $\boldsymbol{M} \in \mathbb{R}^{12n \times 12n}$ and $\boldsymbol{K} \in \mathbb{R}^{12n \times 12n}$, and

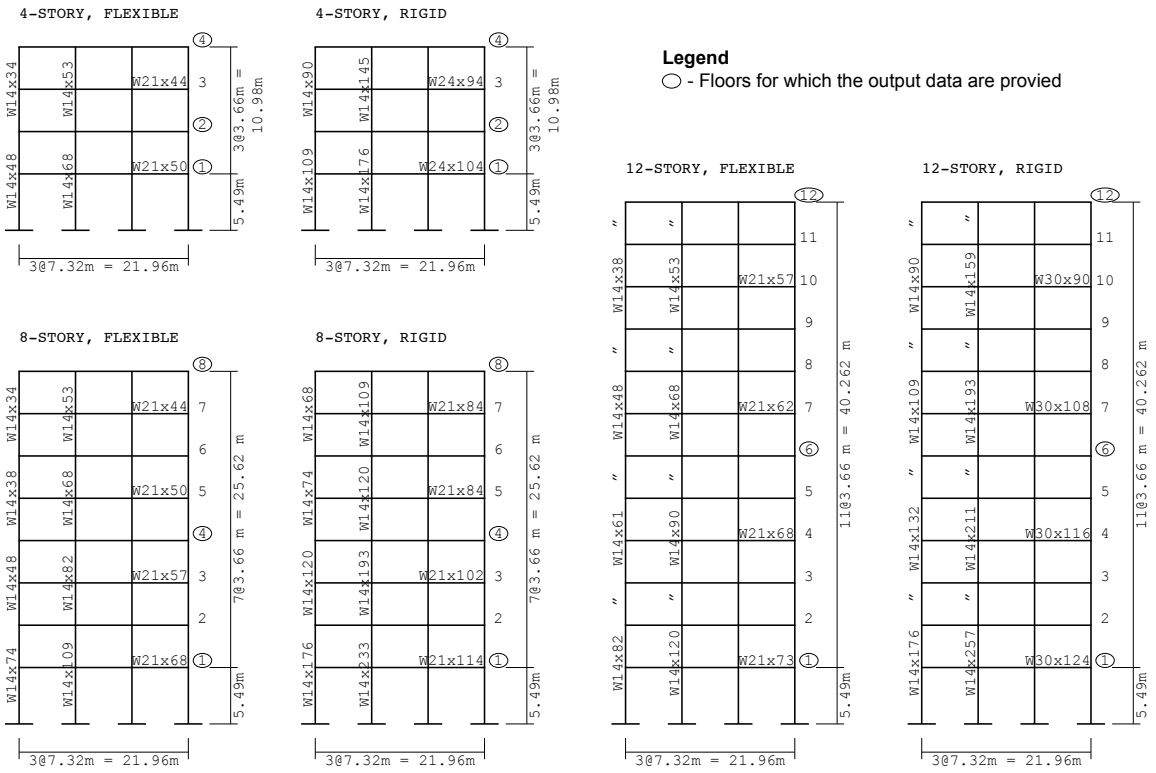


FIGURE 10.1: Planar frames used as representative designs [138] and levels for which floor acceleration data were recorded.

the displacement vector is $\boldsymbol{d} = [x_1, z_1, \phi_1, ..., x_{4n}, z_{4n}, \phi_{4n}]^\intercal$. The equations of motion are as follows:

$$\boldsymbol{M}\ddot{\boldsymbol{d}} + \boldsymbol{K}\boldsymbol{d} = -\boldsymbol{M}\boldsymbol{J}\ddot{u}_g \tag{10.1}$$

where the influence vector,

$$\boldsymbol{J} = [1\ \ 0\ \ 0\ \ \cdots\ \ 1\ \ 0\ \ 0]^\intercal \in \mathbb{R}^{12n}\,, \tag{10.2}$$

applies the lateral ground motion $u_g(t)$ to the lateral nodal degrees of freedom, $x_i$.

In a free response, $u_g(t) \equiv 0$ and the equations of motion (Equation (10.1)) are

$$\boldsymbol{M}\ddot{\boldsymbol{d}} + \boldsymbol{K}\boldsymbol{d} = \boldsymbol{0}\,. \tag{10.3}$$

Additional floor mass was determined by varying the added mass applied to the (horizontal) beam elements until the first natural period matched those reported by Santa-Anna and

Miranda [138]. Table 10.1 gives the first four natural frequencies of the frames considered and the mass distribution.

## 10.3 Model Reduction for Hysteretic Systems

Previous methods of model reduction for hysteretic structures have either been limited to reducing only the linear aspects of the system (retaining all the nonlinear elements present in the system at some computational expense) [140, 141] or have approximated the nonlinear system using modal superposition with time-varying modes [142, 143]. In the reduced-order modeling method presented here, the elastic restoring forces of a condensed linear model are simply replaced by hysteretic forces. The reduced linear model is computed via dynamic condensation [144]. The coordinates of the condensed model correspond to selected coordinates of the full model, and the condensed model matches the full model at an arbitray selected frequency. The hysteretic forces are evolutionary [52, 145] and are calibrated to match the push-over behavior of the detailed inelastic frame model. Note that the number of hysteretic variables need not be larger than the number of condensed coordinates and time-varying (or 'nonlinear') modes are not involved.

TABLE 10.1: Natural frequencies for frames considered in both the full model and the reduced model.

| # of stories $n$ | Frame | Added mass ($10^3$ kg) | Full model ($\boldsymbol{M}, \boldsymbol{K}$) natural frequencies (Hz) | | | | Reduced model ($\tilde{\boldsymbol{M}}, \tilde{\boldsymbol{K}}$) natural frequencies (Hz) | | | |
|---|---|---|---|---|---|---|---|---|---|---|
| | | | $f_{\mathrm{n}1}$ | $f_{\mathrm{n}2}$ | $f_{\mathrm{n}3}$ | $f_{\mathrm{n}4}$ | $\tilde{f}_{\mathrm{n}1}$ | $\tilde{f}_{\mathrm{n}2}$ | $\tilde{f}_{\mathrm{n}3}$ | $\tilde{f}_{\mathrm{n}4}$ |
| 4 | flexible | 20.8 | 0.79 | 2.50 | 4.76 | 6.92 | 0.79 | 2.52 | 4.91 | 7.32 |
| | rigid | 19.5 | 1.37 | 4.39 | 8.33 | 12.06 | 1.37 | 4.44 | 8.69 | 12.96 |
| 8 | flexible | 20.6 | 0.52 | 1.47 | 2.53 | 3.73 | 0.52 | 1.47 | 2.56 | 3.80 |
| | rigid | 19.5 | 0.85 | 2.36 | 4.17 | 6.01 | 0.85 | 2.37 | 4.22 | 6.15 |
| 12 | flexible | 20.7 | 0.38 | 1.07 | 1.85 | 2.65 | 0.38 | 1.08 | 1.85 | 2.67 |
| | rigid | 19.8 | 0.65 | 1.86 | 3.21 | 4.62 | 0.65 | 1.87 | 3.25 | 4.72 |

### *10.3.1 Dynamic Guyan condensation*

The full models $(\boldsymbol{M}, \boldsymbol{K})$ developed with FRAME3DD are very large and therefore a model reduction is required. We condense the model with dynamic Guyan condensation, exactly retaining the first natural frequency $\omega_1^2$. The primary coordinates which we wish to retain are the lateral displacements of the column second from the left, which we denote $\boldsymbol{d}_\mathrm{p} \in \mathbb{R}^n$. The secondary coordinates $\boldsymbol{d}_\mathrm{s} \in \mathbb{R}^{11n}$ are the remaining degrees of freedom. The model in Equation (10.1) can be transformed and partitioned as follows:

$$\begin{bmatrix} \boldsymbol{M}_{\mathrm{pp}} & \boldsymbol{M}_{\mathrm{ps}} \\ \boldsymbol{M}_{\mathrm{sp}} & \boldsymbol{M}_{\mathrm{ss}} \end{bmatrix} \begin{Bmatrix} \ddot{\boldsymbol{d}}_\mathrm{p} \\ \ddot{\boldsymbol{d}}_\mathrm{s} \end{Bmatrix} + \begin{bmatrix} \boldsymbol{K}_{\mathrm{pp}} & \boldsymbol{K}_{\mathrm{ps}} \\ \boldsymbol{K}_{\mathrm{sp}} & \boldsymbol{K}_{\mathrm{ss}} \end{bmatrix} \begin{Bmatrix} \boldsymbol{d}_\mathrm{p} \\ \boldsymbol{d}_\mathrm{s} \end{Bmatrix} = - \begin{bmatrix} \boldsymbol{M}_{\mathrm{pp}} & \boldsymbol{M}_{\mathrm{ps}} \\ \boldsymbol{M}_{\mathrm{sp}} & \boldsymbol{M}_{\mathrm{ss}} \end{bmatrix} \begin{bmatrix} \boldsymbol{J}_\mathrm{p} \\ \boldsymbol{J}_\mathrm{s} \end{bmatrix} \ddot{u}_\mathrm{g} \tag{10.4}$$

or, for free response (Equation (10.3)),

$$\begin{bmatrix} \boldsymbol{M}_{\mathrm{pp}} & \boldsymbol{M}_{\mathrm{ps}} \\ \boldsymbol{M}_{\mathrm{sp}} & \boldsymbol{M}_{\mathrm{ss}} \end{bmatrix} \begin{Bmatrix} \ddot{\boldsymbol{d}}_\mathrm{p} \\ \ddot{\boldsymbol{d}}_\mathrm{s} \end{Bmatrix} + \begin{bmatrix} \boldsymbol{K}_{\mathrm{pp}} & \boldsymbol{K}_{\mathrm{ps}} \\ \boldsymbol{K}_{\mathrm{sp}} & \boldsymbol{K}_{\mathrm{ss}} \end{bmatrix} \begin{Bmatrix} \boldsymbol{d}_\mathrm{p} \\ \boldsymbol{d}_\mathrm{s} \end{Bmatrix} = \begin{Bmatrix} \boldsymbol{0} \\ \boldsymbol{0} \end{Bmatrix}. \tag{10.5}$$

Assuming solutions $\boldsymbol{d}_\mathrm{p}(t) = \bar{\boldsymbol{d}}_\mathrm{p} \sin \omega t$ and $\boldsymbol{d}_\mathrm{s}(t) = \bar{\boldsymbol{d}}_\mathrm{s} \sin \omega t$, the partitioned eigenvalue problem is

$$\begin{bmatrix} \boldsymbol{K}_{\mathrm{pp}} - \omega^2 \boldsymbol{M}_{\mathrm{pp}} & \boldsymbol{K}_{\mathrm{ps}} - \omega^2 \boldsymbol{M}_{\mathrm{ps}} \\ \boldsymbol{K}_{\mathrm{sp}} - \omega^2 \boldsymbol{M}_{\mathrm{sp}} & \boldsymbol{K}_{\mathrm{ss}} - \omega^2 \boldsymbol{M}_{\mathrm{ss}} \end{bmatrix} \begin{Bmatrix} \bar{\boldsymbol{d}}_\mathrm{p} \\ \bar{\boldsymbol{d}}_\mathrm{s} \end{Bmatrix} = \begin{Bmatrix} \boldsymbol{0} \\ \boldsymbol{0} \end{Bmatrix} \tag{10.6}$$

The condensation transformation matrix is

$$\tilde{\boldsymbol{T}} = \begin{bmatrix} \boldsymbol{I}_{n \times n} \\ -(\boldsymbol{K}_{\mathrm{ss}} - \omega^2 \boldsymbol{M}_{\mathrm{ss}})^{-1} (\boldsymbol{K}_{\mathrm{sp}} - \omega^2 \boldsymbol{M}_{\mathrm{sp}}) \end{bmatrix}_{12n \times n} \quad \Rightarrow \quad \begin{Bmatrix} \boldsymbol{d}_\mathrm{p} \\ \boldsymbol{d}_\mathrm{s} \end{Bmatrix} = \tilde{\boldsymbol{T}} \boldsymbol{d}_\mathrm{p}, \tag{10.7}$$

and is applied to Equation (10.4),

$$\tilde{\boldsymbol{M}} \ddot{\boldsymbol{d}}_\mathrm{p} + \tilde{\boldsymbol{K}} \boldsymbol{d}_\mathrm{p} = -\tilde{\boldsymbol{\mu}} \ddot{u}_\mathrm{g} \tag{10.8}$$

in which

$$\tilde{\boldsymbol{M}} = \tilde{\boldsymbol{T}}^\mathsf{T} \begin{bmatrix} \boldsymbol{M}_{\mathrm{pp}} & \boldsymbol{M}_{\mathrm{ps}} \\ \boldsymbol{M}_{\mathrm{sp}} & \boldsymbol{M}_{\mathrm{ss}} \end{bmatrix} \tilde{\boldsymbol{T}}, \quad \tilde{\boldsymbol{K}} = \tilde{\boldsymbol{T}}^\mathsf{T} \begin{bmatrix} \boldsymbol{K}_{\mathrm{pp}} & \boldsymbol{K}_{\mathrm{ps}} \\ \boldsymbol{K}_{\mathrm{sp}} & \boldsymbol{K}_{\mathrm{ss}} \end{bmatrix} \tilde{\boldsymbol{T}}, \quad \tilde{\boldsymbol{\mu}} = \tilde{\boldsymbol{T}}^\mathsf{T} \begin{bmatrix} \boldsymbol{M}_{\mathrm{pp}} & \boldsymbol{M}_{\mathrm{ps}} \\ \boldsymbol{M}_{\mathrm{sp}} & \boldsymbol{M}_{\mathrm{ss}} \end{bmatrix} \begin{bmatrix} \boldsymbol{J}_\mathrm{p} \\ \boldsymbol{J}_\mathrm{s} \end{bmatrix}. \tag{10.9}$$

The reduced model $(\tilde{\boldsymbol{M}}, \tilde{\boldsymbol{K}})$ exactly matches the modal dynamics at $\omega$, which can be any frequency. We select $\omega = \omega_{\mathrm{n}1}$, the first natural frequency of the full model $(\boldsymbol{M}, \boldsymbol{K})$. In so doing, we have reduced the dimension of the model by a factor of 12 (full: $12n$ DOF; reduced: $n$ DOF). The first four natural frequencies of the reduced model are given in Table 10.1. We see a good match between the first few natural frequencies, with divergence for the higher modes. The reduced model can be thought of as a stick model with communication between all the stories, i.e. $\tilde{\boldsymbol{M}}$ and $\tilde{\boldsymbol{K}}$ are fully populated, in general.

### *10.3.2 Extended Rayleigh damping*

Classical damping, in the form of extended Rayleigh damping [146], is incorporated into the reduced model (Equation (10.8)). A proportional damping matrix can be made up of a combination of the mass and stiffness matrices, as follows:

$$\tilde{\boldsymbol{C}} = \sum_{p \in \mathcal{P}} c_p \tilde{\boldsymbol{M}} (\tilde{\boldsymbol{M}}^{-1} \tilde{\boldsymbol{K}})^p \tag{10.10}$$

in which the coefficients $c_p$ are arbitrary. The powers $p$ determine the bases, given by $\tilde{\boldsymbol{M}}(\tilde{\boldsymbol{M}}^{-1}\tilde{\boldsymbol{K}})^p$, over which $\tilde{\boldsymbol{C}}$ is expanded. Rayleigh damping is a limiting case of Equation (10.10) in which only the terms $p = 0$ and $p = 1$ are retained in the series.

The generalized damping ratio associated with any mode $\omega_m$ is

$$\zeta_m = \frac{1}{2\omega_m} \sum_{p \in \mathcal{P}} c_p \omega_m^{2p} \tag{10.11}$$

By selecting the powers $p$, a set of $\omega_m$ (which need not be the natural frequencies), and the corresponding $\zeta_m$, the coefficients $c_p$ are evaluated for the simultaneous solution of Equation (10.11). The desired damping ratios $\zeta_m$ are obtained exactly at the specified frequencies $\omega_m$, and is approximated at intermediate frequencies.

The powers $\mathcal{P} = \{-1,\ 0, +1, +2, +3\}$ were selected for all cases. Note that for $n = 4$ an additional frequency was needed to be able to uniquely solve for the coefficients; the five

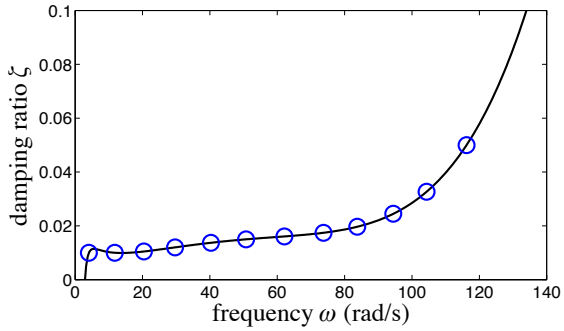


FIGURE 10.2: Extended Rayleigh damping (damping ratio versus frequency): (—) polynomial fit, (○) natural frequencies $\omega_{\mathrm{n}i}$.

frequencies and damping ratios used were

$$\boldsymbol{\omega} = [\omega_{\mathrm{n}1} \;\; (\omega_{\mathrm{n}1}+\omega_{\mathrm{n}2})/2 \;\; \omega_{\mathrm{n}2} \;\; \omega_{\mathrm{n}3} \;\; \omega_{\mathrm{n}4}] \tag{10.12a}$$

$$\boldsymbol{\zeta} = [0.01 \;\; 0.01 \;\; 0.01 \;\; 0.012 \;\; 0.05] \tag{10.12b}$$

where $\omega_{\mathrm{n}i}$ is the $i$th natural frequency of the system in Equation (10.8). For $n = 8$ and $n = 12$ the five frequencies and damping ratios are

$$\boldsymbol{\omega} = [\omega_{\mathrm{n}1} \;\; \omega_{\mathrm{n}2} \;\; \omega_{\mathrm{n}4} \;\; (\omega_{\mathrm{n}4} + \omega_{\mathrm{n}n})/2 \;\; \omega_{\mathrm{n}n}] \tag{10.13a}$$

$$\boldsymbol{\zeta} = [0.01 \;\; 0.01 \;\; 0.012 \;\; 0.02 \;\; 0.05] \,. \tag{10.13b}$$

Figure 10.2 shows the equivalent Rayleigh damping fit using Equation (10.11) for the flexible, 12-story structure. The increased damping in the higher modes helps with numerical stability.

Once the coefficients $c_p$ are determined, the condensed damping matrix $\tilde{\boldsymbol{C}}$ is found from Equation (10.10). Now, the condensed equations of motion are

$$\tilde{\boldsymbol{M}}\ddot{\boldsymbol{d}}_{\mathrm{p}} + \tilde{\boldsymbol{C}}\dot{\boldsymbol{d}}_{\mathrm{p}} + \tilde{\boldsymbol{K}}\boldsymbol{d}_{\mathrm{p}} = -\tilde{\boldsymbol{\mu}}\ddot{u}_{\mathrm{g}} \tag{10.14}$$

where vector $\tilde{\boldsymbol{\mu}}$ and matrices $\tilde{\boldsymbol{M}}$ and and $\tilde{\boldsymbol{K}}$ are given above.

### *10.3.3 Three-dimensional, symmetrical model*

So far, we have only been looking at a planar frame. We assume that the 3D model is orthotropic in the $x$ and $y$ directions with identical structural properties. The vectors

$\boldsymbol{x} = [x_1, x_2, ..., x_n]^\mathsf{T}$ and $\boldsymbol{y} = [y_1, y_2, ..., y_n]^\mathsf{T}$ are the displacements of the $i$th story, relative to the base, in the $x$ and $y$ directions, respectively. There is no coupling via mass or stiffness eccentricity; coupling will be treated with the hysteretic model (Section 10.3.4). Therefore, the decoupled equations of motion are

$$\tilde{\boldsymbol{M}}\ddot{\boldsymbol{x}} + \tilde{\boldsymbol{C}}\dot{\boldsymbol{x}} + \tilde{\boldsymbol{K}}\boldsymbol{x} = -\tilde{\boldsymbol{\mu}}\ddot{u}_{\mathrm{g}x} \tag{10.15a}$$

$$\tilde{\boldsymbol{M}}\ddot{\boldsymbol{y}} + \tilde{\boldsymbol{C}}\dot{\boldsymbol{y}} + \tilde{\boldsymbol{K}}\boldsymbol{y} = -\tilde{\boldsymbol{\mu}}\ddot{u}_{\mathrm{g}y} \tag{10.15b}$$

where $u_{\mathrm{g}x}$ and $u_{\mathrm{g}y}$ are the ground disturbances applied at the base of the structure.

### *10.3.4 Treatment of biaxial hysteresis*

In this subsection, the uncoupled, reduced structural model in Equation (10.15) is coupled with a biaxial hysteresis model which possesses an *isotropic* yield surface. The hysteresis model is a generalization of the Park-Wen model [145], which is itself an extension of the uniaxial Bouc-Wen model [147, 148]. Appendix D explains the derivation of the proposed hysteretic model for coupled biaxial hysteretic behavior in which the 'knee' from pre-yield to post-yield can be adjusted while maintaining an isotropic yield surface.

The lower-triangular matrix

$$\mathbf{T} = \begin{bmatrix} 1 & 0 & \cdots & 0 \\ 1 & 1 & \ddots & \vdots \\ \vdots & \ddots & \ddots & 0 \\ 1 & \cdots & 1 & 1 \end{bmatrix} \tag{10.16}$$

relates the translations with respect to the ground, $\boldsymbol{x}$ and $\boldsymbol{y}$, to the relative inter-story deflections, denoted $\boldsymbol{u}_x = [u_{x1}, ..., u_{xn}]^\mathsf{T}$ and $\boldsymbol{u}_y = [u_{y1}, ..., u_{yn}]^\mathsf{T}$, respectively. That is,

$$\boldsymbol{x} = \mathbf{T}\boldsymbol{u}_x \;\Rightarrow \boldsymbol{u}_x = \mathbf{T}^{-1}\boldsymbol{x} \tag{10.17a}$$

$$\boldsymbol{y} = \mathbf{T}\boldsymbol{u}_y \;\Rightarrow \boldsymbol{u}_y = \mathbf{T}^{-1}\boldsymbol{y}\,. \tag{10.17b}$$

Transforming Equation (10.15) to relative coordinates,

$$\tilde{\boldsymbol{M}}_u\ddot{\boldsymbol{u}}_x + \tilde{\boldsymbol{C}}_u\dot{\boldsymbol{u}}_x + \tilde{\boldsymbol{K}}_u\boldsymbol{u}_x = -\tilde{\boldsymbol{\mu}}_u\ddot{u}_{\mathrm{g}x} \tag{10.18a}$$

$$\tilde{\boldsymbol{M}}_u \ddot{\boldsymbol{u}}_y + \tilde{\boldsymbol{C}}_u \dot{\boldsymbol{u}}_y + \tilde{\boldsymbol{K}}_u \boldsymbol{u}_y = -\tilde{\boldsymbol{\mu}}_u \ddot{u}_{\mathrm{g}y} \tag{10.18b}$$

where the matrices $\tilde{\boldsymbol{M}}_u = \mathbf{T}^\intercal \tilde{\boldsymbol{M}} \mathbf{T}$, $\tilde{\boldsymbol{C}}_u = \mathbf{T}^\intercal \tilde{\boldsymbol{C}} \mathbf{T}$, $\tilde{\boldsymbol{K}}_u = \mathbf{T}^\intercal \tilde{\boldsymbol{K}} \mathbf{T}$, and $\tilde{\boldsymbol{\mu}}_u = \mathbf{T}^\intercal \tilde{\boldsymbol{\mu}}$.

Now, instead of elastic restoring forces, we take the inter-story shear forces to be

$$\tilde{\boldsymbol{K}}_u \boldsymbol{u}_x \to \kappa \tilde{\boldsymbol{K}}_u \boldsymbol{u}_x + (1-\kappa) \tilde{\boldsymbol{K}}_u \boldsymbol{z}_x \tag{10.19a}$$

$$\tilde{\boldsymbol{K}}_u \boldsymbol{u}_y \to \kappa \tilde{\boldsymbol{K}}_u \boldsymbol{u}_y + (1-\kappa) \tilde{\boldsymbol{K}}_u \boldsymbol{z}_y \tag{10.19b}$$

in which $\kappa$ is the ratio of the post-yield stiffness to pre-yield (elastic) stiffness. The auxiliary variables $\boldsymbol{z}_x = [z_{x1}, ..., z_{xn}]^\intercal$ and $\boldsymbol{z}_y = [z_{y1}, ..., z_{yn}]^\intercal$ are the isotropic hysteretic displacements, which are given by the *generalized* Park-Wen model [66, 145] as presented in Appendix D.

$$\dot{\boldsymbol{z}}_x = \dot{\boldsymbol{u}}_x - \boldsymbol{z}_x \circ \boldsymbol{\iota} \tag{10.20a}$$

$$\dot{\boldsymbol{z}}_y = \dot{\boldsymbol{u}}_y - \boldsymbol{z}_y \circ \boldsymbol{\iota} \tag{10.20b}$$

where the operator "$\circ$" is the element-wise multiplication of two vectors; and the function $\boldsymbol{\iota} \equiv \boldsymbol{\iota}(\boldsymbol{z}_x, \boldsymbol{z}_y, \dot{\boldsymbol{u}}_x, \dot{\boldsymbol{u}}_y)$ accounts for the effects of the biaxial interaction as follows [66]:

$$\boldsymbol{\iota} = \{\boldsymbol{\beta} \circ \mathrm{abs}(\dot{\boldsymbol{u}}_x \circ \boldsymbol{z}_x) - \boldsymbol{\gamma} \circ \dot{\boldsymbol{u}}_x \circ \boldsymbol{z}_x - \boldsymbol{\beta} \circ \mathrm{abs}(\dot{\boldsymbol{u}}_y \circ \boldsymbol{z}_y) - \boldsymbol{\gamma} \circ \dot{\boldsymbol{u}}_y \circ \boldsymbol{z}_y\} \circ (\boldsymbol{z}_x \circ \boldsymbol{z}_x + \boldsymbol{z}_y \circ \boldsymbol{z}_y)^{\frac{\eta-2}{2}}. \tag{10.21}$$

The parameters $\beta_i$ and $\gamma_i$ govern the hysteretic behavior of the system. The parameter $\eta$ governs the smoothness of the transition from the linear to the nonlinear range [149], effectively adjusting the 'knee' of the hysteresis loop. The yield displacement $z_{i,\mathrm{yield}}$ is given by

$$z_{i,\mathrm{yield}} = 1 \Big/ \sqrt[\eta]{\beta_i + \gamma_i}\,. \tag{10.22}$$

Letting $\rho \in [0, 1]$,

$$\beta_i = \frac{\rho}{z_{i,\mathrm{yield}}^{\eta}} \quad \text{and} \quad \gamma_i = \frac{1-\rho}{z_{i,\mathrm{yield}}^{\eta}}\,. \tag{10.23}$$

By varying $\rho$, the hysteresis loop changes, as illustrated in Figure 10.3.

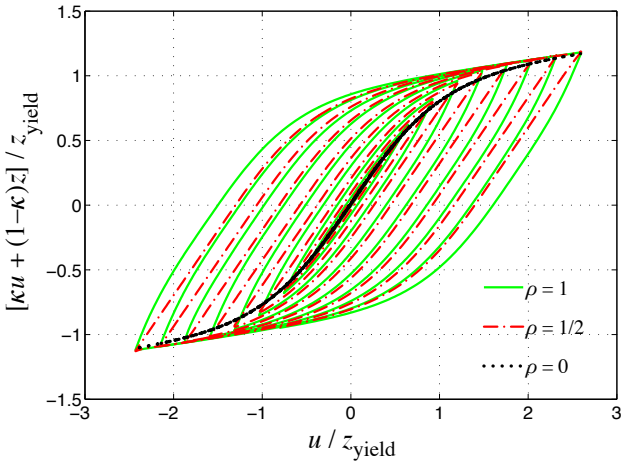


FIGURE 10.3: Representative hysteresis loops for $\kappa = 0.1$ and $\eta = 2$.

Substituting Equations (10.19) into Equation (10.18) yields

$$\tilde{\boldsymbol{M}}_u \ddot{\boldsymbol{u}}_x + \tilde{\boldsymbol{C}}_u \dot{\boldsymbol{u}}_x + \kappa \tilde{\boldsymbol{K}}_u \boldsymbol{u}_x + (1-\kappa)\tilde{\boldsymbol{K}}_u \boldsymbol{z}_x = -\tilde{\boldsymbol{\mu}}_u \ddot{u}_{\text{g}x} \tag{10.24a}$$

$$\tilde{\boldsymbol{M}}_u \ddot{\boldsymbol{u}}_y + \tilde{\boldsymbol{C}}_u \dot{\boldsymbol{u}}_y + \kappa \tilde{\boldsymbol{K}}_u \boldsymbol{u}_y + (1-\kappa)\tilde{\boldsymbol{K}}_u \boldsymbol{z}_y = -\tilde{\boldsymbol{\mu}}_u \ddot{u}_{\text{g}y} \,. \tag{10.24b}$$

Premultiply Equation (10.24) by $\mathbf{T}^{-\mathsf{T}}$ and substituting the expressions for $\boldsymbol{u}_x$ and $\boldsymbol{u}_y$ from Equation (10.17), we transform the equations of motion back to absolute coordinates:

$$\tilde{\boldsymbol{M}}\ddot{\boldsymbol{x}} + \tilde{\boldsymbol{C}}\dot{\boldsymbol{x}} + \kappa \tilde{\boldsymbol{K}}\boldsymbol{x} + (1-\kappa)\tilde{\boldsymbol{K}}\mathbf{T}\boldsymbol{z}_x = -\tilde{\boldsymbol{\mu}}\ddot{u}_{\text{g}x} \tag{10.25a}$$

$$\tilde{\boldsymbol{M}}\ddot{\boldsymbol{y}} + \tilde{\boldsymbol{C}}\dot{\boldsymbol{x}} + \kappa \tilde{\boldsymbol{K}}\boldsymbol{y} + (1-\kappa)\tilde{\boldsymbol{K}}\mathbf{T}\boldsymbol{z}_y = -\tilde{\boldsymbol{\mu}}\ddot{u}_{\text{g}y} \tag{10.25b}$$

where

$$\dot{\boldsymbol{z}}_x = \mathbf{T}^{-1}\dot{\boldsymbol{x}} - \boldsymbol{z}_x \circ \boldsymbol{\iota} \tag{10.26a}$$

$$\dot{\boldsymbol{z}}_y = \mathbf{T}^{-1}\dot{\boldsymbol{y}} - \boldsymbol{z}_y \circ \boldsymbol{\iota} \tag{10.26b}$$

and

$$\boldsymbol{\iota} = \left\{\boldsymbol{\beta}\circ\text{abs}[(\mathbf{T}^{-1}\dot{\boldsymbol{x}})\circ\boldsymbol{z}_x] - \boldsymbol{\gamma}\circ(\mathbf{T}^{-1}\dot{\boldsymbol{x}})\circ\boldsymbol{z}_x - \boldsymbol{\beta}\circ\text{abs}[(\mathbf{T}^{-1}\dot{\boldsymbol{y}})\circ\boldsymbol{z}_y] - \boldsymbol{\gamma}\circ(\mathbf{T}^{-1}\dot{\boldsymbol{y}})\circ\boldsymbol{z}_y\right\}\circ(\boldsymbol{z}_x\circ\boldsymbol{z}_x + \boldsymbol{z}_y\circ\boldsymbol{z}_y)^{\frac{\eta-2}{2}}.$$

Define the state vector to be $\mathbf{x}^{\mathsf{T}}(t) = [\boldsymbol{x}^{\mathsf{T}}\ \dot{\boldsymbol{x}}^{\mathsf{T}}\ \boldsymbol{z}_x^{\mathsf{T}}\ \boldsymbol{y}^{\mathsf{T}}\ \dot{\boldsymbol{y}}^{\mathsf{T}}\ \boldsymbol{z}_y^{\mathsf{T}}] \in \mathbb{R}^{6n}$. Equations (10.24) and (10.25) can be re-written in state-space form, as follows:

$$\dot{\mathbf{x}} = \begin{bmatrix} \boldsymbol{A} & \mathbf{0} \\ \mathbf{0} & \boldsymbol{A} \end{bmatrix}\mathbf{x} + \begin{bmatrix} \boldsymbol{B} & \mathbf{0} \\ \mathbf{0} & \boldsymbol{B} \end{bmatrix}\begin{Bmatrix} \boldsymbol{z}_x\circ\boldsymbol{\iota} \\ \boldsymbol{z}_y\circ\boldsymbol{\iota} \end{Bmatrix} + \begin{bmatrix} \boldsymbol{B}_{\text{g}} & \mathbf{0} \\ \mathbf{0} & \boldsymbol{B}_{\text{g}} \end{bmatrix}\begin{Bmatrix} \ddot{u}_{\text{g}x} \\ \ddot{u}_{\text{g}y} \end{Bmatrix} \tag{10.27}$$

for which

$$\boldsymbol{A} = \begin{bmatrix} \mathbf{0} & \boldsymbol{I} & \mathbf{0} \\ -\kappa\tilde{\boldsymbol{M}}^{-1}\tilde{\boldsymbol{K}} & -\tilde{\boldsymbol{M}}^{-1}\tilde{\boldsymbol{C}} & -(1-\kappa)\tilde{\boldsymbol{M}}^{-1}\tilde{\boldsymbol{K}}\mathbf{T} \\ \mathbf{0} & \mathbf{T}^{-1} & \mathbf{0} \end{bmatrix}; \quad \boldsymbol{B} = \begin{bmatrix} \mathbf{0} \\ \mathbf{0} \\ -\boldsymbol{I} \end{bmatrix}; \quad \boldsymbol{B}_{\mathrm{g}} = \begin{bmatrix} \mathbf{0} \\ -\tilde{\boldsymbol{M}}^{-1}\tilde{\boldsymbol{\mu}} \\ \mathbf{0} \end{bmatrix}.$$

### *10.3.5 Model verification via pushover analyses*

Finally, to verify that the condensed hysteretic system behaves similarly to the full inelastic model, static pushover curves [150] generated using EPFRAME [151] for the full model $(\boldsymbol{M}, \boldsymbol{K})$ will be compared to quasi-static pushover curves for the condensed, hysteretic model $(\tilde{\boldsymbol{M}}, \tilde{\boldsymbol{K}})$. The program EPFRAME returns the load-deflection relationships of elastic-plastic collapse analyses on planar frames. EPFRAME is limited to 2D analyses, so the best we can do is compare the planar response in a given direction, say the $x$-direction. Recall, the structure is assumed to be equivalent in the $x$- and $y$-directions, and only through the hysteretic model are the responses coupled.

Figure 10.4 shows the base shear versus the displacement ratio for a variety of cases: The solid lines indicate the roof displacement ratio, $x_n$ normalized by the structure height; the dashed lines indicate the first-story displacement ratio $x_1/h_1$. Results of the quasistatic elastic, perfectly-plastic EPFRAME analyses are given by the blue lines with circles and squares indicating the formation of a plastic hinge; beyond the largest displacement ratios, the structure collapses because the first-story possesses no additional elastic resistance.

Dynamic tests using the condensed, hysteretic model were performed using a linearly-increasing base acceleration, $\ddot{u}_{gx}(t) \propto t$. For all cases shown, $\rho$ was taken to be $1/2$. Three values of $\kappa$ are considered: $\kappa = 0$, 0.1, and 1. For $\kappa = 1$, the system behaves purely elastically, and in all cases, the black lines pass through the first-point of the EPFRAME analysis. The case $\kappa = 0$ was used to calibrate the model to the EPFRAME analysis. To tune the proposed model, a yield displacement level $z_{i,\mathrm{yield}}$ (Equation (10.22)) needed to first be

determined. The following relationships were chosen for the flexible and rigid structures:

$$z_{i,\text{yield}} = \begin{cases} 0.01 \times h_i & : \quad \text{flexible} \\ 0.009 \times h_i & : \quad \text{rigid} \end{cases} \tag{10.28}$$

where $h_i$ is the $i$th inter-story height. Using these values, a roughly equivalent failure load level was achieved as compared to the EPFRAME-determined value.

Figure 10.5 shows the effect of changing the knee-sharpness parameter $\eta$ on the displacement at which the inelastic model diverges from the elastic system. A value of $\eta = 7$ was chosen such that the condensed model diverges from elastic behavior at roughly 0.7% drift ratio in the first-story, which is representative of actual structures. A value of $\kappa = 0.1$ will be used in future simulations to model strain-hardening effects that cannot be captured with an elastic, perfectly-plastic model

## 10.4 Selected Earthquake Ground Motions

The performance of damped and undamped RISs is examined for fifty bidirectional earthquake ground motion records (twenty-two far-fault, fourteen near-fault, and fourteen near-fault with a pulse earthquakes). The ground motions used in this study are from the ATC-63 Project [124], whose primary objective is to create a methodology to determine seismic performance factors for inelastic, collapse-sensitive structures. The ATC-63 project selected sets of ground motion records form the Pacific Earthquake Engineering Research Center Next Generation Attenuation (PEER-NGA) project database [152]. The selected records are classified into three categories: Far-Fault (FF), Near-Fault without a Pulse (NFNP), and Near-Fault with a Pulse (NFP). The categories are divided so as to have roughly similar response and ground motion characteristics, e.g. magnitude $M > 6.5$ crustal earthquakes with peak ground velocity PGV $> 15$ cm/s and peak ground acceleration PGA $> 0.3\ g$. For the FF set, epicenter distance $> 10$ km; for the NFNP and NFP sets, epicenter distance $\leq 10$ km.

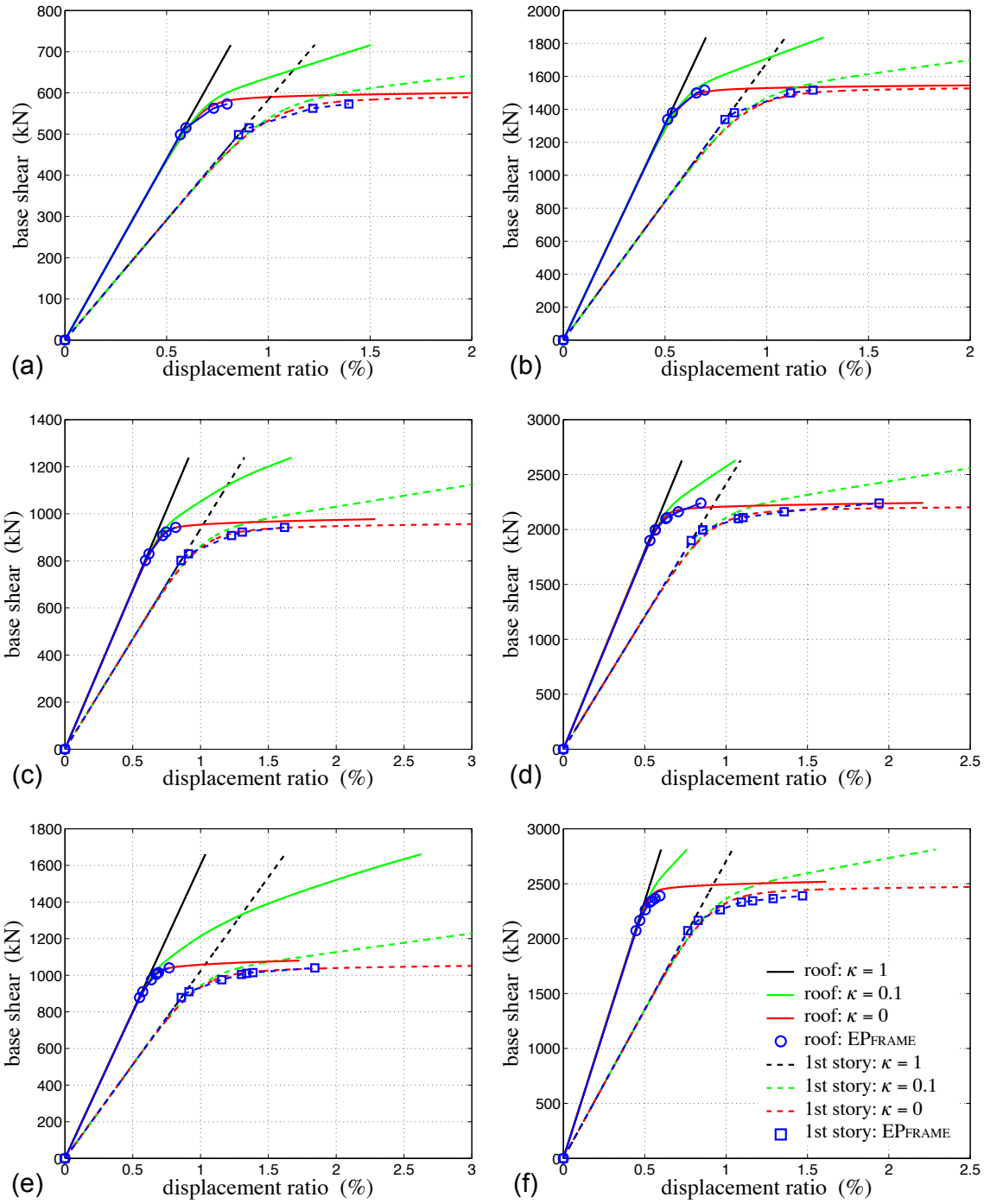


FIGURE 10.4: Base shear force versus roof (solid) and 1st-story (dashed) drift ratio for $\eta = 7$: (a) 4-story, flexible structure; (b) 4-story, rigid structure; (c) 8-story, flexible structure; (d) 8-story, rigid structure; (e) 12-story, flexible structure; (f) 12-story, rigid structure. (— $\kappa = 1$; — $\kappa = 0.1$; — $\kappa = 0$; ○ EPFRAME, roof; □ EPFRAME, 1st story.)

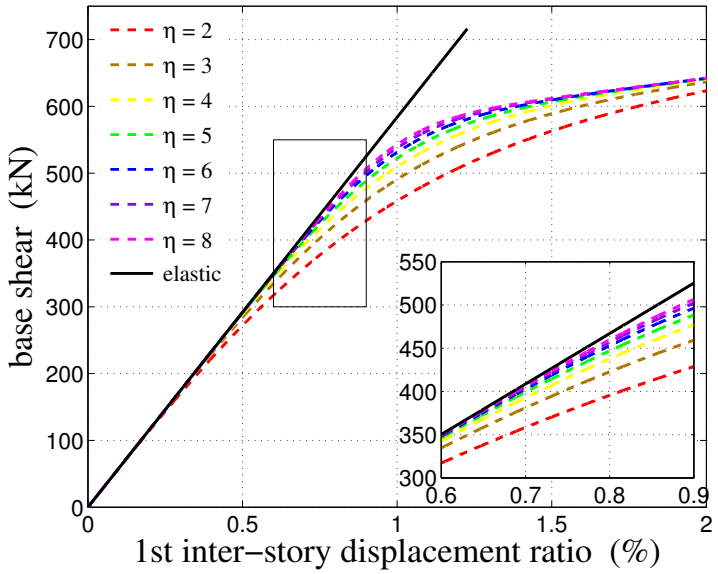


FIGURE 10.5: Base shear force versus 1st-story drift ratio for knee-sharpness parameter $\eta$ values of 2, 3, ..., 8 (from bottom to top) compared to elastic system (—): 4-story, flexible structure.

Each set is normalized so each record in the set has the same PGV, in a square-root sum-of-squares (SRSS) sense. SRSS was chosen, instead of geometric mean (GM), because it provides a rotation-independent (objective) measure of PGV [153]. Each record was integrated via the trapezoidal rule, and the peak radial PGVs were calculated and tabulated. Tables 10.4, 10.5, and 10.6 give the ground motion statistics of the fifty ATC-63 ground motion records used in this study. For each category (FF, NFNP, NFP), the ground motions are normalized to two intensity levels, *moderate* and *strong*, which are categorized in Table 10.2. Additional details are provided in the ATC-63 project website [124].

TABLE 10.2: Scaled peak ground velocities (PGVs) of the selected moderate and strong ground motions.

| | Peak Ground Velocity (PGV) [cm/s] | | |
|---|---|---|---|
| | Far-Fault (FF) | Near-Fault w/o Pulse (NFNP) | Near-Fault w/ Pulse (NFP) |
| *Moderate* | 16.5 | 26 | 40 |
| *Strong* | 33 | 52 | 80 |

## 10.5 Assessment of the Seismic Performance of Rolling Isolation Systems

### *10.5.1 Response analysis*

The seismic responses of damped and undamped RISs are determined by performing a transient dynamic analyses of each isolation system and its supporting building. The building and RIS responses are modeled as *uncoupled*, ignoring the dynamic interaction between building and nonstructural components. Such an analysis leads to substantial savings in computational costs and also avoids numerical difficulties that could arise in the coupled system due to large differences in the properties of the two systems [154]. Furthermore, uncoupled analyses are slightly more conservative than coupled analyses when the ratio of the component mass to the floor mass is small (<1%) and the natural frequency of the component are close to a modal frequency of the structure. For cases in which no modal frequency matches the component frequency, the uncouple analysis is very accurate.

The fifty moderate and the fifty strong bidirectional earthquake ground motion records (Section 10.4) are applied to the six structures (Section 10.2). The total acceleration floor responses at three heights—1st story, mid-height, and roof, as indicated in Figure 10.1—are recorded and then applied to the validated undamped and damped RIS models (Chapters 4 and 9). The peak relative displacement ($d_{\mathrm{R}}^{\max}$) and the peak total acceleration ($a_{\mathrm{T}}^{\max}$) of the RISs are recorded.

A total of six hundred simulations are performed which can be thought of as a *sampling* of representative response scenarios for RIS installations. As such, *empirical* peak-response CDFs are constructed for the various scenarios. The definition of the distribution function is $F(x) = \mathbb{P}(X \leq x)$. We can empirically estimate the CDF as

$$F(x) = \frac{\#\text{ of sample values } \leq x}{N} = \frac{1}{N}\sum_{i=1}^{N} 1_{x_i \leq x} \tag{10.29}$$

where $1_A$ is the indicator of event $A$, and $N$ is the total number of samples.

For the six structures, Figures 10.6–10.11 present the peak-displacement empirical CDFs, $F(d_{\mathrm{R}}^{\max})$, under (a-b) FF, (c-d) NFNP, and (e-f) NFP ground motions at the two loading intensities—(a,c,e) moderate and (b,d,f) strong. The CDFs are plotted on Normal distribution axes. It is important to note that the peak relative displacement $d_{\mathrm{R}}^{\max}$ is bounded below by zero and above by the bowl diameter (approximately 22 cm). For values of $d_{\mathrm{R}}^{\max} > 22$ cm, the steel ball-bearing impacts with the bowl lip, acting as a hard displacement limit.

From these figures, it may be observed that, in general, the peak displacement responses are smaller at lower attachment points. That is, the 1st story CDFs exhibit support at lower values of $d_{\mathrm{R}}^{\max}$ than the mid-height CDFs, which are themselves lower than the roof CDFs. This effect is taken into consideration in non-structural component design codes [89, 155]. For example, the SEI/ASCE 7-10 provisions [89] on non-structural component demands defines a linear variation of peak floor acceleration up the height of the building. The equipment design spectral acceleration is proportional to the floor height coefficient $(1 + 2z/h)$, where $z/h$ is the component attachment height $z$ over the height of the building $h$. For the three attachment locations in the three structures, the floor height coefficient are given in Table 10.5.1. For the 4-, 8- and 12-story structures, the demands at the 1st story are 56, 45 and 41 percent of the demands at the roof. Figures 10.6–10.11 demonstrate similar dependence on the equipment attachment height. In a majority of the structures and load intensities, when the RIS is attached at the 1st story, there is greater

TABLE 10.3: Floor height coefficients.

| | Floor Height Coefficient | | |
|---|---|---|---|
| | 1st story | mid-height | roof |
| 4-story | 1.67 | 2.11 | 3.00 |
| 8-story | 1.35 | 2.06 | 3.00 |
| 12-story | 1.24 | 2.04 | 3.00 |

than a 90 percent probability that the a peak displacement will not exceed 20 cm. Whereas, at higher attachment points (mid-height and roof), nearly all the the cases exhibit peak displacements in excess of 20 cm, especially under *strong* ground motions.

As demonstrated in Chapter 9, when supplemental damping is included in an RIS, the displacement demands of the RIS are decreased, improving the performance and better protecting the isolated object. In all cases, the damped RIS distribution functions fall to the left (lower peak displacements) than the undamped RIS distributions. Therefore, damped RISs outperform the undamped RISs, in terms of peak displacement.

Figures 10.12 and 10.13 show the peak-acceleration empirical CDFs, $F(a_{\mathrm{T}}^{\max})$, for stiff and rigid structures, respectively, subject to the suite of far-fault ground motions. The CDFs are plotted on log-Normal axes. Due to the cone-shaped profile of the bowls (see Section 4.4.1), the peak acceleration in the absence of impacts is limited by the bowl's slope and damping: 0.13 $g$ in the undamped RIS, and 0.20 $g$ in the damped RIS (because of the additional rolling resistance). These limits are exhibited in Figures 10.12 and 10.13 by vertically aligned points in the CDF. A histogram (or probability density function) of the peak acceleration response would have a narrow mode at these acceleration values. However, in cases with impacts, the peak total accelerations are very high, up to 20 $g$. In such cases, the isolation system fails to perform properly, and the isolated object may topple or otherwise fail.

One can also observe from Figures 10.12 and 10.13 that structures with natural periods close to the RIS natural period (approximately 1.2 s) tend to have larger peak displacements. Three of the structures—4-story, flexible; 8-story, rigid; and 12-story, rigid—have especially large acceleration responses. The first natural periods ($1/f_{\mathrm{n1}}$) of these structures are, respectively, 1.27, 1.18, and 1.54 s, which are close to the RIS natural period. Whereas, the other structures—4-story, rigid; 8-story, flexible; and 12-story, flexible—-do not have natural periods near the RIS natural period. These structures have first natural periods of 0.73, 1.92, and 2.63 sec, respectively. The 8- and 12-story, flexible structures have

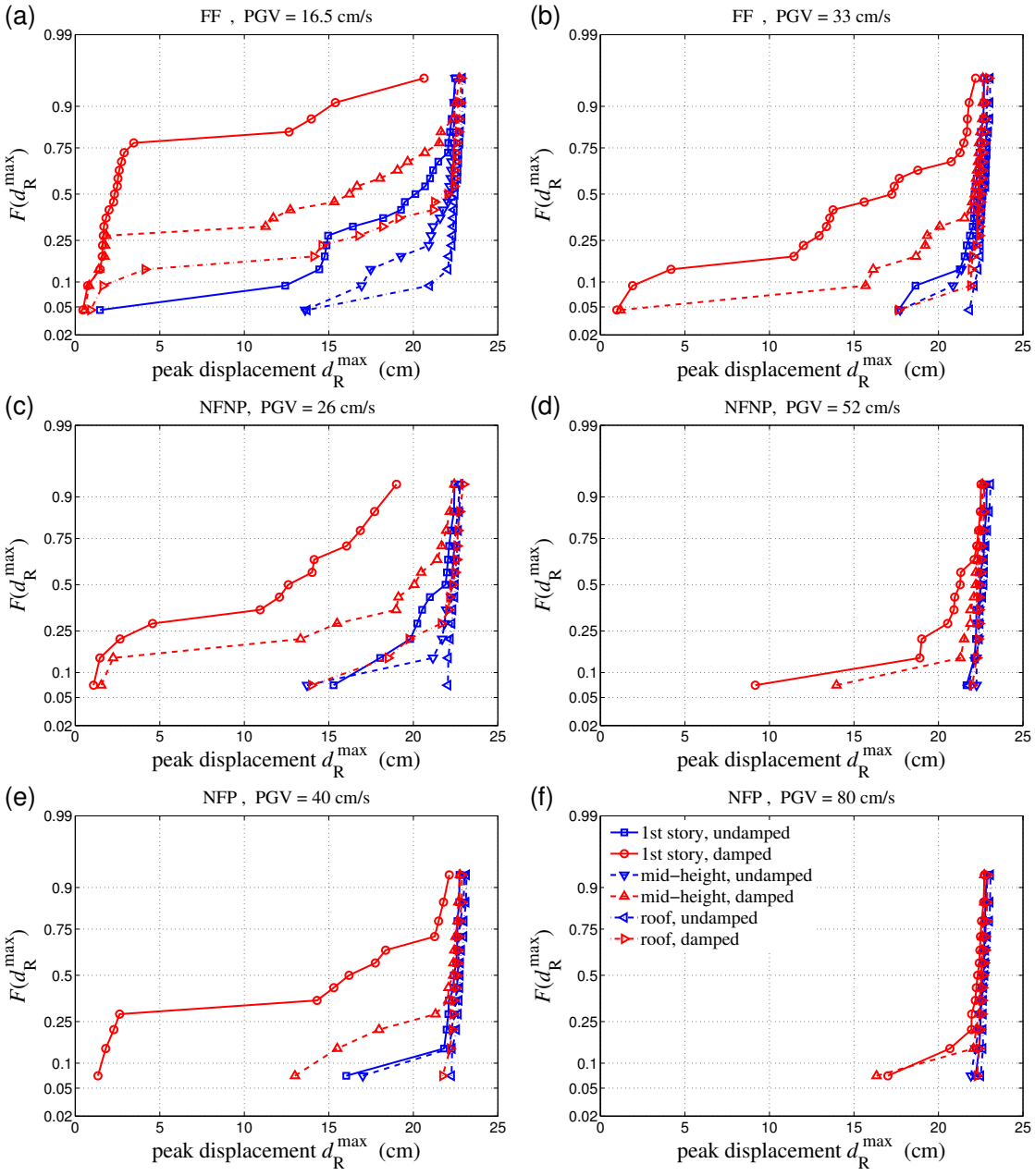


FIGURE 10.6: Peak displacement ($d_R^{max}$) empirical CDFs for **4-story, flexible structure**: (a) FF, PGV = 16.5 cm/s; (b) FF, PGV = 33 cm/s; (c) NFNP, PGV = 26 cm/s; (d) NFNP, PGV = 52 cm/s; (e) NFP, PGV = 40 cm/s; (f) NFP, PGV = 80 cm/s.

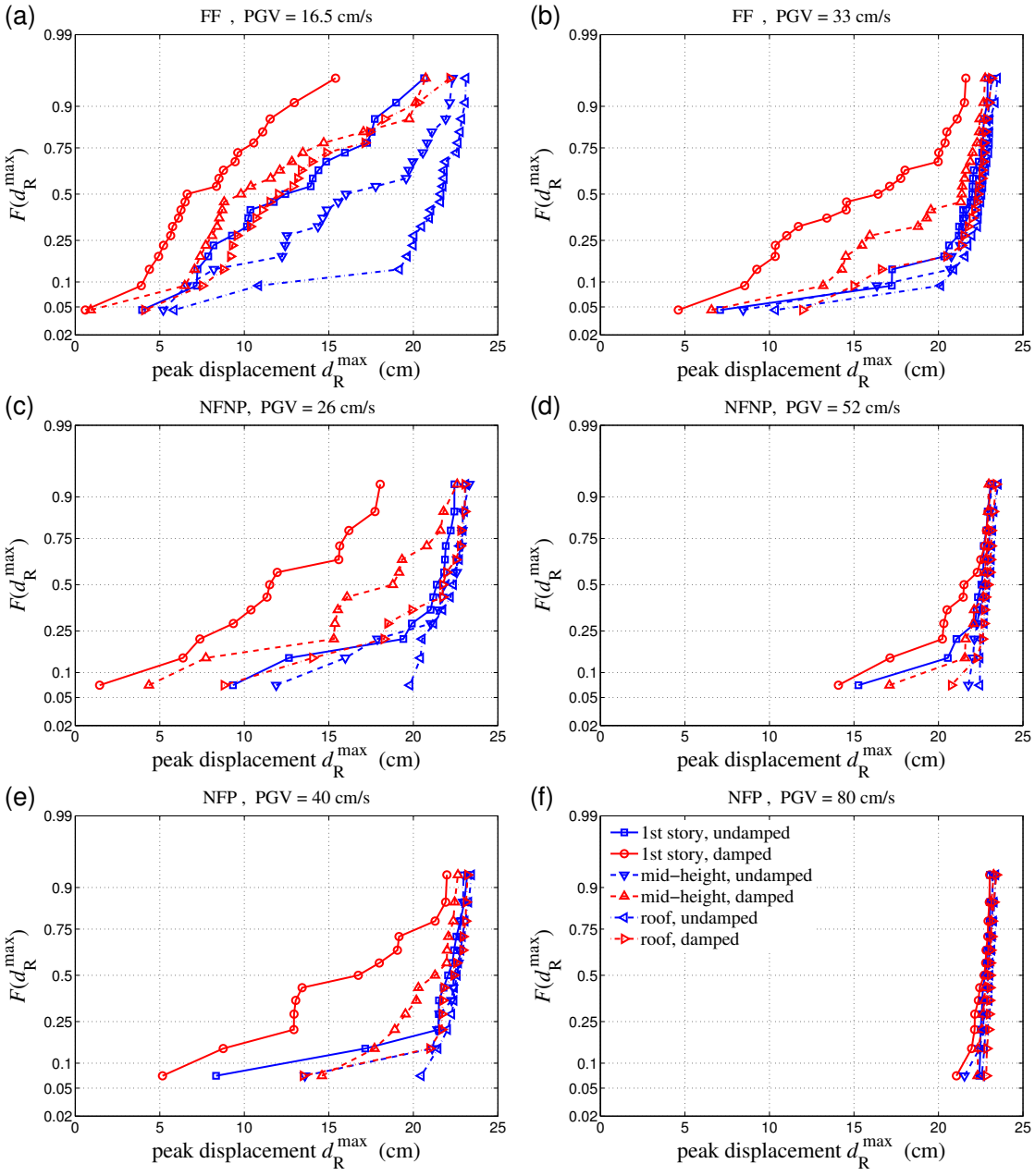


FIGURE 10.7: Peak displacement ($d_R^{max}$) empirical CDFs for **4-story, rigid structure**: (a) FF, PGV = 16.5 cm/s; (b) FF, PGV = 33 cm/s; (c) NFNP, PGV = 26 cm/s; (d) NFNP, PGV = 52 cm/s; (e) NFP, PGV = 40 cm/s; (f) NFP, PGV = 80 cm/s.

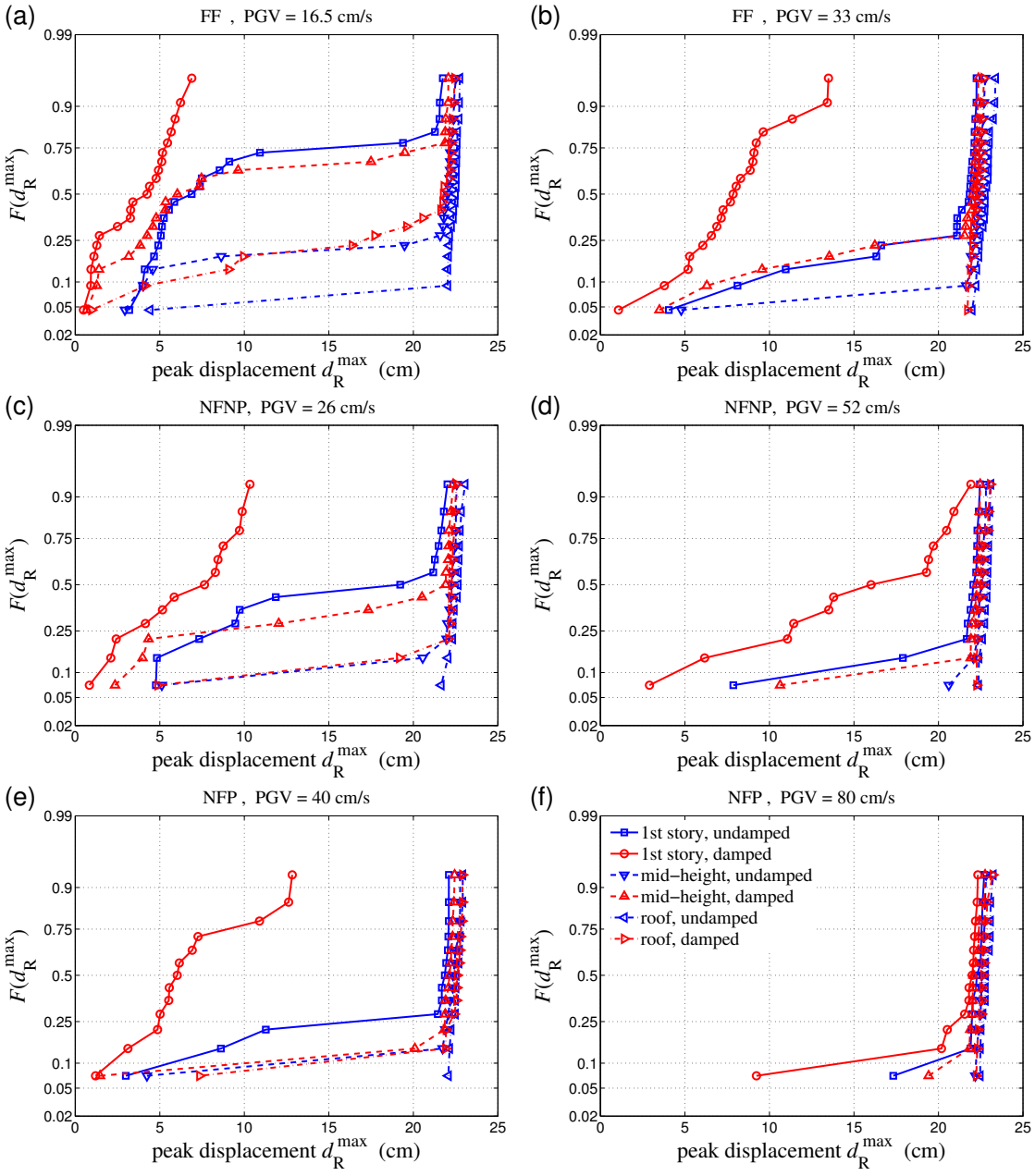


FIGURE 10.8: Peak displacement ($d_R^{max}$) empirical CDFs for **8-story, flexible structure**: (a) FF, PGV = 16.5 cm/s; (b) FF, PGV = 33 cm/s; (c) NFNP, PGV = 26 cm/s; (d) NFNP, PGV = 52 cm/s; (e) NFP, PGV = 40 cm/s; (f) NFP, PGV = 80 cm/s.

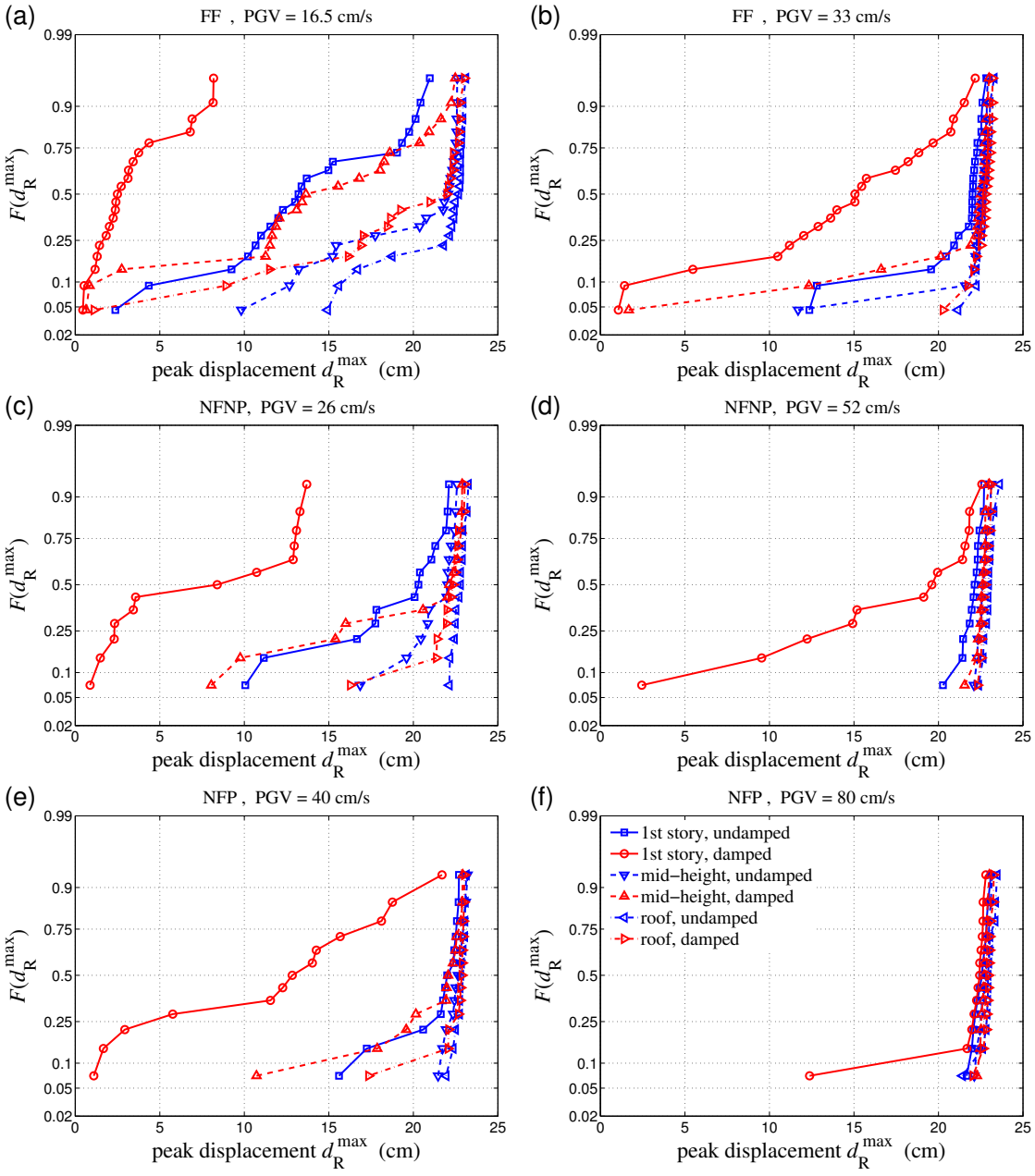


FIGURE 10.9: Peak displacement ($d_R^{max}$) empirical CDFs for **8-story, rigid structure**: (a) FF, PGV = 16.5 cm/s; (b) FF, PGV = 33 cm/s; (c) NFNP, PGV = 26 cm/s; (d) NFNP, PGV = 52 cm/s; (e) NFP, PGV = 40 cm/s; (f) NFP, PGV = 80 cm/s.

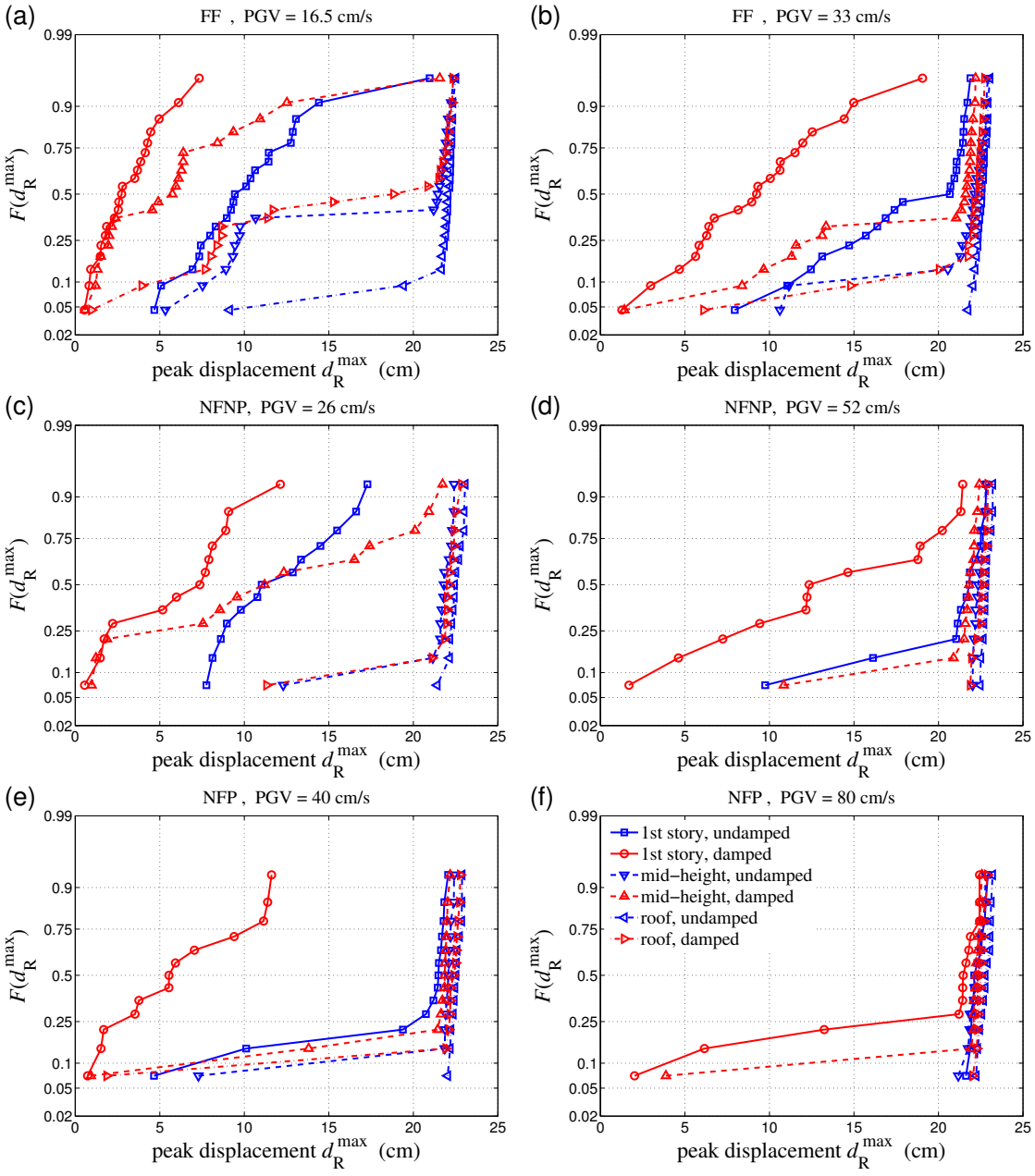


FIGURE 10.10: Peak displacement ($d_R^{max}$) empirical CDFs for **12-story, flexible structure**: (a) FF, PGV = 16.5 cm/s; (b) FF, PGV = 33 cm/s; (c) NFNP, PGV = 26 cm/s; (d) NFNP, PGV = 52 cm/s; (e) NFP, PGV = 40 cm/s; (f) NFP, PGV = 80 cm/s.

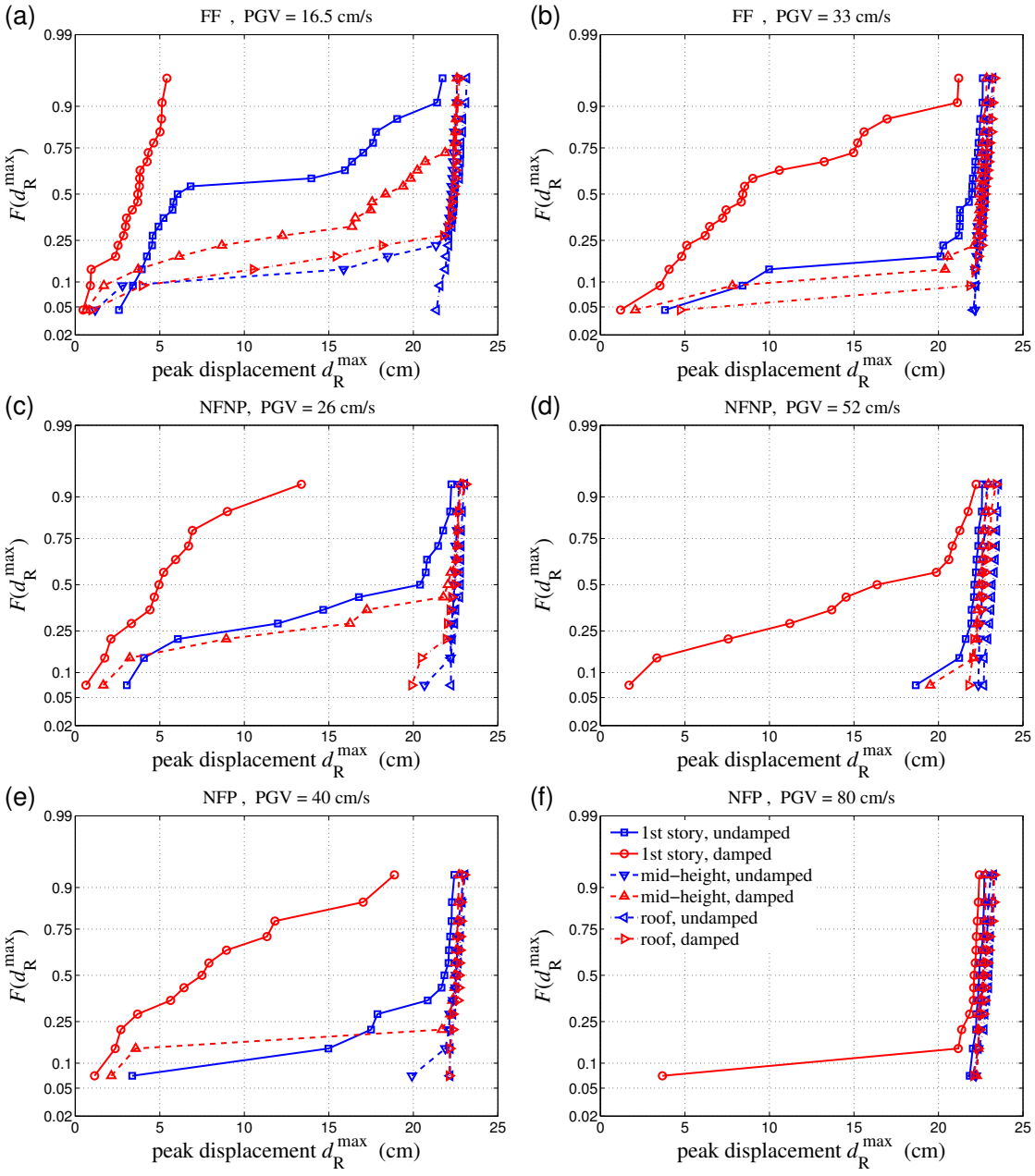


FIGURE 10.11: Peak displacement ($d_R^{max}$) empirical CDFs for **12-story, rigid structure**: (a) FF, PGV = 16.5 cm/s; (b) FF, PGV = 33 cm/s; (c) NFNP, PGV = 26 cm/s; (d) NFNP, PGV = 52 cm/s; (e) NFP, PGV = 40 cm/s; (f) NFP, PGV = 80 cm/s.

second natural periods ($1/f_{n2}$) of 0.68 and 0.93 s, respectively. Therefore, the application of isolation systems in structures with natural periods near 1.2 s should be avoided.

### *10.5.2 General design guidelines*

The following general guidelines are supported by the foregoing time-series analyses and peak-response empirical CDFs:

- As suggested by non-structural component design provisions [89], the floor accelerations increase in the upper floors of the buildings, and hence the RIS displacement and acceleration responses increase in the upper floors. Therefore, one should locate the isolated components as close to the first floor as possible. The floor level of the installation is not as important for low-rise structures (e.g. 4 stories).

- The peak acceleration response of an RIS may increase when the supporting building possesses a (first or higher) mode that is close to the RIS's natural period. Structures with natural periods in the 1.1 s to 1.6 s range are not as suitable for the RIS in this study.

- The deformation demand on damped RISs are significantly lower than on undamped RISs, which was suggested previously in Chapter 9. Supplemental damping via rubber rolling surfaces is capable of improving the performance of RISs for high-intensity motions.

Installations adhering to these recommendations are not likely to experience isolation displacement demands in excess of 22 cm for ground motions with a PGV up to 50 cm/s for damped isolation systems, and a PGV up to 25 cm/s for undamped RISs.

It is worthwhile to note that, because these analyses were performed using an *uncoupled* structure-isolator approach, the calculated peak responses are conservative. Thus, the suggested bounds on the structure's fundamental period could be conservative.

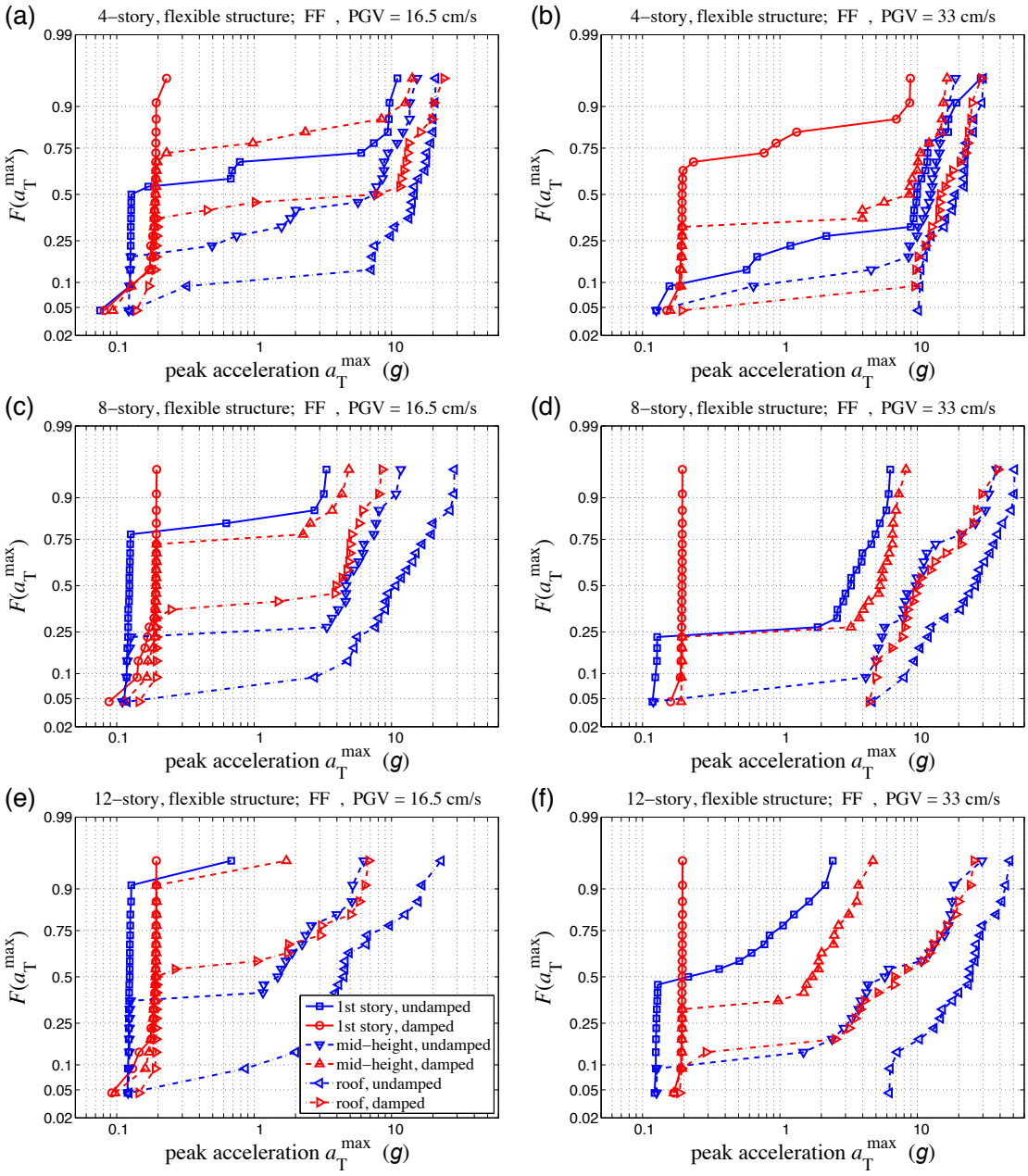


FIGURE 10.12: Peak acceleration ($a_T^{max}$) empirical CDFs for **flexible structures** subject to Far-Field (FF) ground motions: (a) 4-story structure, PGV = 16.5 cm/s; (b) 4-story structure, PGV = 33 cm/s; (c) 8-story structure, PGV = 16.5 cm/s; (d) 8-story structure, PGV = 33 cm/s; (e) 12-story structure, PGV = 16.5 cm/s; (f) 12-story structure, PGV = 33 cm/s.

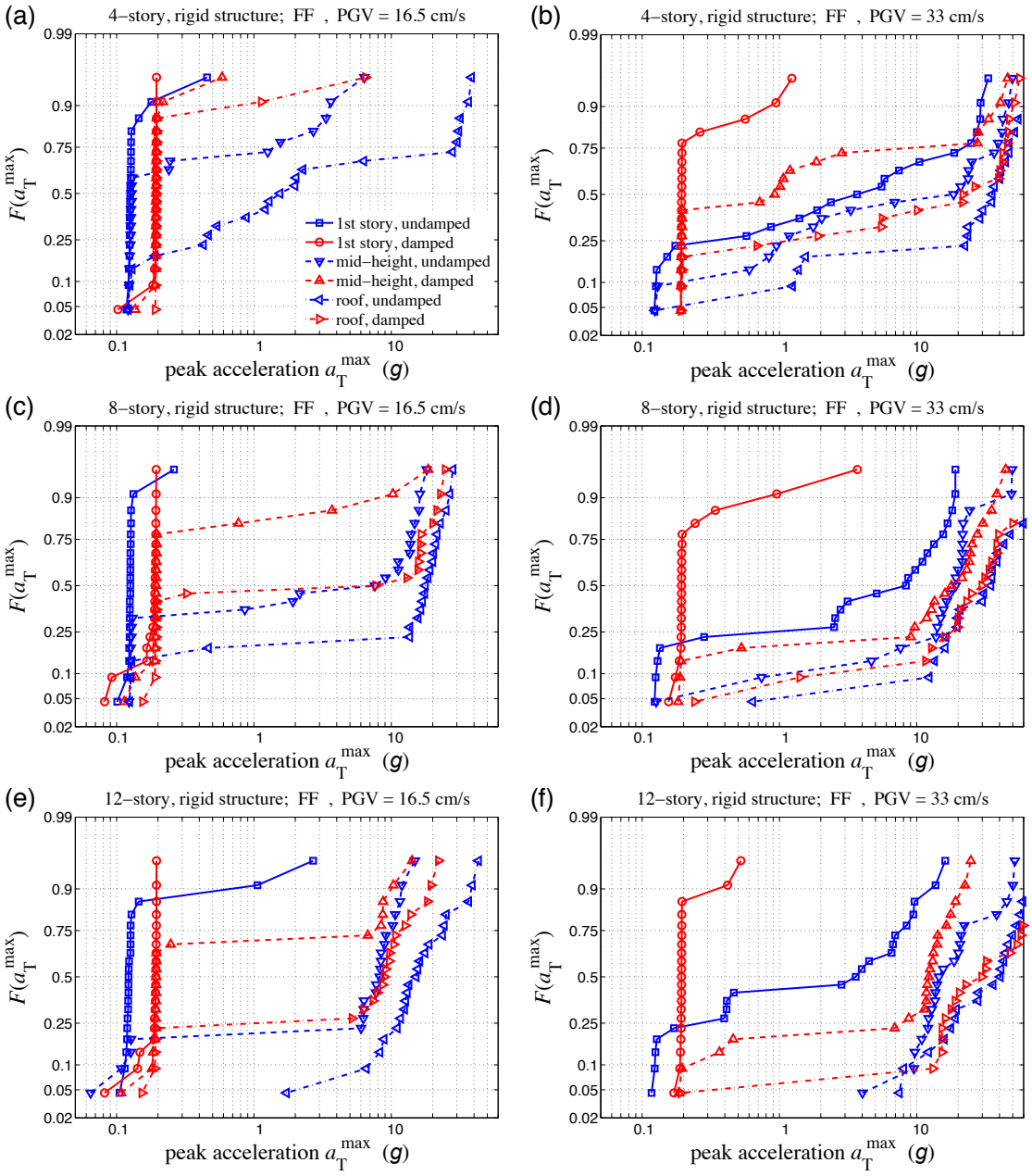


FIGURE 10.13: Peak acceleration ($a_T^{max}$) empirical CDFs for **rigid structures** subject to Far-Field (FF) ground motions: (a) 4-story structure, PGV = 16.5 cm/s; (b) 4-story structure, PGV = 33 cm/s; (c) 8-story structure, PGV = 16.5 cm/s; (d) 8-story structure, PGV = 33 cm/s; (e) 12-story structure, PGV = 16.5 cm/s; (f) 12-story structure, PGV = 33 cm/s.

## 10.6 Summary

The purpose of this chapter has been to utilize the experimentally-validated predictive models derived in Chapters 4 and 9 to assess the performance of damped and undamped RISs. In an attempt to study a range of potential installations, we select six code-designed structures of varying height and stiffnesses from Ref. [137], which are representative of existing buildings in California. However, unlike the analysis performed in that paper, we consider biaxial horizontal responses of the structures instead of rectilinear floor responses. A new approach to model reduction for hysteretic systems was presented, in which the orthogonal, inter-story responses of the structure are coupled by the novel, biaxial hysteretic model derived in Appendix D.

The study comprises the time-history analyses of undamped and damped RISs alternatively attached to the six structures. Each of the analyses is performed under an ensemble of fifty, scaled earthquake ground motions classified into three categories: Far-Fault (FF), Near-Fault without a Pulse (NFNP), and Near-Fault with a Pulse (NFP). We considered two shaking intensities and constructed empirical CDFs of the peak displacement and the peak acceleration responses. From these CDFs we suggest general design recommendations which should be heeded if RISs are being considered for the protection of vital objects. In summary, the damped RIS always outperforms the undamped RIS over all the cases considered, structures with fundamental periods tuned to the natural period of the RIS should be avoided, and the isolated components should be located as close to the ground as possible.

The foregoing conclusions are obviously valid only for the RISs and ground motions herein considered. Therefore, it is recommended that additional studies be conducted with different building types and different ground motions to verify these conclusions. Additionally, different levels of supplemental damping in the RIS should be investigated so as to optimize the isolation system's performance.

TABLE 10.4: Far-Fault (FF) ground motions selection for present study.

| ATC-63 number | PEER NGA | PSA1.0 ($g$) | | PGV (cm/s) | |
|---|---|---|---|---|---|
| | | comp#1 | comp#2 | GM | SRSS |
| 1 | 0953 | 1.02 | 0.94 | 54.2 | 76.5 |
| 2 | 0960 | 0.38 | 0.63 | 43.3 | 56.7 |
| 3 | 1602 | 0.72 | 1.16 | 59.7 | 63.6 |
| 4 | 1787 | 0.35 | 0.37 | 34.2 | 44.1 |
| 5 | 0169 | 0.26 | 0.48 | 29.7 | 33.7 |
| 6 | 0174 | 0.24 | 0.23 | 38.4 | 47.7 |
| 7 | 1111 | 0.31 | 0.29 | 35.7 | 38.5 |
| 8 | 1116 | 0.33 | 0.23 | 32.8 | 44.2 |
| 9 | 1158 | 0.43 | 0.61 | 55.3 | 62.2 |
| 10 | 1148 | 0.11 | 0.11 | 28.5 | 42.7 |
| 11 | 0900 | 0.50 | 0.33 | 36.9 | 56.4 |
| 12 | 0848 | 0.20 | 0.36 | 34.6 | 42.5 |
| 13 | 0752 | 0.46 | 0.28 | 34.5 | 38.3 |
| 14 | 0767 | 0.27 | 0.38 | 43.1 | 49.7 |
| 15 | 1633 | 0.35 | 0.54 | 47.3 | 54.7 |
| 16 | 0721 | 0.31 | 0.25 | 45.2 | 52.4 |
| 17 | 0725 | 0.33 | 0.34 | 30.9 | 35.9 |
| 18 | 0829 | 0.54 | 0.39 | 47.9 | 51.4 |
| 19 | 1244 | 0.49 | 0.95 | 87.5 | 115.0 |
| 20 | 1485 | 0.30 | 0.43 | 38.9 | 46.9 |
| 21 | 0068 | 0.25 | 0.15 | 18.2 | 19.7 |
| 22 | 0125 | 0.25 | 0.30 | 25.1 | 31.0 |

TABLE 10.5: Near-Fault without a pulse (NFNP) ground motions selection for present study.

| ATC-63 number | PEER NGA | PSA1.0 ($g$) | | PGV (cm/s) | |
|---|---|---|---|---|---|
| | | comp#1 | comp#2 | GM | SRSS |
| 15 | 0126 | 0.81 | 0.42 | 61.5 | 72.0 |
| 16 | 0160 | 0.44 | 0.44 | 53.9 | 55.4 |
| 17 | 0165 | 0.41 | 0.37 | 29.3 | 32.0 |
| 18 | 0495 | 0.53 | 0.29 | 43.2 | 48.1 |
| 19 | 0496 | 0.16 | 0.29 | 30.7 | 35.4 |
| 20 | 0741 | 0.55 | 0.45 | 49.0 | 56.4 |
| 21 | 0753 | 0.53 | 0.50 | 49.7 | 56.0 |
| 22 | 0825 | 0.42 | 0.73 | 90.4 | 128.3 |
| 23 | 1004 | 0.62 | 1.00 | 74.2 | 78.4 |
| 24 | 1048 | 0.81 | 0.40 | 48.0 | 63.4 |
| 25 | 1176 | 0.38 | 0.35 | 60.5 | 72.9 |
| 26 | 1504 | 0.75 | 0.75 | 72.4 | 99.4 |
| 27 | 1517 | 2.54 | 0.86 | 92.6 | 119.5 |
| 28 | 2114 | 0.69 | 0.82 | 96.1 | 146.5 |

TABLE 10.6: Near-Fault with a pulse (NFP) ground motions selection for present study.

| ATC-63 number | PEER NGA | PSA1.0 ($g$) | | PGV (cm/s) | |
|---|---|---|---|---|---|
| | | comp#1 | comp#2 | GM | SRSS |
| 1 | 0181 | 0.43 | 0.60 | 83.5 | 117.4 |
| 2 | 0182 | 0.66 | 0.64 | 79.2 | 109.4 |
| 3 | 0292 | 0.25 | 0.41 | 46.9 | 52.4 |
| 4 | 0723 | 0.97 | 0.51 | 77.2 | 115.9 |
| 5 | 0802 | 0.47 | 0.32 | 48.5 | 55.9 |
| 6 | 0821 | 0.98 | 0.37 | 73.0 | 95.5 |
| 7 | 0828 | 0.92 | 0.70 | 69.2 | 98.0 |
| 8 | 0879 | 0.43 | 0.34 | 111.1 | 147.0 |
| 9 | 1063 | 1.96 | 0.47 | 109.2 | 167.0 |
| 10 | 1086 | 0.89 | 0.65 | 95.4 | 131.6 |
| 11 | 1165 | 0.29 | 0.28 | 27.0 | 30.0 |
| 12 | 1503 | 1.33 | 1.10 | 106.0 | 133.6 |
| 13 | 1529 | 0.60 | 0.58 | 93.8 | 117.6 |
| 14 | 1605 | 0.54 | 0.73 | 70.8 | 87.4 |

# 11

# Summary, Conclusions, and Future Work

Based on the results of this dissertation, a number of general conclusions were developed. In this chapter we first summarize the conclusions obtained in each chapter. Next, as a continuation of this work, we discuss some studies which could be helpful in further development of this research.

## 11.1 Summary and Conclusions

The research presented in this dissertation has explored the benefits and limitations of the current state-of-the-art in rolling equipment isolation systems (RISs). The objectives of this dissertation were primarily three-fold: (i) develop accurate, nonlinear models representative of RISs which are capable of reproducing experimental phenomena; (ii) propose and test novel methods to improve the performance of RISs; and (iii) rigorously evaluate current and new isolation technologies by quantifying their seismic performances.

In the first part of this dissertation, we established an experimentally-validated model of an RIS and demonstrated the isolation capabilities of a single, undamped RIS. In Chapter 3, a high-fidelity RIS model was derived using d'Alembert-Lagrange's principle for

nonholonomic systems. Due to kinematics of rolling balls between non-parallel planes, RISs have nonholonomic constraints which, when modeled using an energy method, must be treated delicately. In addition to developing an analytical model, Chapter 3 experimentally optimizes parameters for the potential energy function and the damping model using a Levenberg-Marquardt nonlinear least squares algorithm. Experimental free-response histories were used to fit a linear-viscous damping model; the laboratory setup was shown to have low damping that increased with equipment mass. As a consequence of the bowl profile, lateral and rotational response motions are highly coupled, and the dynamic response of these isolation systems cannot be predicted exactly or reproduced experimentally. In Chapter 3 and Appendix A, we numerically investigated the chaotic tendencies of the RIS and compute significantly positive Lyapunov exponents. Due to this nature of these rolling isolation systems, uniaxial responses are not plausible, and realistic response simulations must incorporate the coupling of the lateral and rotational responses. In Chapter 4 we compared experimentally-measured and numerically-predicted free and forced response motions, which showed acceptable agreement, while measured and predicted peak-response spectra showed excellent agreement. The validated model was then used to compute the spectrum of peak floor motions for which displacement demands equal capacity. This spectrum was compared to floor motion spectra provided by ASCE 7-10 and showed the RIS's current displacement capacity is insufficient in some cases.

Following that analysis, we presented three new technologies to overcome the system's current limitations. The first technology, presented in Chapters 5 and 6, explored increasing the displacement capacity of the isolator by stacking two RISs on top of one another, called the double RIS. In Chapter 5 we expanded the RIS model derived in Chapter 3 to the double RIS. Then in Chapter 6 we validated the double RIS model by comparing measured and predicted free and forced trajectories and peak responses. This technology holds considerable promise (double the displacement capacity), but as of yet, is underdeveloped. Large accelerations were measured and predicted in the middle-frame, and

hazardous impacts were seen for some cases in which the full displacement capacity was not achieved.

The second technology, presented in Chapters 7 and 8, involved equipping the RIS with semi-active damping devices to improve the system's performance. Using a proof of principle approach, we presented a general approach to compute the optimal performance of a constrained control system in Chapter 7. The method finds optimal Lagrange multipliers to enforce inequality state and/or control constraints which are then used in solving the Euler-Lagrange equations. A saturation procedure is developed whereby the unconstrained, proposed control is saturated to the most restrictive constraint, and, in so doing, the complementary slackness condition produces consistent expressions for the Lagrange multipliers. In Chapter 8 we apply this method to determine the optimal performance of a semi-active RIS. Comparisons are made between the responses of the optimal, "clipped-optimal," and viscous controlled isolation system. The results show that the responses of the optimal controller are comparable to those of the "clipped-optimal" controlled system in the short period regime, and better than those of the viscous controlled system. In the long-period range, the optimal solution is comparable to the passive viscous scheme and outperforms the "clipped-optimal" controlled system.

The third technology, presented in Chapter 9, involved supplementing the damping in the RIS by increasing the rolling resistance via rubber-lined bowls, termed a damped RIS. We incorporated an experimentally-calibrated rolling-resistance model into the RIS model derived in Chapter 3. The proposed model was shown to effectively predict both free- and forced-response histories and peak responses in terms of both relative displacements and total accelerations. Decreasing the displacement demand via supplemental damping was shown to enhance the behavior of this RIS for near-resonant excitations.

The final chapter of this dissertation evaluated the seismic performance of the undamped and damped RISs. Six code-designed structures of varying height and stiffness were condensed using a new approach to model reduction for hysteretic systems, in which

the orthogonal inter-story responses of the structure are coupled by a novel, biaxial hysteretic model (Appendix D). The study comprised time-history analyses of the RISs at varying attachment locations within the structures under recorded bidirectional ground motions. We concluded the damped RIS outperforms the undamped RIS over all the cases considered, structures with fundamental periods tuned to the natural period of the RIS (1.1–1.3 s) should be avoided, and the isolated components should be located as close to the ground as possible. These conclusions were corroborated by the conclusions of Chapter 9.

## 11.2 Future Work

This research is a first step toward providing a theoretical background for the idea of high-performance equipment isolation and represents ongoing work. As a continuation of this research, the following are several areas which have the potential for further investigation:

- In theory, by stacking two RISs one on top of the other, the isolator's displacement capacity would double, preventing large accelerations and equipment failure. However, Chapter 6 demonstrated that, with its current configuration and bowl shape, the double RIS has the drawback of impacts in the middle-frame, which in turn produces large accelerations in the isolated object. While the double RIS holds considerable promise, more work is required to optimize the system's performance. Namely, using the models developed in this dissertation, it would be straightforward to tune the bowl profiles in the first- and second-subsystems to prevent impacts in the middle-frame prior to capacity-level displacements.

- A second possible direction for this research would be on the application of the semi-active control procedure to the nonlinear isolator model developed in Chapter 3. For the semi-active control algorithm presented in this dissertation, no form of the plant was assumed—without loss of generality we studied a linear plant. However, global

optimality of the controller could not be ensured for lack of a proof and solution calculation cost may be prohibitive. Thus it is recommended that a new algorithm be designed that can solve the introduced two-point boundary-value problem robustly with less computational cost. Additional extensions and applications of the optimal control method were suggested in Section 7.6.1.

- The damped RIS tested in this dissertation showed high levels of damping which, while effective in reducing isolator drifts, may increase equipment accelerations at high frequencies [56]. In Chapter 9, we presented an experimental set-up and testing protocol to characterize the rolling resistance of any viscoelastic sheet. By varying the thickness or material properties of the viscoelastic layer, the rolling resistance can be adjusted. Designing the proper viscoelastic sheet for a particular RIS installation could be accomplished by tuning the parameterized rolling resistance model presented in Chapter 9. In addition, the validated models in this dissertation were developed to be general enough to permit arbitrary bowl profiles or platform geometries, which could be optimized as well.

- This dissertation introduces the analytical model for an RIS in seismic hazard mitigation. The qualification standard for telecommunication equipment and essential electrical components, defined by Network Equipment Building Systems (NEBS), is widely-adopted for the payloads representative of RISs. Laboratory test are costly and time prohibitive, however, using our experimentally-validated model, a robust hazard analysis may be performed quite easily in accordance with NEBS. As a result, tolerance limits for displacement capacities and damping levels may be established in order to maintain a specified level of seismic safety.

# Appendix A

## On the Chaotic Response of a Nonlinear Rolling Isolation System

Isolation systems protect fragile objects from potentially-damaging shocks and shakes by mechanically decoupling motions of the object from motions of the surrounding environment. Shock and vibration isolation systems have been applied to systems ranging from the micron scale to the scale of entire buildings. Many isolation systems operate within a linear range, while others have strong nonlinearities. The focus of this chapter is on the chaotic response of a rolling-pendulum vibration isolation system. An experimentally-calibrated model is reduced to a single-degree-of-freedom nonlinear system. The nonlinearities involve softening behavior at intermediate responses and stiff impacts at large amplitudes. This model is investigated numerically to explore and establish the influence of harmonic forcing parameters on the chaotic nature of responses. Rich chaotic behavior is exhibited in the case where the response includes impacts.

## A.1 Background

Seismic isolation is widely implemented for the protection of structures and their contents from earthquake hazards [2, 14]. Seismic isolators decouple the horizontal motions of the ground or a building floor from the response of the building or its contents by introducing compliant interfaces. Passive vibration isolators can be classified into three categories: sliding bearings, elastomeric bearings, and rolling isolators [156]. Rolling isolation systems are commonly used to protect critical infrastructure facilities [157] and/or the mission-critical, yet fragile, objects housed inside the structure [2]. In particular, this chapter focuses on the nonlinear behavior of a rolling isolation system for light ($\approx$ 1 tonne) objects [37]. For further background on the operation process of these systems, see Ref. [1].

Prior studies on the nonlinear behavior of rolling isolation systems have focused on the one-dimensional behavior of systems that do not incorporate stiff displacement-limiting boundaries. The analysis of nonlinear seismic isolation is not without precedence. Chung *et al.* [28] investigated a system comprised of rods rolling over a horizontal surface, and by eccentrically locating the pin in the circular isolators, nonlinearities are realized. Numerous studies have been performed to analyze the dynamics and attenuation capabilities of structures isolated by non-circular rods rolling between horizontal surfaces (e.g. [29,158]). Frictional elements and spherical rolling surfaces have been investigated for their application to seismic isolation in buildings [31, 35, 44]. Barghian and Shahabi [159] achieved a rocking-pendulum isolator by using "mushroom-shaped" spherical columns. Ismail *et al.* [11] proposed a roll-in-cage isolation system, which was shown to be effective at protecting motion-sensitive equipment. Pranesh and Sinha [17] proposed a variable frequency pendulum system, possessing an elliptical potential surface which produces a softening effect with displacement. More recently, Lu *et al.* [22] proposed a polynomial surface whose parameters can be tuned to achieve softening and stiffening regions.

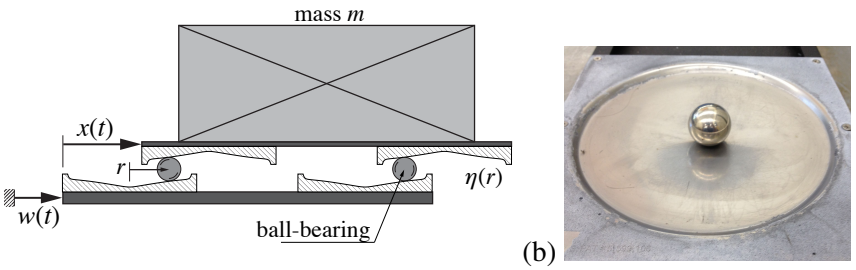


FIGURE A.1: (a) Schematic of a rolling isolation system, and (b) experimental ISO-Base ball-bearing and bowl.

In these applications, nonlinearities are introduced with the intension of reducing resonant-like behavior. No previous study has investigated the effects of stiff displacement-limiting boundaries. Neither has any previous study investigated the chaotic behavior of variable-curvature isolation systems. In this chapter we consider the influence of manufacturing imperfections and impact boundaries on the nonlinear response of a rolling isolation system.

This study focuses on a widely-implemented equipment isolation platform [1]. In this system, a mass (representing shock-sensitive equipment) is isolated via a rolling-pendulum mechanism; spherical stainless steel ball-bearings roll between concave conical bowls, decoupling the motion of the isolated mass from the motion of the floor. The nonlinear governing equations of motion are determined from Lagrange's equation for a harmonically driven system. The damping in the mathematical model has been experimentally calibrated to tests on the full-scale prototype. A radially-symmetric function is fit to high-resolution photogrammetric measurements of the shape of the conical bowls. Measurements of sixteen separate specimens provides an estimate of the variability in the shape of the bowl. A linear viscous damping model is fit to experimental free-response histories. With the reduction of the calibrated model to rectilinear motion, the nonlinear behavior of the system is studied over a range of harmonic forcing parameters.

## A.2 Mathematical Modeling

The single-degree-of-freedom model presented in this section is reduced from a fourteen-state model of a three-degree-of freedom isolation platform with eight nonholonomic constraints [38].

Consider a single-degree-of-freedom rolling isolation system consisting of a mass $m$, being forced at its base by disturbance $w(t)$, as shown in Figure A.1. In a displaced configuration $x(t)$, the mass undergoes a vertical displacement governed by the bowl profile function $\eta(r)$. For shallow bowls, the vertical component of velocity may be neglected, and the kinetic energy of the system is

$$T = \tfrac{1}{2}m(\dot{w} + \dot{x})^2. \tag{A.1}$$

Assuming the ball-bearings remain on the centerline between the bowl centers, i.e. $r = |x/2|$, the potential energy of the system is

$$V = 2mg\eta(|x/2|) \tag{A.2}$$

where $g$ is the acceleration due to gravity.

The Lagrange function is given by $L = T - V$, and the equation of motion is found from Lagrange's equation:

$$\frac{\mathrm{d}}{\mathrm{d}t}\left(\frac{\partial L}{\partial \dot{x}}\right) - \frac{\partial L}{\partial x} = Q^{\mathrm{D}} \tag{A.3}$$

where $Q^{\mathrm{D}}$ contains any non-conservative forces. The resulting equation of motion is

$$m(\ddot{w} + \ddot{x}) + mg\eta'(|x/2|)\mathrm{sgn}(x) = Q^{\mathrm{D}} \tag{A.4}$$

where $\mathrm{sgn}(\cdot)$ is the signum function and the prime notation denotes differential with respect to radius, i.e. $\eta'(r) = \mathrm{d}\eta(r)/\mathrm{d}r$. The base forcing is harmonic at frequency $\omega$ and amplitude $A$: $\ddot{w}(t) = A\sin(\omega t)$. This nonlinear (autonomous) system has three states $(x, \dot{x}, t)$, which allows for the possibility of chaotic trajectories.

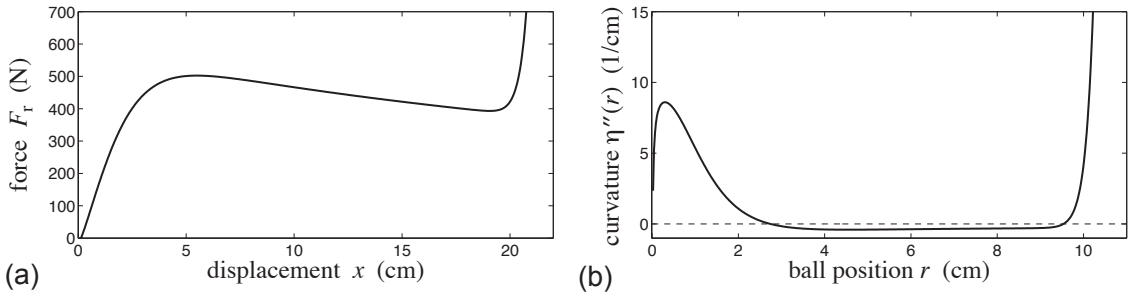


FIGURE A.2: (a) Force-displacement relationship from quasi-static response simulation, and (b) bowl curvature.

### *A.2.1 Bowl profile function*

The bowl profile function $\eta(r)$ determines the gravitational potential, which is fundamental to the behavior of the system. The bowls used in the isolation system [1] were designed to have a conical radial profile (see Figure A.1(b)), such that the accelerations experienced by the isolated mass are bounded by the slope of the conical surface ($\max|\ddot{x} + \ddot{w}| \approx 0.1\ g$). However, due to the manufacturing process, whereby thin stainless steel sheets are stamped in a mold, the bowls are not perfectly conical. In Chapter 3, the bowl profile parameterization (Equation (3.44)) was fit to sixteen photogrammetric measurements. In Equation (3.44), the first term accounts for the conical shape of the bowl with a rounded bottom, the second term accounts for the lip at the outer edge of the bowl where $r \approx 10$ cm, and the third term accounts for the negative curvature where $2 < r < 10$ cm. Figure 3.5(a) shows the resolution of the photogrammetry data, Figure 3.5(b) shows the mean fitted bowl function, and the fitted $\beta_i$ values are given in Table 3.1.

### *A.2.2 Force-displacement relationship*

The gravitational restoring force $F_r = mg\eta'(|x/2|)\text{sgn}(x)$ is plotted versus displacement in Figure A.2(a). Note that $F_r$ is proportional to the bowl gradient $\eta'(r)$. The conical bowl profile was designed for acceleration control; i.e., for constant $\eta'(r)$, the restoring force is constant and, accordingly, accelerations are restricted. However, due to the manufacturing process, imperfections, in the form of negative curvature (see Figure A.2(b)), are

present in the laboratory specimen. Thus, a softening effect is seen at displacements in the range $4 < |x| < 20$ cm, and the gravitational restoring force does not increase monotonically with displacement—three distinct displacements correspond to the same level of forcing. At large displacements ($|x| > 20$ cm), the restoring force increases exponentially ($\sim r^{57}$), providing a stiff displacement limit. Thus, the system may experience impacts under large-amplitude loading scenarios. Possibility of impact is suggestive of the possibility of chaotic trajectories [88], and will be investigated further in Subsection A.3.2.

### *A.2.3 Mass-dependent damping model*

In rolling isolation systems, energy is dissipated at the interface between the ball-bearings and the steel bowls [76]. Harvey and Gavin [38] investigated the energy dissipation mechanisms by analyzing the energy content of experimental free responses, and showed that a linear viscous damping model was appropriate. The damping forces act at each ball location and are proportional to the ball-bearing velocities, with damping rate $C_\mathrm{b}$ experimentally fitted for six levels of mass. The centers of gravity of the ball-bearings have half the velocity of the mass, $\dot{x}$. Thus, the dissipative force in the planar case is

$$Q^\mathrm{D} = -2C_\mathrm{b}\dot{x} \tag{A.5}$$

where the damping rate $C_\mathrm{b}$ is mass-dependent with the following relationship [38]:

$$C_\mathrm{b}(m) = 0.000229\, m^2 + 0.02884\, m \tag{A.6}$$

in which $m$ is measured in kg and $C_\mathrm{b}$ is measured in N s/m. nonlinear damping characteristics are known to produce chaotic responses in harmonically excited isolators [160], but will not be investigated here. A more advanced damping model is an extension of the present work and is a topic of further study.

## A.3 Numerical Simulation

The equation of motion with damping and harmonic disturbance is

$$\ddot{x} + (2C_\mathrm{b}/m)\dot{x} + g\eta'(|x/2|)\mathrm{sgn}(x) = -A\sin(\omega t), \tag{A.7}$$

for which the mass of the isolated equipment is 500 kg. The experimentally-fitted damping rate, from Equation (A.6), is 71.67 N s/m, corresponding to an equivalent damping ratio of approximately 1.75%.

Letting $\mathbf{z} := [x\ \dot{x}]^T$, the equation of motion (Equation (A.7)) may be expressed in state-space form as follows:

$$\dot{\mathbf{z}} = \mathbf{f}(\mathbf{z}, t) = \begin{bmatrix} 0 & 1 \\ 0 & -2C_\mathrm{b}/m \end{bmatrix}\mathbf{z} + \begin{bmatrix} 0 \\ -g\eta'(|x/2|)\mathrm{sgn}(x) - A\sin(\omega t) \end{bmatrix}, \tag{A.8}$$

with initial conditions $\mathbf{z}_0 = \mathbf{z}(0)$. Equation (A.8) is solved using a fourth-order Runge-Kutta algorithm with a fixed time-step of $\Delta t = 0.001$ s. In the stiff regime under large displacements (~23 cm), the linearized natural frequency is approximately 115 Hz—nearly one ninth the integrator sampling rate (1 kHz), which is sufficient to ensure numerical stability. Two cases of loading are investigated numerically: (i) unforced response, $A = 0$; and (ii) harmonically-forced response, $A \in [1, 12]$ m/s$^2$ and $\omega \in [\pi, 5\pi/2]$ rad/s. Harmonic disturbances are roughly representative of the floor motion this system would experience within a building responding to very-long duration ground motions, such as those experienced in tall buildings shaken by large but distant earthquakes.

### *A.3.1 Unforced response*

In free vibration, we set the disturbance to be zero, i.e. $A = 0$, and start the system from a non-zero initial condition. First, we find the undamped natural periods $T_\mathrm{n}$ of the system by varying the initial displacement $x_0 = x(0)$, under zero initial velocity $\dot{x}(0) = 0$ cm/s. The displacement up-crossing rate is computed over several cycles to estimate the period

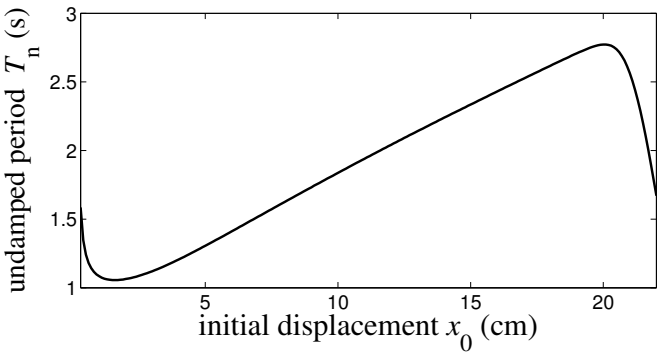


FIGURE A.3: Undamped natural period $T_n$.

of oscillation when damping rate $c$ is set to zero. Figure A.3 shows the displacement-dependent natural periods of the undamped system, which range from 1 s to nearly 3 s. Over the majority of the initial displacement range ($2 < x_0 < 20$ cm), the natural period increases with initial displacement, but at the extremes ($x_0 < 2$ cm and $x_0 > 20$ cm) the period decreases with initial displacement. It has been suggested that displacement-dependent natural frequencies are beneficial in the isolation of structures [17, 22].

Next, the damped unforced response is analyzed in which the initial displacement and velocity are $x(0) = 20$ cm and $\dot{x}(0) = 0$ cm/s. Figure A.4 shows trajectories and the phase projection of the unforced response. The damped natural period of the system can be approximated from the time history of displacement $x(t)$, Figure A.4(a). The period of the first oscillation is 2.4 s, with subsequent oscillations decreasing in period: peak-to-peak periods are {1.86, 1.54, 1.36, 1.26, 1.20, 1.18} s for the second through seventh cycles. The oscillation periods lengthen again once the displacements are below 2 cm. This is consistent with the undamped natural period analysis above, Figure A.3.

The velocity time history $\dot{x}(t)$ is nearly a triangle wave initially, becoming sinusoidal once the displacement oscillations decay to below 12 cm. This can be seen in the phase projection (Figure A.4(b)), as well: initially the phase projection takes a diamond shape and becomes elliptical as displacements decay. This phenomenon is attributed to the particular shape of the bowl. In the middle displacement regime ($6 < |x/2| < 12$ cm), the bowl

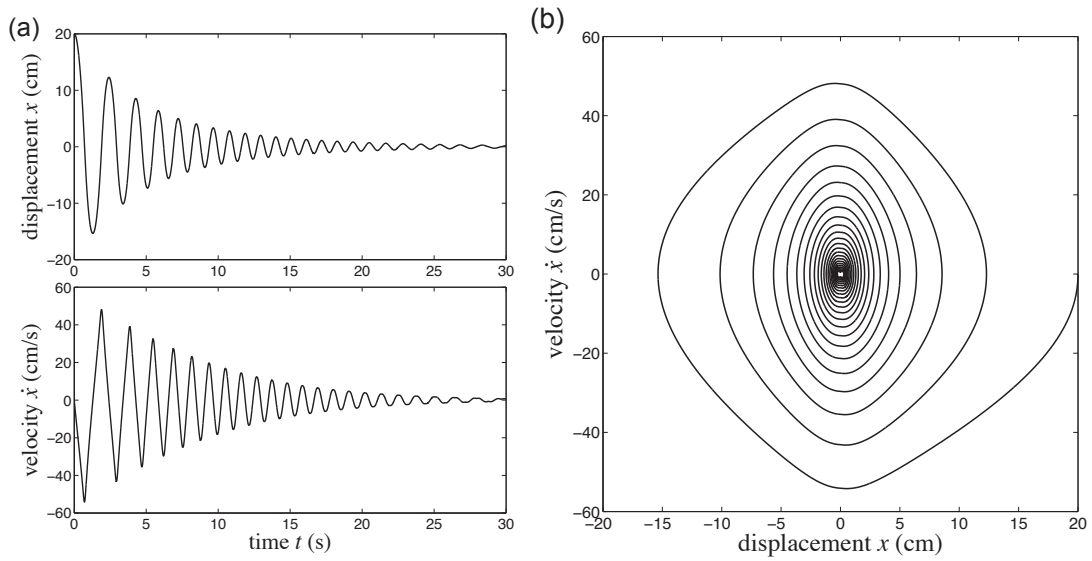


FIGURE A.4: Unforced response simulation. (a) Time-history trajectories and (b) phase projection.

is roughly conical, which corresponds to a piece-wise linear velocity history. Whereas, at small displacements ($|x/2| < 6$ cm), the bowl is nearly quadratic, corresponding to a sinusoidal velocity history.

### *A.3.2 Harmonically-forced response*

We set the forcing to be sinusoidal and perform an extensive parameter study by varying the disturbance amplitude $A \in [1, 12]$ m/s$^2$ and frequency $\omega \in [\pi, 5\pi/2]$ rad/s. All harmonically-forced responses are performed from an initial condition of $x(0) = \dot{x}(0) = 0$. Response frequency characteristics, Lyapunov exponents (LEs), bifurcation diagrams, phase projections, and Poincaré maps demonstrate the nonlinear and chaotic behavior of this system.

The principal Lyapunov exponent $\lambda_{\max}$ is defined as follows [83]:

$$\lambda_{\max} = \lim_{K \to \infty} \frac{1}{t_K} \sum_{k=1}^{K} \ln \frac{\|\mathbf{v}_k\|}{\delta_0} \tag{A.9}$$

where $\mathbf{v}_k$ is the incremental deviation of the scaled previous state $\mathbf{z}_{k-1}$, which is renormalized to a Euclidean norm of $\delta_0$ at each time step $t_k = k\Delta t$. The quantity $\ln(\|\mathbf{v}_k\|/\delta_0)$ gives a

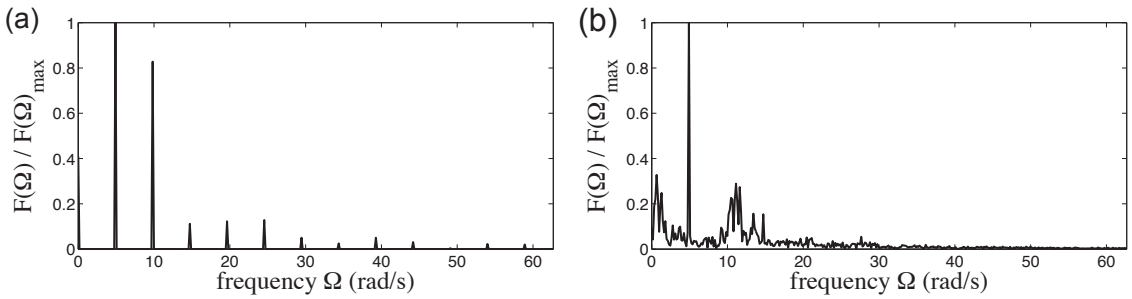


FIGURE A.5: Comparison of DFT for (a) periodic ($A$ = 5.5 m/s$^2$) and (b) chaotic ($A$ = 8.0 m/s$^2$) responses, $\omega = 1.5625\pi$.

measure of the divergence or convergence of neighboring trajectories [84]. Allowing the simulation to run long enough after transients have dissipated (100 cycles of response), the algorithm approximates the average divergence rate of nearby trajectories. A system is said to be chaotic if $\lambda_{\max} > 0$ [83].

Wiebe and Virgin [161] have recently developed an alternative approach to determining if a response is chaotic. The method takes advantage of the non-smooth nature of the Discrete Fourier Transform (DFT) of chaotic responses. Figure A.5 shows the DFTs of typical periodic and chaotic responses for two levels of amplitude $A$. The selection of the roughness (quantified by the number of peaks) needed to label a response is purely heuristic, however Figures A.5(a) and A.5(b) show that there is a clear dichotomy in the peak counts for a periodic and a chaotic response. Classifying chaos according to a DFT peak count criteria is not sensitive to the peak count threshold. Thresholds in the range of 20–90 peaks yield similar results and show good agreement with LEs.

*Chaotic boundaries and attractors*

Figure A.6(a) shows chaotic and non-chaotic domains in the disturbance parameter space ($A$, $\omega$) obtained via DFTs over a refined (200×200) grid. The shading code is: (*blue*) chaotic ($\geq$ 25 peaks) and (*yellow*) non-chaotic ($<$ 25 peaks). The red circle on the chart in Figure A.6(a) corresponds to the chaotic attractor in Figure A.6(b), at $\omega = 1.5625\pi$, $A$ = 8.0 m/s$^2$.

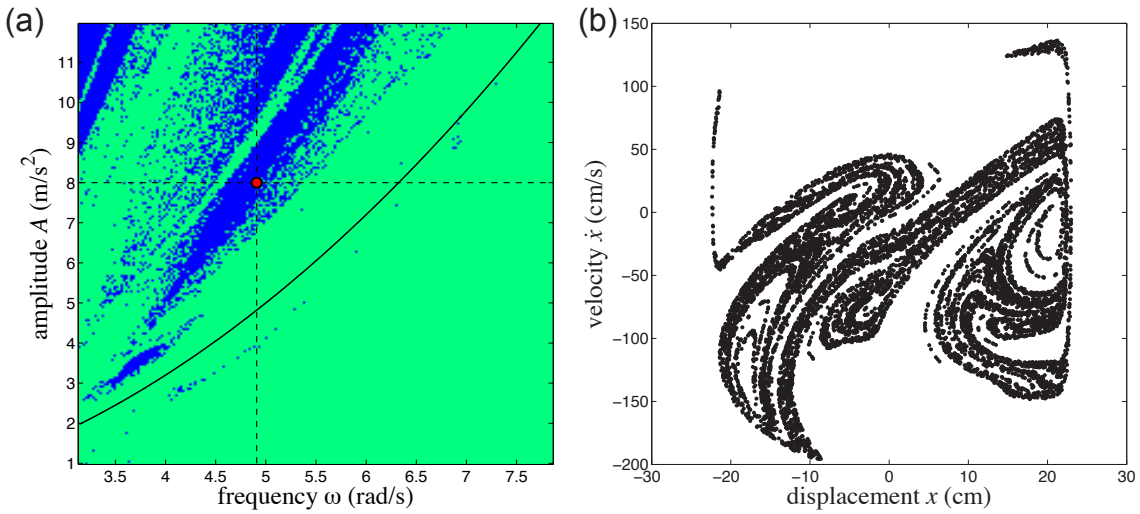


FIGURE A.6: (a) Chaotic boundaries and (b) an example of a chaotic attractor, corresponding to the red circle in (a), $\omega = 1.5625\pi$, $A = 8.0$ m/s$^2$.

Chaotic domains are generally located in the top left of the graph, corresponding to low-frequency, high-amplitude disturbances. A harmonic acceleration record with amplitude $A$ and frequency $\omega$ has a displacement amplitude equal to $A/\omega^2$. For an ideal isolator (i.e. perfectly decoupled), when the base displacement exceeds the bowl limits (i.e. 20 cm) impacts will occur. The solid black line in Figure A.6(a) is the theoretical impact limit: $0.2\omega^2$. It is in the regime $A > 0.2\omega^2$, impacts are seen, leading to chaotic behavior. A narrow chaotic band is observed just below the line $A = 0.2\omega^2$. The discrepancy between the black line and this chaotic band can be attributed to the non-perfect decoupling and damping.

It should be noted that the chaotic boundary chart is constructed for a single choice of initial conditions and therefore does not provide competing basin of attraction information. At the onset of an earthquake, the at-rest initial condition is most realistic. Under varying initial conditions the chaotic boundaries may fluctuate, but the major features (i.e. chaotic domains primarily in the low-frequency, high-amplitude regime), in general, are unaffected.

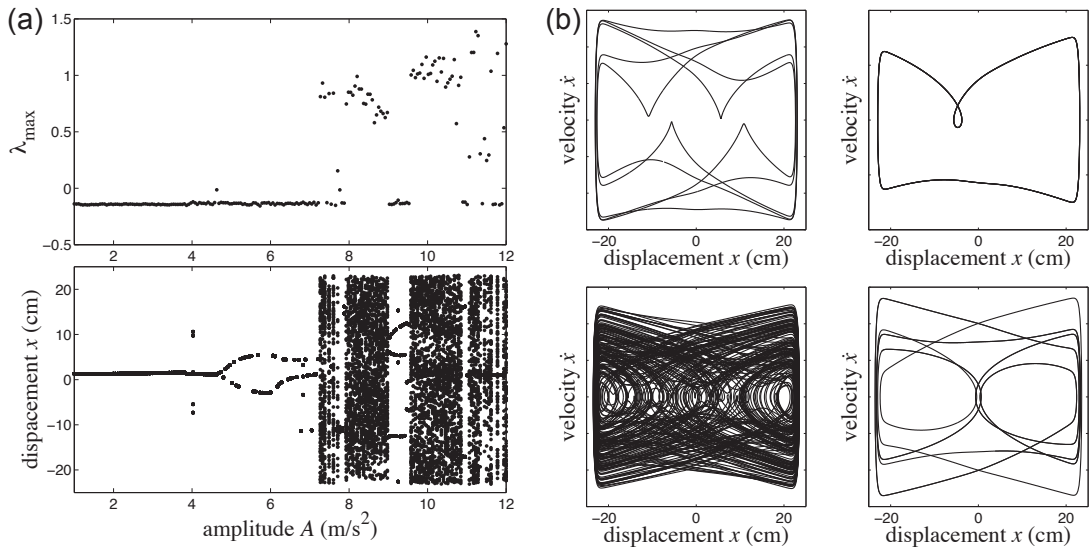


FIGURE A.7: (a) Largest Lyapunov exponent $\lambda_{\max}$ (top) and bifurcation diagram (bottom) with periodic windows, $\omega = 1.5625\pi$ rad/s. (b) Phase projections for four amplitudes: (top left) $A = 4.025$ m/s$^2$, (top right) $A = 5.5$ m/s$^2$, (bottom left) $A = 8.0$ m/s$^2$, and (bottom right) $A = 9.25$ m/s$^2$.

*Effects of disturbance amplitude A*

Next, we investigate the influence of the disturbance amplitude $A$ on the system's behavior. We fix the forcing frequency $\omega = 1.5625\pi$ rad/s and sweep through amplitudes $A \in [1, 12]$ m/s$^2$, as indicated in Figure A.6(a) by the vertical dashed line. The resulting LEs, and corresponding bifurcation diagrams, are shown in Figure A.7(a). Positive LEs indicating chaotic bands are seen, with interspersed non-chaotic bands. To generate the Poincaré bifurcation diagrams, we collect the displacements at 100 disturbance period windows, i.e. $x(2\pi k/\omega)$, $k = 1, ..., 100$. These displacements are then plotted versus amplitude $A$ in Figure A.7(a).

At $A = 4.025$ m/s$^2$, period-5 motion is exhibited, with a slightly elevated LE. The phase projection is shown in Figure A.7(b) in the top-left frame.

The bifurcation diagram (Fig A.7(a)) indicates that anti-symmetric paths exist, and branch near $A = 4.65$ m/s$^2$. Both anti-symmetric solutions were recorded; an example of one response ($A = 5.5$ m/s$^2$) is shown in Figure A.7(b) in the top-right frame. The anti-symmetric solution is not shown. The DFT for this case (Figure A.5(a)) has 12 peaks,

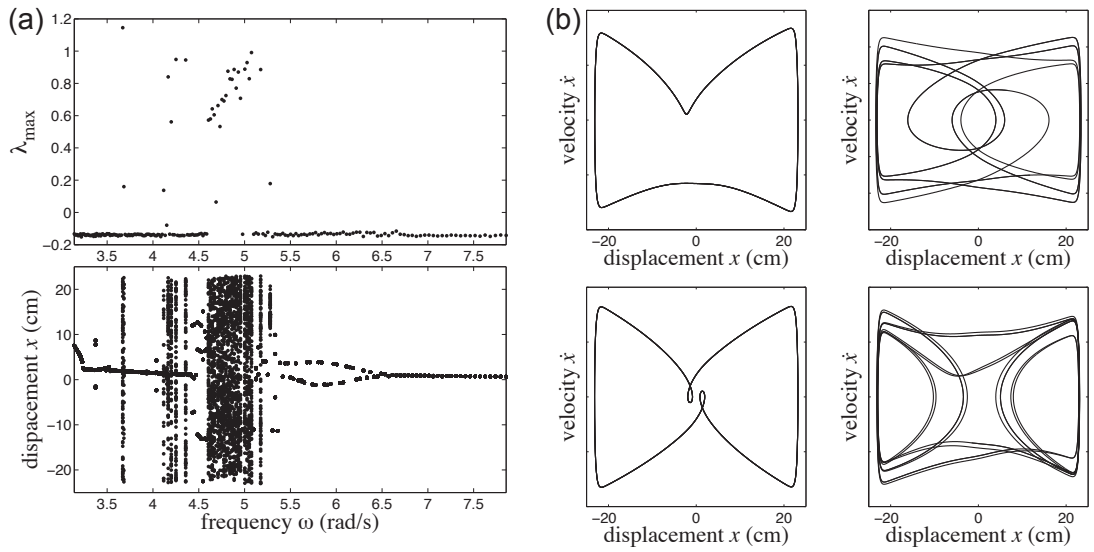


FIGURE A.8: (a) Largest Lyapunov exponent $\lambda_{\max}$ (top) and bifurcation diagram (bottom) with periodic windows, $A = 8$ m/s$^2$. (b) Phase projections for four frequencies: (top left) $\omega = 2\pi$ rad/s, (top right) $\omega = 10\pi/7$ rad/s, (bottom left) $\omega = 5\pi/4$ rad/s, and (bottom right) $\omega = 2\pi/1.962$ rad/s.

indicating a non-chaotic response.

A chaotic band over $A \in [7.875, 9.0]$ m/s$^2$ is seen in the bifurcation diagram, and the bottom-left frame of Figure A.7(b) shows an example of a chaotic phase portrait at $A = 8.0$ m/s$^2$. The corresponding LE is $\lambda_{\max} = 0.73$ and the number of peaks in the DFT (Figure A.5(b)) is 115, both indicating a chaotic response. In general, good correspondence is seen between the LE and DFT methodologies.

A narrow non-chaotic band ($A \in [9.0, 9.5]$ m/s$^2$), exhibiting period-4 motion, is indicated in the bifurcation diagram. The bottom-right frame of Figure A.7(b) shows an example of one simulation ($A = 9.25$ m/s$^2$). At such large amplitudes, the isolated mass bounces against the lip until the disturbance switches directions.

*Effects of disturbance frequency $\omega$*

Finally, we investigate the influence of the disturbance frequency $\omega$ on the system's behavior. We fix the forcing amplitude $A = 8$ m/s$^2$ and sweep through frequency $\omega \in [\pi, 5\pi/2]$ rad/s, as indicated in Figure A.6(a) by the horizontal dashed line. The resulting

LEs, and corresponding bifurcation diagrams, are shown in Figure A.8(a). Similar to the amplitude sweep, positive LEs and chaotic bands are seen, with interspersed non-chaotic bands.

Moving from high to low frequency, the bifurcation diagram (Figure A.8(a)) indicates that anti-symmetric paths exist, and branch near $\omega = 6.5$ rad/s. Both anti-symmetric solutions were recorded; an example of one response ($\omega = 2\pi$ rad/s) is shown in Figure A.8(b) in the top-left frame. The anti-symmetric solution is not shown.

Over the range $\omega \in [5.1, 5.25]$ rad/s, narrow chaotic and non-chaotic bands are tightly interspersed. This corresponds to the leading edge of the chaotic band in Figure A.6(a). Then, for $\omega \in [4.6, 5.1]$ rad/s, a thick chaotic band is seen, followed by a period-3 window over $\omega \in [4.375, 4.6]$ rad/s. An example period-3 phase projection is given by the top-right frame of Figure A.8(b).

Symmetric, periodic motion is predominantly exhibited over the non-chaotic band $\omega \in [3.7, 4.1]$ rad/s. The phase portrait for one such response is shown in the bottom-left frame of Figure A.8(b). A narrow non-chaotic band ($\omega = 2\pi/1.962$ rad/s), exhibiting period-4 motion, is indicated in the bifurcation diagram. The bottom-right frame of Figure A.8(b) shows the corresponding phase portrait.

## A.4 Summary

In this chapter, an experimentally-calibrated, nonlinear model for the rectilinear dynamics of a rolling pendulum isolation system is presented. It is shown that under harmonic excitation a nonlinear rolling-type isolator may exhibit chaotic behavior over certain excitation parameter regimes and a specific operating condition. An extensive parameter study was performed, through which the influence of the disturbance amplitude and frequency was investigated. In the absence of impact this system is almost entirely non-chaotic; at large-amplitude, low-frequency disturbances, chaotic behavior was shown. Furthermore,

impacts lead to period amplification and anti-symmetric bifurcations.

From an engineering view-point, predictability of system responses is paramount; thus, chaotic responses may be undesirable. Knowing that impacts are more likely to produce chaotic responses in general, isolation systems should be designed to avoid impacts by either (a) increasing the systems' displacement capacities or (b) decreasing the displacement demand via additional damping.

This study will thus provide a foundation for future work, including experimental validation and non-harmonic excitation. Impacts of the ball-bearing with the bowl lip have been shown to induce chaotic responses, and the effect of impacts on isolation performance is another topic of future research.

# Appendix B

## Assessing the Accuracy of Vision-Based Accelerometry

Video-based motion measurement enables convenient tracking of multiple points in a plane with a single sensor: a CCD video camera. This chapter presents a method to easily assess the accuracy of accelerations computed from the tracking of positions measured via video and quantifies these errors for a consumer-grade camera. A signal with time-dependent frequency and amplitude is applied to a shake table, and the motion of LED targets are tracked. The tracked target positions are filtered and twice-differentiated to compute accelerations. These vision-based acceleration measurements are time-synchronized with conventional accelerometer measurements. The vision-based and conventional acceleration measurements are directly compared, and through a series of experiments, an extensive investigation of the acceleration measurement sensitivity to signal frequency and amplitude is carried out.

## B.1 Background

Vision-based motion measurement methods can track the motion of multiple points with a single sensor [38, 162–164]. Recently, Leifer *et al.* [165] compared twice-differentiated videogrammetry tracking data with conventional accelerometer measurements, and investigated how applying a smoothing filter [166] to the data enhanced the measurement accuracy. The potential of video-based acceleration measurements was exemplified through experiments. Leifer *et al.* recommended a few continuations, including [165]:

- Investigate additional filtering approaches to reduce displacement noise to enhance acceleration measurements.
- Investigate the frequency-dependent degradation of video-based acceleration measurements.

In this chapter, we seek to address these two points by presenting and demonstrating a straight-forward procedure to test the accuracy of vision-based systems. Previous research has only tested measurement accuracy at distinct frequencies for fixed amplitude (e.g. [167, 168]). Here we present a tracking signal which has time-dependent frequency and amplitude. The sensitivity of the signal error to frequency and amplitude is quantified by directly comparing the vision-based measurements to conventional sensors—an LVDT and a MEMS accelerometer. We investigate the limits imposed by the camera frame-rate as the signal frequency approaches the Nyquist frequency. Finally, an extensive parameter study is performed to characterize the vision-based acceleration measurement accuracy over a wide amplitude-frequency range.

## B.2 Photogrammetric Procedure

### *B.2.1 The set-up*

The video-based monitoring system utilized in this research consists of a *consumer-grade* 1280×720 pixel progressive scan Flip SlideHD video camera, with a fixed frame-rate of 30 frames per second (fps). The camera was positioned with its focal axis oriented vertically, perpendicular to a platform which moved horizontally. The 2.5 m distance was selected to ensure that at peak displacements the plane would remain in the filed of view. A single-axis, servo-hydraulic actuator moved the platform with a peak velocity of 50 cm/s and a peak stroke of ±7.5 cm. Displacement and acceleration responses were collected at a sample rate of 200 Hz with an LVDT and a MEMS accelerometer. Five Oznium LEDs were controlled by the data acquisition to turn on and off precisely at the start and end of the test, allowing for exact synchronization between the digitized sensor records and the video.

### *B.2.2 Video image processing and calibration*

Recorded videos were processed with the MATLAB Image and Video Processing toolbox. The average target area for each LED target can vary from 45 to 140 pixels depending on the grayscale formatting, thresholding, and ambient light. A linear calibration was used to map the pixel coordinates to the physical coordinates. The pixel-to-physical calibration was roughly 1.6 mm per imaging element pixel.

### *B.2.3 Computing acceleration from position*

Kienle *et al.* [169] suggest that numerical filtering could be used to improve the accuracy of acceleration computed from twice-differentiated vision-based displacement data. Previous approaches to differentiating vision-based data [165] involved a smoothing filter prior to differentiation to eliminate high-frequency noise components caused by inherent measurement uncertainty. In this study we differentiate and filter simultaneously in the

frequency domain.

The discrete time series $u_k$ ($1 \le k \le K$) is first de-trended, then windowed:

$$\hat{u}_k = w_k \cdot (u_k - \alpha j - \beta) \tag{B.1}$$

where $j = k - K/2$, $\alpha = \sum(ju_k)/\sum(j^2)$, $\beta = \sum(u_k)/K$, and $w_k$ is a tapered window function given by

$$w_k = \begin{cases} \frac{1}{2}[1 - \cos\frac{10\pi(k-1)}{K}], & 1 \le k < \frac{K+10}{10} \\ 1, & \frac{K+10}{10} \le k < \frac{9K}{10} \\ \frac{1}{2}[1 + \cos\frac{10\pi(k-K+K/10)}{K}], & \frac{9K}{10} \le k \le K \end{cases} . \tag{B.2}$$

The filtered signal is recovered from the inverse FFT of the Fourier coefficients of the filtered and differentiated signal,

$$y = \mathcal{F}^{-1}[H(f_k)D(f_k)\mathcal{F}[\hat{u}]] \tag{B.3}$$

where $\mathcal{F}[\hat{u}]$ are the Fourier coefficients computed from the forward FFT of $\hat{u}_k$, $H(f_k)$ is a smooth band-pass filter transfer function, and $D(f_k) = -(2\pi f_k)^2$ is the differentiation transfer function for which $D(f_1) = D(0) = 1$.

## B.3 Experimental Accuracy Assessment

### *B.3.1 Sine-sweep signal tracking*

The displacement signal to be tracked is a geometric up-chirp function with time-varying amplitude.

$$s(t) = \bar{s}_0 \exp[-r\,(t - t_0)^q] \sin\phi(t),\ t \in [t_0, t_\mathrm{f}] \tag{B.4}$$

where $\bar{s}_0 = \bar{s}(t_0)$ and the amplitude decay rate $r$ is such that the final amplitude $\bar{s}_\mathrm{f} = \bar{s}(t_\mathrm{f})$, viz.

$$r = \ln\left(\bar{s}_0/\bar{s}_\mathrm{f}\right) t_\mathrm{f}^{-q} . \tag{B.5}$$

The phase and instantaneous frequency are, respectively,

$$\phi(t) = 2\pi\frac{f_0 t + (f_\mathrm{f} - f_0)t^{p+1}}{(p+1)t_\mathrm{f}^p}, \quad \bar{f}(t) = \mathrm{d}\phi(t)/\mathrm{d}t . \tag{B.6}$$

For these tests, $\bar{s}_0/\bar{s}_f = 5$, $p = 2$, and $q = 2$.

The measured instantaneous displacement amplitude $\bar{d}(t)$ and acceleration amplitude $\bar{a}(t)$ are the moduli of the Hilbert transformed-LVDT signals $d(t)$ and $a(t)$:

$$\bar{d}(t) = \left|\mathcal{H}(d)(t)\right|, \quad \bar{a}(t) = \left|\mathcal{H}(a)(t)\right| . \tag{B.7}$$

The measured instantaneous frequency $\bar{f}(t)$ is the differentiated (unwrapped) phase of $\mathcal{H}(d)(t)$:

$$\bar{f}(t) = \mathrm{d}[\arg(\mathcal{H}(d)(t))]/\mathrm{d}t . \tag{B.8}$$

Figure B.1 shows (a) a representative LVDT measured displacement history $d(t)$ and the corresponding instantaneous amplitude $\bar{d}(t)$ and frequency $\bar{f}(t)$, and (b) a MEMS accelerometer measured acceleration history $a(t)$ and the corresponding instantaneous amplitude $\bar{a}(t)$.

### *B.3.2 Video signal synchronization*

To synchronize the LVDT and video records, the displacement measured by video image processing $d^*(t)$ is compared to time-shifted displacement measured by the LVDT $d(t+\tau)$. The constant $\tau \in [0, 1/30]$ sec is optimized to minimize the root mean square (RMS) difference between the two signals. Figure B.2 illustrates the RMS error for varying $\tau$; there is a unique minimum, corresponding to $\tau^*$.

## B.4 Results and Discussion

### *B.4.1 Time-series analyses*

A total of sixteen experiments were conducted in which the disturbance signal $s(t)$ applied to the shake table was scaled from 15–90% of the shake table's stroke limit. Taking LVDT and MEMS accelerometer measurements to be 'true,' define the vision-based measurement errors as

$$E_d(t) = d(t) - d^*(t) \qquad \text{(displacement error)} \tag{B.9}$$

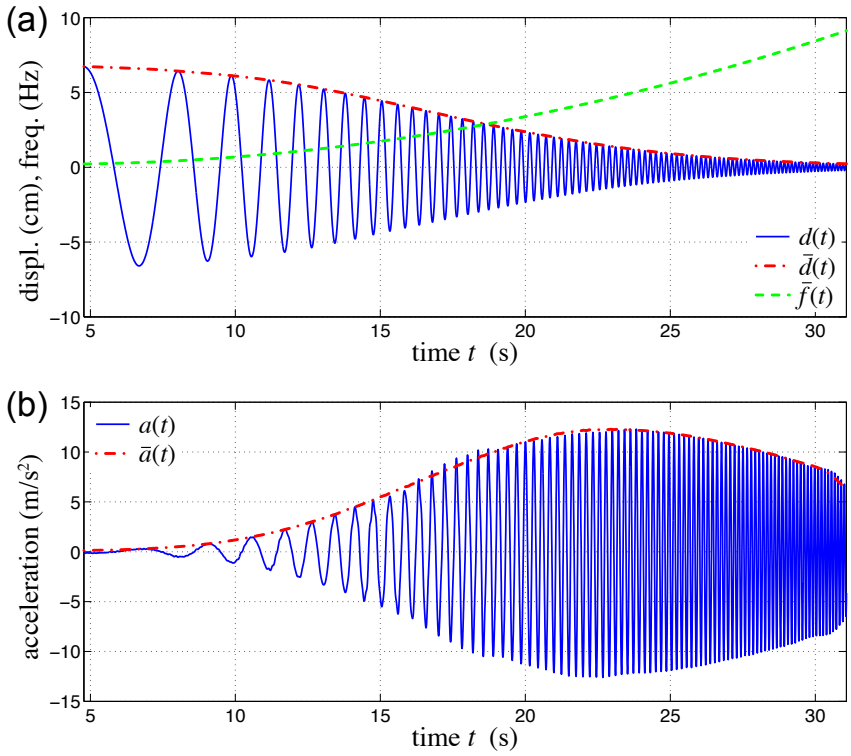


FIGURE B.1: (a) LVDT measurements after signal processing: (blue —) displacement $d$, (red $-\cdot-$) instantaneous displacement amplitude $\bar{d}$, and (green $- - -$) instantaneous frequency $\bar{f}$; (b) MEMS accelerometer measurements after signal processing: (blue —) acceleration $a$ and (red $-\cdot-$) instantaneous acceleration amplitude $\bar{a}$.

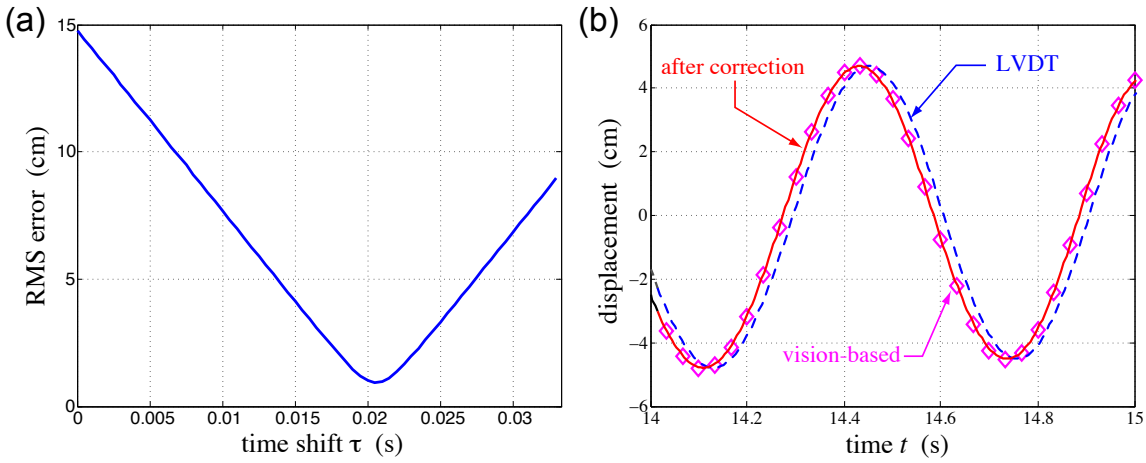


FIGURE B.2: Video signal synchronization: (a) root mean square (RMS) error for varying time-shift constant $\tau$, (b) pre- and post-synchronized signals.

$$E_a(t) = a(t) - \ddot{d}^*(t) \qquad \text{(acceleration error)} \qquad \text{(B.10)}$$

where $\ddot{d}^*(t)$ is the twice-differentiated vision-based displacement signal (Section B.2.3).

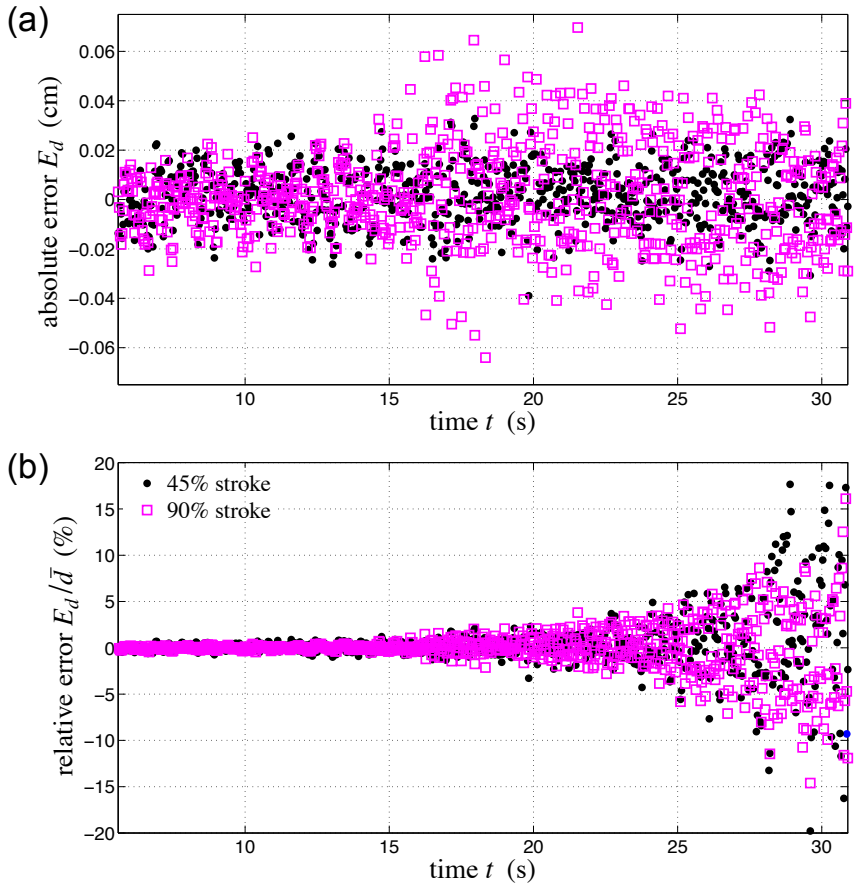


FIGURE B.3: (a) Absolute displacement error $E_a$ and (b) relative displacement error $E_d/\bar{d}$ versus time $t$: (•) 45% and (□) 90% of shake table's stroke.

Figure B.3 illustrates the absolute and relative displacement errors, $E_d$ and $E_d/\bar{d}$, at two intensities: 45% and 90% of the shake table's stroke limit. The amplitude of $E_d$ is nearly constant with mean error amplitudes of approximately 0.015 and 0.009 cm, which may be due to the camera not being perfectly perpendicular to the platform. The relative errors for both intensities are approximately equal and range from 1 to nearly 20 percent.

The vision-based measurements are sampled at 30 Hz while the highest frequency content of the motion is around 9 Hz, which is below the Nyquist frequency (15 Hz). In order to investigate the influence of frequency content of the test-subject motion increasing towards the Nyquist frequency on acceleration accuracy as recommended in Ref. [165], the 30 Hz vision-based displacement measurements were down-sampled by a factor of

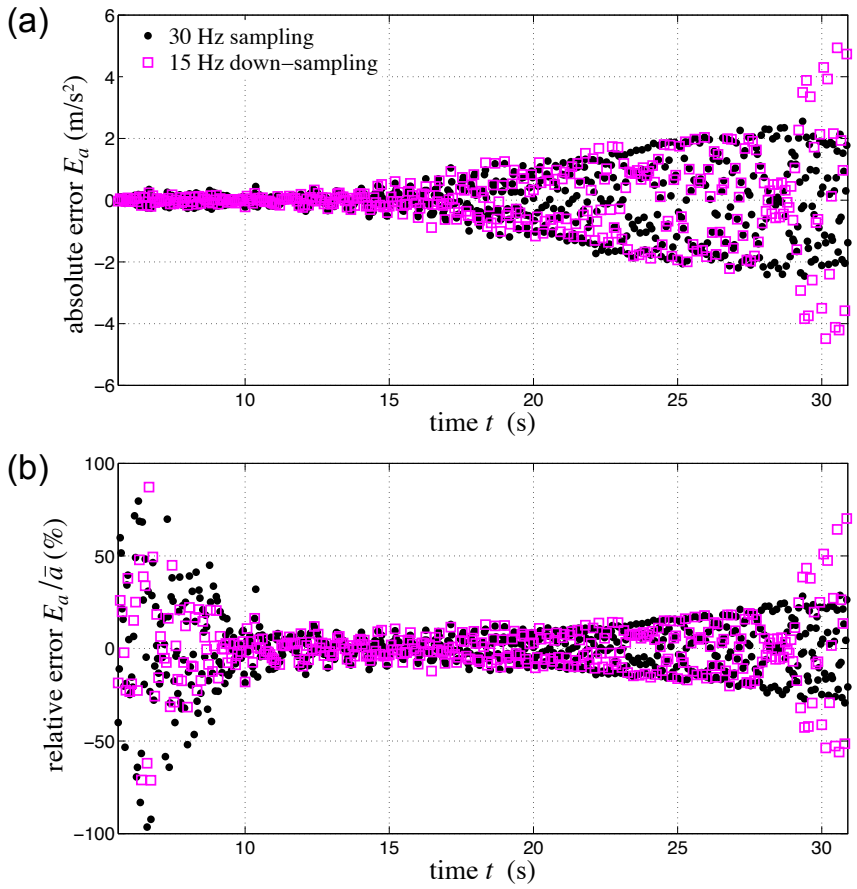


FIGURE B.4: (a) Absolute acceleration error $E_a$ and (b) relative acceleration error $E_a/\bar{a}$ versus time $t$: (•) 30 Hz sampling and (□) 15 Hz down-sampling.

two. Note that the $E_d$ is a function of only the image resolution (Section B.2.1), the video calibration (Section B.2.2), and the signal synchronization (Section B.3.2), and thus is unaffected by the sampling rate.

The absolute and relative acceleration errors, $E_a$ and $E_a/\bar{a}$, are shown in Figure B.4 for the two sampling frequencies. The acceleration error $E_a$ varies with amplitude and frequency. The down-sampled acceleration errors are similar to the 30 Hz measurement errors for instantaneous frequencies below the Nyquist frequency (7.5 Hz). Above the Nyquist frequency, the down-sampled $E_a$ doubles, with relative error greater than 50%. Large relative errors (nearly 100%) are seen at $t < 10$ s due to the small acceleration amplitudes (see Figure B.1).

### *B.4.2 Sensitivity of acceleration accuracy*

Combining the data for all sixteen experiments, contours of equal absolute acceleration error $|E_a|$ are given in Figure B.5 where the gray lines indicate the lines in amplitude-frequency space tested in each of the sixteen experiments. In general, the acceleration error increases with instantaneous frequency and acceleration/displacement amplitude, as indicated by the red regions in the upper-right of the plots. From contour plots such as these, experiments can be designed to operate in an amplitude-frequency regime that meets specified acceleration accuracy requirements.

## B.5 Summary

This chapter presents a simple means of assessing the accuracy of vision-based accelerometry using sine-sweep signals that posses broad frequency content and quantifies acceleration tracking errors for a commercial-grade video camera. An FFT-based filtering and differentiation technique was applied to vision-based position data to measure the accelerations of a shake table. Good correspondence was seen between traditional (MEMS accelerometer) and vision-based acceleration measurements. Vision-based measurements are *fundamentally* discrete digital signals, and hence there is *no avoiding* the aliasing of high-frequency motions. If the frequency content of the test-subject motion equals or exceeds the Nyquist frequency, then acceleration measurement errors increase dramatically. Finally, contour plots of absolute acceleration error provides a visual means of analyzing the frequency and amplitude dependence of acceleration measurement errors. The techniques and procedure described in this chapter can be extended and applied to *any* vision-based measurement system (e.g. planar or full three-dimensional tracking), permitting a comprehensive analysis into the potentials and limitations of vision-based accelerometry.

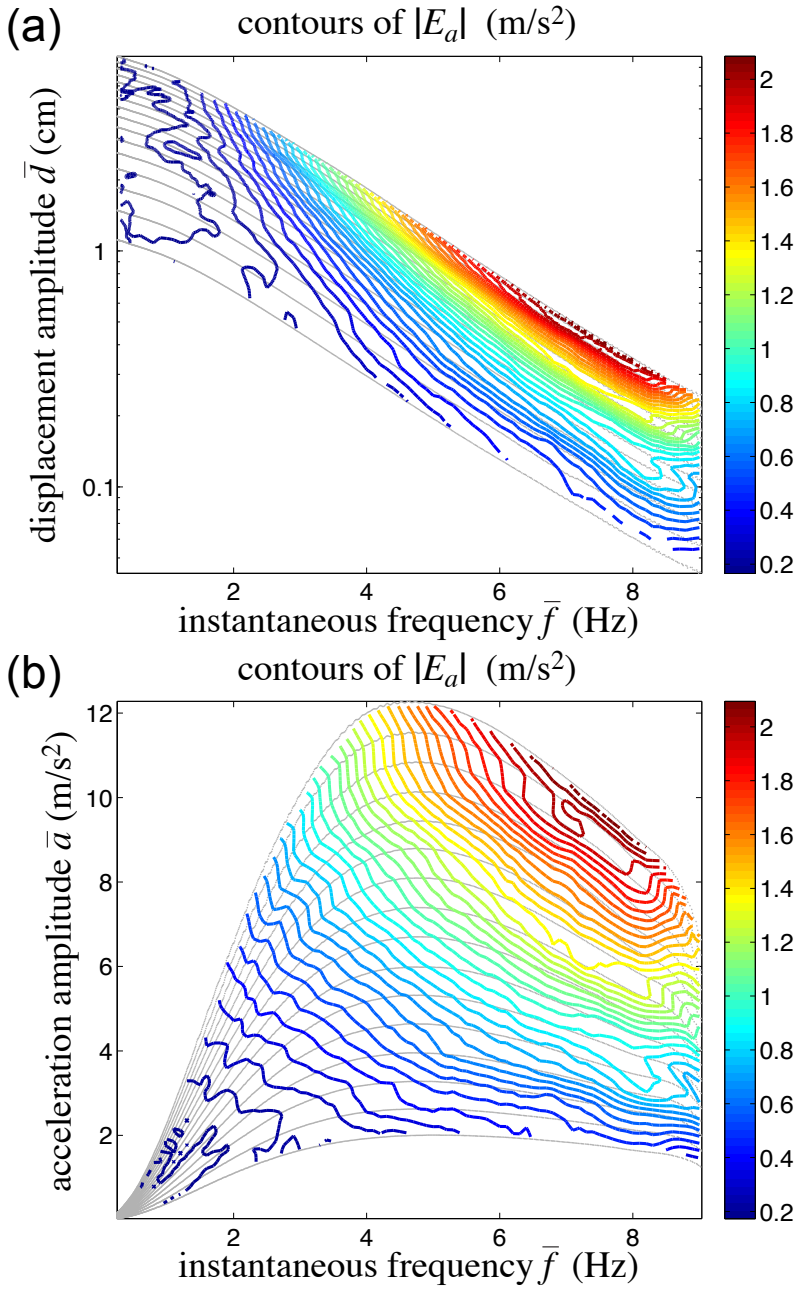


FIGURE B.5: Contours of equal absolute acceleration error $|E_a|$ in (a) $\bar{d}$-$\bar{f}$ space and (b) $\bar{a}$-$\bar{f}$ space. The gray lines indicate the sixteen experiments over which the contours are computed.

# Appendix C

## Optimal Control MATLAB Functions

The full MATLAB code used to generate the figures in Section 7.5 may be found at `http://www.duke.edu/~hpgavin/osc`. The essentials are given below.

Sample code to run `bvp4c.m`:

```
global A B Bw Q R S T umax cmax dt nT n
% initialize parameters: A, B, Bw <- eq'n (7.23); w, t <- eq'ns (7.26-7.29); and
%     Q, R, S, T, umax, cmax <- Section 7.5.3
nT = length(t); dt = t(2)-t(1)% length and time step of disturbance record
x0 = zeros(n,1);  lf = zeros(n,1); % initial states and terminal costates
options = bvpset('NMax',20*nT,'Stats','on');      % set options
solinit = bvpinit(t,5*eps*ones(2*n,1));           % initialize solution
sol = bvp4c(@(t,z) zdot(t,z,w), @(z0,zf) bcfun(z0,zf,x0,lf,n),solinit,options);
z = deval(sol,t); x = z(1:n,:); l = z(n+1:2*n,:); % extract states and costates
```

Unconstrained BVP function:

```
function zdot = zdot(t,z,w)
global A B Bw Q R S T cmax dt nT n
i = min(nT-1,floor(t/dt)+1);                    % the current time step
wi = w(i) + (w(i+1)-w(i))/dt*(t - (i-1)*dt);    % interpolate disturbance
x = z(1:n); p = z(n+1:2*n);                     % state and co-state vectors
uactive = -R\(S'*x + B'*l);                     % unconstrained optimal control
[usat,mu] = sat(x,uactive,l);  % saturated controls and Lagrange multipliers
% BVP equations for states and co-states ...
zdot = [ A*x        + B*usat + Bw*wi
        -Q*x - A'*l - S*usat + lambda(2)*cmax*T*usat ];
```

Boundary condition (BC) function:

```
function bc = bcfun(z0,zf,x0,lf,n)
bc = [ z0(1:n,1)-x0 ; zf(n+1:2*n,end)-lf ];
```

Saturation function:

```
function [usat,mu] = sat(x,uactive,l)
global umax cmax B R S T
c = [ uactive^2 - umax^2 ; uactive*(uactive - cmax*T'*x) ]; % constraints
v = T'*x;       % velocity across semi-active damper
if c(1) <= 0 && c(2) <= 0
   usat = uactive;   mu = [ 0 ; 0 ]; return
elseif uactive*v < 0
   usat = 0;         mu = [ 0 ; -(S'*x+R*usat+B'*l)/(2*usat-cmax*v) ]; return
elseif abs(v) > umax/cmax
   usat = umax*sign(v); mu = [ -(S'*x+R*usat+B'*l)/(2*usat) ; 0 ]; return
elseif v == 0
   usat = 0;         mu = [ 0 ; 0 ]; return
else
   usat = cmax*v;    mu = [ 0 ; -(R*usat+S'*x+B'*l)/(2*usat-cmax*v) ]; return
end
```

# Appendix D

# Truly Isotropic Biaxial Hysteresis with Arbitrary Knee Sharpness

The inelastic responses of framed structures and seismic isolation systems undergoing biaxial (horizontal) shaking are coupled. In existing models for biaxial coupling of hysteretic behavior, the smoothness (or 'knee') of the transition from elastic to yielding behavior can not be modified without affecting the shape of the yield surface. This chapter presents a model for coupled biaxial hysteretic behavior in which the knee from pre-yield to post-yield can be adjusted while maintaining an isotropic yield surface.

## D.1 Introduction

Earthquake ground motions are multiaxial phenomena, involving displacements and rotations in three spatial dimensions. When framed structures and structures with inelastic or frictional seismic isolation systems responding to multiaxial shaking incur inelastic deformations, the occurrence of yielding affects responses in all horizontal coordinates. As such, horizontal inelastic responses are intrinsically coupled; unidirectional simulation of inelastic response cannot incorporate strength reduction due to out-of-plane motions, and

are therefore non-conservative. Nevertheless, planar models remain prevalent in the analysis of strong ground motion responses [170].

The biaxial hysteretic behavior of seismic isolation systems and framed structures with regular plan are isotropic and orthotropic, respectively. The transition from pre-yield elastic response to post-yield inelastic response can occur gradually, as in the case of lead-rubber seismic isolation bearings, or can occur in a more-discontinuous manner, as in the case of sliding bearings. The sharpness of this transition affects many aspects of hysteretic responses, including cumulative dissipated energy and the uniqueness of constant ductility spectra [171]. A model for the coupled isotropic biaxial behavior of inelastic components and structures that encompasses smooth and sharp knees would be of use in modeling a range of structural systems.

The model for biaxial inelastic behavior presented in this chapter is an extension of simple evolutionary models [172]. Evolutionary models for inelastic behavior are computationally and analytically convenient. Existing evolutionary models for biaxial hysteretic behavior that allow for different levels of sharpness in the elastic-to-inelastic transition are not isotropic (i.e. rotationally-invariant). The model presented here is truly isotropic and enables the modeling of a wider range of hysteretic behavior than previously possible. Before presenting the new model, uniaxial and biaxial hysteretic models are reviewed.

## D.2 Background

### *D.2.1 Bouc-Wen uniaxial hysteretic model*

The Bouc-Wen uniaxial model of hysteresis was originally proposed by Bouc [147] and subsequently extended and applied by Wen [148]. The non-dimensionalized[1] displacement $u$ and the dimensionless hysteretic quantity $z$ satisfy the following differential equa-

[1] The normalizing constant for $u$ is the yield displacement $\Delta$. Therefore, $u$ can be thought of as a measure of ductility.

tion:

$$\dot{z} = A\dot{u} - \beta\,|\dot{u}|\,|z|^{\eta-1}z - \gamma\,\dot{u}\,|z|^{\eta} \equiv A\dot{u} - |z|^{\eta}[\beta\,\mathrm{sign}(\dot{u}z) + \gamma]\,\dot{u} \tag{D.1}$$

in which the signum function $\mathrm{sign}(\cdot) = (\cdot)/|\cdot|$, and the parameters $A$, $\beta$, $\gamma$, and $\eta$ control the shape of the hysteresis. The parameter $\eta$ governs the smoothness of the elastic-to-inelastic transition [149], effectively adjusting the 'knee' of the hysteresis loop. For a typical value of $\eta = 2$,

$$\dot{z} = A\dot{u} - \beta\,|\dot{u}z|\,z - \gamma\,(\dot{u}z)\,z \equiv A\dot{u} - z^2[\beta\,\mathrm{sign}(\dot{u}z) + \gamma]\,\dot{u} \tag{D.2}$$

The *yield displacement* $\Delta$, which equals the ultimate hysteretic displacement $z_\mathrm{u}$, is obtained when $\mathrm{d}z/\mathrm{d}u = 0$, to wit,

$$\Delta = |z_\mathrm{u}| = \sqrt[\eta]{A/(\beta+\gamma)} \tag{D.3}$$

Extensions to Equation (D.1) can account for degrading stiffness [173], pinching hysteresis [174], and asymmetric hysteresis [175].

### *D.2.2 Park-Wen biaxial hysteretic model*

The Bouc-Wen uniaxial hysteretic model was extended by Park *et al.* [145] to account for the effect of biaxial interactions. The hysteretic components $z_x$ and $z_y$ in the two orthogonal directions obey the following coupled differential equations [145]:

$$\dot{z}_x = A\dot{u}_x - z_x\{\beta|\dot{u}_x z_x| + \gamma(\dot{u}_x z_x) + \beta|\dot{u}_y z_y| + \gamma(\dot{u}_y z_y)\} \tag{D.4a}$$

$$\dot{z}_y = A\dot{u}_y - z_y\{\beta|\dot{u}_x z_x| + \gamma(\dot{u}_x z_x) + \beta|\dot{u}_y z_y| + \gamma(\dot{u}_y z_y)\} \tag{D.4b}$$

or equivalently

$$\dot{z}_x = A\dot{u}_x - z_x\{z_x[\beta\,\mathrm{sign}(\dot{u}_x z_x) + \gamma]\dot{u}_x + z_y[\beta\,\mathrm{sign}(\dot{u}_y z_y) + \gamma]\dot{u}_y\} \tag{D.5a}$$

$$\dot{z}_y = A\dot{u}_y - z_y\{z_x[\beta\,\mathrm{sign}(\dot{u}_x z_x) + \gamma]\dot{u}_x + z_y[\beta\,\mathrm{sign}(\dot{u}_y z_y) + \gamma]\dot{u}_y\} \tag{D.5b}$$

in which $u_x$ and $u_y$ are the orthogonal, non-dimensional displacement components. The model of Equations (D.4) and (D.5) were derived so that the response to uniaxial loading along any direction in the $x$-$y$ plane would reduce to an equation of the form of Equation

(D.2). Therefore, Equations (D.4) are *rotationally-invariant* (or isotropic). The Park-Wen biaxial hysteretic model has been used extensively to model friction and yielding hysteresis, e.g. Refs. [132, 176–178]. However, the uniaxial behavior of the model is a limited subclass ($\eta = 2$) of the more-general Bouc-Wen model.

### *D.2.3 Wang-Wen biaxial hysteretic model*

Wang and Wen [179] attempted to generalize the hysteretic model of Ref. [145] to include cases with $\eta > 2$. The Wang-Wen biaxial hysteretic model is as follows:

$$\dot{z}_x = A\dot{u}_x - z_x\{\beta|\dot{u}_x||z_x|^{\eta-1} + \gamma\dot{u}_x|z_x|^{\eta} + \beta|\dot{u}_y||z_y|^{\eta-1} + \gamma\dot{u}_y|z_y|^{\eta}\} \tag{D.6a}$$

$$\dot{z}_y = A\dot{u}_y - z_y\{\beta|\dot{u}_x||z_x|^{\eta-1} + \gamma\dot{u}_x|z_x|^{\eta} + \beta|\dot{u}_y||z_y|^{\eta-1} + \gamma\dot{u}_y|z_y|^{\eta}\} \tag{D.6b}$$

or equivalently

$$\dot{z}_x = A\dot{u}_x - z_x\{z_x|z_x|^{\eta-2}[\beta\,\mathrm{sign}(\dot{u}_x z_x) + \gamma]\,\dot{u}_x + z_y|z_y|^{\eta-2}[\beta\,\mathrm{sign}(\dot{u}_y z_y) + \gamma]\,\dot{u}_y\} \tag{D.7a}$$

$$\dot{z}_y = A\dot{u}_y - z_y\{z_x|z_x|^{\eta-2}[\beta\,\mathrm{sign}(\dot{u}_x z_x) + \gamma]\,\dot{u}_x + z_y|z_y|^{\eta-2}[\beta\,\mathrm{sign}(\dot{u}_y z_y) + \gamma]\,\dot{u}_y\} \tag{D.7b}$$

There is a clear similarity between Equation (D.1) and Equations (D.6) and (D.7), and thus such a proposition is not illogical. In fact, along the principal axes (i.e. $\dot{u}_x = z_x = 0$ or $\dot{u}_y = z_y = 0$) Equations (D.6) collapse to Equation (D.1) for arbitrary $\eta$. Equations (D.6) were originally proposed to investigate the effects of connection failure on the structural response of steel buildings under multidirectional earthquakes [179], and have since been used to model the biaxial bending response of reinforced concrete columns [180]; in both cases, the smoothness parameter $\eta$ was taken to be two.

Unlike the Park-Wen model, Equations (D.6) are *not* rotationally-invariant for $\eta \neq 2$ [181]. Consider a simple rectilinear displacement path along a line passing through the origin with selected anti-clockwise rotation angle $\theta$ from the $x$-axis, namely

$$z_x = z\cos\theta,\ z_y = z\sin\theta,\ u_x = u\cos\theta,\ u_y = u\sin\theta \tag{D.8}$$

Substituting Equations (D.8) into Equations (D.7), the unidirectional hysteretic equation is as follows:

$$\dot{z} = A\,\dot{u} - \left(\beta\,|\dot{u}|\,|z|^{\eta-1}z + \gamma\,\dot{u}\,|z|^{\eta}\right) \times \left(|\cos^{\eta}\theta| + |\sin^{\eta}\theta|\right) \tag{D.9}$$

This equation shows that the hysteretic behavior along different directions can differ, depending on the value of $\eta$. Only when $\eta = 2$ are Equations (D.6) rotationally-invariant, which corresponds to the Park-Wen system (Equations (D.4)).

The angle-dependent yield displacement along $\theta$ is obtained from Equation (D.9):

$$\Delta(\theta) = \sqrt[\eta]{A/(\beta+\gamma)} \times \sqrt[\eta]{|\cos^{\eta}\theta| + |\sin^{\eta}\theta|} \tag{D.10}$$

The yield displacement along the $x$- and $y$-axes, denoted $\Delta_x = \Delta(0)$ and $\Delta_y = \Delta(\pi/2)$, are equivalent, and reduce to the Bouc-Wen yield displacement, i.e. $\Delta_x = \Delta_y = \Delta$. However, for arbitrary $\theta$, the yield surface varies with $\eta$. If $\eta = 1$, the yield surface traces a square whose diagonals align with the $x$- and $y$-axes. If $\eta = 2$, the yield surface traces a circle, which represents equal capacity along any direction [145]. If $\eta > 2$, the yield surface traces a square with rounded corners whose diagonals align with $\theta = \pi/4$ and $3\pi/4$. In the limit $\eta \to \infty$, the yield surface traces a square whose diagonals align with $\theta = \pi/4$ and $3\pi/4$; the yield strength along the $x$-axis is independent of the displacement along the $y$-axis, and the effect of interaction is eliminated [181].

## D.3 A Truly Isotropic Biaxial Hysteretic Model

Consider again a rectilinear displacement path described by Equations (D.8). Along the displacement path, the following trigonometric relationships hold:

$$u = u_x\cos\theta + u_y\sin\theta,\quad \dot{u} = \dot{u}_x\cos\theta + \dot{u}_y\sin\theta,\quad z = z_x\cos\theta + z_y\sin\theta,\quad \dot{z} = \dot{z}_x\cos\theta + \dot{z}_y\sin\theta \tag{D.11}$$

Substituting Equations (D.8) and (D.11) into the right-hand side of Equation (D.1), and through some algebraic manipulation, Equation (D.1) can be rewritten as

$$\dot{z} = \{A\dot{u}_x - (\beta|\dot{u}_x z_x| + \gamma\dot{u}_x z_x + \beta|\dot{u}_y z_y| + \gamma\dot{u}_y z_y)\left(z_x^2 + z_y^2\right)^{\frac{\eta-2}{2}} z_x\}\cos\theta$$

$$+ \{A\dot{u}_y - (\beta|\dot{u}_x z_x| + \gamma\dot{u}_x z_x + \beta|\dot{u}_y z_y| + \gamma\dot{u}_y z_y)\left(z_x^2 + z_y^2\right)^{\frac{\eta-2}{2}} z_y\}\sin\theta \quad \text{(D.12)}$$

By the last expression of Equation (D.11), the terms in braces multiplying $\cos\theta$ and $\sin\theta$—which do *not* depend on the angle $\theta$—are, respectively, equivalent to $\dot{z}_x$ and $\dot{z}_y$, viz.,

$$\dot{z}_x = A\dot{u}_x - z_x(\beta|\dot{u}_x z_x| + \gamma\dot{u}_x z_x + \beta|\dot{u}_y z_y| + \gamma\dot{u}_y z_y)\left(z_x^2 + z_y^2\right)^{\frac{\eta-2}{2}} \quad \text{(D.13a)}$$

$$\dot{z}_y = A\dot{u}_y - z_y(\beta|\dot{u}_x z_x| + \gamma\dot{u}_x z_x + \beta|\dot{u}_y z_y| + \gamma\dot{u}_y z_y)\left(z_x^2 + z_y^2\right)^{\frac{\eta-2}{2}} \quad \text{(D.13b)}$$

By construction, the system has the hysteretic property of the Bouc-Wen model with arbitrary $\eta$ along *any* rectilinear displacement path. Therefore, Equations (D.13) are *rotationally-invariant*, and the system is truly isotropic. Note that for $\eta = 2$, we recover the Park-Wen model (Equations (D.4)). The yield displacement in any direction is, by construction, given by Equation (D.3), and thus traces a circle with radius $\Delta = \sqrt[\eta]{A/(\beta+\gamma)}$. This derivation for a biaxial system generalizes to the tensorial Karray-Bouc-Casciati model [182, 183]. As with the Park-Wen and Wang-Wen models, this model is easily extended to consider orthotropic systems ($\Delta_x \neq \Delta_y$) via a simple linear transformation [145].

## D.4 Numerical Examples

In this section, numerical examples demonstrate and compare the proposed model (Equations (D.13)) to the anisotropic Wang-Wen model (Equations (D.6)). In all numerical simulations, $A$, $\beta$, and $\gamma$ are taken to be unity, $1/2$, and $1/2$, respectively; therefore, the ratio $A/(\beta+\gamma)$ is equal to unity, and the yield displacement $\Delta$ is unity for all $\eta$. Three values of $\eta$ are considered: $\eta = 1$ (red dotted), 2 (blue dashed), and 5 (black solid).

### *D.4.1 Unidirectional motion*

Figure D.1 shows simulated hysteretic loops produced by the models of Equations (D.6) and (D.13) for unidirectional motion in which

$$u_x(t) = t\cos\theta\sin 2\pi t, \qquad u_y(t) = t\sin\theta\sin 2\pi t \quad \text{(D.14)}$$

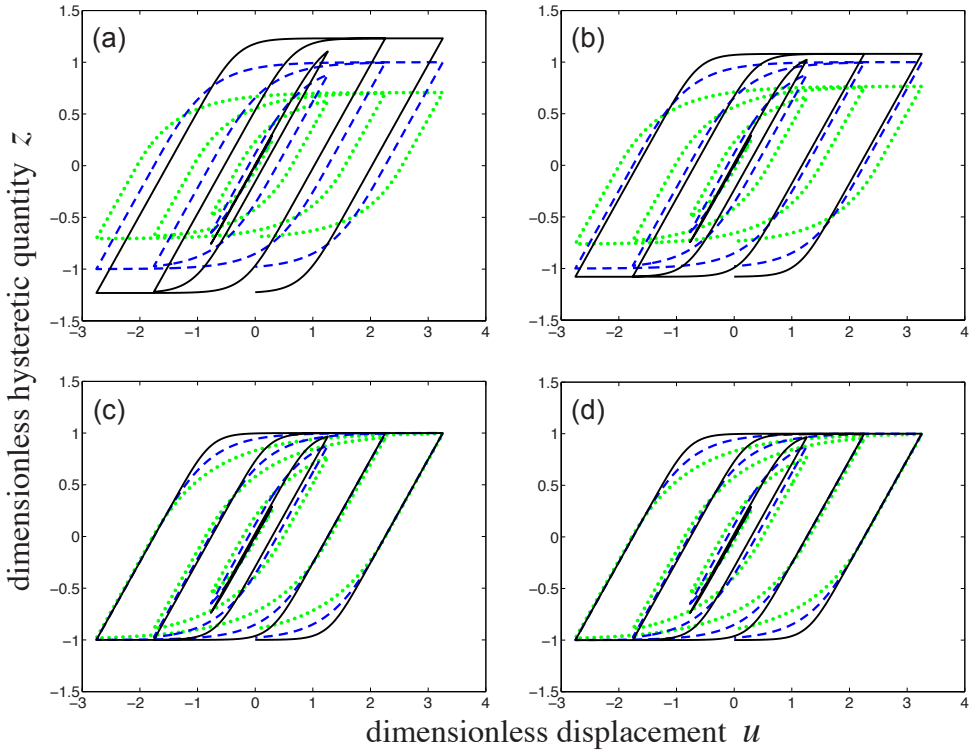


FIGURE D.1: Simulated hysteretic behavior under unidirectional motion of (a-b) Wang-Wen model and (c-d) proposed model for (a,c) $\theta = \pi/4$ and (b,d) $\theta = \pi/8$: $\eta = 1$ (• • •), 2 (– – –), and 5 (——).

with $\theta = \pi/4$ and $\pi/8$.

The Wang-Wen model, as previously discussed, has an $\eta$- and $\theta$-dependent yield displacement. In Figure D.1(a), the yield displacement (i.e. the saturating limit on $z$) increases with $\eta$; for a fixed $\eta \neq 2$, the yield displacement differs for $\theta = \pi/4$ and $\pi/8$ (Figures D.1(a) and D.1(b)). Whereas for the proposed model (Figures D.1(c-d)), the hysteretic loops are identical for different values of $\theta$; the yield displacement is constant for all values of $\eta$. The sharpness of the hysteretic 'knee' increases with increasing $\eta$ for both the Wang-Wen model (Figures D.1(a-b)) and the proposed model (Figures D.1(c-d)),

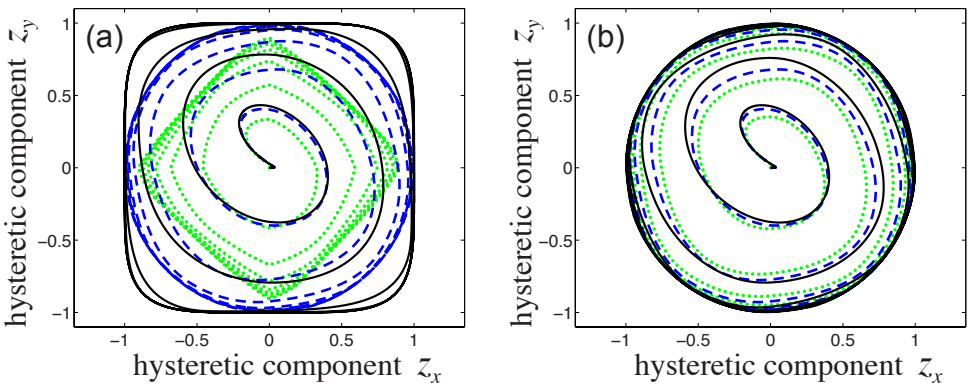


FIGURE D.2: Simulated hysteretic behavior under bidirectional motion of (a) Wang-Wen model and (b) proposed model: $\eta = 1$ (• • •), 2 (– – –), and 5 (——).

### *D.4.2 Bidirectional motion*

Figure D.2 shows simulated hysteretic loops produced by the proposed model of Equations (D.13) for bidirectional motion in which

$$u_x(t) = (t/5)\cos 2\pi t, \qquad u_y(t) = (t/5)\sin 2\pi t \tag{D.15}$$

The parametric equations (D.15) are for an Archimedean spiral. As $t \to \infty$ the $z_x$ and $z_y$ trajectories approach the yielding surface. The yield surface for the Wang-Wen model (Figure D.2(a)) does not trace a circle; the yield surfaces for $\eta = 1$, 2, and 5 are, respectively, a square with diagonals in line with the $x$- and $y$-axes, a circle, and a rounded-corner square with diagonals at $\theta = \pi/4$ and $3\pi/4$. Whereas, the proposed model (Equations (D.13)) has a circular yielding surface that is independent of the value of $\eta$, as shown in Figure D.2(b).

## D.5 Summary

In this brief note, we have investigated the generalization of the Bouc-Wen hysteretic model for biaxial motion. It has been shown that previous approaches are either (i) not general enough—restricted to an elastic-to-inelastic transition parameter $\eta$ of two—or (ii) not rotationally-invariant, resulting in an anisotropic yield surface. This chapter presents

a new biaxial hysteretic model that is truly isotropic for hysteretic behavior that can vary continuously from smooth to bilinear. This model reduces to the same Bouc-Wen model for rectilinear motion in any direction. The flexibility of this new model over existing models is illustrated by example.

# Bibliography


[1] WorkSafe Technologies, Inc., ISO-Base platform (2011).
URL http://www.worksafetech.com/

[2] W. D. Iwan, The earthquake design and analysis of equipment isolation systems, Earthquake Engineering and Structural Dynamics 6(12) (1978) 523–534. doi:10.1002/eqe.4290060602.

[3] B. D. Notohardjono, J. Wilcoski, J. B. Gambill, Design of earthquake resistant server computer structures, Journal of Pressure Vessel Technology 126(1) (2004) 66–74. doi:10.1115/1.1638389.

[4] H. Khechfe, M. Noori, Z. Hou, J. M. Kelly, G. Ahmadi, An experimental study on the seismic response of base-isolated secondary systems, Journal of Pressure Vessel Technology 124 (2002) 81–88. doi:10.1115/1.1445795.

[5] C. Alahan, F. Şahin, Protecting vibration-sensitive contents: an investigation of floor accelerations in seismically isolated buildings, Bulletin of Earthquake Engineering 9 (2011) 1203–1226. doi:10.1007/s10518-010-9236-0.

[6] R. Villaverde, Seismic design of secondary structures: state-of-the-art, Journal of Structural Engineering 123 (1997) 1011–1019. doi:10.1061/(ASCE)0733-9445(1997)123:8(1011).

[7] M. F. Dimentberg, Y. K. Lin, R. Zhang, Toppling of computer-type equipment under base excitation, Journal of Engineering Mechanics 119 (1993) 145–160. doi:10.1061/(ASCE)0733-9399(1993)119:1(145).

[8] D. Lopez Garcia, T. T. Soong, Sliding fragility of block-type non-structural components. Part 1: Unrestrained components, Earthquake Engineering and Structural Dynamics 32 (2003) 111–129. doi:10.1002/eqe.217.

[9] T. C. Hutchinson, S. R. Chaudhuri, Benchshelf system dynamic characteristics and their effects on equipment and contents, Earthquake Engineering and Structural Dynamics 35 (2006) 1631–1651. doi:10.1002/eqe.596.

[10] D. Lopez Garcia, T. T. Soong, Sliding fragility of block-type non-structural components. Part 2: Restrained components, Earthquake Engineering and Structural Dynamics 32 (2003) 131–149. doi:10.1002/eqe.218.

[11] M. Ismail, J. Rodellar, F. Ikhouane, An innovative isolation bearing for motion-sensitive equipment, Journal of Sound and Vibration 326 (2009) 503–521. doi:10.1016/j.jsv.2009.06.022.

[12] G. F. Demetriades, M. C. Constantinou, A. M. Reinhorn, Study of wire rope systems for seismic protection of equipment in buildings, Engineering Structures 15 (1993) 321–334. doi:10.1016/0141-0296(93)90036-4.

[13] Y. L. Xu, B. Li, Hybrid platform for high-tech equipment protection against earthquake and microvibration, Earthquake Engineering and Structural Dynamics 35 (2006) 943–967. doi:10.1002/eqe.564.

[14] F. Naeim, J. M. Kelly, Design of seismic isolated structures, John Wiley & Sons, New York, NY, 1999.

[15] R. S. Jangid, Optimum friction pendulum system for near-fault motions, Engineering Structures 27 (2005) 249–259. doi:10.1016/j.engstruct.2004.09.013.

[16] M. Hamidi, M. H. El Naggar, On the performance of SCF in seismic isolation of the interior equipment of buildings, Earthquake Engineering and Structural Dynamics 36 (2007) 1581–1604. doi:10.1002/eqe.708.

[17] M. Pranesh, R. Sinha, VFPI: an isolation device for aseismic design, Earthquake Engineering and Structural Dynamics 29 (2000) 603–627. doi:10.1002/(SICI)1096-9845(200005)29:5<603::AID-EQE927>3.3.CO;2-N.

[18] C. S. Tsai, T.-C. Chiang, B.-J. Chen, Experimental evaluation of piecewise exact solution for predicting seismic responses of spherical sliding type isolated structures, Earthquake Engineering and Structural Dynamics 34 (2005) 1027–1046. doi:10.1002/eqe.430.

[19] D. M. Fenz, M. C. Constantinou, Behaviour of the double concave Friction Pendulum bearing, Earthquake Engineering and Structural Dynamics 35 (2006) 1403–1424. doi:10.1002/eqe.589.

[20] D. M. Fenz, M. C. Constantinou, Spherical sliding isolation bearings with adaptive behavior: Theory, Earthquake Engineering and Structural Dynamics 37 (2008) 163–183. doi:10.1002/eqe.751.

[21] D. M. Fenz, M. C. Constantinou, Spherical sliding isolation bearings with adaptive behavior: Experimental verification, Earthquake Engineering and Structural Dynamics 37 (2008) 185–205. doi:10.1002/eqe.750.

[22] L.-Y. Lu, T.-Y. Lee, S.-W. Yeh, Theory and experimental study for sliding isolators with variable curvature, Earthquake Engineering and Structural Dynamics 40 (2011) 1609–1627. doi:10.1002/eqe.1106.

[23] P. Murnal, R. Sinha, Earthquake resistant design of structures using the Variable Frequency Pendulum Isolator, Journal of Structural Engineering 128 (2002) 870–880. doi:10.1061/(ASCE)0733-9445(2002)128:7(870).

[24] P. Murnal, R. Sinha, Behavior of torsionally coupled structures with variable frequency pendulum isolator, Journal of Structural Engineering 130(7) (2004) 1041–1054. doi:10.1061/(ASCE)0733-9445(2004)130:7(1041).

[25] D. P. Soni, B. B. Mistry, R. S. Jangid, V. R. Panchel, Seismic response of the double variable frequency pendulum isolator, Structural Control and Health Monitoring 18 (2011) 450–470. doi:10.1002/stc.384.

[26] C. S. Tsai, W.-S. Chen, T.-C. Chiang, B.-J. Chen, Component and shaking table tests for full-scale multiple friction pendulum system, Earthquake Engineering and Structural Dynamics 35 (2006) 1653–1675. doi:10.1002/eqe.598.

[27] G. Mosqueda, A. S. Whittaker, G. L. Fenves, Characterization and modeling of friction pendulum bearings subjected to multiple components of excitation, Journal of Structural Engineering 130(3) (2004) 433–442. doi:10.1061/(ASCE)0733-9445(2004)130:3(433).

[28] L. L. Chung, C. Y. Yang, H. M. Chen, L. Y. Lu, Dynamic behavior of nonlinear rolling isolation system, Structural Control and Health Monitoring 16 (2009) 32–54. doi:10.1002/stc.305.

[29] R. S. Jangid, Y. B. Londhe, Effectiveness of elliptical rolling rods for base isolations, Journal of Structural Engineering 124(4) (1998) 49–472. doi:10.1061/(ASCE)0733-9445(1998)124:4(469).

[30] R. S. Jangid, Stochastic seismic response of structures isolated by rolling rods, Engineering Structures 22(8) (2000) 937–946. doi:10.1016/S0141-0296(99)00041-3.

[31] Q. Zhou, X. Lu, Q. Wang, D. Feng, Q. Yao, Dynamic analysis on structures base-isolated by a ball system with restoring properties, Earthquake Engineering and Structural Dynamics 27 (1998) 773–791. doi:10.1002/(SICI)1096-9845(199808)27:8<773::AID-EQE749>3.0.CO;2-A.

[32] E. Y. Antonyuk, N. P. Plakhtienko, Dynamic processes in a spheroidal seismic-damping mechanism, International Applied Mechanics 41(1) (2005) 90–97. doi:10.1007/s10778-005-0063-y.

[33] L. Guerreiro, J. Azevedo, A. H. Muhr, Seismic tests and numerical modeling of a rolling-ball isolation system, Journal of Earthquake Engineering 11(1) (2007) 49–66. doi:10.1080/13632460601123172.

[34] A. Kasalanati, A. Reinhorn, M. Constantinou, D. Sanders, Experimental study of ball-in-cone isolation system, in: Building to Last: Proceedings of the 15th Structures Congress, ASCE, New York, 1997, pp. 1191–1195.

[35] T. W. Lin, C. C. Chern, C. C. Hone, Experimental-study of base-isolation by free rolling rods, Earthquake Engineering and Structural Dynamics 24(12) (1995) 1645–1650. doi:10.1002/eqe.4290241207.

[36] C. S. Tsai, Y.-C. Lin, W.-S. Chen, H. C. Su, Tri-directional shaking table tests of vibration sensitive equipment with static dynamics interchangeable-ball pendulum system, Earthquake Engineering and Engineering Vibration 9 (2010) 103–112. doi:10.1007/s11803-010-9009-4.

[37] Z. A. Kemeny, Ball-in-cone rolling isolation systems, U.S. Patent 5599106 (1997).

[38] P. S. Harvey Jr, H. P. Gavin, The nonholonomic and chaotic nature of a rolling isolation system, Journal of Sound and Vibration 332 (2013) 3535–3551. doi:10.1016/j.jsv.2013.01.036.

[39] P. S. Harvey Jr, H. P. Gavin, J. T. Scruggs, Optimal performance of constrained control systems, Journal of Smart Materials and Structures 21 (2012) 085001. doi:10.1088/0964-1726/21/8/085001.

[40] Y.-C. Fan, C.-H. Loh, J. N. Yang, P.-Y. Lin, Experimental performance evaluation of an equipment isolation using MR dampers, Earthquake Engineering and Structural Dynamics 38 (2009) 285–305. doi:10.1002/eqe.844.

[41] H. P. Gavin, A. Zaicenco, Performance and reliability of semi-active equipment isolation, Journal of Sound and Vibration 306 (2007) 74–90. doi:10.1016/j.jsv.2007.05.039.

[42] P.-Y. Lin, T.-K. Lin, Control of seismically isolated bridges by magnetorheological dampers and a rolling pendulum system, Structural Control and Health Monitoring 19 (2012) 278–294. doi:10.1002/stc.431.

[43] S. Cui, Integrated design methodology for isolated floor systems in single-degree-of-freedom structural fuse systems, Ph.D. thesis, State University of New York, Buffalo (2012).

[44] E. Y. Antonyuk, N. P. Plakhtienko, Dynamic modes of one seismic-damping mechanism with frictional bonds, International Applied Mechanics 40(6) (2004) 702–708. doi:10.1023/B:INAM.0000041399.99257.b3.

[45] V. P. Legeza, Analytic determination of the amplitudefrequency characteristic of a nonlinear vibroprotective system with roller dampers, Strength of Materials 36 (2005) 282–290. doi:10.1007/s11223-005-0033-y.

[46] E. Matta, A. De Stefano, B. F. Spencer Jr, A new passive rolling-pendulum vibration absorber using a non-axial-symmetrical guide to achieve bidirectional tuning, Earthquake Engineering and Structural Dynamics 38 (2009) 1729–1750. doi:10.1002/eqe.929.

[47] A. H. Muhr, G. Bergamo, Shaking table tests on rolling-ball rubber-layer isolation system, in: 14th European Conference on Earthquake Engineering, 2010.

[48] D. Foti, A. Catalan Goni, S. Vacca, On the dynamic response of rolling base isolation systems, Structural Control and Health Monitoring 20 (2013) 639–648. doi:10.1002/stc.1538.

[49] Z. Kemeney, ISO-Base™ Seismic Isolation Platform: Technical documentation (October 2003).
URL http://63.247.64.102/~isobasec/downloads/ISOTekBook_Issue2.pdf

[50] B. Myslimaj, S. Gamble, D. Chin-Quee, A. Davies, B. Breukelman, Base isolation technologies for seismic protection of museum artifacts, in: The 2003 IAMFA Annual Conference in San Francisco, California, IAMFA, San Francisco, CA, 2003.

[51] C. Alahan, H. P. Gavin, Reliability of base isolation for the protection of critical equipment from earthquake hazards, Engineering Structures 27 (2004) 1435–1449. doi:10.1016/j.engstruct.2005.04.007.

[52] P. S. Harvey Jr, H. P. Gavin, A simplified and experimentally-validated predictive model of a rolling isolation system, Earthquake Engineering and Structural Dynamics (under review).

[53] P. S. Harvey Jr, H. P. Gavin, Modelling of stacked rolling isolation platforms, International Journal of Non-Linear Mechanics (under review).

[54] P. S. Harvey Jr, H. P. Gavin, Vibration suppression using stacked rolling isolation systems: modeling and experimental results, Journal of Vibration and Acoustics (under review).

[55] N. Mostaghel, M. Hejazi, J. Tanbakuchi, Response of sliding structures to harmonic support motion, Earthquake Engineering and Structural Dynamics 11 (1983) 355–366. doi:10.1002/eqe.4290110305.

[56] J. M. Kelly, The role of damping in seismic isolation, Earthquake Engineering and Structural Dynamics 28 (1999) 3–20. doi:10.1002/(SICI)1096-9845(199901)28:1<3::AID-EQE801>3.0.CO;2-D.

[57] L. Y. Lu, G. L. Lin, A theoretical study on piezoelectric smart isolation system for seismic protection of equipment in near-fault areas, Journal of Intelligent Material Systems and Structures 20 (2009) 217–232. doi:10.1177/1045389X08091120.

[58] S. Nagarajaiah, S. Narasimhan, Smart base isolated benchmark building part II: Phase I sample controllers for linear isolation systems, Structural Control and Health Monitoring 13 (2006) 589–604. doi:10.1002/stc.100.

[59] R. F. Stengel, Optimal control and estimation, Dover, New York, NY, 1994.

[60] R. Luus, Piecewise linear continuus optimal control by iterative dynamic programming, Industrial & Engineering Chemistry Research 32 (1993) 859–865. doi:10.1021/ie00017a014.

[61] M. Sznaier, M. J. Damborg, Suboptimal control of linear systems with state and control inequality constraints, in: Proceedings of the 26th IEEE Conference on Decision and Control, 1987, pp. 761–762.

[62] F. Sadek, B. Mohraz, Semiactive control algorithms for structures with variable dampers, Journal of Engineering Mechanics 124(9) (1998) 981–990.

[63] P. S. Harvey Jr, R. Wiebe, H. P. Gavin, On the chaotic response of a nonlinear rolling isolation system, Physica D 256-257 (2013) 36–42. doi:j.physd.2013.04.013.

[64] P. S. Harvey Jr, H. P. Gavin, J. T. Scruggs, J. M. Rinker, Determining the physical limits on semi-active control performance: A tutorial, Structural Control and Health Monitoring (accepted).

[65] P. S. Harvey Jr, G.-P. Zéhil, H. P. Gavin, A validated predictive model for damped rolling pendulum isolation systems, Earthquake Engineering and Structural Dynamics (under review).

[66] P. S. Harvey Jr, H. P. Gavin, Truly isotropic biaxial hysteresis with arbitrary knee sharpness, Earthquake Engineering and Structural Dynamics (under review).

[67] D. T. Greenwood, Advanced dynamics, Cambridge University Press, New York, NY, 2003.

[68] F. E. Udwadia, R. E. Kalaba, A new perspective on constrained motion, Proceedings of the Royal Society A 439 (1992) 407–410.

[69] M. R. Flannery, d'Alembert-Lagrange analytical dynamics for nonholonomic systems, Journal of Mathematical Physics 52 (2011) 032705. doi:10.1063/1.3559128.

[70] J. R. Ray, Nonholonomic constraints, American Journal of Physics 34 (1966) 1202–1203.

[71] O. E. Fernandez, A. M. Bloch, Equivalence of the dynamics of nonholonomic an variational nonholonomic systems for certain initial data, Journal of Physics A 41 (2008) 344005. doi:10.1088/1751-8113/41/34/344005.

[72] C. Lanczos, The variational principles of mechanics, Dover Publications, New York, NY, 1970.

[73] M. Moshre-Torbati, J. A. Forrester, A. I. J. Forrester, A. J. Keane, M. J. Brennan, S. J. Elliott, Novel active and passive anti-vibration mountings, Journal of Sound and Vibration 331 (2012) 1532–1541. doi:10.1016/j.jsv.2011.12.005.

[74] W. H. Robinson, Energy absorber U.S. Patent 6321492 B1.

[75] G. Stuve, Earthquake bearing U.S. Patent 5071261.

[76] D. G. Flom, M. Bueche, Theory of rolling friction for spheres, Journal of Applied Physics 30 (1959) 1725–1730. doi:10.1063/1.1735043.

[77] M. R. Flannery, The enigma of nonholonomic constraints, American Journal of Physics 73(3) (2005) 265–272. doi:10.1119/1.1830501.

[78] M. R. Flannery, The elusive d'Alembert-Lagrange dynamics of nonholonomic systems, American Journal of Physics 79(9) (2011) 932–944. doi:10.1119/1.3563538.

[79] K. A. Levenberg, A method for the solution of certain non-linear problems in least squares, Quarterly of Applied Mathematics 2 (1944) 164–168.

[80] D. Marquardt, An algorithm for least-squares estimation of nonlinear parameters, SIAM Journal on Applied Mathematics 11(2) (1963) 431–441.

[81] K. L. Yung, Y. Xu, Non-linear expressions for rolling friction of a soft ball on a hard plane, Nonlinear Dynamics 33 (2003) 33–41. doi:10.1023/A:1025582521870.

[82] S. H. Strogatz, Nonlinear dynamics and chaos, Perseus Books Publishing, LLC, Cambridge, MA, 1994.

[83] X. C. Xie, Dynamic stability of structures, Cambridge University Press, New York, NY, 2006.

[84] A. Wolf, J. B. Swift, H. L. Swinney, J. A. Vastano, Determining Lyapunov exponents from a time series, Physica D 16(3) (1985) 285–317. doi:10.1016/0167-2789(85)90011-9.

[85] J. Podany, Advances in the protection of museum collections from earthquake damage, J. Paul Getty Museum, 2008.

[86] C.-M. Chang, B. F. Spencer Jr, Active base isolation of buildings subjected to seismic excitations, Earthquake Engineering and Structural Dynamics 39 (2010) 1493–1512. doi:10.1002/eqe.1040.

[87] MATLAB, no. version 7.13.0.564, The MathWorks Inc., Natick, Massachusetts, 2011.

[88] L. N. Virgin, C. J. Begley, Grazing bifurcations and basins of attraction in an impact-friction oscillator, Physica D 130 (1999) 43–57. doi:10.1016/S0167-2789(99)00016-0.

[89] ASCE/SEI 7-10, Minimum design loads for buildings and other structures, Structural Engineering Institute of ASCE, Reston, VA, 2010.

[90] G.-P. Zéhil, H. P. Gavin, Simplied approaches to viscoelastic rolling resistance, International Journal of Solids and Structures 50 (2012) 853–86. doi:10.1016/j.ijsolstr.2012.09.025.

[91] C. J. Begley, L. N. Virgin, Impact response and the influence of friction, Journal of Sound and Vibration 211 (1998) 801–818. doi:10.1006/jsvi.1997.1389.

[92] D. B. Moore, S. W. Shaw, The experimental response of an impacting pendulum system, International Journal of Non-Linear Mechanics 25 (1990) 1–16. doi:10.1016/0020-7462(90)90034-7.

[93] Q. K. Ghori, N. Ahmed, Principles of Lagrange and Jacobi for nonholonomic systems, International Journal of Non-Linear Mechanics 34 (1999) 823–829. doi:10.1016/S0020-7462(98)00052-3.

[94] A. D. Lewis, R. M. Murray, Variational principles for constrained systems: theory and experiment, International Journal of Non-Linear Mechanics 30 (1995) 793–815. doi:10.1016/0020-7462(95)00024-0.

[95] Z. K. Peng, Z. Q. Lang, X. J. Jing, S. A. Billings, G. R. Tomlinson, L. Z. Guo, The transmissibility of vibration isolators with a nonlinear antisymmetric damping characteristic, Journal of Vibration and Acoustics 132 (2010) 014501–1–014501–7. doi:10.1115/1.4000476.

[96] Y.-T. Choi, N. M. Wereley, Shock isolation systems using magnetorheological dampers, Journal of Vibration and Acoustics 130 (2008) 024503–1–024503–6. doi:10.1115/1.2775517.

[97] M. Heertjes, N. van de Wouw, Nonlinear dynamics and control of a pneumatic vibration isolator, Journal of Vibration and Acoustics 128 (2006) 439–448. doi:10.1115/1.2128642.

[98] G. W. Housner, L. A. Bergman, T. K. Caughey, A. G. Chassiakos, R. O. Claus, S. F. Masri, R. E. Skelton, T. T. Soong, B. F. Spencer, J. T. P. Yao, Structural control: Past, present, and future, Journal of Engineering Mechanics 123 (1997) 897–971. doi:10.1061/(ASCE)0733-9399(1997)123:9(897).

[99] M. D. Symans, M. C. Constantinou, Semi-active control systems for seismic protection of structures: a state- of-the-art review, Engineering Structures 21 (1999) 469–487. doi:10.1016/S0141-0296(97)00225-3.

[100] S. Nagarajaiah, Adaptive passive, semiactive, smart tuned mass dampers: identification and control using empirical mode decomposition, Hilbert transform, and short-term Fourier transform, Structural Control and Health Monitoring 16 (2009) 800–841. doi:10.1002/stc.349.

[101] J. Kang, H. S. Kim, D. G. Lee, Mitigation of wind response of a tall building using semi-active tuned mass dampers, Structural Design of Tall and Special Buildings 20 (2011) 552–565. doi:10.1002/tal.609.

[102] D. F. Ledezma-Ramirez, N. S. Ferguson, M. J. Brennan, Shock isolation using an isolator with switchable stiffness, Journal of Sound and Vibration 330 (2011) 868–882. doi:j.jsv.2010.09.016.

[103] D. T. R. Pasala, S. Nagarajaiah, K. M. Grigoriadis, Tracking control of variable stiffness hysteretic-systems using linear-parameter-varying gain-scheduled controller, Smart Structures and Systems 9 (2012) 373–392.

[104] G. W. Rodgers, J. G. Chase, T. Roland, G. A. MacRae, Spectral analysis for a semi-active-passive net-zero base-shear design concept, Earthquake Engineering and Structural Dynamics 41 (2012) 1207–1216. doi:10.1002/eqe.1177.

[105] I. L. Cassidy, J. T. Scruggs, S. Behrens, H. P. Gavin, Design and experimental characterization of an electromagnetic transducer for large-scale vibratory energy harvesting applications, Journal of Intelligent Material Systems and Structures 22 (2011) 2009–2024. doi:10.1177/1045389X11421824.

[106] C. Chen, W.-H. Liao, A self-sensing magnetorheological damper with power generation, Smart Materials and Structures 21 (2012) 025041. doi:10.1088/0964-1726/21/2/025014.

[107] Z. Jiang, R. E. Christenson, A fully dynamic magneto-rheological fluid damper model, Smart Materials and Structures 21 (2012) 065002. doi:10.1088/0964-1726/21/6/065002.

[108] S. Laflamme, D. Taylor, M. A. Maane, J. J. Connor, Modified friction device for control of large-scale systems, Structural Control and Health Monitoring 19 (2012) 548–564. doi:10.1002/stc.454.

[109] G. L. Lin, C. C. Lin, L. Y. Lu, Y. B. Ho, Experimental verification of seismic vibration control using a semi-active friction tuned mass damper, Earthquake Engineering and Structural Dynamics 41 (2012) 813–830. doi:10.1002/eqe.1162.

[110] D. E. Kirk, Optimal Control Theory, An Introduction, Prentice Hall, 1970.

[111] H. E. Tseng, J. K. Hedrick, Semi-active control laws - optimal and sub-optimal, Vehicle System Dynamics 23 (1994) 545–569. doi:10.1080/00423119408969074.

[112] D. Hrovat, D. L. Margolis, M. Hubbard, An approach toward the optimal semi-active suspension, Journal of Dynamic Systems, Measurement, and Control 110 (1988) 288–296. doi:10.1115/1.3152684.

[113] J. Leavitt, F. Jabbari, J. E. Bobrow, Optimal performance of variable stiffness devices for structural control, Journal of Dynamic Systems, Measurement, and Control 129 (2007) 171–177. doi:10.1115/1.2432360.

[114] C. E. García, D. M. Prett, M. Morari, Model predictive control: Theory and practice—A survey, Automatica 25 (1989) 335–248. doi:10.1016/0005-1098(89)90002-2.

[115] N. Giorgetti, A. Bemporad, H. E. Tseng, D. Hrovat, Hybrid model predictive control application towards optimal semi-active suspension, International Journal of Control 79 (2006) 521–533. doi:10.1109/ISIE.2005.1528942.

[116] T. Butsuen, The design of semi-active suspension for automotive vehicles, Ph.D. Thesis, Massachusetts Institute of Technology, Department of Mechanical Engineering (1989).

[117] J. Kierzenka, L. F. Shampine, A BVP solver based on residual control and the MATLAB PSE, ACM Transactions on Mathematical Software 27(3) (2001) 299–316. doi:10.1145/502800.502801.

[118] L. F. Shampine, I. Gladwell, S. Thompson, Solving ODEs with matlab, Cambridge University Press, 2003.

[119] A. E. Bryson, Y. C. Ho, Applied optimal control: optimization, estimation, and control, Hemisphere, Washington, D.C., 1975.

[120] T. J. Gordon, Non-linear optimal control of a semi-active vehicle suspension system, Chaos, Solitons & Fractals 5 (9) (1995) 1603–1617. doi:10.1016/0960-0779(94)00166-N.

[121] D. Hrovat, F. Barak, M. Rabins, Semi-active versus passive or active tuned mass dampers for structural control, Journal of Engineering Mechanics 109 (9) (1983) 691–705. doi:10.1061/(ASCE)0733-9399(1983)109:3(691).

[122] J. P. Den Hartog, Mechanical Vibration, Dover, 1985.

[123] W.-L. He, A. K. Agrawal, Analytical model of ground motion pulses for the design and assessment of seismic protective systems, Journal of Structural Engineering 134 (2008) 1177–1188. doi:10.1061/(ASCE)0733-9445(2008)134:7(1177).

[124] Applied Technology Council, Quantification of building seismic performance factors.
URL https://www.atcouncil.org/Projects/atc-63-project.html

[125] H. P. Gavin, C. Alhan, Guidelines for low-transmissibility semi-active vibration isolation, Journal of Smart Materials and Structures 14 (2005) 297–306. doi:10.1088/0964-1726/14/2/001.

[126] Y. L. Xu, H. J. Liu, Z. C. Yang, Hybrid platform for vibration control of high-tech equipment in buildings subject to ground motion. Part 1: Experiment, Earthquake Engineering and Structural Dynamics 32 (2003) 1185–1200. doi:10.1002/eqe.267.

[127] K. Yi, K. Hedrick, Dynamics tire force control by semiactive suspension, Journal of Dynamic Systems, Measurement, and Control 115 (1993) 465–474. doi:doi:10.1115/1.2899124.

[128] D. Karnopp, M. J. Crosby, R. A. Harwood, Vibration control using semi-active force generators, ASME Journal of Engineering for Industry 96 (1974) 619–626. doi:10.1115/1.3438373.

[129] C. Poussot-Vassal, O. Sename, L. Dugard, P. Gáspár, Z. Szabó, J. Bokor, A new semi-active suspension control strategy through LPV techniques, Control Engineering Practice 16 (2008) 1519–1534. doi:10.1016/j.conengprac.2008.05.002.

[130] H. Iemura, M. H. Pradono, Simple algorithm for semi-active seismic response control of cable-stayed bridges, Earthquake Engineering and Structural Dynamics 34 (2005) 409–423. doi:10.1002/eqe.440.

[131] N. R. Sandell Jr, P. Varaiya, M. Athans, M. G. Safonov, Survey of decentralized control methods for large scale systems, IEEE Transactions on Automatic Control 23(2) (1978) 108–128. doi:10.1109/TAC.1978.1101704.

[132] M. C. Constantinou, A. S. Mokha, A. S. Reinhorn, Teflon bearings in base isolation II: Modeling, Journal of Structural Engineering 116 (2) (1990) 455–474. doi:10.1061/(ASCE)0733-9445(1990)116:2(455).

[133] C. C. Marin-Artieda, A. S. Whittaker, Theoretical studies of the XY-FP seismic isolation bearing for bridges, Journal of Bridge Engineering 15 (2010) 631–638. doi:10.1061/(ASCE)BE.1943-5592.0000103.

[134] J. A. Greenwood, D. Tabor, The friction of hard sliders on lubricated rubber: The importance of deformation losses, Proceedings of the Physical Society 71 (6) (1958) 989–1001. doi:10.1088/0370-1328/71/6/312.

[135] G.-P. Zéhil, H. P. Gavin, Three-dimensional boundary element formulation of an incompressible viscoelastic layer of finite thickness applied to the rolling resistance of a rigid sphere, International Journal of Solids and Structures 50 (2013) 833–842. doi:10.1016/j.ijsolstr.2012.11.020.

[136] P. S. Harvey Jr, H. P. Gavin, Assessing the accuracy of vision-based accelerometry, Experimental Mechanics (in press). doi:10.1007/s11340-013-9783-9.

[137] R. P. Santa-Ana, E. Miranda, Strength reduction factors for multi-degree-of-freedom systems, in: Proc. 12th World Conf. on Earthquake Engineering, Auckland, New Zealand, 2000.

[138] S. R. Chaudhuri, R. Villaverde, Effect of building nonlearity on seismic response of nonstructural components: A parametric study, Journal of Structural Engineering 134 (2008) 661–670. doi:10.1061/(ASCE)0733-9445(2008)134:4(661).

[139] H. P. Gavin, FRAME3dd: Static and Dynamic Structural Analysis of 2D and 3D Frames.
URL http://frame3dd.sourceforge.net/

[140] F. Bamer, C. Bucher, Application of the proper orthogonal decomposition for linear and nonlinear structures under transient excitations, Acta Mechanica 223 (2012) 2549–2563. doi:10.1007/s00707-012-0726-9.

[141] R. Kappagantu, B. F. Feeny, An "optimal" modal reduction of a system with frictional excitation, Journal of Sound and Vibration 224 (1999) 863–877. doi:10.1006/jsvi.1999.2165.

[142] L. F. Geschwindner, Non-linear dynamic analysis of modal superposition, Journal of Structural Division-ASCE 107 (1981) 2325–2336.

[143] R. Villaverde, M. M. Hanna, Efficient mode superposition algorithm for seismic analysis of nonlinear structures, Earthquake Engineering and Structural Dynamics 21 (1992) 849–858. doi:10.1002/eqe.4290211002.

[144] M. Paz, Dynamic condensation, AIAA Journal 22 (1985) 724–727.

[145] Y. J. Park, Y. K. Wen, A. H.-S. Ang, Random vibration of hysteretic systems under bi-directional ground motion, Earthquake Engineering and Structural Dynamics 14 (1986) 543–557. doi:10.1002/eqe.4290140405.

[146] R. W. Clough, J. Penzien, Dynamics of Structures, 2nd Edition, Computers and Structures, Inc., 2003.

[147] R. Bouc, Forced vibration of mechanical systems with hysteresis, in: Proceedings of the Fourth Conference on Nonlinear Oscillation, Prague, Czechoslovakia, 1967.

[148] Y.-K. Wen, Method for random vibration of hysteretic systems, Journal of Engineering Mechanics 102 (1976) 249–263.

[149] C. W. Wong, Y. Q. Ni, J. M. Ko, Stead-state oscillation of hysteretic differential model II: Performance analysis, Journal of Engineering Mechanics 120 (11) (1994) 2299–2325. doi:10.1061/(ASCE)0733-9399(1994)120:11(2271).

[150] B. G. Neal, The plastic method of structural analysis, 3rd Edition, Chapman & Hall, New York, 1977.

[151] H. Lee, EPFRAME: Elastic Plastic Analysis of a Plane Frame (1986).
URL http://nees.org/tools/epframe/

[152] Pacific Earthquake Engineering Research Center, Next Generation Attenuation Database (2005).
URL http://peer.berkeley.edu/nga/

[153] J. P. Stewart, N. A. Abrahamson, G. M. Atkinson, J. W. Baker, D. M. Boore, Y. Bozorgnia, K. W. Campbell, C. D. Comartin, I. M. Idriss, M. Lew, M. Mehrain, J. P. Moehle, F. Naeim, T. A. Sabol, Representation of bidirectional ground motions for design spectra in building codes, Earthquake Spectra 27 (2011) 927–937. doi:10.1193/1.3608001.

[154] Y. Chen, T. T. Soong, Seismic response of secondary systems, Engineering Structures 10 (1988) 218–228. doi:10.1016/0141-0296(88)90043-0.

[155] NZS 1170.5:2004, Structural Design Actions Part 5: Earthquake Actions - New Zealand, Standards New Zealand, New Zealand, 2004.

[156] R. A. Ibrahim, Recent advances in nonlinear passive vibration isolators, Journal of Sound and Vibration 314 (2008) 371–452. doi:10.1016/j.jsv.2008.01.014.

[157] T.-W. Lin, C. C. Hone, Base isolation by free rolling rods under basement, Earthquake Engineering and Structural Dynamics 22 (1993) 261–273. doi:10.1002/eqe.4290220307.

[158] J. W. Butterworth, Seismic response of a non-concentric rolling isolator system, Advances in Structural Engineering 9 (2006) 39–53. doi:10.1260/136943306776232918.

[159] M. Barghian, A. B. Shahabi, A new approach to pendulum base isolation, Structural Control and Health Monitoring 14 (2007) 177–185. doi:10.1002/stc.115.

[160] B. Ravindra, A. K. Mallik, Chaotic response of a harmonically excited mass on an isolator with non-linear stiffness and damping characteristics, Journal of Sound and Vibration 182 (1995) 345–353. doi:10.1006/jsvi.1995.0203.

[161] R. Wiebe, L. N. Virgin, A heuristic method for identifying chaos from frequency content, Chaos 22 (2012) 013136. doi:10.1063/1.3675624.

[162] P. Olaszek, Investigation of the dynamic characteristic of bridge structures using a computer vision method, Measurement 25 (1999) 227–236. doi:10.1016/S0263-2241(99)00006-8.

[163] A. M. Wahbeh, J. P. Caffrey, S. F. Masri, A vision-based approach for the direct measurement of displacements in vibrating systems, Journal of Smart Materials and Structures 12 (2003) 785–794. doi:10.1088/0964-1726/12/5/016.

[164] R. Jiang, D. V. Jauregui, Development of a digital close-range photogrammetric bridge deflection measurement system, Measurement 43 (2010) 1431–1438. doi:10.1016/j.measurement.2010.08.015.

[165] J. Leifer, B. J. Weems, S. C. Kienle, A. M. Sims, Three-dimensional acceleration measurement using videogrammetry tracking data, Experimental Mechanics 51 (2011) 199–217. doi:10.1007/s11340-010-9352-4.

[166] A. Savitzky, M. Golay, Smoothing and differentiation of data by simplified least squares procedures, Analytical Chemistry 36 (1964) 1627–1639. doi:10.1021/ac60214a047.

[167] C. C. Chang, Y. F. Ji, Flexible videogrammetric technique for three-dimensional structural vibration measurement, Journal of Engineering Mechanics 133 (2007) 656–664. doi:10.1061/(ASCE)0733-9399(2007)133:6(656).

[168] Y. Fukuda, M. Q. Feng, M. Shinozuka, Cost-effective vision-based system for monitoring dynamic response of civil engineering structures, Structural Control and Health Monitoring 17 (2010) 918–936. doi:10.1002/stc.360.

[169] S. C. Kienle, A. M. Sims, J. Leifer, Full-field acceleration measurement using videogrammetry, in: Proceedings of the 26th International Modal Analysis Conference, Orlando, FL, 2008.

[170] M. Power, B. Chiou, N. Abrahamson, Y. Bozorgnia, T. Shantz, C. Roblee, An overview of the NGA project, Earthquake Spectra 24 (1) (2008) 3–21. doi:10.1193/1.2894833.

[171] J.-K. Song, H. P. Gavin, Effect of hysteretic smoothness on inelastic response spectra with constant-ductility, Earthquake Engineering and Structural Dynamics 40 (2011) 771–788. doi:10.1002/eqe.1058.

[172] M. Ismail, F. Ikhouane, J. Rodellar, The hysteresis Bouc-Wen model, a survey, Archives of Computational Methods in Engineering 16 (2009) 161–188. doi:10.1007/s11831-009-9031-8.

[173] M. V. Sivaselvan, A. M. Reinhorn, Hysteretic models for deteriorating inelastic structures, Journal of Engineering Mechanics 126 (6) (2000) 633–640. doi:10.1061/(ASCE)0733-9399(2000)126:6(633).

[174] T. T. Baber, M. N. Noori, Random vibration of degrading, pinching systems, Journal of Engineering Mechanics 111 (1985) 1010–1026. doi:10.1061/(ASCE)0733-9399(1985)111:8(1010).

[175] J. Song, A. Der Kiureghian, Generalized Bouc-Wen model for highly asymmetric hysteresis, Journal of Engineering Mechanics 132 (2006) 610–618. doi:10.1061/(ASCE)0733-9399(2006)132:6(610).

[176] R. S. Jangid, Seismic response of sliding structures to bidirectional earthquake excitation, Earthquake Engineering and Structural Dynamics 25 (1996) 1301–1306. doi:10.1002/(SICI)1096-9845(199611)25:11<1301::AID-EQE618>3.0.CO;2-3.

[177] R. S. Jangid, Computational numerical models for seismic response of structures isolated by sliding systems, Structural Control and Health Monitoring 12 (2005) 117–137. doi:10.1002/stc.59.

[178] H. P. Gavin, P. S. Harvey Jr, Isoductile response spectra for triaxial ground motions (in preparation).

[179] C.-H. Wang, Y.-K. Wen, Evaluation of pre-northridge low-rise steel buildings I: Modeling, Journal of Structural Engineering 126 (2000) 1160–1168. doi:10.1061/(ASCE)0733-9445(2000)126:10(1160).

[180] H. Rodrigues, X. Romão, A. Andrade-Campos, H. Varum, A. Arêde, A. G. Costa, Simplified hysteretic model for the representation of the biaxial bending response

of RC columns, Engineering Structures 44 (2012) 146–158. doi:10.1016/j.engstruct.2012.05.050.

[181] C. S. Lee, H. P. Hong, Statistics of inelastic responses of hysteretic systems under bidirectional seismic excitation, Engineering Structures 32 (10) (2010) 20742086. doi:10.1016/j.engstruct.2010.03.008.

[182] M. A. Karray, R. Bouc, Étude dynamique dun systéme disolation antisismique, Annales de l'ENIT 3 (1989) 43–60.

[183] F. Casciati, Stochastic dynamics of hysteretic media, Structural Safety 6 (2-4) (1989) 259–269. doi:10.1016/0167-4730(89)90026-X.

[184] P. S. Harvey Jr, H. P. Gavin, Performance limits imposed by semi-active damping constraints, in: Proceedings of the 2010 American Controls Conference, 2010, pp. 732–737.

[185] P. S. Harvey Jr, H. P. Gavin, Approximate solutions to nonlinearly-constrained optimal control problems, in: Proceedings of the 2011 American Controls Conference, 2011, pp. 3122–3128.

[186] P. S. Harvey Jr, J. T. Scruggs, H. P. Gavin, A dual method for determining the performance limits of a semiactively constrained control systems, in: Proceedings of the 2012 American Controls Conference, 2012, pp. 1549–1554.

# Biography

Philip Scott Harvey, Jr. was born on March 15, 1987 in Edenton, NC. He received both his B.S.E. and M.S. degrees in Civil and Environmental Engineering from Duke University in Durham, NC in 2009 and 2012, respectively. His Masters thesis was completed under the advisement of Prof. Henri Gavin and was entitled "Modeling and Control of an Equipment Isolation System for Critical Facilities." In all, Scott has authored or co-authored ten journal articles [38, 39, 52–54, 63–66, 136] and three conference papers [184–186] through the course of his Ph.D. research. In addition, he was awarded the James B. Duke Fellowship by Duke University, won the American Controls Conference (ACC) student travel award (selected by an ACC Organizing Committee), and received funding to participate in the Asia-Pacific Summer School in Smart Structures Technology in Tokyo, Japan. Following his Ph.D., Scott has accepted a post-doctoral research position with Prof. Lawrence Virgin at Duke University starting in August 2013.